

The Adsorption of Molybdate($\text{Mo(VI)}\text{O}_4^{2-}$) and Vanadate($\text{V(V)}\text{O}_4^{3-}$) to Iron Oxides

A thesis submitted to The University of Manchester for the degree of

Doctor of Philosophy

in the Faculty of Science and Engineering

2021

Jing Zhang

Department of Earth & Environmental Sciences

Blank page

Contents

List of Figures	9
List of Tables	17
List of Abbreviations	20
Thesis Abstract.....	21
Declaration.....	22
Copyright Statement	23
Acknowledgements.....	24
About the Author	25
1. Project Introduction and Thesis Structure.....	26
1.1 Background	26
1.2 Aims and Objectives	29
1.3 Thesis Structure.....	31
2. Literature Review.....	34
2.1 Molybdenum (Mo)	34
2.1.1 Mo Application in Industry	34
2.1.2 Mo Environmental Geochemistry	34
2.1.3 Role of Molybdenum in Plant, Animal and Human Health	37
2.1.4 Occurrence and Distribution of Mo in the Environment.....	39
2.1.4.1 Mo in Surface and Ground Water.....	39
2.1.4.2 Mo in Rocks, Sediments, Minerals and Soils	42
2.2 Vanadium	44
2.2.1 V Application in Industry	44
2.2.2 Vanadium Environmental Geochemistry	44

2.2.3 Role of V in Plant, Animal and Human Health.....	47
2.2.4 Occurrence and Distributions of V in the Environment.....	48
2.2.4.1 V in Soils, Minerals and Rocks	48
2.2.4.2 V in Groundwater and Surface Water.....	52
2.3 Iron Oxides.....	55
2.3.1 Hematite.....	55
2.3.2 Magnetite	56
2.3.3 Biogenic Magnetite.....	57
2.4 Mo Interaction with Iron Oxides.....	58
2.4.1 Mo Sorption to Iron Oxides.....	58
2.4.2 Surface Adsorption Modeling	60
2.4.3 Attenuated Total Reflection-Fourier Transform Infrared (ATR-FTIR) of Mo Adsorption	62
2.4.4 X-ray Absorption Spectroscopy (XAS) Studies of Mo Adsorption	65
2.4.5 Mo Redox Processes.....	70
2.4.6 Mo Reduction by Iron Oxides	71
2.5 V Interaction with Iron Oxides.....	72
2.5.1 V Sorption to Iron Oxides	72
2.5.2 Adsorption Models	73
2.5.3 Attenuated Total Reflectance-Fourier Transform Infrared Spectroscopy (ATR-FTIR) Studies of V Adsorption	74
2.5.4 X-ray Absorption Spectroscopy (XAS) Studies of V Adsorption.....	76
2.5.5 V Reduction by Iron Oxides	79
2.6 Summary	81
3. Research Methods.....	83

3.1 Experimental Overview.....	83
3.2 Iron(oxyhydr)oxide Synthesis	83
3.2.1 Synthesis of Hematite.....	84
3.2.2 Synthesis of Magnetite	84
3.2.3 Synthesis of Biogenic magnetite	86
3.2.3.1 Cell Cultures	87
3.3 Adsorption Experiments.....	88
3.3.1 Solution Experiment for Mo(VI) Adsorption to Hematite	88
3.3.2 Solution Experiment for V(V) Adsorption to Hematite	89
3.3.3 Solution Experiment for Mo(VI) and V(V) Adsorption to Magnetite and Biogenic Magnetite	90
3.4 Aqueous Geochemistry	90
3.4.1 Geochemical/Isotherm Adsorption Model	90
3.4.2 Ferrozine Assay	91
3.4.3 Inductively Coupled Plasma Atomic Emission Spectroscopy (ICP-AES) and Inductively Coupled Plasma Mass Spectrometry (ICP-MS).....	92
3.5 Solid Analysis	93
3.5.1 X-ray Diffraction (XRD).....	93
3.5.2 Brunauer-Emmett-Teller (BET) Surface Area Analysis	94
3.5.3 Transmission Electron Microscopy (TEM).....	95
3.5.4 Attenuated Total Reflection-Fourier Transform Infrared Spectroscopy (ATR-FTIR)	96
3.5.5 X-ray Photoelectron Spectroscopy (XPS)	98
3.6 Synchrotron Techniques.....	99
3.6.1 Synchrotron Radiation.....	99

3.6.2 X-ray Absorption Spectroscopy (XAS).....	100
3.6.2.1 X-ray Absorption Near Edge Structure (XANES).....	102
3.6.2.2 Extended X-ray Absorption Fine Structure (EXAFS)	104
3.6.2.3 B18 Beamline.....	105
3.6.2.4 I20 Beamline.....	105
3.6.2.5 The F-test	107
4. Adsorption of Octahedral Mono-molybdate and Poly-molybdate onto Hematite: A Multi-technique Approach	109
4.1 Abstract	109
4.2 Introduction	110
4.3 Experimental Methods	114
4.4 Results and Discussion.....	116
4.5 Conclusions	128
Supporting Information for Chapter 4	130
5. A Multi-technique Approach on the Investigation of Mono- and Poly-vanadate (VO_4^{3-}) Adsorption to Hematite.....	142
5.1 Abstract	142
5.2 Introduction	143
5.3 Experimental Methods	147
5.4 Results and Discussion.....	149
5.5 Conclusions	164
6. Molybdate ($\text{Mo(VI)}\text{O}_4^{2-}$) Adsorption to Magnetite and Biogenic magnetite	166
6.1 Abstract	166
6.2 Introduction	167
6.3 Experimental Methods	170

6.4 Results and Discussion.....	172
6.5 Conclusions	183
7. Conclusions and Future Work	184
7.1 Conclusions	184
7.2 Future Work	188
8. References.....	191
9. Appendices.....	203
9.1 Appendix 1: Vanadate ($V(V)O_4^{3-}$) Adsorption to Magnetite and Biogenic Magnetite	203
9.2 Appendix 2: Travel Bursaries and Conference Presentations	206

Blank page

List of Figures

Figure 2-1 3D model of A. molybdate (MoO_4^{2-}) and B. polymolybdate ($\text{Mo}_7\text{O}_{24}^{6-}$) (Davantès and Lefèvre 2013). Red atoms are O and the purple atom is Mo.	35
Figure 2-2 Distribution of Mo(VI) speciation as function of pH at initial Mo concentration of 0.03-0.1 mM. Adapt from (Ozeki et al. 1988).	37
Figure 2-3 Structure of vanadate. A. Tetrahedral monovanadate (VO_4^{3-}). B. Octahedral decavanadate ($\text{V}_{10}\text{O}_{28}^{6-}$) (Evans Jr 1966).....	46
Figure 2-4 Eh-pH diagram for V aqueous species in V-O-H system from (Peacock and Sherman 2004). The concentration of total V is 5×10^{-5} m (~2.5 ppm).	46
Figure 2-5 Diagrams for aqueous V speciation at 100, 500, 1000, and 5000 μM based on thermodynamic data using PHREEQCi (Version 3.1.5) from (Vessey et al. 2020).....	47
Figure 2-6 Major deposits of V in the world from (Imtiaz et al. 2015). V occurrence varies in different minerals such as vanadinite, roscoelite, patronite, chileite, and carnotite. The average V concentration ranges from 3 to 310 mg/kg, but 1600 mg/g is contained in phosphate rocks.	50
Figure 2-7 Vanadium global biogeochemical cycle from (Schlesinger et al. 2017, Gustafsson 2019). All values are in 10^9 grams per year (Gg V yr^{-1}).	51
Figure 2-8 Crystal structure of hematite by ball-and-stick model from (Wu et al. 2015). The red atoms are O and the green ones are Fe.	56
Figure 2-9 Crystal structure of magnetite by ball-and-stick model from (Noh et al. 2014). Fe atoms are in blue and O atoms are in red.	57
Figure 2-10 Structure of inner-sphere and outer-sphere complexation (Arce et al. 2011).	58
Figure 2-11 Mo adsorption to hematite (A) and magnetite (B) as function of pH from (Goldberg et al. 1996, Verbinen et al. 2012).	60

Figure 2-12 ATR-FTIR spectra of Mo(VI) adsorbed to hematite in varying conditions from (Davantes et al. 2017)	64
Figure 2-13 Normalized Mo K-edge XANES for standards and samples from Fe/Mo system at t = 0-96 h from (Das et al. 2016)	66
Figure 2-14 Normalized Mo K-edge XANES for standards (Na_2MoO_4 , MoO_3 and MoO_2) and samples from Mo(VI) incorporation in hematite, goethite and ferrihydrite with spectra inset with more detailed pre-edge feature. goe 1.0 and hem_1.0 represent the initial Mo:Fe molar ratio of 1.0 in goethite and hematite, respectively. 6L-Feh_0.1 means the initial Mo:Fe molar ratio of 0.1 in six-line ferrihydrite. aFrom (Görn et al. 2021).	67
Figure 2-15 Mo(VI) tetrahedral and octahedral structure on goethite octahedral surface. a. Tetrahedral molecule of $\text{Mo}(\text{VI})\text{O}_4$. b. Octahedral molecule of $\text{Mo}(\text{VI})\text{O}_6$. c. Edge-sharing Mo(VI) inner-sphere complex via mononuclear Mo-O ₂ -Fe linkage (between MoO_4 and FeO_6). d. Corner-sharing MoO_4 inner-sphere complex via binuclear Mo-O ₂ -Fe ₂ linkage. e. Corner-sharing (between MoO_6 and FeO_6) $[(\text{MoO}_6)_2]$ inner-sphere complex via binuclear Mo-O ₂ -Fe ₂ linkage from (Arai 2010).	69
Figure 2-16 Simulated adsorbed Mo on hematite structures from (Davantes et al. 2017)	70
Figure 2-17 V(V) (2.5 ppm and 25 ppm) adsorption to goethite at 25 °C and I = 0.1 NaNO_3 after 144 h equilibration time from (Peacock and Sherman 2004).....	73
Figure 2-18 ATR-FTIR spectra on V(V)-adsorbed hematite and ferrihydrite and the corresponding V(V) species and symmetry from (Vessey et al. 2020).....	75
Figure 2-19 V K-edge XANES spectra of V reference compounds, V^{5+} -adsorbed solids, $\text{V}^{3+}/\text{V}^{4+}$ -substituted mineral, and highly weathered soil samples from (Wisawapipat and Kretzschmar 2017).....	77

Figure 2-20 V(V) molecular geometry clusters. (a) $\text{VO}_2(\text{OH})_2$ bidentate edge-sharing, (b) $\text{VO}_2(\text{OH})_2$ bidentate corner-sharing, (c) $\text{VO}_3(\text{OH})$ on bidentate corner, (d) VO_4 on bidentate corner. The unit of bond lengths is Å. From (Peacock and Sherman 2004).....	79
Figure 2-21 V molecular geometry clusters. Atoms' colours indicate V(V) (yellow), V(IV) (green), O (red), and Fe(II) (purple). From (Vessey and Lindsay 2020).....	81
Figure 3-1 Synthesised hematite particles.	84
Figure 3-2 Synthesised magnetite.	85
Figure 3-3 (A) Labelled set of Applikon Bioreactor for magnetite synthesis. (1) Automated Chemostat system (Applikon Bioreactor), (2) remote stirrer, (3) head plate and reaction vessels, (4) reaction vessel with reagents (0.2 M FeCl_3 and 0.3 M HCl), (5) sampling port with syringe to inject NH_4OH solution, (6) a glass of water to check if N_2 's out. (B) Chemostat head plate zoom in. A and B (7) sample port, A and B (8) N_2 in, A and B (9) N_2 out. (B10)-(B13) were sealed to keep anaerobic condition.	86
Figure 3-4 An example of Mo(VI) adsorption to hematite experiments.	89
Figure 3-5 The formation of Fe(II)-ferrozine complex from (Stookey 1970, Viollier et al. 2000).	91
Figure 3-6 An illustration of basic Bragg's law, adapted from (Waseda et al. 2011).	93
Figure 3-7 FEI Talos F200A for TEM analysis.	96
Figure 3-8 Schematic of ATR-FTIR technique presenting the infrared beam reflecting through the ATR crystal and then exiting before being recorded by the detector. Adapted from (Mudunkotuwa et al. 2014).	98
Figure 3-9 A simplified diagram of a modern synchrotron, adapted from Willmott (Willmott 2019).	100
Figure 3-10 An example of the molybdate spectrum showing regions in the X-ray absorption spectroscopy.....	102

Figure 3-11 A spectrum showing the areas in x-ray absorption spectroscopy from (Ravel and Newville 2005).....	103
Figure 4-1 A. 0.6×10^{-4} M and 5×10^{-4} M Mo(VI) adsorption onto hematite at pH 3-12 in 0.1 M and 0.01 M NaCl solutions. B. PHREEQC data on Mo speciation at pH 2-11.2 at Mo concentration of 5×10^{-4} M in 0.01 M NaCl.....	118
Figure 4-2 A. ATR-FTIR data for Mo(VI)-adsorbed hematite at Mo(VI) concentration of 0.6×10^{-4} - 2×10^{-3} M at pH 4. B. ATR-FTIR data for Mo(VI)-adsorbed hematite at pH 3-10 at Mo(VI) concentration of 5×10^{-4} M. C. Peak fitted for ATR-FTIR data on 5×10^{-4} M Mo(VI)-adsorbed hematite at pH 3 (black lines are experimental spectra, coloured lines are fitted peaks).	120
Figure 4-3 XANES data for A. standards and 5×10^{-4} M Mo(VI)-adsorbed hematite samples at pH 3-9, B. zoomed in pre-edge peaks (20004 eV) for standards and samples at pH 4 and 7	123
Figure 4-4 Mo(VI) octahedral on the iron octahedral structure of hematite surface via inner-sphere corner-sharing bidentate binuclear adsorption complex. A. Mono-molybdate adsorbed on the hematite surface. B. Polymolybdate adsorbed on the hematite surface.....	127
Figure SI4-1 X-ray diffraction of synthesized hematite.	132
Figure SI4-2 Mo(VI) isotherm adsorption to hematite in 0.1 M (dark spot) and 0.01 M (red spot) NaCl solutions at initial Mo(VI) concentration of 0.01×10^{-4} - 2×10^{-3} M (0.1 - 200 ppm) at pH 7. Langmuir isotherm fitting for Mo(VI) adsorption onto hematite at initial Mo(VI) concentration less than 6×10^{-4} M (60 ppm). The equilibrium of the Langmuir isotherm model is $Q_e = Q_{max} \times b \times C_e / (1 + b \times C_e)$, where Q_e (mg Mo/g adsorbent) is the adsorbed amount at equilibrium. Q_{max} (mg/g) is the maximum adsorption capacity. b (l/mg) is a constant. C_e is the residual adsorbent concentration in solution at equilibrium (Verbinnen et al. 2012).....	133

Figure SI4-3 TEM characterization of samples from 0.6×10^{-4} M Mo(VI) in solution adsorption to hematite in 0.01 M NaCl solution at pH 7.....	134
Figure SI4-4 A. C 1s spectra of the analysed hematite samples. Charge correction was applied to the spectra to line the main C-C feature to 284.8 eV. B. Mo 3d spectra for hematite samples. All spectra were charge referenced to the C 1s spectra.	135
Figure SI4-5 PHREEQC modeling on Mo speciation at pH between 2 to 11 at Mo concentration of 0.6×10^{-4} M in 0.01 M NaCl.....	136
Figure SI4-6 ATR-FTIR analysis for 0.6×10^{-4} M Mo(VI)-adsorbed hematite (A) and 2×10^{-3} M Mo(VI)-adsorbed hematite (B).	136
Figure SI4-7 XANES analysis for Mo standards and 0.6×10^{-4} M Mo(VI)-adsorbed hematite at pH 3-10 in 0.01 M NaCl.	138
Figure SI4-8 Fourier transform (black lines) and its EXAFS fitting (red dash) of 0.6×10^{-4} M (A) and 5×10^{-4} M (B) Mo(VI)-adsorbed hematite at pH 3-10 in 0.01 M NaCl and Mo(VI) standards.	139
Figure 5-1 A. 1.2×10^{-4} M and 1.2×10^{-3} M V(V) adsorption onto hematite in 0.1 M and 0.01 M NaCl solutions at pH 3-13.5. B. $2 \times 10^{-6} - 1.2 \times 10^{-3}$ M V(V) isotherm adsorption to hematite with Langmuir isotherm fitting at pH 7 in 0.1 and 0.01 M NaCl.	151
Figure 5-2 PHREEQC modeling on V(V) speciation at pH between 2 to 11 at V(V) concentration of 1.2×10^{-3} M (A) and 1.2×10^{-4} M (B) in 0.01 M NaCl.....	152
Figure 5-3 ATR-FTIR on 1.2×10^{-3} M V adsorption to hematite at pH 3-13.5 in 0.01 M NaCl.	154
Figure 5-4 V(V) species present in different pH and V(V) concentration systems. Structure is adapted from Vessey et al (2020) (Vessey et al. 2020).	155
Figure 5-5 XAS spectra for 1.2×10^{-3} M and 1.2×10^{-4} M V(V) adsorbed to hematite at a variety of pH. A. XANES for standards and 1.2×10^{-3} M V(V)-adsorbed hematite samples at	

pH 3-12. B. XANES for standards and 1.2×10^{-4} M V(V)-adsorbed hematite samples at pH 3-9. C. and D. are zoomed in pre-edge feature for 1.2×10^{-3} M and 1.2×10^{-4} M V(V)-adsorbed hematite, respectively.	157
Figure 5-6 EXAFS (A) and Fourier Transform (B) spectra for 1.2×10^{-3} M and 1.2×10^{-4} M V(V) adsorption to hematite at pH 3-9 in 0.01 M NaCl. The 10^{-3} M in figures represent samples at 1.2×10^{-3} M V(V) and the 10^{-4} M in figures represent samples at 1.2×10^{-4} M V(V).	159
Figure 5-7 V(V) tetrahedral on the iron octahedral structure of hematite via inner-sphere corner-sharing bidentate binuclear adsorption complex (1.2×10^{-3} M V(V) at pH 9, & 1.2×10^{-4} M V(V) at pH 3-9).	164
Figure 6-1 Mo(VI) adsorption onto magnetite and biogenic magnetite. (A) Mo(VI) adsorption to magnetite at pH from 4 to 12 in 0.1 and 0.01 M NaCl solution at initial Mo(VI) concentration of 0.6×10^{-4} M. (B) Mo(VI) adsorption to biogenic magnetite at pH from 5.5 to 12 in 0.01 M NaCl solution at initial Mo(VI) concentration of 0.6×10^{-4} M. (C) Mo(VI) adsorption to magnetite at pH 7 at initial Mo(VI) concentration of 0.1×10^{-5} M - 1.7×10^{-3} M. (D) Mo(VI) isotherm adsorption to magnetite at pH 7 at initial Mo(VI) concentration from 0.1×10^{-5} M to 1.7×10^{-3} M with Langmuir isotherm fitting.	174
Figure 6-2 PHREEQC modeling of Mo(VI) speciation at pH between 2 to 11.5 at a Mo concentration of 0.6×10^{-4} M in 0.01 M NaCl.	175
Figure 6-3 Mo K-edge XANES spectra for Mo(IV) and Mo(VI) standards and 0.6×10^{-4} M Mo-adsorbed magnetite and biogenic magnetite at pH 5.5-13.2 in 0.01 M NaCl solution. Mag is magnetite and Biomag is biogenic magnetite.	177
Figure 6-4 K ³ -weighted Mo EXAFS spectra for 0.6×10^{-4} M Mo(VI)-adsorbed magnetite at pH 5.5-13.2 in 0.01 M NaCl solution.	181
Figure 9-1 X-ray diffraction of synthesized magnetite.	203

Figure 9-2 V(V) adsorption onto magnetite and biogenic magnetite at a variety of conditions.

(A) V(V) adsorption to magnetite at pH from 2 to 13 in 0.1 and 0.01 M NaCl solution at initial V(V) concentration of 10^{-4} M. (B) V(V) adsorption to biogenic magnetite at pH 5.5-12 in 0.01 M NaCl solution at initial V(V) concentration of 10^{-4} M. (C) V(V) adsorption to magnetite at pH 7 in 0.1 and 0.01 M NaCl solution at initial V(V) concentration of 2×10^{-6} - 4×10^{-3} M. (D) V(V) isotherm adsorption to magnetite at pH 7 at initial V(V) concentration from 2×10^{-6} - 4×10^{-3} M with Langmuir isotherm fitting.205

Blank page

List of Tables

Table 1-1 Author contributions to chapter 4	31
Table 1-2 Author contributions to chapter 5	32
Table 1-3 Author contributions to chapter 6	33
Table 2-1 Summary data for Mo ($\mu\text{g/L}$) in groundwaters across Europe from (Smedley et al. 2014).	40
Table 2-2 Mo means in $\mu\text{g/L}$ (Kubota 1975, Smedley et al. 2003, Guo and Wang 2005).	41
Table 2-3 Average Mo concentration in surface waters across UK from (Smedley et al. 2014).	42
Table 2-4 V concentration in soils in different countries (Chen et al. 2020).	52
Table 2-5 V concentration in rainfall in various locations from (Schlesinger et al. 2017)....	54
Table 2-6 Previous FTIR studies for adsorbed Mo(VI) onto lepidocrocite (Davantes et al. 2017).	65
Table 2-7 The maximum adsorption capacity (Qm) of varying iron oxide adsorbents for V(V) removal (Mthombeni et al. 2016).	74
Table 3-1 Summary of experiments carried out during this PhD project.	83
Table 3-2 Composition of the modified freshwater enrichment medium (nutrient broth acetate fumarate (NBAF)) (Lovley and Phillips 1988, Mulroy 2020).....	88
Table 3-3 Parameters in EXAFS equation and their explanation (Newville 2004, Calvin 2013, Newville 2014).....	105
Table 3-4 key features of B18 and I20 beamline at Diamond Light Source.....	106
Table 4-1 Mo(VI) EXAFS fitting parameters.	128
Table SI4-1 ATR-FTIR spectra for adsorbed Mo(VI) ions.	137
Table SI4-2 Mo(VI) EXAFS fitting parameters.	140

Table 5-1 Adsorbed vanadate ions and dissolved V species IR band from literature (Griffith 1967, Griffith and Lesniak 1969, Twu and Dutta 1989, Twu and Dutta 1990, Salak et al. 2012, Vessey et al. 2020).....	154
Table 5-2 V(V) EXAFS fitting parameters.....	163
Table 6-1 Linear Combination Fitting of Mo K-edge XANES Mo(VI)-adsorbed magnetite and biogenic magnetite at pH 5.5-13.2 in 0.01 M NaCl.....	178
Table 6-2 EXAFS fitting parameter for 0.6×10^{-4} M Mo(VI)-adsorbed to magnetite at pH 5.5-13.2 and MoO ₂ standard.	182

Blank page

List of Abbreviations

XAS	X-ray Absorption Spectroscopy
EXAFS	Extended X-ray Absorption Fine Structure
XANES	X-ray Absorption Near Edge Structure
ATR-FTIR	Attenuated Total Reflection-Fourier Transform Infrared Spectroscopy
PHREEQC	PHREEQC Geochemical Modelling
TEM	Transmission Electron Microscopy
XPS	X-ray Photoelectron Spectroscopy
ICP-AES	Inductively Coupled Plasma Atomic Emission Spectroscopy
ICP-MS	Inductively Coupled Plasma Mass Spectrometry
XRD	X-ray Diffraction
BET	Brunauer-Emmett-Teller
DFT + U	Density Functional Theory + U correction
EDS	Energy Dispersive X-ray Spectroscopy
HAADF	High Angle Annular Dark Field
UV-VIS	Ultra-Violet – Visible spectroscopy
FT	Fourier Transform

Thesis Abstract

Molybdenum (Mo) and vanadium (V) are important trace elements and potential environmental contaminants in many surface and subsurface environmental systems. Mo commonly occurs as the tetrahedral oxyanion molybdate ($\text{Mo(VI)}\text{O}_4^{2-}$) and V can occur in several oxidation states including V(III), V(IV), V(V), however it is environmentally transportable in the more toxic, oxidised forms as vanadyl ($\text{V(IV)}\text{O}^{2+}$) and vanadate ($\text{V(V)}\text{O}_4^{3-}$). The widespread iron oxides have a controlling effect on the mobility of contaminated metals due to their high surface areas.

This project applied multiple techniques including ATR-FTIR and XAS to holistically characterise the adsorption behaviour of Mo(VI) and V(V) to iron oxides under a range of environmental conditions (e.g. pH, adsorbate concentrations), and identify the changes of oxidation states and species, and determine bonding environment of Mo and V onto these mineral surfaces. The first study investigated Mo(VI) adsorption to hematite and indicated low pH (3-4) and high Mo(VI) concentrations ($\geq 0.5 \text{ mM}$) contribute to the formation of polymolybdate and at low concentration and neutral to high pH an octahedral corner-sharing bidentate binuclear adsorption complex was observed. The second study of V(V) adsorption to hematite showed a gradual change of coordination environment from a mixture of octahedral decavanadate and tetrahedral polyvanadate at pH 3 to a tetrahedral monovanadate (via corner-sharing bidentate complex) dominating at pH 9. The third project investigated Mo(VI) adsorption to Fe(II)-bearing iron oxides (e.g. magnetite) and suggested three processes: 1. adsorption occurred at pH 5.5 via octahedral corner-sharing bidentate binuclear complex, 2. reduction of Mo(VI) to Mo(IV) to MoO_2 occurred at pH>9, and 3. At pH 7, Mo dominantly adsorbed on magnetite and 3.7% of Mo(VI) reduced to $\text{Mo(IV)}\text{O}_2$. Collectively, these thesis results provide a detailed molecular scale understanding of the poly- or mono- Mo(VI) and V(V) adsorption and reduction mechanisms and give a comprehensive dataset for determining the environmental mobility of Mo and V in a variety of geochemical scenarios.

Declaration

The author of this thesis declares that no portion of the work referred to in this thesis has been submitted in support of an application for another degree or qualification of this or any other university or other institute of learning.

Copyright Statement

- i. The author of this thesis (including any appendices and/or schedules to this thesis) owns certain copyright or related rights in it (the “Copyright”) and s/he has given The University of Manchester certain rights to use such Copyright, including for administrative purposes.
- ii. Copies of this thesis, either in full or in extracts and whether in hard or electronic copy, may be made only in accordance with the Copyright, Designs and Patents Act 1988 (as amended) and regulations issued under it or, where appropriate, in accordance with licensing agreements which the University has from time to time. This page must form part of any such copies made.
- iii. The ownership of certain Copyright, patents, designs, trademarks and other intellectual property (the “Intellectual Property”) and any reproductions of copyright works in the thesis, for example graphs and tables (“Reproductions”), which may be described in this thesis, may not be owned by the author and may be owned by third parties. Such Intellectual Property and Reproductions cannot and must not be made available for use without the prior written permission of the owner(s) of the relevant Intellectual Property and/or Reproductions.
- iv. Further information on the conditions under which disclosure, publication and commercialisation of this thesis, the Copyright and any Intellectual Property and/or Reproductions described in it may take place is available in the University IP Policy (see <http://documents.manchester.ac.uk/DocuInfo.aspx?DocID=487>), in any relevant Thesis restriction declarations deposited in the University Library, The University Library’s regulations (see <http://www.manchester.ac.uk/library/aboutus/regulations>) and in The University’s policy on Presentation of Theses.

Acknowledgements

Firstly, I would like to appreciate all the help from my supervisors Sam Shaw and Vicky Coker. I want to extend my great thanks for their constant guidance, patience and support, and believing in my ability throughout the whole PhD process. They provide opportunities to challenge me to improve, allow me to gain confidence in my research and aid me to succeed. I have learnt a lot from them over the last few years. I would also like to thank China Scholarship Council for funding this research.

I would like to acknowledge the support of Diamond Light Source providing beamtime awards, and I thank Giannantonio Cibin, Steve Parry and Matteo Aramini for their beamline assistance. A huge thanks to Fred Mosselmans for his expertise and help to the EXAFS related analysis.

I am grateful to Roy Wogelius, Luis Batista de Carvalho, Louise Natrajan, John Waters, Ilya Strashnow, Paul Lythgoe, Heath Bagshaw, Liam Abrahamsen, and Chris Boothman for assistance with data acquisition.

My gratitude goes to the Geomicrobiology research group for making my PhD much easier. Special thanks go to Ellen, Luke, Tom, Matt, Sul, Dawn, Faraaz and Lynn for their help during and outside of work.

To my friends Bob, Chao, Xue and Jingyue, thank you for being there for me. Many thanks go to Jianpeng and Lin for the help and advice throughout the PhD journey.

To my family, especially my wonderful parents, thank you for your love and support. I appreciate everything you have done for me.

About the Author

Jing graduated from the University of Manchester in 2016, gaining a master's degree in Pollution and Environmental Control. During her masters, Jing studied the removal efficiency of heavy metals from acid mine drainage using limestone, supervised by Sam Shaw. This enjoyable postgraduate project led Jing to decide to pursue research further. Jing joined the Geomicrobiology group in the Department of Earth and Environmental Sciences in 2017 to undertake the project for which is reported in this thesis.

1. Project Introduction and Thesis Structure

This thesis is about two key oxyanions, molybdenum (Mo) and vanadium (V), and their adsorption behaviour on iron oxide particles including hematite, magnetite and biogenic magnetite under a variety of conditions (pH, ionic strength and adsorbate concentrations), applying multiple technique approach (aqueous analysis, PHREEQC, ATR-FTIR, XAS etc.).

1.1 Background

Molybdenum (Mo) is predominantly used in metallurgical applications as an alloying element in the production of stainless steel or cast iron alloys (Stiefel, 2002, Smedley and Kinniburgh, 2017), and also in the production of flame retardants, lubricant additive, ceramics, pigments and catalysts for high temperature chemical processes (Smedley and Kinniburgh, 2017, Verbinnen et al., 2012). China, Chile and the USA are three of the largest producers of Mo, with representatively 35% - 40%, 22% - 23% and 14% - 20% of world production from the mining activities (200000 tons) (Frascoli and Hudson-Edwards, 2018).

Molybdenum tends to exist as a trace element within ore deposits however, mining and processing activities can result in wastes with relatively high Mo contents (up to 4000 mg/kg Mo for tailings), and contaminate water, sediments and soils in surrounding areas (Huang et al., 2010, Solongo et al., 2018). Mo is the primary product that is mined by Mo porphyry deposits, and is by-product of Cu porphyry and other Cu-bearing ores, with Mo content range from 11.8 to 235 mg/kg (Kropschot, 2010, Smedley and Kinniburgh, 2017, Seal II, 2012). The highest Mo concentration was recorded as 3985 mg/kg in tailings from Cu-polymetallic ores (including Cu porphyry ores) in the Gyama Valley, Tibet (Huang et al., 2010) and high level of dissolved Mo in groundwater in porphyry copper deposit area was reported from 2 to 475 mg/L, significantly exceeding WHO guidelines for drinking water quality advise that the safety-based Mo value (70 µg/L) (Smedley and Kinniburgh, 2017, Leybourne and Cameron,

2008, Balandis et al., 2005, WHO, 2003). A great number of secondary minerals (e.g. ferrimolybdate($\text{Fe(III)}_2(\text{MoO}_4)_3 \cdot n(\text{H}_2\text{O})$)) can be formed by the oxidation of molybdenite (Mo(IV)S_2) in weathered porphyry deposits (Smuda et al., 2014) and the high solubility of Mo(VI) in Cu-Mo mine waters can lead to high Mo concentrations (e.g. 2670 - 3900 $\mu\text{g/L}$ in the Machalí Cachapoal Province, Chile), even under quite low oxygen concentration conditions (Frascoli and Hudson-Edwards, 2018, Smuda et al., 2014). High environmental concentrations of Mo can have detrimental effects on environmental system e.g. causing yellow-orange chlorosis in leaves (100-1000 mg/kg depending on crops' type) (Gupta, 1997, Gupta and Gupta, 1998) and molybdenosis (intake of Mo > 5 mg/kg in forage) in ruminants inducing copper deficiency (Arai, 2010). Acute Mo exposure in humans can result in anaemia, gout and diarrhoea, and Long-term exposure related to a loss of appetite, fatigue, weakness, joint pain and liver dysfunction (Smedley and Kinniburgh, 2017, WHO, 2003).

Vanadium (V) is a key component of non-ferrous and ferrous alloys due to its physical properties of hardness, strength and fatigue resistance (Moskalyk and Alfantazi, 2003). V is also commonly used in iron made tools, superconducting magnets and rust resistant steels (Emsley, 2011), as well as being seeing increased demand as a component in mass energy storage batteries and sulfuric acid production (Watt et al., 2018).

Global anthropogenic activities (such as fossil fuel burning, metal mining and steel making) are important factors that have led to an increase in concentration of vanadium (V) in soil, water and the atmosphere, and vanadium has the highest anthropogenic enrichment factor (AEF) of all trace elements in the atmosphere and the fourth highest AEF in rivers (Mejia et al., 2007, Imtiaz et al., 2015, Watt et al., 2018, Vessey et al., 2020). The rise in discharges of V to the environment is attributed, in part, to an increase in V-rich industry wastes such as steel slags and ash from waste incineration (Watt et al., 2018). The leaching of V from petroleum coke and emission from fossil combustion has been reported to lead to increasing

environmental pollution, with the median pseudo-total V concentration of 60.4 mg/kg (a range from 1.28 to 537 mg/kg) in European soils (Wisawapipat and Kretzschmar, 2017) and up to 703 mg/kg V has been reported in the alluvial soils polluted by the phosphate ore process industry (Cappuyns and Slabbinck, 2012, Cappuyns and Swennen, 2014). In mining areas high V concentration of 709 mg/kg has been observed in the topsoil in China (Teng et al., 2009) and 3505 mg/kg has been reported by (Cappuyns and Swennen, 2014), which is significantly exceed the environmental guidelines of V in soils for invertebrates and plants (This guideline varies from different countries (e.g. 130 mg/kg in Canada, 42 mg/kg in Netherlands)) (Imtiaz et al., 2015). Long-term exposure in humans to V can increase blood pressure, reduce the number of red blood cells and lead to neurological effects (Baran and Nriagu, 1998). Therefore, the increasing anthropogenic activities have resulted in an increase release of Mo and V in the environment, leading to the potential threat to the natural environment and attracting significant attention from researchers (Smedley and Kinniburgh, 2017).

Mo commonly occurs in oxic environments as the tetrahedral oxyanion molybdate ($\text{Mo(VI)}\text{O}_4^{2-}$) (Brinza et al., 2015). It is also a redox-sensitive element that forms poorly soluble Mo(IV) phases e.g. MoO_2 , within certain reducing environments such as humic and fulvic acid (Reddy et al., 1997). Various polymolybdate ($\text{Mo(VI)}_7\text{O}_{24}^{6-}$, $\text{HMo(VI)}_7\text{O}_{24}^{5-}$) with octahedral coordination plays an important role at high concentrations ($[\text{Mo}] > 10^{-4}$ M) and acidic pH (< 5) (Cruywagen, 1999, Davantes et al., 2017, Ozeki et al., 1988, Mitchell, 2009). Whereas, V can occur in several oxidation states including V(II), V(III), V(IV), V(V), however it is environmentally transportable in the more toxic, oxidised forms V(IV) as vanadyl ($\text{V(IV)}\text{O}^{2+}$) and V(V) as vanadate ($\text{V(V)}\text{O}_4^{3-}$) (Taylor et al., 2012). In aqueous systems, V(V) can be present as polymeric species e.g. octahedral decavanadate ($\text{H}_x\text{V(V)}_{10}\text{O}_{28}^{x-6}$) and tetrahedral metavanadate ($\text{V(V)}\text{O}_3\text{x}^-$) at higher concentration ($[\text{V}] = \sim 100 \mu\text{mol/L}$) and acidic pH (< 7) (Wisawapipat and Kretzschmar, 2017, Peacock and Sherman, 2004).

Iron minerals are ubiquitous in soils and marine sediments and have an important effect on controlling the mobility of contaminated metals in the subsurface, in particular through absorption of metals due to the high surface area of minerals such as hematite (α -Fe(III)₂O₃), magnetite (Fe(II)Fe(III)₂O₄), biogenic magnetite, ferrihydrite (Fe(III)(OH)₃), and goethite (α -Fe(III)OOH) (Xu et al., 2006a, Xu et al., 2006b, Zhang and Sparks, 1989, Brinza et al., 2008, Brinza et al., 2019, Brinza et al., 2015, Gustafsson, 2003, Larsson et al., 2017, Vessey and Lindsay, 2020, Vessey et al., 2020, Arai, 2010, Peacock and Sherman, 2004, Goldberg et al., 1996, Goldberg et al., 1998, Das et al., 2016, Das and Hendry, 2013). The Fe(II)-bearing iron oxides (e.g. magnetite (Fe(II)Fe(III)₂O₄)), containing both Fe(II) and Fe(III), allows extensive attenuation of contaminated metals (e.g. Mo and V) through coupled adsorption and reduction (Vessey and Lindsay, 2020).

Factors that impact the capacity of a surface to absorb toxic metals (e.g. Mo and V) include pH, adsorbate concentrations, and ionic strength and these we are currently investigating in relation to Mo and V absorption to hematite, magnetite and biogenic magnetite (magnetite formed by an Fe(III)-reducing bacterium). Understanding in situ metalloid surface speciation and bonding mechanisms on mineral surfaces is important to predicting the bioavailability and mobility of these contaminated metals in subsurface and surface environments.

1.2 Aims and Objectives

The aims of this PhD project are to holistically characterise the adsorption and redox action of molybdate (Mo(VI)O₄²⁻) and vanadate (V(V)O₄³⁻) to hematite (α -Fe(III)₂O₃), magnetite (Fe(II)Fe(III)₂O₄) and biogenic magnetite under a variety of environmental conditions (such as pH, adsorbate concentrations and ionic strength), and identify the changes in Mo and V speciation, and determine the bonding environment of Mo(VI) and V(V) onto the these widespread iron oxide surfaces, combining a multiple technique approach including aqueous

chemical analyses, PHREEQC geochemical modelling, Langmuir isotherm modelling, X-ray powder diffraction (XRD), Brunauer–Emmett–Teller (BET), Inductively coupled plasma atomic emission spectroscopy (ICP-AES), Inductively coupled plasma mass spectrometry (ICP-MS), Attenuated Total Reflection-Fourier Transform Infrared Spectroscopy (ATR-FTIR), Transmission Electron Microscopy (TEM), X-ray Photoelectron Spectroscopy (XPS), X-ray Absorption near edge structure (XANES), Extended X-ray Absorption Fine Structure (EXAFS) and X-ray magnetic circular dichroism (XMCD). The following objectives have been explored in the PhD project.

- To produce the hematite particles and enable the study of the adsorption process of Mo(VI) onto this iron oxide under varying conditions including pH, Mo(VI) concentration and ionic strength in chapter 4. Develop PHREEQC models and explore ATR-FTIR methodology to characterize the mono- or poly- Mo(VI) speciation. Determine the oxidation states changes and bonding environment of Mo(VI) on hematite using X-ray absorption spectroscopy (XAS).
- To enable the study of the adsorption process of V(V) onto hematite under varying conditions including pH, V(V) concentration and ionic strength in chapter 5. Develop PHREEQC models and explore ATR-FTIR to characterize the mono- or poly- V(V) speciation. Also, apply X-ray absorption spectroscopy (XAS) to determine the oxidation states changes and bonding environment for V(V)-adsorbed hematite.
- To produce chemical-synthesised magnetite and biogenic magnetite (using a pure culture of the *G. sulfurreducens*) in chapter 6. Investigate of the adsorption of Mo(VI) and V(V) onto these two mineral surfaces under varying environmentally relevant conditions (pH, adsorbate concentrations and ionic strength). Use X-ray absorption spectroscopy (XAS) to determine the oxidation states changes and bonding

environment for Mo(VI) and V(V) adsorbed magnetite and biogenic magnetite, as well as characterization of the reduction process of Mo(VI) to magnetite nanoparticles.

1.3 Thesis Structure

Chapter 2 presents an in-depth review of the relevant literature. A critical analysis of the analytical techniques used in this project is provided in Chapter 3 to give the detailed background of methodology that has been performed throughout the PhD project. Chapters 4 and 5 are research chapters written as advanced drafts for journal submission. Chapter 6 is a research work in progress.

Chapter 4 presents mono- or poly- molybdate adsorption to hematite, which has been submitted to *Journal of Hazardous Materials*. This project used a multi-technique approach to characterise the adsorption behaviour, speciation changes and bonding mechanisms of Mo(VI) on the hematite surface whilst changing a variety of conditions including pH, Mo(VI) concentration and ionic strength. This project provides a detailed understanding of the atomic scale adsorption mechanism and can be used to predict the environmental behaviour of Mo(VI) as a function of geochemical parameters. Table 1-1 shows the author contributions to this project.

Table 1-1 Author contributions to chapter 4.

Author	Contributions
J. Zhang	Designed experiments, developed methodology, prepared samples and analysed data (excluding XPS), modelled data (PHREEQC, XAS), and wrote the manuscript.
V. Coker	Designed experiments, developed methodology, guided XAS data preparation and collection, edited the manuscript.
J. F. W. Mosselmans	Assisted with EXAFS data modelling and reviewed the manuscript.
S. Shaw	Designed experiments, developed methodology, guided XAS data preparation and collection, edited the manuscript.

Chapter 5 investigated the adsorption of vanadate species to hematite, for submission to *Environmental Science & Technology* in 2021. This project used a multi-technique approach to characterise the adsorption behaviour, speciation changes and bonding mechanisms of V(V) on the hematite surface in molecular scale under changing geochemical conditions including pH, V(V) concentration and ionic strength. This project combined ATR-FTIR and XAS techniques to provide a detailed molecular scale understanding of the V(V) adsorption mechanisms. This is associated with aqueous analysis and geochemical modelling (PHREEQC) to provide a comprehensive dataset for determining the environmental mobility of V in a variety of geochemical scenarios. Table 1-2 shows the author contributions to this project.

Table 1-2 Author contributions to chapter 5.

Author	Contributions
J. Zhang	Designed experiments, developed methodology, prepared samples and analysed data (aqueous solution data and ATR-FTIR), modelled data (PHREEQC, XAS), and wrote manuscript.
V. Coker	Designed experiment, developed methodology, guided with XAS data preparation and collection, edited the manuscript.
J. F. W. Mosselmans	Assisted with EXAFS data modelling and reviewed the manuscript.
L.A.E. Batista de Carvalho	Assisted with XAS data collection and reviewed the manuscript.
S. Shaw	Designed experiment, developed methodology, guided XAS data preparation and collection, edited the manuscript.

Chapter 6 is a study of the adsorption of Mo(VI) to magnetite and biogenic magnetite, which is presented as a manuscript for submission to *ACS Earth and Space Chemistry* in 2022. This project investigated the adsorption and reduction behaviour of Mo(IV) onto magnetite and biogenic magnetite, under varying geochemical conditions including pH, V(V) concentration and ionic strength, applying aqueous analysis, PHREEQC, and XAS to provide a detailed molecular scale understanding of the Mo(VI) interaction mechanisms to the redox sensitive

iron oxide particles (magnetite and biogenic magnetite). Table 1-3 shows the author contributions to this project.

Table 1-3 Author contributions to chapter 6.

Author	Contributions
J. Zhang	Designed experiments, developed methodology, prepared samples and analysis data, modelled data (PHREEQC, XAS, XMCD), and wrote manuscript.
V. Coker	Designed experiments, developed methodology, guided with XAS and XMCD data preparation and collection, modelled XMCD data, and edited the manuscript.
J. F. W. Mosselmans	Assisted with EXAFS data modelling and reviewed manuscript.
S. Shaw	Designed experiment, developed methodology, guided with XAS and XMCD data preparation and collection, edited the manuscript.

2. Literature Review

2.1 Molybdenum (Mo)

2.1.1 Mo Application in Industry

Mo is mainly used in metallurgical applications as an alloying element in the production of stainless steel or cast iron alloys (Stiefel, 2002, Smedley and Kinniburgh, 2017), and also in the production of flame retardants, lubricant additive, ceramics, pigments and catalysts for high temperature chemical processes (Smedley and Kinniburgh, 2017, Verbinnen et al., 2012). The release of Mo in environment can occur through both agricultural and industrial contamination, e.g. fossil-fuel combustion and mine waste (Smedley and Kinniburgh, 2017, Zhang and Reardon, 2003, Morrison and Spangler, 1992).

2.1.2 Mo Environmental Geochemistry

Mo commonly occurs in the natural environment as a dissolved oxyanion in solution, and the major oxidation states are Mo(VI) under oxic conditions, such as tetrahedral molybdate ($\text{Mo(VI)}\text{O}_4^{2-}$), consisting of a central metal ion surrounded by four oxygen atoms (Figure 2-1) (Verbinnen et al., 2012), while under anoxic conditions, Mo is predominantly in the Mo(IV) oxidation state (Stiefel, 2002) where it often forms poorly soluble Mo(IV) phases, for example $\text{Mo(IV)}\text{O}_2$ (Reddy et al., 1997). Both soluble and insoluble compounds can occur for Mo in the environment, even though the insoluble $\text{Mo(IV)}\text{O}_2$ is rarely found (Cook, 2001). Soluble compounds include ammonium molybdate ($(\text{NH}_4)_2\text{Mo(VI)}\text{O}_4$), calcium molybdate ($\text{CaMo(VI)}\text{O}_4$) and molybdenum trioxide ($\text{Mo(VI)}\text{O}_3$), whereas sparingly soluble compounds include molybdenum dioxide ($\text{Mo(IV)}\text{O}_2$) and molybdenum disulphide ($\text{Mo(IV)}\text{S}_2$) typically form within anoxic conditions (Smedley et al., 2014). A natural metallic form could not be found in the natural environment (Stiefel, 2002).

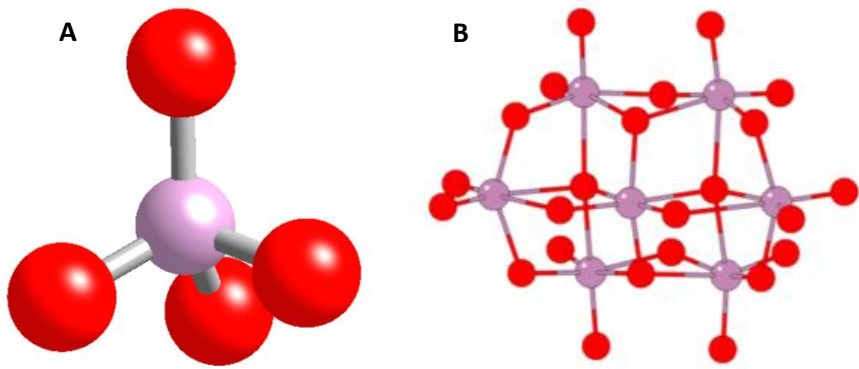


Figure 2-1 3D model of A. molybdate (MoO_4^{2-}) and B. polymolybdate ($\text{Mo}_7\text{O}_{24}^{6-}$) (Davantès and Lefèvre, 2013). Red atoms are O and the purple atom is Mo.

Both pH and Mo concentration play important roles in Mo species in solution. In nature waters Mo mainly occurs as Mo(VI) and Mo(V) oxidation states as oxyanions including $\text{Mo(VI)}\text{O}_4^{2-}$, $\text{HMo(VI)}\text{O}_4^-$, $\text{H}_2\text{Mo(VI)}\text{O}_4$, $\text{HMo(V)}\text{O}_4^{2-}$ depending on the environmental pH (Weidner and Ciesielczyk, 2019, Montero-Serrano et al., 2009). The dissociated tetrahedral $\text{Mo(VI)}\text{O}_4^{2-}$ is the predominant species at pH > 5 in dilute solutions (such as soil and natural waters) (Figure 2-2) (Cruywagen, 1999, Stiefel, 2002, Ozeki et al., 1988, Mitchell, 2009, Davantes et al., 2017). At pH < 5 and Mo concentration less than 1 mM, two protonated forms ($\text{H}_2\text{Mo(VI)}\text{O}_4$ and $\text{HMo(VI)}\text{O}_4^-$) can be found, although $\text{HMo(VI)}\text{O}_4^-$ is rarely dominant (Smedley and Kinniburgh, 2017, Ozeki et al., 1988). $\text{H}_2\text{Mo(VI)}\text{O}_4$ is more correctly written as $\text{MoO}_3(3\text{H}_2\text{O})$ according to a structural view, as Ultraviolet Resonance Raman (UVRR) spectroscopy shows a vibrational frequency of molybdic acid (H_2MoO_4) at 919 cm^{-1} , which is due to Mo=O symmetric stretches given by a trioxo-species, and $\text{MoO}_3(3\text{H}_2\text{O})$ provides the best agreement from trioxo-species (Oyerinde et al., 2008). There are only tetrahedral monomolybdate species at low Mo concentrations (less than 0.03 mM), whereas octahedral polymolybdate ($\text{Mo(VI)}_7\text{O}_{24}^{6-}$, $\text{HMo(VI)}_7\text{O}_{24}^{5-}$, $\text{H}_2\text{Mo(VI)}_6\text{O}_{21}^{6-}$, $\text{Mo(VI)}_8\text{O}_{26}^{4-}$) forms with increasing of Mo concentration (> 0.1 mM) in acidic conditions (pH < 5) (Ozeki et al., 1988, Mitchell, 2009,

Cruywagen, 1999, Davantes et al., 2017). Between pH 4-8, Mo is found as the dissolved Mo(VI) anion and will precipitate to form molybdate salts at high concentrations (e.g. CaMoO₄ and MgMoO₄) in oxic soils (Reddy et al., 1990). CaMoO₄ is stable in both solid and solution phase and MgMoO₄ can be a dominant Mo soluble species in the seawater (Smedley and Kinniburgh, 2017). Mo(V) is difficult to sustain in natural waters unequivocally, Mo(V) can be detected in sediment porewaters using Mo(V)/Mo(VI) separation techniques (Wang et al., 2011, Wang et al., 2010). Mo(V) can also be found in some natural dissolved organics (e.g. fulvic acid) and as Mo(V)O₂⁺in some anoxic environments, (Wang et al., 2010, Smedley and Kinniburgh, 2017).

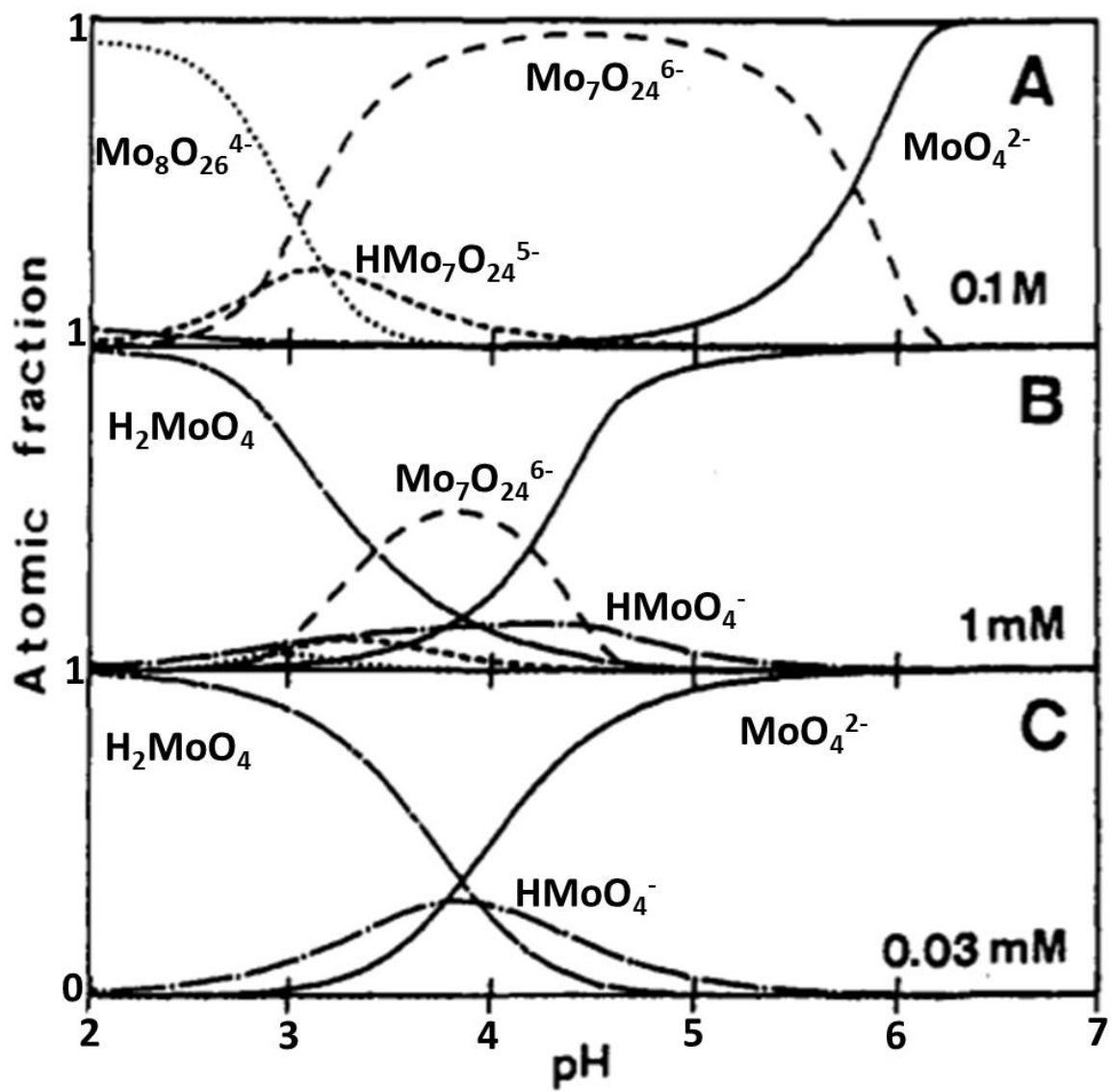


Figure 2-2 Distribution of Mo(VI) speciation as function of pH at initial Mo concentration of 0.03-0.1 mM. Adapted from (Ozeki et al., 1988).

2.1.3 Role of Molybdenum in Plant, Animal and Human Health

Mo was important to the early evolution of life in the oceans as low concentrations of Mo delayed evolution in the early sulphidic and anoxic ocean (Smedley and Kinniburgh, 2017, Parnell and Lindgren, 2016). Mo is also an essential micronutrient and an important trace element for plants (such as lettuce, tomatoes and asparagus), microorganisms, animals and humans (Arnon and Stout, 1939). Mo contributes to the electron transfer reactions during

nitrate reduction and nitrogen fixation in agro-ecosystem (Arai, 2010), and deficiency of Mo commonly leads to the symptoms of chlorosis and a yellowing of leaves due to the delay of anthesis, inhibits tasselling, flowering, and the development of sporogenous tissues in crops and a decrease of fertility (Agarwala et al., 1978, Martin et al., 1995, Smedley et al., 2014). Mocos, a pterin-based Mo cofactor, is well-known to be involved in Mo-dependent enzymes and a deficiency of them in humans can lead to early childhood death and neurological abnormalities (Wahl et al., 2010). An average Mo level of 0.23 mg/kg was reported to be beneficial for plant growth. The daily requirement of Mo for humans is estimated in the range of 75-250 µg (Council, 1989). The upper intake amount of Mo from United States Food & Nutrition Board guideline is 2 mg/day (0.3 mg/day for infants 1-3 years) (Smedley and Kinniburgh, 2017). However, high Mo concentrations can be harmful to crops causing yellow-orange chlorosis on young leaves with brown tints (Gupta, 1997). Molybdenosis can occur in ruminants if the intake of total Mo level is over 5 mg/kg in forage by inducing copper deficiency and was observed that a diet where Mo is over 30 mg/L inhibits the uptake of copper in the gastrointestinal tract and leads to the limitation of the complexation of copper with thiomolybdate (MoS_4^{2-}), which plays important enzymatic role in connective tissues (Arai, 2010). Cattle exhibit symptoms of molybdenosis (including anorexia, anaemia, diarrhoea, hair discoloration, joint abnormalities and osteoporosis) when they eat 10-20 ppm or more Mo toxic plants (Kubota, 1975, Underwood, 1971, Smedley and Nicoll, 2014). High concentrations of Mo can be harmful in humans too, although this situation is less common, and the symptoms are limited. Acute exposure (10 mg/kg of body weight per day) of Mo is linked to gout, anaemia and diarrhoea, whereas chronic occupational exposure can lead to anorexia, anemia, diarrhea, fatigue, liver dysfunction, lack of appetite, joint pain, osteoporosis, slow growth, tremor and weakness (Goldberg et al., 1996, WHO, 2003).

2.1.4 Occurrence and Distribution of Mo in the Environment

2.1.4.1 Mo in Surface and Ground Water

Mo is found sporadically in groundwater and is most common in oxic alkaline systems (Rango et al., 2010). The WHO guidelines for drinking water quality advise that the safety-based Mo value is 70 µg/L, however this guideline is not promulgated as this value is rarely observed in drinking water (WHO, 2003). In groundwater, Mo is often associated with other anions and oxyanions (such as As, V, U, HCO₃), which is related to the lack of sorption affinity between Mo and anionic species in oxic alkaline environments (Smedley and Kinniburgh, 2017, Ayotte et al., 2011). Mo concentration has been observed to be lower under sulphidic conditions due to the sorption or other reactions between Mo and solid sulphide phases (Smedley and Kinniburgh, 2017).

High Mo values in groundwater can be affected by climate and have been observed in arid areas due to the evaporation and increased salinity of groundwater (Ayotte et al., 2011). Both oxic and anoxic conditions have been observed to produce high-Mo groundwaters, but all related to alkaline conditions (pH > 7) (Ayotte et al., 2011).

The concentration of Mo in United Kingdom (UK) ground- and surface- waters are, in most cases, low at 2 µg/L or less, comparing with the WHO health-based maximum guideline value for Mo (70 µg/L) (Smedley et al., 2014, WHO, 2003). Data for 1735 groundwater samples in the UK indicate Mo concentrations of 0.035 - 1.8 µg/L with a median of 0.2 µg/L and maximum report of 89 µg/L. The maximum Mo concentration in groundwater across Europe was reported in Norway as 96 µg/L (Table 2-1). A range of Mo concentration of 0.13 - 4.9 µg/L was reported for 3063 samples from USA groundwater, with the media of 1 µg/L and maximum level of 4700 µg/L (Ayotte et al., 2011, Smedley and Kinniburgh, 2017).

Table 2-1 Summary data for Mo ($\mu\text{g/L}$) in groundwaters across Europe from (Smedley et al., 2014).

Aquifer	Min	Median	Mean	Max	N
Aveiro Quaternary and Cretaceous aquifers, Portugal	<0.1	0.12	0.45	13.2	144
Cenomanian aquifer, Czech Republic	<2	<2	<0.8	6.2	43
Turonian aquifer, Czech Republic	<2	<2	<2	3.5	61
Miocene Sand aquifer, Jutland, Denmark		0.2		1.2 ^a	64
Neogene aquifer, Flanders, Belgium	<0.1	0.05	0.46	8.3	40
Quaternary aquifer, Bulgaria	0.1	1	1	8	18
Crystalline bedrock aquifer, Norway		1.4		96	476

^a 90th percentile.

In some aquifers, Mo concentrations are reported to increase down groundwater flow gradients because the aquifer is confined below a poorly-permeable overlying strata and the redox conditions of aquifer changes from oxic to anoxic (Smedley and Kinniburgh, 2017). In some anoxic aquifers, for example in China and USA, high Mo values have been identified in fluviolacustrine and alluvial aquifers (Table 2-2) (Kubota, 1975, Guo and Wang, 2005, Smedley et al., 2003). In these aquifers, the elevating Mo concentrations are associated with Mn-and Fe-reducing conditions due to the reductive dissolution of Mn/Fe oxides (Smedley and Kinniburgh, 2017, Kubota, 1975).

Table 2-2 Mo means in µg/L (Kubota, 1975, Smedley et al., 2003, Guo and Wang, 2005).

Region	General location	Amount of samples	Average concentration of Mo (µg/L)
Washington, USA	Alluvial floodplains	20	1500
	Stream valley		11250
Idaho, USA	Alluvial floodplains	4	1500
	Stream valley		2700
Montana, USA	Alluvial floodplains	3	400
	Glacial drift plains	1	400
	Stream valley		9600
Wyoming, USA	Glacial drift plains	3	500
Colorado, USA	Stream valley		5350
Huhhot Basin, China (>100 m depth)	Quaternary fluviolacustrine	14	1.6 (< 0.1-14)
Huhhot Basin, China (<100 m depth)	Holocene fluviolacustrine	59	1.9 (< 0.1-63)
Datong, China	Holocene fluviolacustrine	91	0.1-269

Ash, including volcanic ash (e.g. Argentina) and rhyolitic ash (e.g. Ethiopia), is also an important source for Mo in the environment, and results in increasing dissolved Mo in groundwater (Smedley and Kinniburgh, 2017). Rhyolitic and volcanogenic ash in sedimentary aquifers has led to an increased level of Mo in Rift Valley groundwater in Ethiopia, with the Mo concentration rising from 0.53 µg/L to 446 µg/L (Rango et al., 2010). Coal ash has been suspected to contaminate anoxic groundwater in USA, with Mo concentrations over 44 µg/L found when investigating 44 wells in Caledonia, USA (Lourigan and Phelps, 2013).

High Mo concentration in surface water can be observed in ore, ash deposits and sulphide-mineralised areas (Smedley et al., 2014, Smedley and Kinniburgh, 2017). Data for 11600 samples from UK surface waters (stream waters) were collated and indicate 0.08-2.44 µg/L

Mo with a median of 0.57 µg/L and maximum report of 230 µg/L (Table 2-3) (Smedley et al., 2014). The highest Mo concentration of 230 µg/L in streamwaters in northern England is likely related to the contamination from coal and fly ash as streams are found to close to coal-fired power stations (Smedley and Kinniburgh, 2017). The highest Mo concentration in lakes was reported in San Joaquin Valley lakes, CA, USA, at 2850 µg/L (138-23700 µg/L) (Smedley and Kinniburgh, 2017, Bradford et al., 1990).

Table 2-3 Average Mo concentration in surface waters across UK from (Smedley et al., 2014).

Water type	Range (average) (µg/L)	Number
Rainwater	0.2	
Streamwater		
World median streams	0.5	
Streams, Wales	<9–200 (<9)	13,337
Streams, Humber-Trent	0.06–2.7 ^b (0.68)	
River Tweed (Teviot)	0–4.2 (0.39)	119
River Wear	0.20–10.3 (1.46)	55
River Swale (Catterick)	0–5.00 (0.61)	172
River Nidd	0–4.32 (0.78)	184
River Ure	0–3.0 (0.51)	180
River Ouse (Acaster)	0–4.47 (0.95)	144
River Derwent	0–26 (0.90)	173
River Wharfe	0–4.92 (0.72)	192
River Aire	0.32–70.3 (23.5)	196
River Calder	0.57–19.7 (4.70)	176
River Don	0.70–20.1 (8.88)	180
River Trent	1.75–9.80 (5.05)	153
River Great Ouse	1.1–40.2 (3.34)	58
River Thames (Day's Lock)	0.5–10.0 (2.85)	108
River Thames (Howbery Park)	0.91–9.60 ^c (2.80)	
Upland streams (baseflow), Wales	0–14.7 (0.20 ^a)	67
Upland stream (stormflow), Wales	0–11.2 (0.36 ^a)	67

^a Median. BGS (1999) data were determined by ICP-OES; all others determined by ICP-MS.

^b 10th, 90th percentile values.

^c A recorded value of 1588 µg/L for this site is treated as spurious.

2.1.4.2 Mo in Rocks, Sediments, Minerals and Soils

A variety of secondary metal molybdate compounds including ferrimolybdite ($\text{Fe}_2(\text{MoO}_4)_3 \cdot n\text{H}_2\text{O}$), wulfenite (PbMoO_4), powellite (CaMoO_4), lindgrenite ($\text{Cu}_3(\text{MoO}_4)_2(\text{OH})_2$), ilsemannite ($\text{Mo}_3\text{O}_8 \cdot n\text{H}_2\text{O}$), and jordisite (MoS_2) are produced through the weathering of sulphide ore minerals (Smedley and Kinniburgh, 2017, Brellat et al., 2016). Mo is found in many secondary minerals either through adsorption to the mineral surface or in solid solutions,

and it is difficult to unambiguously define the Mo state in these minerals (Smedley and Kinniburgh, 2017). Sedimentary rocks can contain high concentrations of Mo, which is linked to the redox conditions (e.g. sulphate-reducing conditions) and depends on mineralogy and lithology (Smedley and Kinniburgh, 2017, Das et al., 2007). High concentrations of Mo can occur in ore-mineralised (sulfidic ore deposits, particularly porphyry systems) areas as well as groundwaters associated with oil shale and black shale (Smedley and Kinniburgh, 2017). Mo is generally more abundant in muds and shales when compared to carbonates and sandstones and the largest Mo concentrations are typically observed in euxinic condition where sediments are rich in sulphur and organic carbon because Mo has a strong affinity for these resulting in the formation of reducing conditions which favours Mo deposition (thiomolybdates) (Smedley and Kinniburgh, 2017). The concentration range of Mo in shales is from 1-3 mg/kg to 32-34 mg/kg (Och et al., 2013, Das et al., 2007), with more than 60 mg/kg Mo observed in black shales with higher levels of sulphur and organic compounds (Smedley and Kinniburgh, 2017). High levels of Mo(IV), has been found under anoxic conditions in oil shale from the Cretaceous aquifers in Jordan, relating to the dissolved SO₄ and other trace element (e.g. Cr, Ni and U) (Al Kuisi et al., 2015).

Uncontaminated soils typically contain Mo concentration less than 10 mg/kg and data of 6559 top soils samples collected from Humber-Trent area of England reported Mo contents of 0.4 – 43 mg/kg, with median of 2.2 mg/kg (Smedley and Kinniburgh, 2017). High Mo median levels in soils were reported from Coal Measures, Carboniferous Limestone, and Cretaceous clays and ironstones, while low median ones was found on the Mercia Mudstone, Chalk and red-bed Triassic Sherwood Sandstone (Smedley et al., 2014).

Anomalous levels of Mo can be observed in soils in mining/mineralization and industrial settings. Mining exploitation results in wastes containing high values of Mo with up to 4000 mg/kg Mo for tailings, significantly exceeding the Mo concentration for non-contaminated

soils (< 10 mg/kg) in surrounding areas (Frascoli and Hudson-Edwards, 2018, Smedley and Kinniburgh, 2017). Mo is the primary product that is mined by Mo porphyry deposits, and is a by-product of Cu porphyry and other Cu-bearing ores (Kropschot, 2010). The highest Mo concentration was recorded as 3985 mg/kg in tailings from Cu-polymetallic ores (including Cu porphyry ores) process in the Gyama Valley, Tibet (Huang et al., 2010).

Mo can be released during sulphide mineral oxidation in mine wastes and then be adsorbed onto secondary Fe(III)-minerals surfaces (such as ferrihydrite, schwertmannite, jarosite etc.) in moderately acidic waters (Smedley and Kinniburgh, 2017, Frascoli and Hudson-Edwards, 2018), and it can also be taken up in some secondary minerals including wulfenite and powellite at neutral or alkaline pH (Smedley and Kinniburgh, 2017).

2.2 Vanadium

2.2.1 V Application in Industry

V is exclusively applied in non-ferrous and ferrous alloys due to its physical properties of high hardness, strength and fatigue resistance (Moskalyk and Alfantazi, 2003). The increasing demand of V in nuclear applications, iron made tools, high speed steel, superconductive magnets and rust resistant steels (Emsley, 2011), as well as in mass energy storage batteries and sulfuric acid production (Imtiaz et al., 2015) has led to an increase of V-rich industry wastes such as steel slags and ash from waste incineration (Watt et al., 2018).

2.2.2 Vanadium Environmental Geochemistry

Vanadium (V) is a redox sensitive and wide-spread trace element in the earth's crust (Lazaridis and Asouhidou, 2003, Vessey et al., 2020). A variety of oxidation states (-1, 0, +2, +3, +4, and +5) exist in the environment with V(IV) and V(V) the predominant oxidation states in subsurface environmental systems (e.g. soils). The former exists mainly as the oxocation vanadyl ($\text{V(IV)}\text{O}^{2+}$) in aqueous solution, while V(V) occurs as the tetrahedral oxyanions VO_4^{3-} .

(Figure 2-3), HVO_4^{2-} , or H_2VO_4^- , depending on the pH value (Figure 2-4) (Larsson et al., 2017, Wisawapipat and Kretzschmar, 2017, Vessey et al., 2020, Watt et al., 2018). VO_4^{3-} is dominant species at pH over 13 and HVO_4^{2-} dominates at pH 9-13 (Vessey et al., 2020). H_2VO_4^- is predominant species at pH 5-9 at V concentration less than 1000 μM (Figure 2-5) (Vessey et al., 2020). Cationic V(V) species (such as VO_2^+), occurring under low pH conditions ($\text{pH} < 3.6$), are regarded as the most mobile and toxic V species. Dissolved V(V) is dominant in oxic seawater and can be reduced to vanadyl V(IV) by H_2S and organic compounds at pH 6 under anoxic conditions (Larsson et al., 2017, Wisawapipat and Kretzschmar, 2017, Crans et al., 1998, Martin and Kaplan, 1998, Breit and Wanty, 1991). Both of V(V) and V(IV) species present in the usual oxygen fugacity range that earth allows, while the divalent state (V(II)) only occurs in highly reduced conditions. This feature provides important information about the redox systems and can be a valuable geochemical probe (Bordage et al., 2011).

V(V) speciation in solution depends on a number of factors including pH, V(V) concentration, and ionic strength. The formation of polyvanadate occurs in a number of different systems including higher concentration and lower pH, e.g. decavanadate ($\text{H}_x\text{V}_{10}\text{O}_{28}^{x-6}$) and metavanadate ($(\text{VO}_3)_x^{x-}$) at higher concentration ($\sim 100 \mu\text{M}$) and acidic conditions ($\text{pH} < 7$), while monovanadate occurs as the dominant species at pH over 7 (Figure 2-5) (Marques et al., 2017, Vessey et al., 2020, Poledniok and Buhl, 2003, Wisawapipat and Kretzschmar, 2017, Peacock and Sherman, 2004, Blackmore et al., 1996). The monovanadate is tetrahedral coordinated, and so are the polyvanadates such as $\text{H}_3\text{V}_2\text{O}_7^-$, $\text{V}_3\text{O}_9^{3-}$, $\text{V}_4\text{O}_{12}^{4-}$, with the exception of octahedrally coordinated V(V) in decavanadate with 10 V atoms situated at three distinct sites, including 6 V atoms in the middle (2 of them situated in the center (site a), surrounded by 4 atoms (site b)), and then capped by 2 atoms at top and bottom (site c) (Vessey et al., 2020).

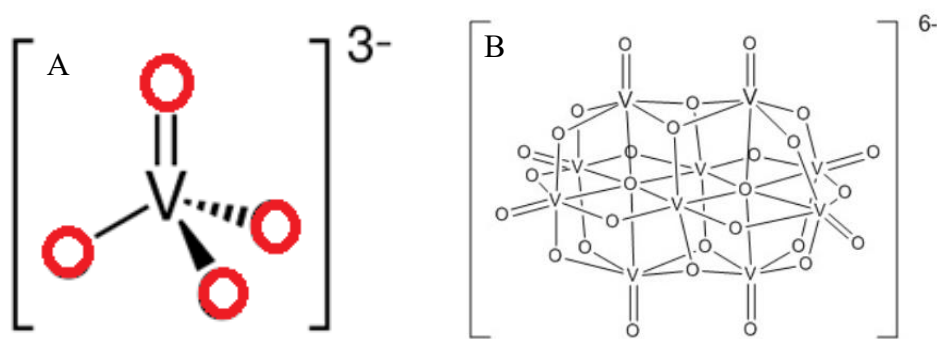


Figure 2-3 Structure of vanadate. A. Tetrahedral monovanadate (VO_4^{3-}). B. Octahedral decavanadate ($\text{V}_{10}\text{O}_{28}^{6-}$) (Evans Jr 1966).

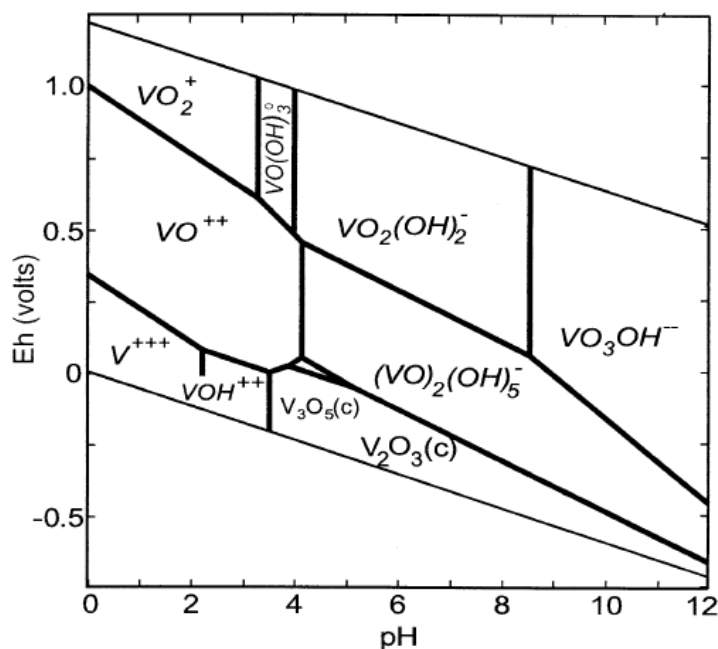


Figure 2-4 Eh-pH diagram for V aqueous species in V-O-H system from (Peacock and Sherman 2004). The concentration of total V is 5×10^{-5} m (~2.5 ppm).

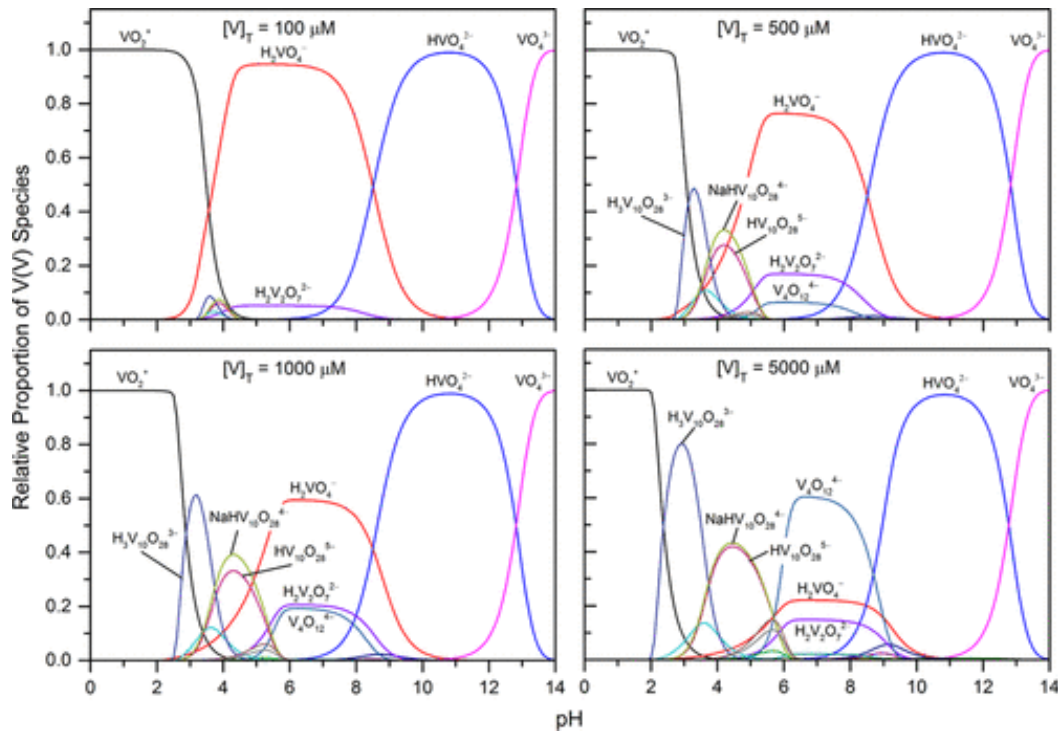


Figure 2-5 Diagrams for aqueous V speciation at 100, 500, 1000, and 5000 μM based on thermodynamic data using PHREEQCi (Version 3.1.5) from (Vessey et al. 2020).

2.2.3 Role of V in Plant, Animal and Human Health

The concentration of V has an important impact on the soil community (e.g. plants, microorganisms and vertebrates) with 130 mg/kg being the optimum criterion of V in soil for vertebrates and vascular plants (Imtiaz et al., 2015). Low concentrations of V are essential for humans, animals and microorganisms, and helps to increase metabolic activity, enzymatic processes, growth and yield in a variety of plants (Wisawapipat and Kretzschmar, 2017, Imtiaz et al., 2015). V deficiency can lead to reproductive anomalies for chicks and goats and induce a harmful impact on bone growth (Nielsen and Uthus, 1990). V plays a key role in nitrogen fixation, chlorophyll and utilization of potassium within plants when the concentration is less than 2 mg/kg (Imtiaz et al., 2015). In field studies, both the sucrose of mature sugar beet roots and the yield of maize cobs were observed to increase after applying V (Singh, 1971, Singh and Wort, 1969). V is also beneficial to humans because it helps to alleviate diabetes,

hypertension, hyperlipidemia, and certain kinds of cancer (Wisawapipat and Kretzschmar, 2017). However, if the V concentration is too high, it will pose a risk to plant growth by causing chlorosis and humans by increasing blood pressure, reducing the number of red blood cells, and even causing neurological effects (Imtiaz et al., 2015, Kabata-Pendias and Pendias, 1999, Singh, 1971). V has been regarded as a potentially dangerous contaminant in the same class with arsenic, lead and mercury (Naeem et al., 2007, Lazaridis and Asouhidou, 2003). When the concentration of V is over 100 µg/L, it becomes toxic in marine systems, whereas it becomes toxic for terrestrial plants when the figure is 10 mg/kg or more in soil. If plants are very sensitive, 1 mg/L of V will cause toxicity in solution (Larsson et al., 2017).

2.2.4 Occurrence and Distributions of V in the Environment

2.2.4.1 V in Soils, Minerals and Rocks

Vanadium(V) is a wide spread trace element in earth crust, with an average concentration of 135 mg/kg in soil, ranking V 5th most abundant element among all the transition metals (Imtiaz et al., 2015). pH and oxidation states play key roles in the geochemical characteristics of V, with an average V concentration range from 10 to 220 mg/kg in soils and 738 mg/kg to 3505 mg/kg in contaminated soils in mining areas (Imtiaz et al., 2015, Połedniok and Buhl, 2003, Panichev et al., 2006, Teng et al., 2009, Cappuyns and Swennen, 2014). Ilmenite ores, titaniferous magnetite and fossil fuel deposits are the main sources of vanadate (Moskalyk and Alfantazi, 2003). Soils rich in V, with mainly V(V), form covers in tropics and subtropics areas because these regions have highly weathered soils in comparison with soils in temperate climate areas. In highly weathered soils, Kaolinite and iron (oxyhydr)oxides, predominate in the clay fractions, which can be potential host minerals to incorporate structural V(III) and/or V(IV)/V(V) (Wisawapipat and Kretzschmar, 2017). V can be present as V(V) sorbed to Fe(III)-HS complexes, humic substances (HS), kaolinite, ferrihydrite and goethite and as V(IV) in the structure of kaolinite, goethite and ferrihydrite (Wisawapipat and Kretzschmar, 2017).

Figure 2-6 shows the major deposits of V across the world, commonly in argillaceous and alkaline igneous rocks (Imtiaz et al., 2015). V occurs in different minerals such as vanadinite, roscoelite, patronite, chileite, and carnotite. The average V concentration ranges from 3 to 310 mg/kg, but 1600 mg/g is observed in phosphate rocks (Imtiaz et al., 2015, Frank et al., 1996). V is often present in phosphate ore and the processing of phosphate rock using acids to produce fertilizer can result in the extraction of vanadate ions into the phosphoric acid, and lead to land contamination (Moskalyk and Alfantazi, 2003). The natural sources of V are mainly V-bearing Fe-Ti oxides found in layered magmatic intrusions, such as those found in the Bushveld Igneous Complex in South Africa (Bordage et al., 2011). Ore deposits containing V-bearing ilmenite (FeTiO_3) (located in the Far East, northwest area of Russia, Siberia, and Urals) and titaniferous magnetite ($\text{Fe(II)(Fe(III),Ti)}_2\text{O}_4$) (found in South Africa, Russia, China, Australia) are the main sources of vanadium within crystalline host rock deposits (Moskalyk and Alfantazi, 2003). In sedimentary lithologies, shales contain greater V concentrations than carbonate rocks and sandstones, with 130 mg/kg vs. 20 mg/kg (Imtiaz et al., 2015).

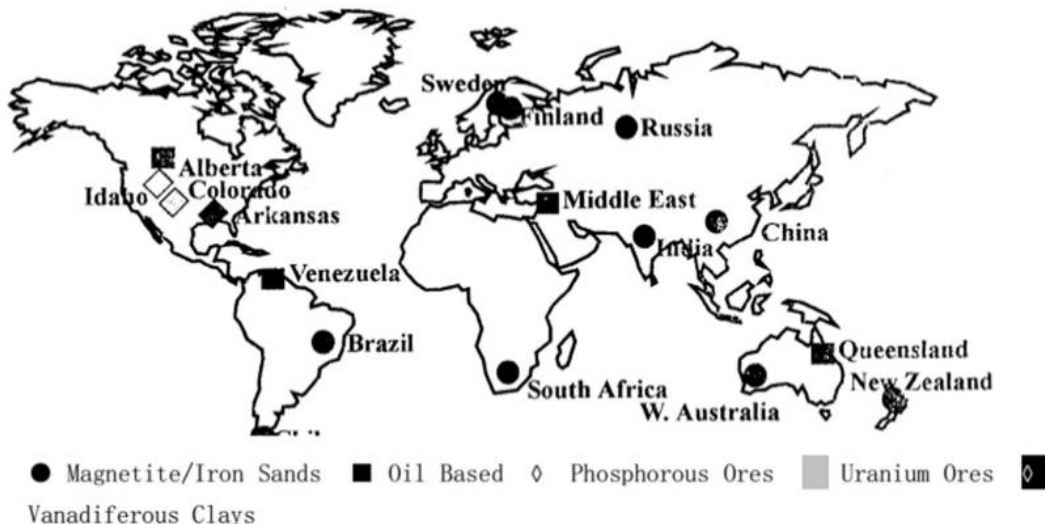


Figure 2-6 Major deposits of V in the world from (Imtiaz et al. 2015). V occurrence varies in different minerals such as vanadinite, roscoelite, patronite, chileite, and carnotite. The average V concentration ranges from 3 to 310 mg/kg, but 1600 mg/g is contained in phosphate rocks.

Figure 2-7 shows the overview of annual fluxes of V in the global biogeochemical cycle, which presents a significant anthropogenic activities component, resulting from fossil fuels, mining and steel making etc. which has led to the increasing concentration of V in soil, water and atmosphere (Gustafsson, 2019, Schlesinger et al., 2017). V has the highest anthropogenic enrichment factor (AEF) of all the trace elements in the atmosphere and the fourth highest AEF in rivers (Mejia et al., 2007, Imtiaz et al., 2015, Watt et al., 2018, Vessey et al., 2020). Burning of fossil fuels, especially oil, has led to a large annual V release as aerosols (100-280 Gg/yr⁻¹) (Figure 2-7) (Schlesinger et al., 2017, Gustafsson, 2019). Mejia (2007) and Imtiaz (2015) reported that there are more than 60 thousand tons of V released into the atmosphere every year due to anthropogenic activities, including mining (Mejia et al., 2007, Imtiaz et al., 2015). Significant concentrations of V compounds occur in fuel oil and large numbers of fly ash deposits, with annually around 2.3×10^3 kg of V released into the environment and about 1.32×10^3 kg of V deposited in soils (Jansson-Charrier et al., 1996, Slack, 1968). The rise in

discharge of V to the environment is attributed, in part, to the increase of V-rich industry wastes such as steel slags and ash from waste incineration (Watt et al., 2018).

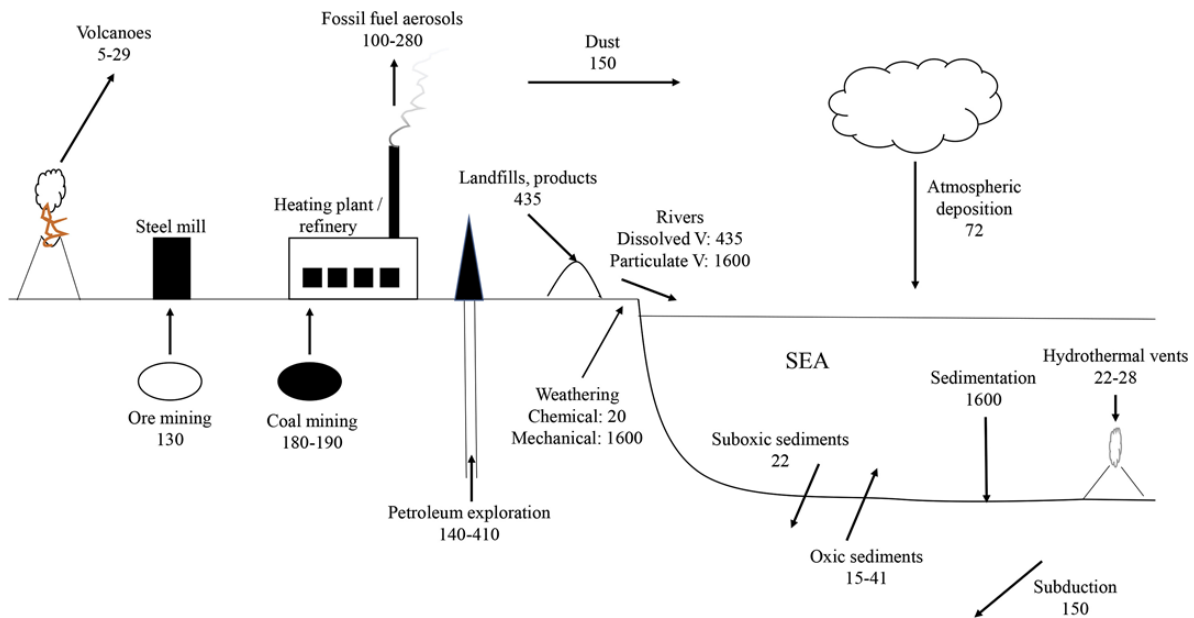


Figure 2-7 Vanadium global biogeochemical cycle from (Schlesinger et al., 2017, Gustafsson, 2019). All values are in 10^9 grams per year (Gg V yr^{-1}).

V concentration value in different countries depends on the mineralogical composition of rocks, with an average value of 108 mg/kg (Table 2-4). The environmental guidelines of V in soils for invertebrates and plants are different from different countries as well, with 180 mg/kg in Czech Republic, 130 mg/kg in Canada, 120 mg/kg in Slovenia, and 42 mg/kg in Netherlands respectively (Imtiaz et al., 2015). However, the soil V standard in USA is very strict due to the observation that V concentrations of 2 mg/kg are toxic to native plants (Efroymson et al., 1996). UK Soil and Herbage Pollutant Survey (UKSHS) reported that the V concentration in UK is 2.18-544 mg/kg, with the median of 39.2 mg/kg (Ross, 2007). The median of V concentration is reported to be 25 mg/kg in the topsoil of Europe, while the value in Japan is reported to be the highest at 250 mg/kg (Chen et al., 2020). Wisawapipat and Kretzschmar (2017) stated that the leaching of V from petroleum coke and emission from fossil combustion leads to an

increase in environmental pollution in European soils, with the median V concentration of 60.4 mg/kg (a range from 1.28 to 537 mg/kg) (Wisawapipat and Kretzschmar, 2017).

Table 2-4 V concentration in soils in different countries (Chen et al., 2020).

Country	Europe	Netherland	Denmark	Portugal	Italy	Sweden	Finland
V concentrations (mg/kg)	25	27.7	31	32	34	69	79
<hr/>							
Country	Russia	USA	China	Japan	Japan	Lithuania	Baltic State
V concentrations (mg/kg)	79-91	36	87.36	250 (Andosols)	94 (Gleysols)	38	18

2.2.4.2 V in Groundwater and Surface Water

V is a key metal contaminant for ground and surface waters impacted mainly by mining (Imtiaz et al., 2015). WHO reported that drinking water generally contains V less than 10 µg/L, but the common range is 1-30 µg/L, with an average value of 5 µg/L (WHO, 1988). In USA, 0.33 µg/L was accepted for V safe limit in drinking water (Imtiaz et al., 2015, DOE, 1999). The investigation of V in groundwater has attracted some groundwater researchers' interest, but the key sources and behaviours of V in ground waters are still not well understood (Imtiaz et al., 2015). The average concentration of V reported in California groundwater is 5 µg/L and the highest concentration was observed in oxic and/or alkaline systems (Gustafsson, 2019, Wright and Belitz, 2010). V concentration can be significantly higher in some areas with V-rich bedrock. For example, a V concentration of 10-20 µg/L was observed in groundwater in Mt. Fuji in Japan where there are V-rich basalts and the concentration in deep groundwater may be up to 147 µg/L (Gustafsson, 2019). 180 µg/L was reported in some drinking water in

Italy, which may pose a threat to health (Arena et al., 2015, Gustafsson, 2019). Considerably lower V concentration also occurs in some areas. For example, the median V concentration of 0.39 µg/L was reported in bottled mineral water in Sweden (Gustafsson, 2019, Rosborg et al., 2005). The dissolved V concentration in lakes and rivers differs depending on the weathering of the bedrock. For example, the median V concentration of 0.1 µg/L was reported in Taiwan dominated by metamorphic rocks, while the value was observed to be 65 µg/L in Nicaragua in rivers draining volcanic rocks (Gustafsson, 2019). The median concentration of V in European stream water is 0.46 µg/L (Reeder, 2006, Borg, 1984, Gustafsson, 2019). V concentrations in rainfall collected in remote areas and in continental areas subject to human activities are shown in Table 2-5 and indicate the median concentration of V in rainfall of 0.03 µg/L for remote sites, while for modern conditions with human activities, the value of ~0.4 µg/L is reported (Schlesinger et al., 2017).

Table 2-5 V concentration in rainfall in various locations from (Schlesinger et al., 2017).

Location	n	Volume-weighted concentration, µg/L
Remote areas		
East Antarctica		0.00046
Coats Land, East Antarctica		0.00056
East Antarctica	12	0.003
Greenland	9	0.015
Enewetak Atoll	14	0.018
Tibetan Plateau, China	79	0.033
Bermuda		0.096
Hawai'i (volcano quiescent)	3	0.13
Korea (rural)	87	0.14
Alps, Switzerland		0.14
Hong Kong, China	32	0.18
Alps, Switzerland		0.223
Continental areas with moderate human activities		
Hiroshima, Japan	152	0.23
Newark, New Jersey, USA	46	0.24
Pensacola, Florida	225	0.274
Lamto, Ivory Coast	50	0.29
Lhasa, Tibet, China	157	0.31
Japan (four sites)		0.38
Tibetan Plateau, China	103	0.43
Culpepper, Virginia	58	0.43
Reston, Virginia	26	0.47
Tokyo, Japan	20	~0.5
Delaware		0.67
Montreal, Canada	65	0.75
Oleiros A Coruna, Spain	18	0.83
South China	37	1.08
Massachusetts,	12	1.1
Rhode Island	269	1.27
Northern China		1.4
Ankara, Turkey	76	2.22
Kollo, Niger	22	2.29
Southern Jordan	27	4.21
Singapore, Malaysia	84	3.54
Nanjing, China		4.6
Mexico City, Mexico	81	5.13

So, anthropogenic emission and natural occurrence play a significant role in increasing Mo and V concentrations in the environment, it is essential and important to remove them from waste water, sediments and soils (Naeem et al., 2007, Smedley and Kinniburgh, 2017). Understanding the molecular scale chemical forms (e.g. monomers or polymers) and

adsorption mechanisms of V and Mo as a function of geochemical condition (e.g. pH and concentration) is key to predicting the environmental behaviour of these contaminants. In addition, the speciation (e.g. oxidation states and coordination chemistry) plays an important role in controlling the toxicity and bioavailability of these contaminants to organisms (Wisawapipat and Kretzschmar, 2017).

2.3 Iron Oxides

Iron oxides such as hematite, magnetite and biogenic magnetite play a significant role in controlling the mobility of toxic elements in contaminated land systems due to their high surface area and reactivity (Goldberg et al., 1996, Goldberg et al., 1998).

2.3.1 Hematite

Hematite ($\alpha\text{-Fe}_2\text{O}_3$) is the widespread iron oxide in soils and rocks. It has a hexagonal close packed (hcp) structure of oxygen with Fe(III) distributed in octahedral interstices (Figure 2-8). Fe(III) ions fill two thirds of the interstitial sites and produce $\text{Fe}(\text{O})_6$ octahedra. A regular two-ion-one-vacancy pattern fills the one third left vacant (Cornell and Schwertmann, 2004).

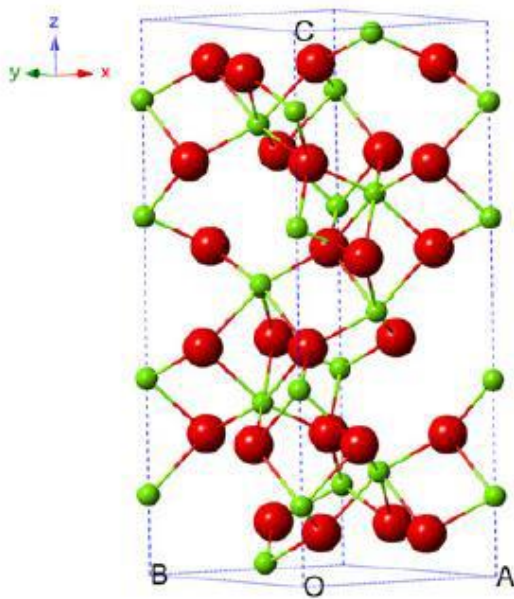


Figure 2-8 Crystal structure of hematite by ball-and-stick model from (Wu et al. 2015). The red atoms are O and the green ones are Fe.

2.3.2 Magnetite

Magnetite (Fe_3O_4) is present as the dominant contributor to the rock magnetism throughout uppermost mantle and earth's crust (Coker et al., 2007). The inverse spinel structure of magnetite is complex because the phase contains both $\text{Fe}(\text{II})$ and $\text{Fe}(\text{III})$ ions and the formula can be written as $\text{Fe}(\text{III})[\text{Fe}(\text{II})\text{Fe}(\text{III})]\text{O}_4$ presenting with octahedral sites containing both $\text{Fe}(\text{II})$ and $\text{Fe}(\text{III})$ and tetrahedral sites containing only $\text{Fe}(\text{III})$ (Figure 2-9) (Cornell and Schwertmann, 2004). Magnetite formation by the processes of magmatic and hydrothermal activity results in various crystal sizes from submicron to several meter thick polycrystalline layers (Coker et al., 2007).

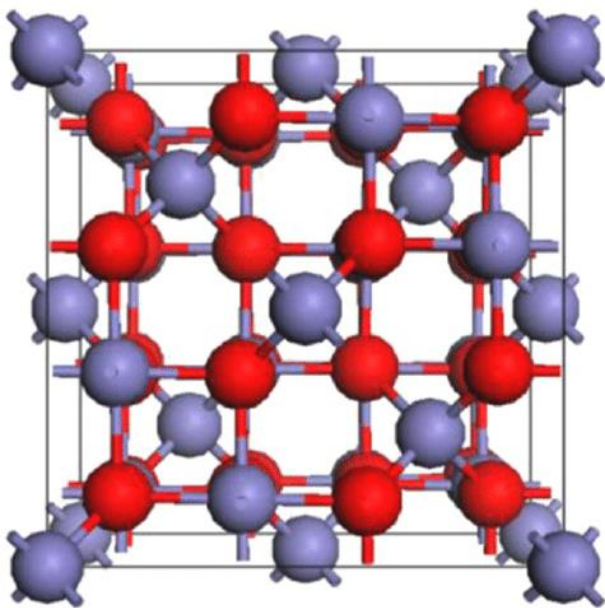


Figure 2-9 Crystal structure of magnetite by ball-and-stick model from (Noh et al. 2014). Fe atoms are in blue and O atoms are in red.

2.3.3 Biogenic Magnetite

Biogenic nanomagnetite is formed through the reductive transformation of ferrihydrite at circumneutral pH using dissimilatory metal reducing bacteria (DMRB), such as *Geobacter sulfurreducens* (Lovley et al., 1987). These specialist bacteria are able to couple the oxidation of organic matter to the reduction of oxidized metals in the environment, such as Fe(III) in ferrihydrite, in order to gain energy for growth (Lloyd et al., 2003). The difference between biogenic magnetite and chemically obtained magnetite (chem-magnetite) is that the biogenic magnetite exhibits smaller crystallite size by powder X-ray diffraction (XRD), but there is no difference in the Fe-O bonding according to the observation from Raman Spectroscopy. This indicates biogenic magnetite is likely to exhibit more compact crystal structure, with less uncoordinated Fe at the surface (Moon et al., 2010). Biogenic nanomagnetite has previously been found to be a highly effective sorbent and reductant of toxic contaminants e.g. Cr(VI) O_4^{2-} (Watts et al., 2015).

2.4 Mo Interaction with Iron Oxides

2.4.1 Mo Sorption to Iron Oxides

Adsorption is the accumulation process of ions, atoms or molecules at the mineral solution interface (Krauskopf, 1979). It includes inner-sphere and outer-sphere complexation. Inner-sphere complexation occurs via ligand exchange reactions with surface functional groups, with adsorbed ions binding directly onto the surface with no water molecules to form intervening layer (Figure 2-10) (Arai, 2010, Smedley and Kinniburgh, 2017). For outer-sphere binding, a layer of water molecules is retained between the surface and the ion by electrostatic interactions and result in less selective binding than inner-sphere complexes (Smedley and Kinniburgh, 2017).

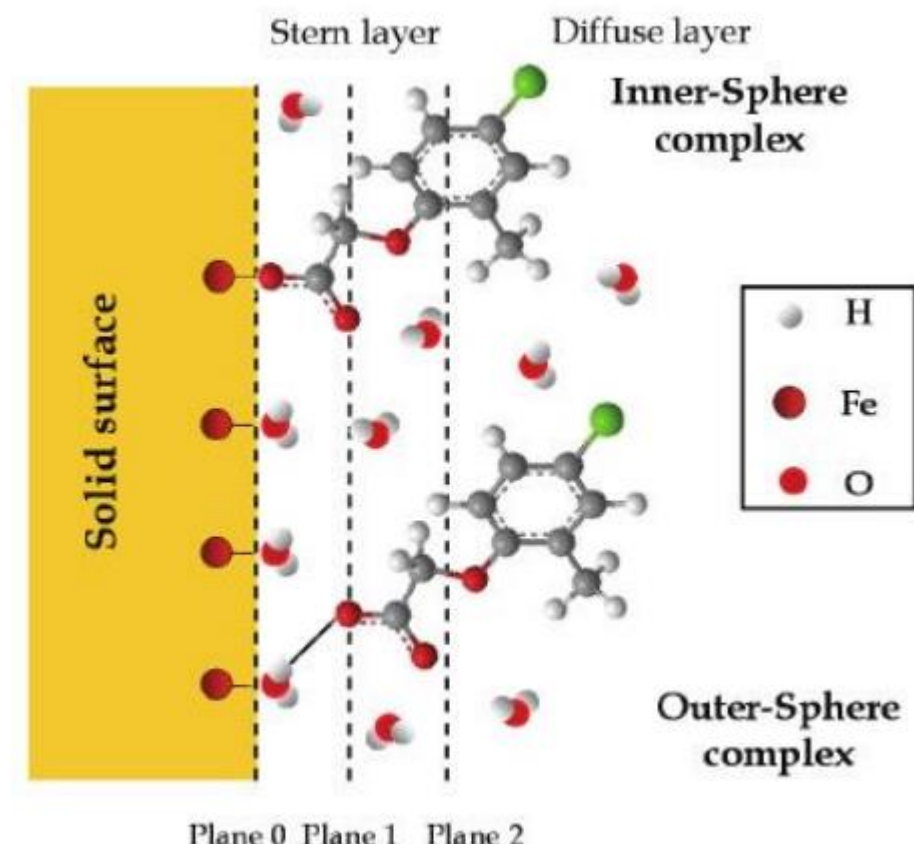


Figure 2-10 Structure of inner-sphere and outer-sphere complexation (Arce et al., 2011).

The aqueous environmental mobility, speciation and bioavailability of Mo are impacted by a variety of geochemical factors, including pH, ionic strength, presence of competitive adsorbates (e.g. phosphate), adsorbent type and Mo oxidation state (e.g. Mo(VI) and Mo(IV) species). There is little affinity for absorption of molybdate ($\text{Mo(VI)}\text{O}_4^{2-}$) to most organic compounds, therefore the transport and fate of Mo(VI) anions in many oxic sub-surface environmental systems is controlled by molybdate adsorption on mineral surfaces, in particular, iron (oxyhydr)oxides nanoparticles e.g. hematite ($\alpha\text{-Fe}_2\text{O}_3$) and goethite ($\alpha\text{-FeOOH}$), due to their high surface area and reactivity (Xu et al., 2013, Wichard et al., 2009). There are a range of studies related to molybdate and tetrathiomolybdate ($\text{Mo(VI)}\text{S}_4^{2-}$) adsorption to iron (oxyhydr)oxides such as goethite (Arai, 2010, Xu et al., 2006a, Zhang and Sparks, 1989), ferrihydrite (Brinza et al., 2008, Brinza et al., 2015, Gustafsson, 2003, Das et al., 2016), hematite (Brinza et al., 2015, Goldberg et al., 1996, Goldberg et al., 1998, Das and Hendry, 2013) and magnetite (Verbinnen et al., 2012, Verbinnen et al., 2013). In general, Mo(VI) adsorbs to iron (oxyhydr)oxides surfaces at low pH with adsorption decreasing rapidly with increasing pH above 5 and little adsorption occurring above pH 8 (Figure 2-11) (Xu et al., 2013, Xu et al., 2006a, Brinza et al., 2008, Gustafsson, 2003, Goldberg et al., 1996, Verbinnen et al., 2012). This indicates that the adsorption behaviour as a function of pH related to the nature of bonding between MoO_4^{2-} and the mineral surface and low pH conditions have more potential to control the mobility of Mo, relative to high pH environments, resulting in the surficial positive groups, which can attract negative molybdate anionic species by electrostatic attraction or ion-pair formation (Smedley and Kinniburgh, 2017, Alfaro et al., 2019). However, at very low pH (e.g. pH<3.5), Fe(III)-(oxyhydr)oxide can dissolve and release sorbed Mo (Smedley and Kinniburgh, 2017).

Phosphate (PO_4^{3-}) is a significant competitive anion to molybdate in solution with a presence of phosphate leading to a up to 40% decrease in Mo adsorption to goethite, whereas there are

little competitive impacts by sulfate (SO_4^{2-}) and silicate (SiO_3^{2-}) (Xu et al., 2006a, Xu et al., 2006b). The ionic strength of the solution has little effect on the adsorption mechanism of Mo to goethite (Goldberg et al., 1996) and the lack of ionic strength dependence indicates the adsorption process involves inner-sphere complexes (chemisorption) rather than outer-sphere surface complex (physisorption) (Zhang and Sparks, 1989, Hayes et al., 1988, Goldberg et al., 1993, Verbinnen et al., 2012).

Previous investigation on Mo(VI) adsorption to the mixed valence iron oxides (perlite-supported magnetite) observed the similar result to that for ferric oxyhydroxides with decreasing adsorption with increasing pH. The adsorption mechanism was indicated to be via inner-sphere complex formation, as adsorption could occur at pH values over pH_{pzc} (pH value at the point of zero charge), with the decreasing adsorption behaviour associated with the decrease concentration of speciation ($\text{H}_2\text{MoO}_4 \cdot 2\text{H}_2\text{O}$) with the increase of pH on the perlite-supported magnetite surface (Verbinnen et al., 2016).

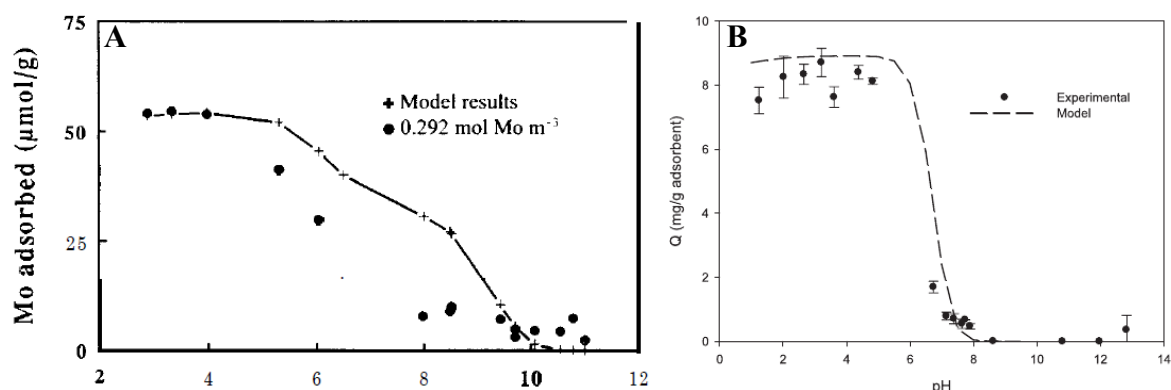


Figure 2-11 Mo adsorption to hematite (A) and magnetite (B) as function of pH from (Goldberg et al. 1996, Verbinnen et al. 2012).

2.4.2 Surface Adsorption Modeling

The classical adsorption isotherms can be modelled using a variety of approaches (such as Langmuir, Freundlich, Diffuse Layer (DLM), MUSIC/CD-MUSIC, CONSTANT

CAPACITANCE (CC)) depending upon the complexity and requirements of the data (Xu et al., 2013, Larsson et al., 2017, Gustafsson and Tiberg, 2015, Verbinnen et al., 2012, Smedley and Kinniburgh, 2017). All models aim to associate the amount of substances bound to surfaces with its content or activity in solution (Smedley and Kinniburgh, 2017).

The Langmuir isotherm model, which describes a surface monolayer adsorption mechanism, is a frequently used approach to fit the observed data (Smedley and Kinniburgh, 2017, Alfaro et al., 2019). Most adsorption data can be fitted reasonably well using a Langmuir isotherm, however the scope is limited because it cannot analyse electrostatic interactions explicitly and the formulation of the competition from other ions (even H⁺/OH⁻) is not considered (Smedley and Kinniburgh, 2017). A Langmuir model is described by the following equilibrium:

$$Q_e = Q_{\max} \times b \times C_e / (1 + b \times C_e) \quad (2-1)$$

where Q_e (mg Mo/g adsorbent) is the adsorbed amount at equilibrium. Q_{max} (mg/g) is the maximum adsorption capacity. b (l/mg) is a constant. C_e is the residual adsorbent concentration in solution at equilibrium (Verbinnen et al., 2012).

The isotherm adsorption of molybdate onto silica-coated magnetite was fitted with Langmuir model at initial Mo(VI) concentration up to 200 mg/L and indicated a maximum adsorption of Mo(VI) was 15.6 mg/g with R factor of 0.956. However, the authors also applied the Langmuir-Freundlich hybrid model with the maximum adsorption of 43.1 mg/g and R factor of 0.993. This showed that the Langmuir-Freundlich hybrid model gave a better interpretation of the adsorption equilibrium as the adsorption mechanism could be via a combination of a surface monolayer chemisorption and diffuse or multilayer physisorption (Alfaro et al., 2019).

2.4.3 Attenuated Total Reflection-Fourier Transform Infrared (ATR-FTIR) of Mo

Adsorption

Mo exists as both tetrahedral monomolybdate (e.g. MoO_4^{2-}) and octahedral polymolybdate (e.g. $\text{Mo}_7\text{O}_{24}^{6-}$), depending on a variety of pH and Mo concentration conditions (Ozeki et al., 1988, Mitchell, 2009, Cruywagen, 1999, Davantes et al., 2017). The monomolybdate occurs at neutral and alkaline systems and low Mo(VI) concentration ($< 10^{-4}$ M), while the heptamolybdate is observed at low pH less than 5 and high Mo(VI) concentration ($> 10^{-4}$ M). Attenuated Total Reflection-Fourier Transform Infrared (ATR-FTIR) is a powerful technique to identify species change and surface polymerization, which is significantly controlled by pH and Mo(VI) concentration (Goldberg et al., 2007).

A previous study using ATR-FTIR on samples with Mo(VI) adsorbed to hematite observed two features at high wavenumber: 1. peaks at $\sim 850 \text{ cm}^{-1}$ and $\sim 910 \text{ cm}^{-1}$ were present in high pH and low concentration (low surface coverage) samples, suggesting Mo(VI) is present as a monomeric adsorbed species; 2. a sharp peak at 970 cm^{-1} was present at low pH and high concentration (high surface coverage) samples, indicative of polymeric Mo(VI) species (Davantes et al., 2017). Two bands at 910 and 850 cm^{-1} that were identified at low surface coverage (high pH) (Figure 2-12 and Table 2-6), consistent with Mo(VI) on lepidocrocite which shows two peaks at 920 and 850 cm^{-1} , indicating the monomeric complex on the surface is consistent across different iron (oxyhydr)oxide phases. These two peaks shifted to 940 and 900 cm^{-1} at higher surface coverage, corresponding with the splitting of asymmetric stretching because of the symmetry reduction of the ion from T_d to C_{3v} . The peaks of 910 cm^{-1} and 850 cm^{-1} at low surface coverage had wide bands (23 and 36 cm^{-1} respectively), while the value decreased to 11 cm^{-1} for the peak of 975 cm^{-1} , indicating a more homogeneous environment. This may be due to the transition from mononuclear adsorbed Mo(VI) at the oxide/solution

interface to Mo(VI) associated with the polymeric species (such as heptamolybdate, $\text{Mo}_7\text{O}_{24}^{6-}$) with C_{2v} symmetry (Davantes et al., 2017).

A peak at 827 cm^{-1} was observed at low surface coverage for Mo adsorbed onto layered double hydroxides, corresponding with the asymmetric stretching ν_3 of tetrahedral MoO_4^{2-} with T_d symmetry (Davantès and Lefèvre, 2013). This peak decreased along with a decrease in pH to 4.49, where octahedral heptamolybdate ($\text{Mo}_7\text{O}_{24}^{6-}$) with C_{2v} symmetry was shown to occur via the formation of a peak $\sim 970 \text{ cm}^{-1}$ (Davantès and Lefèvre, 2013). Overall, these studies indicate that IR can be successfully utilized to investigate the adsorption mechanism of Mo(VI) to the surface of iron (oxyhydr)oxides, including hematite.

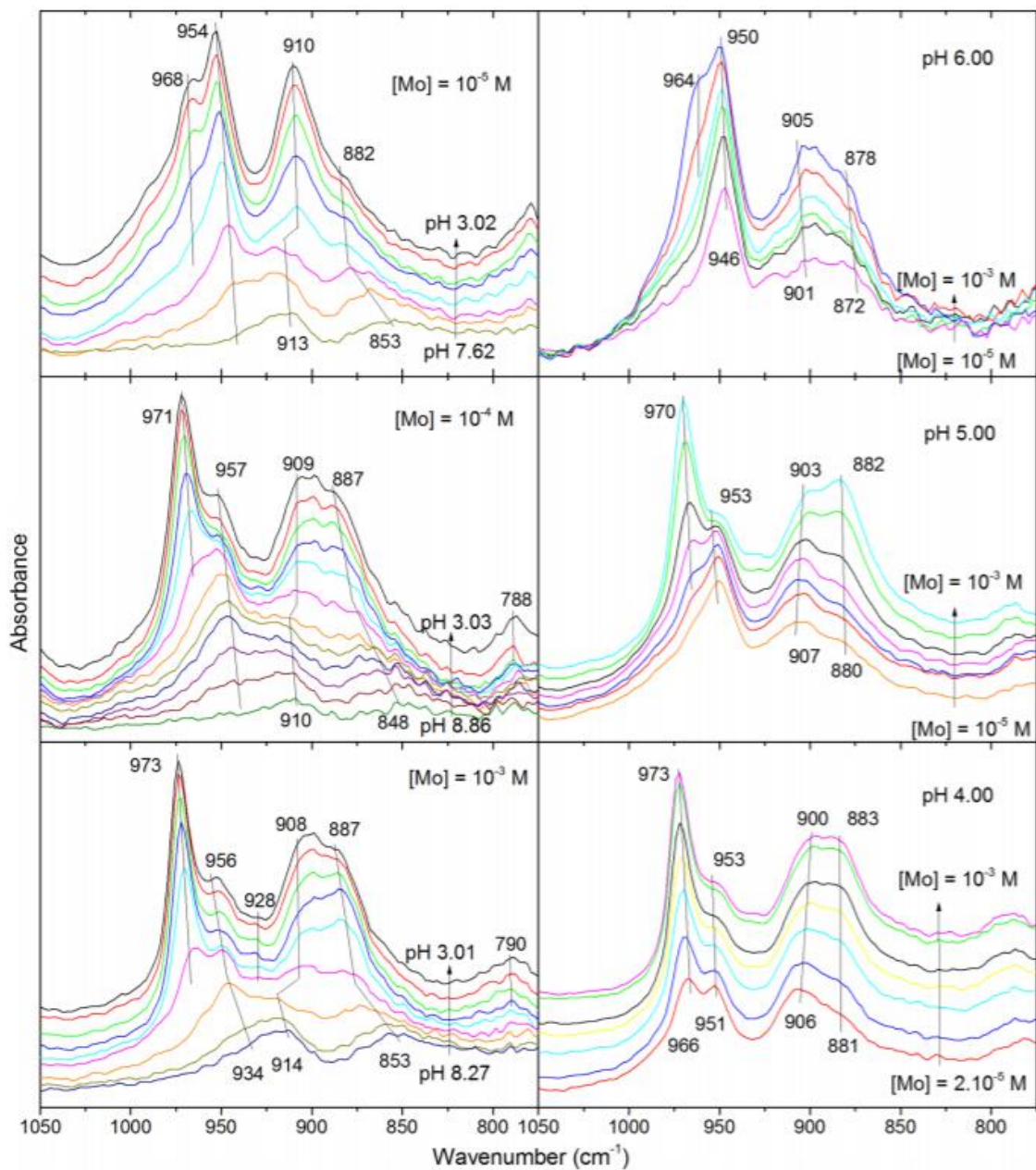


Figure 2-12 ATR-FTIR spectra of Mo(VI) adsorbed to hematite in varying conditions from (Davantes et al. 2017).

Table 2-6 Previous FTIR studies for adsorbed Mo(VI) onto lepidocrocite (Davantes et al., 2017).

Adsorbed samples		Wavenumber (cm ⁻¹)
Mo 1 mM, pH 3	945	903
Mo 1 mM, pH 8.5	918	848

2.4.4 X-ray Absorption Spectroscopy (XAS) Studies of Mo Adsorption

XANES (x-ray absorption near edge structure) and EXAFS (extended x-ray absorption fine structure) enable the study of metal coordination and speciation in solutions and solids. XANES is applied to provide information on the oxidation states and coordination environment of Mo in solids and EXAFS shows local coordination environment of the Mo (e.g. interatomic distances and coordination numbers) (Smedley and Kinniburgh, 2017).

XANES analysis of Mo(VI) standards and Mo(VI)-adsorbed to ferrihydrite, hematite and goethite at neutral pH indicated a pre-edge peak at 20002.8-20004.9 eV which suggest tetrahedral adsorption complex onto these iron oxide minerals (Figure 2-13) (Das et al., 2016, Gustafsson and Tiberg, 2015, Arai, 2010, Brinza et al., 2015, Wharton et al., 2003). In contrast, XANES/EXAFS analysis indicates that Mo(VI) is present in a distorted octahedral coordination environment for the adsorption of Mo(VI) onto the organic acid--rich (fulvic acid) soils (no Mo(VI) reduction being identified), as well as Mo(VI) incorporation in hematite, ferrihydrite and goethite (Figure 2-14) (Gustafsson and Tiberg, 2015, Görn et al., 2021).

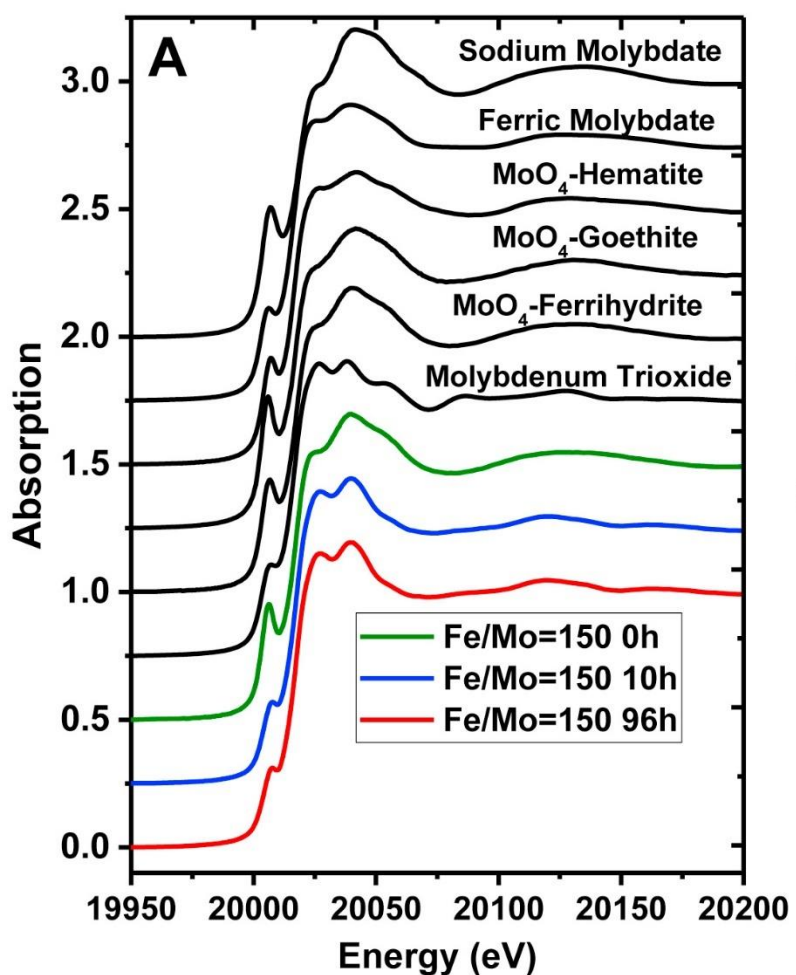


Figure 2-13 Normalized Mo K-edge XANES for standards and samples from Fe/Mo system at t = 0-96 h from (Das et al. 2016).

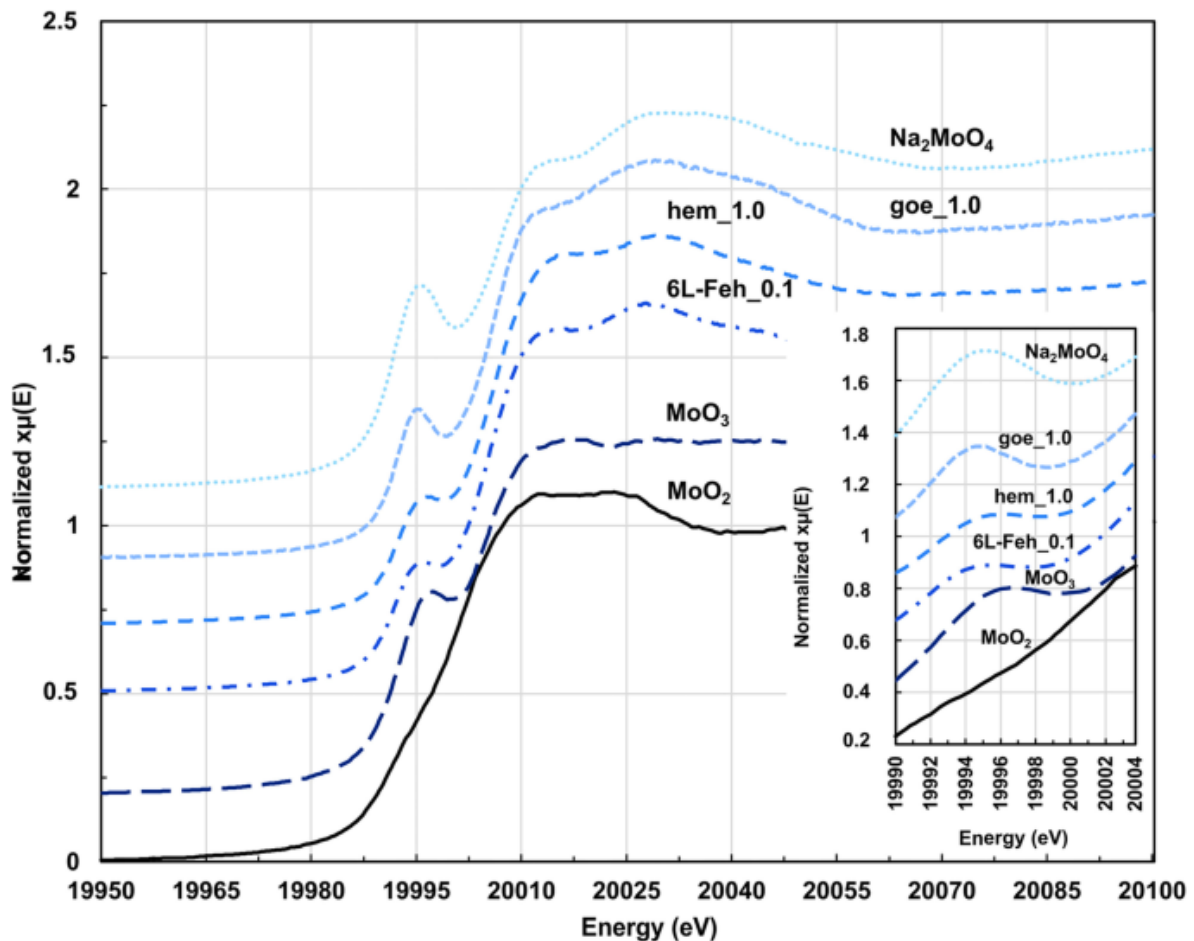


Figure 2-14 Normalized Mo K-edge XANES for standards (Na_2MoO_4 , MoO_3 and MoO_2) and samples from Mo(VI) incorporation in hematite, goethite and ferrihydrite with spectra inset with more detailed pre-edge feature. goe 1.0 and hem_1.0 represent the initial Mo:Fe molar ratio of 1.0 in goethite and hematite, respectively. 6L-Feh_0.1 means the initial Mo:Fe molar ratio of 0.1 in six-line ferrihydrite. aFrom (Görn et al., 2021).

EXAFS can be used to identify both inner and outer sphere complexation of absorbed species on surfaces. A few previous investigations of Mo adsorption mechanisms were performed using EXAFS and indicated that inner-sphere complexation occurs for Mo adsorption to ferrihydrite, goethite, $\alpha\text{-Al}_2\text{O}_3$ and montmorillonite (Goldberg et al., 1996, Xu et al., 2013, Goldberg et al., 1998). Specifically, a tetrahedrally coordinated inner-sphere complex forms at the goethite surface with a mixture of edge-sharing bidentate mononuclear (fitted with one Mo-Fe at 2.8 Å) and corner-sharing bidentate binuclear complexes (fitted with one Mo-Fe at 3.48-

3.53 Å) at near-neutral pH (Figure 2-15) (Arai, 2010, Brinza et al., 2015, Das et al., 2016). A study of Mo adsorption to ferrihydrite surface indicated a tetrahedral corner-sharing structure at pH 7 and pH 8.5 (Brinza et al., 2015). In contrast, at higher pH (~10) Mo(VI) was reported to form an outer-sphere adsorption complex (Das et al., 2016, Kashiwabara et al., 2013) as evidenced by the absence of Mo-Fe shells in Fourier transformed (FT) and radial structure function (RSF) for Mo(VI) adsorbed on ferrihydrite (Das et al., 2016), as well as kaolinite and Al oxide (Goldberg et al., 2007).

In acidic systems (pH 4) the Mo adsorption complex was composed of a mixture of tetrahedrally and octahedrally coordinated Mo(VI) bound via corner-sharing to the goethite surface (Arai, 2010). In addition, evidence of a Mo-Mo single scattering path and the increasing coordination number of Mo-Mo with surface loading for the sample at pH 4 indicated a polymeric species (e.g. a dimer), with Mo in a octahedral coordination environment, similar to the Mo local environment to bamfordite ($\text{Fe(III)}\text{Mo}_2\text{O}_6(\text{OH}_3)\bullet\text{H}_2\text{O}$) (Arai, 2010, Birch et al., 1998). The exact nature of the polymolybdate structure that forms on the surface of iron (oxyhydr)oxides was unclear from this study but, recent DFT calculations suggest a three-dimensional cluster containing three, four or five molybdate ions bonded on the surface forming mixed tetrahedral and octahedral complexes with Mo-Mo distances from 3.25 to 3.72 Å (Figure 2-16) (Davantes et al., 2017) seem produce IR spectra similar to those observed from experimental samples (see above).

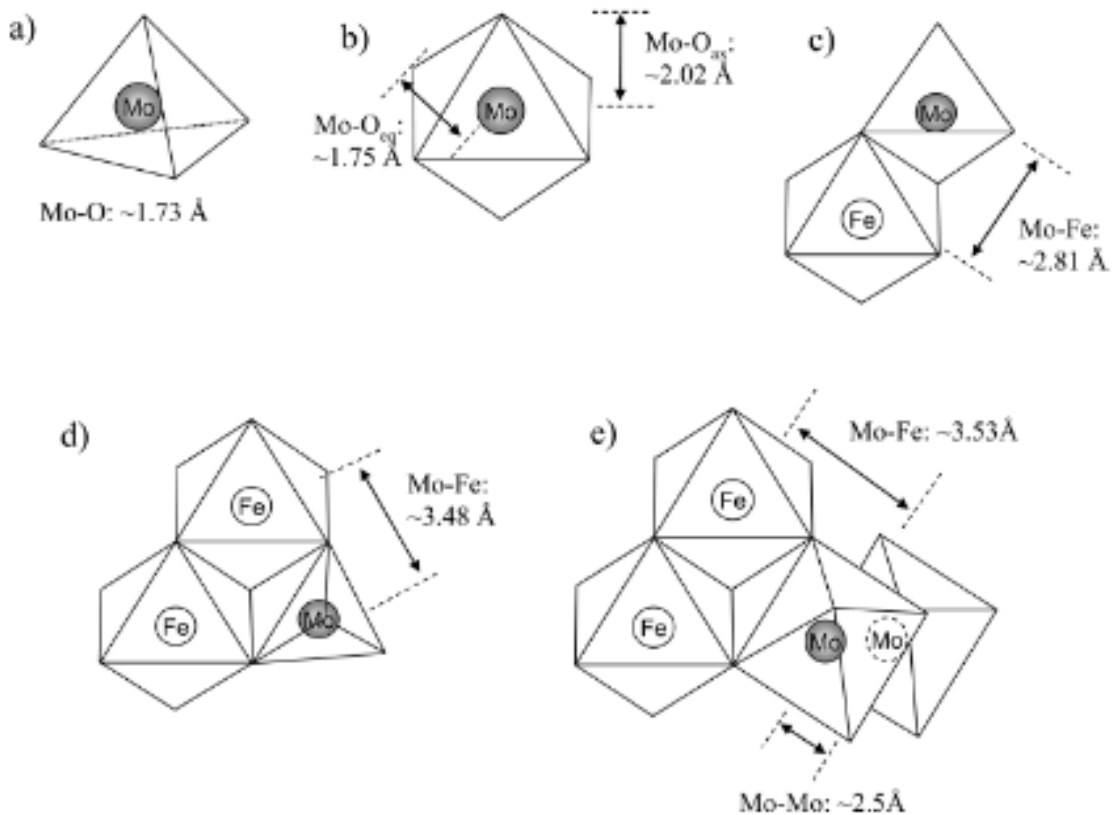


Figure 2-15 Mo(VI) tetrahedral and octahedral structure on goethite octahedral surface. a. Tetrahedral molecule of Mo(VI)O₄. b. Octahedral molecule of Mo(VI)O₆. c. Edge-sharing Mo(VI) inner-sphere complex via mononuclear Mo-O₂-Fe linkage (between MoO₄ and FeO₆). d. Corner-sharing MoO₄ inner-sphere complex via binuclear Mo-O₂-Fe₂ linkage. e. Corner-sharing (between MoO₆ and FeO₆) [(MoO₆)₂] inner-sphere complex via binuclear Mo-O₂-Fe₂ linkage from (Arai, 2010).

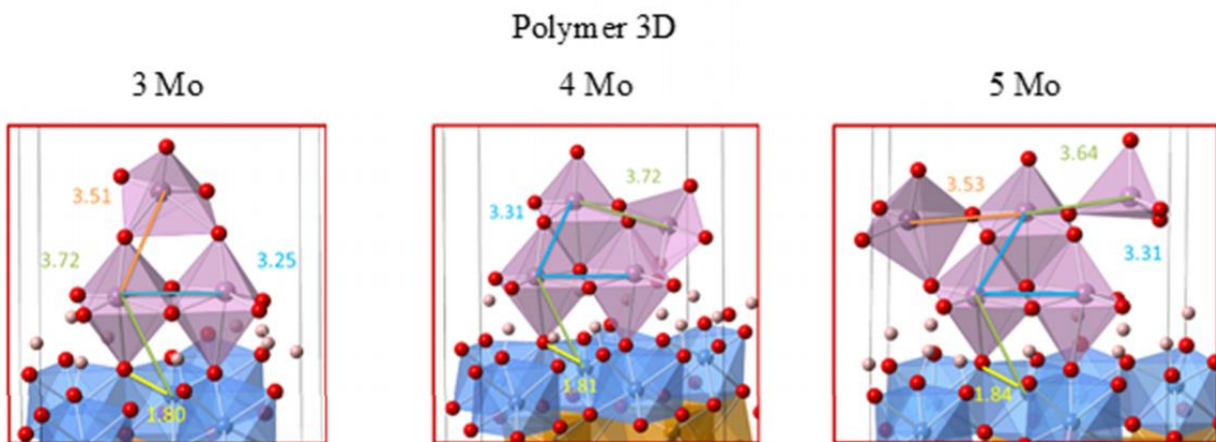


Figure 2-16 Simulated adsorbed Mo on hematite structures from (Davantes et al. 2017).

2.4.5 Mo Redox Processes

Mo is redox-sensitive element that forms insoluble minerals in certain reducing environments and the reduction of Mo(VI) in the environment can occur in a number of systems including reduced soils, stratified oceans, lakes and aged aquifers (Smedley and Kinniburgh, 2017). Mo is very sensitive to H₂S concentration and can become very insoluble and less mobile when Mo(IV)-S mineral are formed and in sulphide-rich waters Mo tends to form Mo-S precipitates (e.g. Molybdenite (Mo(IV)S₂)) (Smedley and Kinniburgh, 2017). Previous study of Mo reduction in sulfidic lake from Dahl et al. stated that the scavenging of Mo in euxinic (sulphide-rich) water starts from the reaction of Mo(VI)O₄²⁻ with aqueous H₂S and forms thiomolybdates (Mo(VI)O_{4-x}S_x²⁻), followed by the reduction of Mo(VI) to Mo(IV) to Mo-polysulfide species (Mo(IV)O(S₄)S²⁻ or Mo(IV)S(S₄)S²⁻) (Dahl et al., 2013). The zero-valent sulfur, presenting in the sulphide-rich water, contributes to the reduction process by breaking the sulfur double bonds in MoOS₃²⁻ and producing a polysulfide ring. This induces the ligand-promoted reduction and forms highly reactive Mo(IV)O(S₄)S²⁻ or Mo(IV)S(S₄)S²⁻ (Dahl et al., 2013, Vorlichek et al., 2004, Wang and Tessier, 2009, Zopfi et al., 2001).

2.4.6 Mo Reduction by Iron Oxides

It is no doubt that the adsorption onto Fe(III) oxides can control the contaminated metals under oxic systems, but the reduction by Fe(II)-bearing iron oxides allows extensive attenuation of contaminants through coupled adsorption and reduction (Vessey and Lindsay, 2020). However, the interaction between molybdate and the mixed valence mineral, magnetite is comparatively poorly studied (Xu et al., 2013, Verbinnen et al., 2012, Verbinnen et al., 2016, Brinza et al., 2008, Gustafsson, 2003, Xu et al., 2006a, Goldberg et al., 1996). Previous work on oxic, redox active metals, metalloids and actinides has shown magnetite to be a highly efficient absorbant and reductant e.g. uranium (U), chromium (Cr), technetium (Tc) (Das et al., 2010, Roberts et al., 2017, Marshall et al., 2015, Jiang et al., 2014, Rajput et al., 2016, Watts et al., 2015, Yalçıntaş et al., 2016). For the removal of Mo removal by the highly efficient absorbant and reductant, there is a study about systems containing zero-valent iron (ZVI) and hybridized zero-valent iron/magnetite/Fe(II) (hZVI) (mixed with ZVI and $\text{Fe(II)}_{\text{aq}}$) and investigated the removal efficiency of Mo(VI) from water and indicated that Mo(VI) was not removed efficiently by a ZVI-only system. However, a rapidly and sustainably removal of Mo(VI) was observed by in a hybridized zero-valent iron/ Fe_3O_4 /Fe(II) (hZVI) system due to the rapid reduction of Mo(VI) to lower valences, with magnetite identified playing a key role in providing an e^- -conducting medium, which contributed to Mo(VI) reduction and immobilization from the aqueous phase (Huang et al., 2012).

There are no known EXAFS studies of Mo(VI) adsorption to mixed iron valency minerals (e.g. magnetite) or the subsequent interactions of Mo(VI) with magnetite given the potential for reduction of Mo(VI) to Mo(IV) by the structural Fe(II) within the magnetite. Therefore, the key molecular scale processes controlling molybdate adsorption and/or reduction on magnetite, as a function of changing geochemical conditions, remains unresolved.

2.5 V Interaction with Iron Oxides

2.5.1 V Sorption to Iron Oxides

A few research about V interaction with iron oxides were studied and V tends to accumulate as V(V) by adsorption to iron oxides when it is added to soils (either V(IV) or V(V) salts) (Naeem et al., 2007, Wehrli and Stumm, 1989). However when the soil is rich in organic acid it predominantly occurs vanadyl(IV) polymerized to the organic matter (Larsson et al., 2017).

In many contaminated subsurface system the mobility and bioavailability of V is controlled by adsorption to environmentally abundant mineral phases (e.g. iron hydrous oxides) within soils and sediments and the adsorption mechanisms of V(V) as a function of geochemical condition e.g. pH, V(V) concentration, is key to predicting the environmental behaviour of this contaminant (Figure 2-17) (Naeem et al., 2007, Wehrli and Stumm, 1989, Wisawapipat and Kretzschmar, 2017, Gustafsson, 2019).

Previous studies on V(V) adsorption onto Fe(III) (hydro)oxide including hematite (Vessey et al., 2020), goethite (Peacock and Sherman, 2004, Zhu et al., 2020), ferrihydrite (Larsson et al., 2017, Brinza et al., 2008, Vessey et al., 2020, Vessey and Lindsay, 2020, Brinza et al., 2019), iron oxyhydroxide (Blackmore et al., 1996), and other Fe(III) (hydro)oxide adsorbents (Naeem et al., 2007) indicating decreasing adsorption with increasing pH. Figure 2-17 shows the adsorption of V(V) to goethite at 25 °C and initial V(V) concentration of 2.5 ppm and 25 ppm in 0.1 NaNO₃ solution after 144 h equilibration time and indicates the majority of V(V) is removed at pH up to 8 for initial low V(V) concentration of 2.5 ppm, while for 25 ppm V(V) the maximum adsorption shown occurs at pH 4 with decreasing as pH increases (Peacock and Sherman, 2004). At low pH (~3), V(V) adsorption occurs via the VO₂⁺ cation forming an inner-sphere surface complex despite the electrostatic repulsion from the positively charged iron

oxide surface, while at high pH (>8), the inner-sphere adsorption complexation of HVO_4^{2-} was proposed to be the key factor (Peacock and Sherman, 2004).

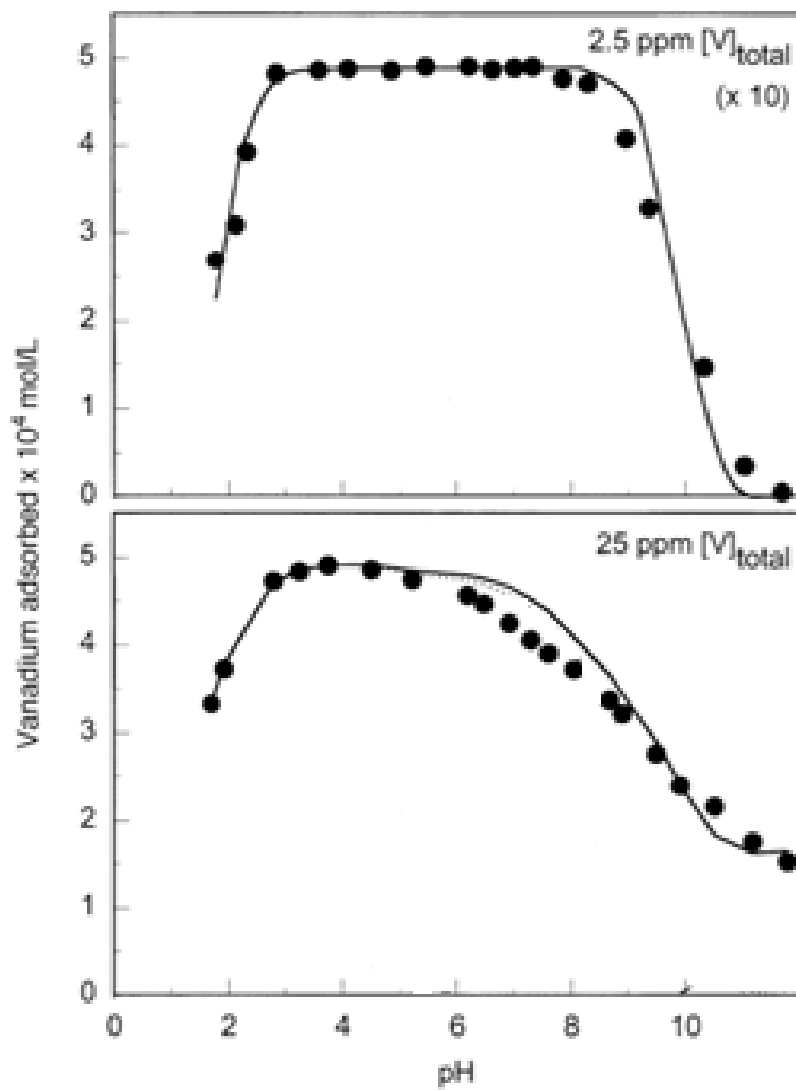


Figure 2-17 V(V) (2.5 ppm and 25 ppm) adsorption to goethite at 25 °C and I = 0.1 NaNO₃ after 144 h equilibration time from (Peacock and Sherman 2004).

2.5.2 Adsorption Models

There is limited investigation on V(V) adsorption to iron oxides applying the Langmuir isotherm model (Eq. 2-1). V(V) adsorption to goethite was investigated at 288 - 308 K using Langmuir model and indicated the maximum adsorption of 7.86 - 8.24 mg/g, with good R factor of 0.999. These data were compared to the data from Freundlich isotherm model, which

had lower R value of 0.952 – 0.968, suggesting the most likely monolayer adsorption process (Zhu et al., 2020).

Previous studies observed that V(V)-adsorbed polypyrrole coated magnetized natural zeolite (MZ-PPY) has high Langmuir adsorption capacity of 65.0 mg/g at 298 K, confirming the endothermic and spontaneous nature throughout the V(V) adsorption process. The maximum adsorption capacity (Q_m) varies due to varying iron oxide adsorbents, with 45.66 mg/g for FeOOH and 111.11 mg/g for Fe(OH)₃ and β -FeOOH, respectively. Since the environmental conditions are different throughout the adsorption process, the comparison of these adsorbents is impossible to obtain (Mthombeni et al., 2016).

Table 2-7 The maximum adsorption capacity (Q_m) of varying iron oxide adsorbents for V(V) removal (Mthombeni et al., 2016).

Adsorbent	Q_m (mg/g)
MZ-PPY	65.0
FeOOH	45.66
Fe(OH) ₃ and β -FeOOH	111.11

2.5.3 Attenuated Total Reflectance-Fourier Transform Infrared Spectroscopy (ATR-FTIR) Studies of V Adsorption

Attenuated total reflectance-Fourier transform infrared spectroscopy (ATR-FTIR) analysis is a surface sensitive technique to determine V speciation at the mineral solution interface. Vessey et al 2020 studied V(V)-adsorption onto ferrihydrite and hematite at pH 5-6 and V(V) concentrations less than 500 μ M (Vessey et al., 2020). At this lower surface loading (where tetrahedral H₂VO₄⁻ dominantly occurs in solution) there were distinct IR bands of 650-850 cm⁻¹, indicating inner-sphere monodentate and bidentate adsorption complexes on the mineral

surfaces (Figure 2-18). At V(V) concentration of 500-2000 μM and pH 3-6, the presence of both (poly)vanadate species and monomeric surface complexes were identified. Polyvanadate (e.g. tetrahedral $\text{H}_2\text{V}_2\text{O}_7^{2-}$ and $\text{V}_4\text{O}_{12}^{4-}$) species, with corresponding IR bands at 930-970 cm^{-1} , were the dominant aqueous species with increasing V(V) concentration and were observed to be present on the hematite surface in all systems (pH 3-6) (Vessey et al., 2020). However, polymers were identified on the ferrihydrite surface only at pH 3 and 4 due to the lack of ATR-FTIR bands at 970 cm^{-1} from the pH 5-6 samples. This indicated the hematite surface promoted polymer formation to a higher degree than ferrihydrite. This is likely to be due to the more crystalline nature of the hematite surface (Vessey et al., 2020, Davantes et al., 2017). At pH 3-4, octahedral decavanadate including $\text{H}_3\text{V}_{10}\text{O}_{28}^{5-}$, $\text{NaHV}_{10}\text{O}_{28}^{5-}$, and $\text{HV}_{10}\text{O}_{28}^{6-}$ are the dominant aqueous species with corresponding the ATR-FTIR peak at $\sim 980 \text{ cm}^{-1}$, therefore it was concluded that decavanadate forms on the hematite and ferrihydrite surface at this low pH (Vessey et al., 2020).

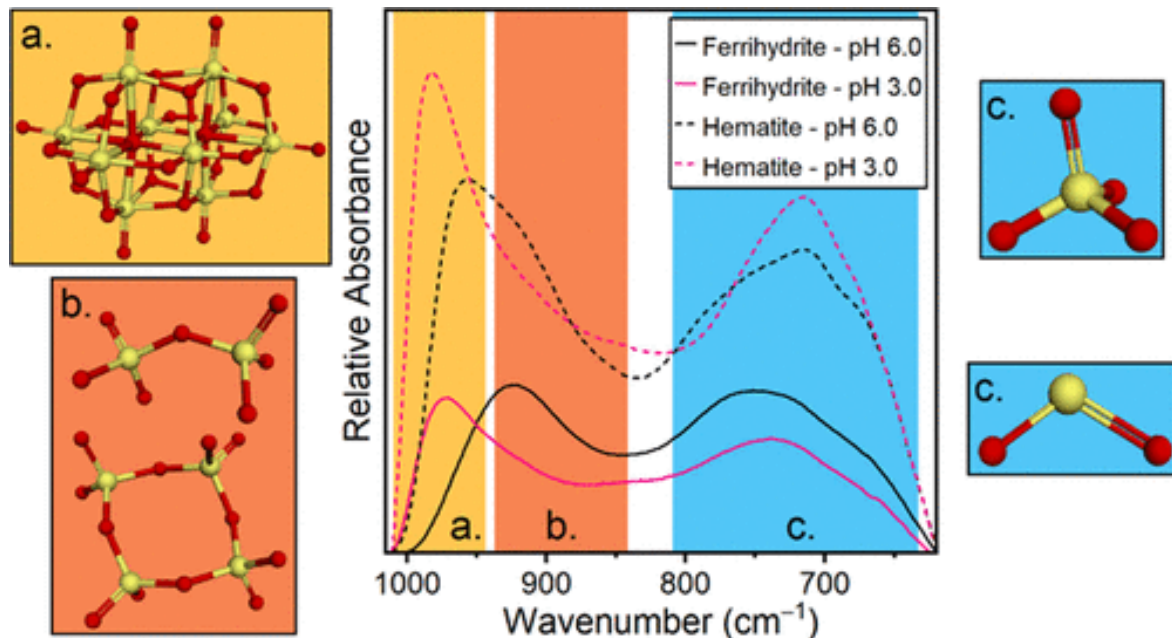


Figure 2-18 ATR-FTIR spectra on V(V)-adsorbed hematite and ferrihydrite and the corresponding V(V) species and symmetry from (Vessey et al. 2020).

2.5.4 X-ray Absorption Spectroscopy (XAS) Studies of V Adsorption

X-ray Absorption Spectroscopy (XAS) is a powerful technique to identify the V(V) oxidation states changes and bonding environment. The changes in oxidation states and symmetry of V can be obtained through V K-edge XANES (X-ray Absorption Near-edge Structure) spectroscopy. An investigation about the chemical species of V observed a strong pre-edge peak at 5470 eV for V_2O_4 and V_2O_5 and is present due to a $1s \rightarrow 3d$ transition. The pre-edge feature can act as an indicator of the V(V) coordination environment asymmetry, which can be distorted tetrahedral (T_d), octahedral (O_h) or square pyramidal (P_y) (Figure 2-19) (Wisawapipat and Kretzschmar, 2017). V(III) sited in V_2O_3 is octahedral coordinated (O_h) and when $V(III)_2O_3$ substituted in magnetite, a distorted octahedral symmetry was proposed as the broad pre-edge peak of XANES spectra is similar to $V(III)_2O_3$ (Figure 2-19) (Wisawapipat and Kretzschmar, 2017, Wong et al., 1984). The adsorption of V(V) onto ferrihydrite is via tetrahedral coordination, while the intensity and pre-edge peak of V(V)-adsorbed gibbsite ($Al(OH)_3$) are mostly close to V(V) $_2O_5$ (Figure 2-19), which contains a VO_5 square base pyramidal (P_y). The difference symmetry of V(V) in these two mineral may be suggest that monomeric VO_4 tetrahedrally adsorbed on ferrihydrite, and polymeric vanadates (VO_5) polymerized in the highly degree on gibbsite (Wisawapipat and Kretzschmar, 2017, Tanaka et al., 1988). Goethite and kaolinite are key host for V(IV), which presents as distorted octahedral geometry in the structure (Gehring et al., 1993, Wisawapipat and Kretzschmar, 2017, Mosser et al., 1996). Overall, XANES is an advanced tool for directly gaining information on the speciation, oxidation states, and geometry of trace elements and the detailed information about the bonding environment can be obtained by the Extended X-ray Absorption Fine Structure (EXAFS).

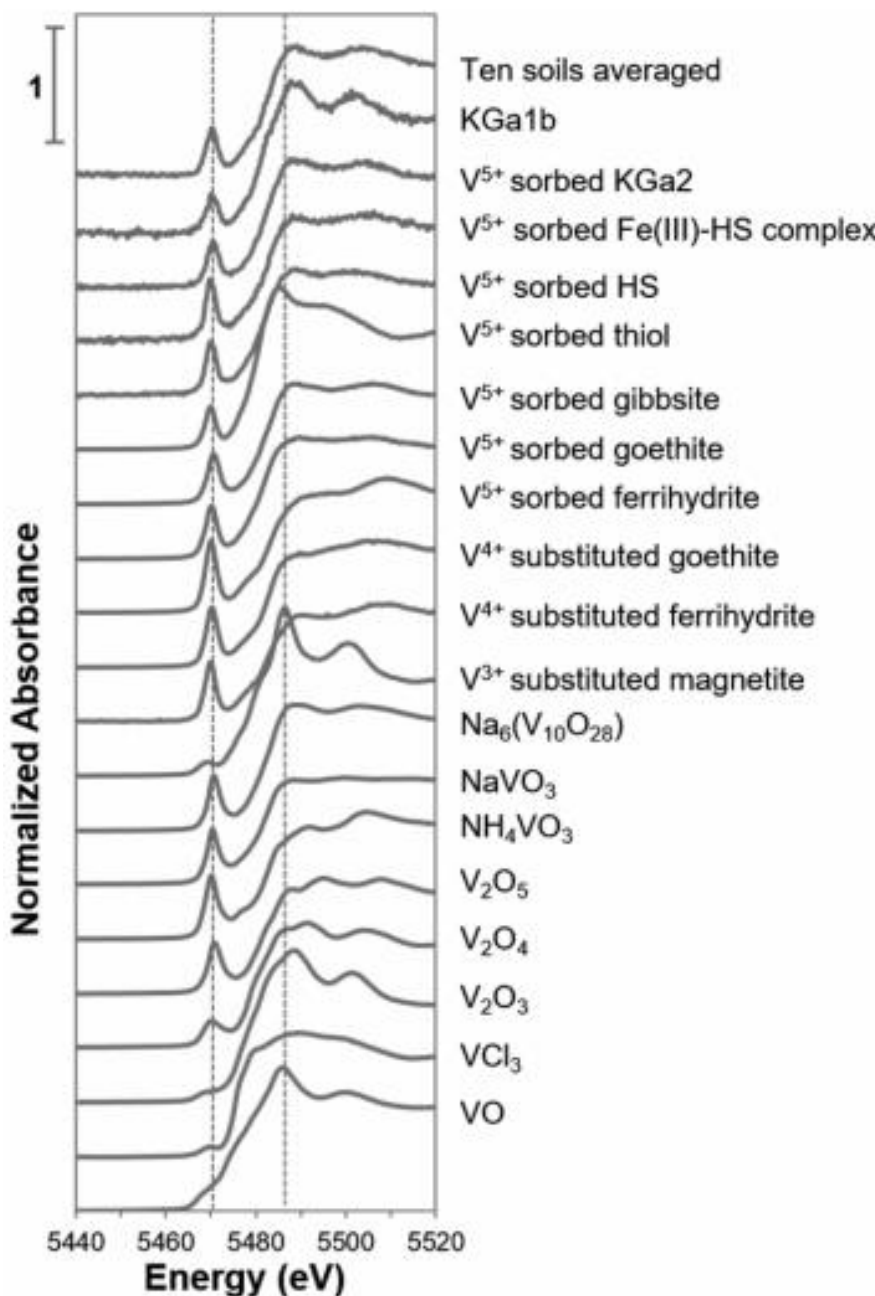


Figure 2-19 V K-edge XANES spectra of V reference compounds, V⁵⁺-adsorbed solids, V³⁺/V⁴⁺-substituted mineral, and highly weathered soil samples from (Wisawapipat and Kretzschmar 2017).

Extended X-ray Absorption Fine Structure (EXAFS) is able to determine chemical bonding mechanisms of elements and provide detailed understanding about interatomic distances, coordination number, and structure around a given atom. The EXAFS analysis of V(V)-

adsorbed to goethite and ferrihydrite at pH 3-9 indicated an inner-sphere tetrahedral coordinated surface complex with four O at ~1.5-1.8 Å (Peacock and Sherman, 2004, Larsson et al., 2017, Brinza et al., 2015, Brinza et al., 2019). This is consistent with protonated tetrahedral VO_4^{3-} as $\text{VO}_2(\text{OH})_2^-$ or $\text{VO}_3(\text{OH})^{2-}$ binding to the surface (Figure 2-20) (Peacock and Sherman, 2004). Distances of 3.2-3.3 Å for V-Fe shells including multi-scattering V-O paths provided evidence of a bidentate corner-sharing adsorption complex to the goethite surface at pH 3-9 (Peacock and Sherman, 2004). However, for V(V) adsorption to ferrihydrite, a distance of 2.8 Å was fitted on V-Fe shell, including multiple V-O-O and V-O-Fe paths, suggested an edge-sharing bidentate adsorption complex (almost V-O₂-Fe surface complex) (Larsson et al., 2017). This edge-sharing bidentate structure is different from that described for goethite, and is thought to form due to the larger proportion of singly coordinated groups on Fe(III) octahedral on ferrihydrite, relative to goethite (Larsson et al., 2017).

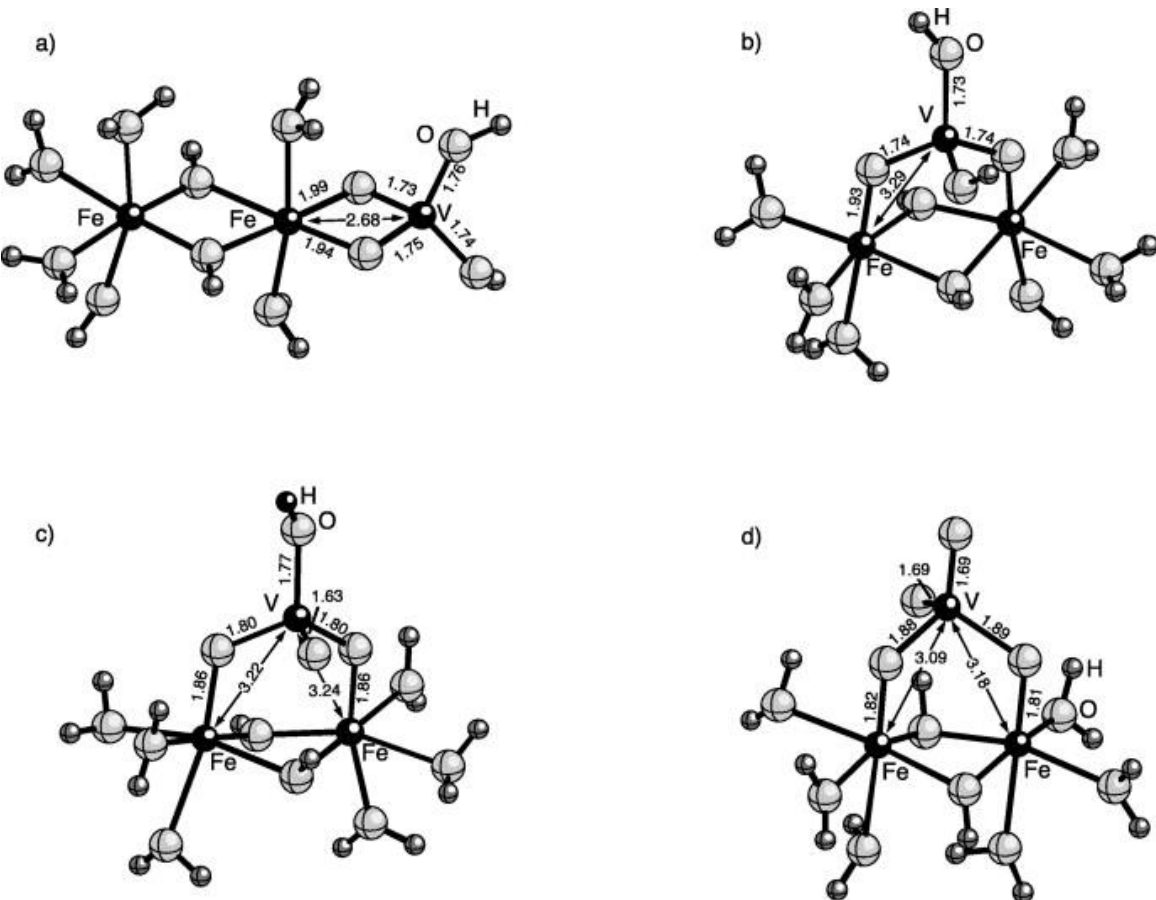


Figure 2-20 V(V) molecular geometry clusters. (a) $\text{VO}_2(\text{OH})_2$ bidentate edge-sharing, (b) $\text{VO}_2(\text{OH})_2$ bidentate corner-sharing, (c) $\text{VO}_3(\text{OH})$ on bidentate corner, (d) VO_4 on bidentate corner. The unit of bond lengths is Å. From (Peacock and Sherman 2004).

2.5.5 V Reduction by Iron Oxides

V(V) has been shown to reduce to V(IV) via the action of Fe(II). Previous studies indicated structural Fe(II) in magnetite and ilmenite(FeTiO_3) can heterogeneously reduce aqueous V(V) to V(IV) at pH 1-7 at 25 °C with the reduction rate decreasing with the pH (White and Peterson, 1996). The reduction of V(V) decreased significantly at pH 5-7 and almost no V(IV) was observed in solution at this pH range. The reduction rate of V(V) by the surfaces of magnetite is faster than that by ilmenite, and on both case V is reduced directly via heterogeneous electron exchange between aqueous V and structural Fe atoms on the oxide/fluid interface (White and Peterson, 1996).

V(V) uptake at circum-neutral pH in anoxic systems by Fe(II)-bearing particles including magnetite can involve adsorption, via corner-sharing bidentate surface complexes, followed by reduction (Vessey and Lindsay, 2020). V(V) was reduced to V(IV) on magnetite surface via surface associated Fe(II). Two V(V)-adsorbed magnetite samples with 3 h and 48 h reaction time were compared to study their bonding environment. For the sample with reaction time of 3 h, a tetrahedral V(V) complex with V-O bond of 1.701 Å and two V-Fe's fitted at 3.33 Å was derived indicating the presence of a tetrahedral corner-sharing bidentate surface complex. The reduction of V(V) to V(IV) was not observed on the magnetite surface at this reaction time (3h) suggested by the V-O shell $\text{V}^{\text{V}}\text{O}_4$ tetrahedron at the distance of 1.701 Å. In contrast, for the sample with a reaction time of 48 h, a V-O shell with a coordination number (CN) of ~3.1 were fitted at 1.673 Å, indicating a mixed V(IV) (as $\text{V}^{\text{IV}}\text{O}^{2+}$) and V(V) (as $\text{V}^{\text{V}}\text{O}_4$) species. ~ 2.1 oxygens were fitted further at 2.24 Å, consistent with $\text{V}^{\text{IV}}\text{O}^{2+}$ forming a bidentate adsorption complex, and V-Fe shells were fitted at 2.65 and 3.31 Å, suggesting a mixed edge- and corner-sharing surface complex (Figure 2-21). This indicated V(V) was reduced to V(IV) by electron transfer on magnetite surface (Vessey and Lindsay, 2020).

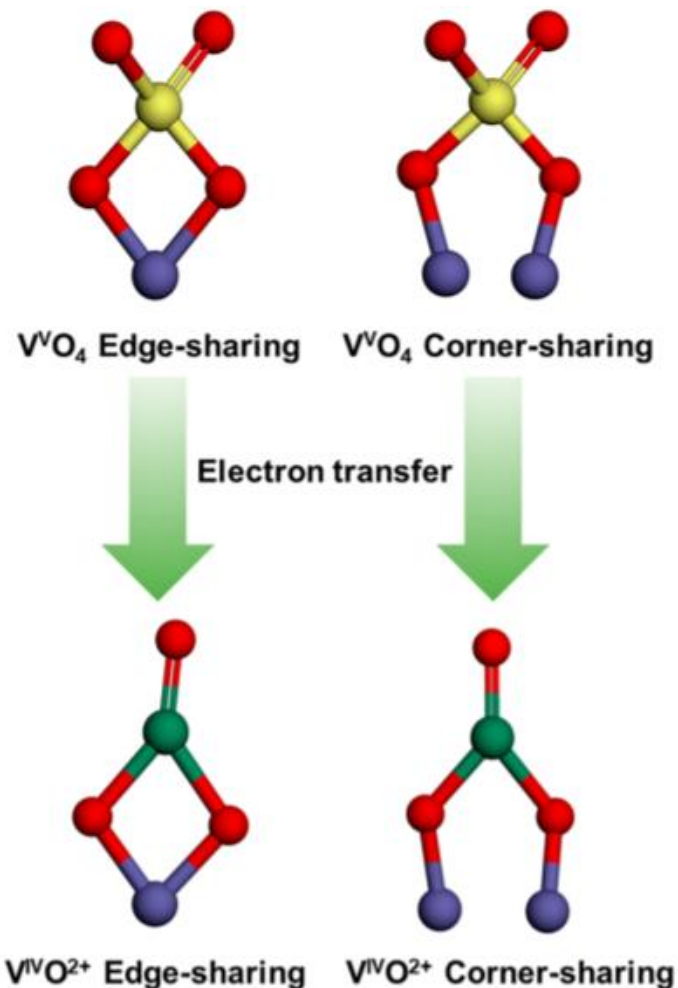


Figure 2-21 V molecular geometry clusters. Atoms' colours indicate V(V) (yellow), V(IV) (green), O (red), and Fe(II) (purple). From (Vessey and Lindsay 2020).

2.6 Summary

This introduction section has given comprehensive background covering molybdenum, vanadium, iron oxides, and the application of multiple advanced techniques (e.g. ATR-FTIR, XANES, EXAFS) on investigating the adsorption, reduction mechanisms, which provides a framework for the investigation performed in Chapter 4, 5 and 6 (see Table 3-1). The aim of this thesis is to holistically characterise the adsorption mechanisms of Mo and V to iron oxides and provide a comprehensive dataset to control the mobility

of these two contaminants in varying environmental conditions, which is a key gap throughout the literature.

3. Research Methods

3.1 Experimental Overview

This chapter describes the experimental methods and techniques, as well as their background and theory, used throughout this PhD project.

Table 3-1 Summary of experiments carried out during this PhD project.

Adsorption investigation	pH	Ionic Strength	Initial concentration	Oxygen conditions	Analytical Techniques	Chapter
Mo adsorption to hematite	3-13.5	0.1/0.01 M NaCl	0.01 x 10 ⁻⁴ - 2 x 10 ⁻³ M (0.1-200 ppm)	Aerobic	XAS, ATR-FTIR, PHREEQC, TEM, XPS, ICP-AES, ICP-MS, XRD, BET	4
V adsorption to hematite	3-13.5	0.1/0.01 M NaCl	2 x 10 ⁻⁶ - 4 x 10 ⁻³ M (0.1-200 ppm)	Aerobic	XAS, ATR-FTIR, PHREEQC, ICP-AES, ICP-MS, XRD, BET	5
Mo adsorption to magnetite and biogenic magnetite	3-13.5	0.1/0.01 M NaCl	0.01 x 10 ⁻⁴ - 2 x 10 ⁻³ M (0.1-200 ppm)	Anaerobic	XAS, ATR-FTIR, PHREEQC, ICP-AES, ICP-MS, XRD, BET, ferrozine assay	6
V adsorption to magnetite and biogenic magnetite	3-13.5	0.1/0.01 M NaCl	2 x 10 ⁻⁶ - 4 x 10 ⁻³ M (0.1-200 ppm)	Anaerobic	PHREEQC, ICP-AES, ICP-MS, XRD, BET	9

XAS: X-ray Absorption Spectroscopy; ATR-FTIR: Attenuated Total Reflection-Fourier Transform Infrared Spectroscopy; PHREEQC: PHREEQC Geochemical Modelling; TEM: Transmission Electron Microscopy; XPS: X-ray Photoelectron Spectroscopy; ICP-AES: Inductively Coupled Plasma Atomic Emission Spectroscopy; ICP-MS: Inductively Coupled Plasma Mass Spectrometry; XRD: X-ray Diffraction; BET: Brunauer-Emmett-Teller.

3.2 Iron(oxyhydr)oxide Synthesis

Three iron oxides were synthesised during this project. All iron oxides in this project including hematite, magnetite and biogenic magnetite (biomagnetite) were synthesised applying a standard literature protocol.

3.2.1 Synthesis of Hematite

Hematite ($\alpha\text{-Fe}_2\text{O}_3$) was synthesised using the method from Schwertmann and Cornell (2000) (Schwertmann and Cornell, 2000a). 2 L of 0.002 M HNO₃ was preheated to 98 °C in a Duran flask. Then 16.16 g Fe(NO₃)₃·9H₂O powder was added resulting in a 0.02 M Fe(III) solution. The solution was maintained at 98 °C for seven days in an oven. The suspension was then centrifuged (Sigma 6-16 KS) at a speed of 9000 rpm, washed (with Deionized Water (DI) water) 5 times and dried (in 40 °C oven overnight). This produced approximately 3g of bright red precipitate (Figure 3-1).



Figure 3-1 Synthesised hematite particles.

3.2.2 Synthesis of Magnetite

Magnetite was obtained using the method of Roberts et al. (2017) (Roberts et al., 2017). In brief, solutions of 0.2 M FeCl₃, 0.1M FeCl₂ and 0.3 M HCl (20 mL) were mixed for 24 hours in an anaerobic chamber at room temperature prior to introducing the Fe(II)/Fe(III) solution into a 28% NH₄OH solution (20 g) (pH 11). The solution was stirred continuously for 15

minutes to reach a final pH of 9 and then left for 24 hours to age. Finally, the magnetite was rinsed 2-3 times with 20 mL degassed DI water using a magnet to maintain the magnetite particles in the bottle before the final solid was suspended in 20 mL of degassed DI water (Figure 3-2). The degassed DI water was obtained by injecting nitrogen (N_2) gas for 30 minutes. The concentration of total Fe(II) in magnetite was measured using the Ferrozine assay (see section 3.4.2).

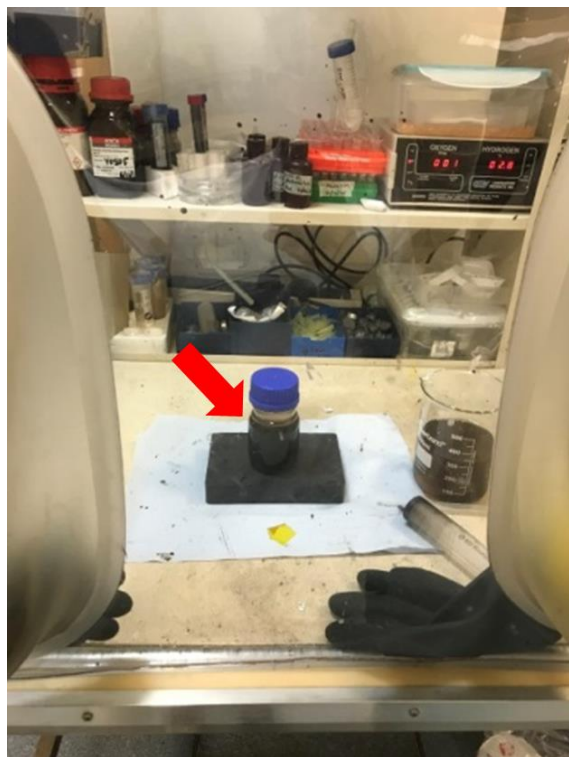


Figure 3-2 Synthesised magnetite.

A chemostat (Applikon Bioreactor) was also used to synthesise magnetite in large batches with a bespoke PEEK head plate on a glass beaker to give an oxygen-free atmosphere. This not only allows anaerobic conditions but also allows the control of temperature, pH, reagent addition and stirring speed, as used by previous studies (Weatherill et al., 2016, Winstanley et al., 2019).

Figure 3-3 shows the diagram of the chemostat setup for magnetite synthesis. The operation steps are the following. Pumped N_2 (8) for 10 minutes to keep the atmosphere in reaction vessel (4) under anaerobic conditions. Use syringe (5) to inject reagents (mixed 0.2 M $FeCl_3$, 0.1M

FeCl_2 and 0.3 M HCl (200 mL)) into the reaction vessel (4) and stir for 24 hours. The chemostat (1) was controlled by PC by operating the ‘my-Control’ software and stirring at 500 rpm. After 24 hours a 28% NH_4OH solution was injected (4) slowly into the vessel with simultaneous stirring at 500 rpm. After finishing 200 g of 28% NH_4OH solution, stirring was continued at 500 rpm for 15 minutes, and then left 24 hours to age. Finally, the synthesised material was removed through the head plate sample port (7) to syringe (5).

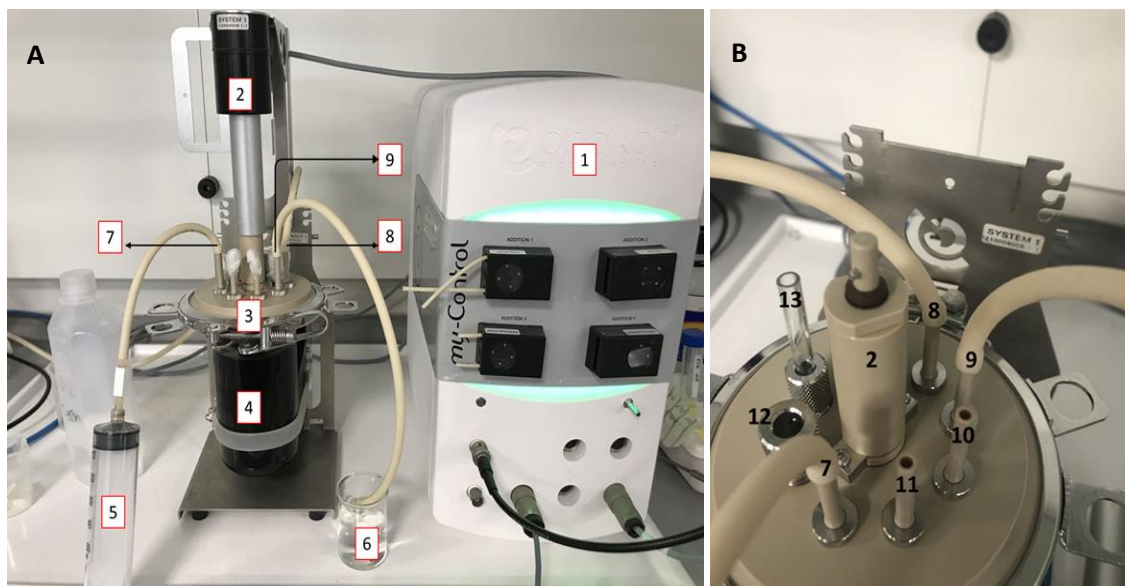


Figure 3-3 (A) Labelled set of Applikon Bioreactor for magnetite synthesis. (1) Automated Chemostat system (Applikon Bioreactor), (2) remote stirrer, (3) head plate and reaction vessels, (4) reaction vessel with reagents (0.2 M FeCl_3 and 0.3 M HCl), (5) sampling port with syringe to inject NH_4OH solution, (6) a glass of water to check if N_2 ’s out. (B) Chemostat head plate zoom in. A and B (7) sample port, A and B (8) N_2 in, A and B (9) N_2 out. (B10)-(B13) were sealed to keep anaerobic condition.

3.2.3 Synthesis of Biogenic magnetite

Biogenic magnetite was produced using the method of (Coker et al., 2008) by the reduction of Fe(III)-oxyhydroxide coupled to the oxidation of sodium acetate in the presence of AQDS using *G. sulfurreducens*, under an atmosphere of $\text{N}_2\text{-CO}_2$ (80:20). Bottles were incubated in

the dark at 30 °C for 2 days before producing a black magnetic precipitate. The precipitate was then washed three times using degassed DI water to remove bacterial cells. The purity of the magnetite particles was checked by the powder X-ray Diffraction (pXRD) (Bruker D8 Advance).

3.2.3.1 Cell Cultures

A culture of *G. sulfurreducens*, obtained from the laboratory culture collection of the geomicrobiology group (University of Manchester), was grown in the anaerobic modified freshwater enrichment medium (nutrient broth acetate fumarate (NBAF)) (Table 3-2) (Lovley and Phillips, 1988, Mulroy, 2020). This basal medium was sterilised by autoclaving at 126 °C in total darkness. The sterilised NBAF, prior to inoculation, was made anaerobic through sparging with 80:20 (vol:vol) N₂-CO₂ gas mix atmosphere for ~ 1 hour.

Cells were harvested at late-log stationary phase by centrifuging for 20 minutes at 4 °C and 12500 g (5000 rpm), with two subsequent washes using 30 mM sodium bicarbonate. An 80:20 N₂-CO₂ gas mix atmosphere was sparged when the cell suspension was transferred between centrifuge tubes and serum bottles, which were used to grow bacteria. Then the optical density (OD₆₀₀) of an aliquot of suspended cells in anaerobic 30 mM sodium bicarbonate buffer (pH 7), relative to a blank of 30 mM sodium bicarbonate buffer, was measured at 600 nm using Jenway 6715 series UV-vis spectrophotometer.

Table 3-2 Composition of the modified freshwater enrichment medium (nutrient broth acetate fumarate (NBAF)) (Lovley and Phillips, 1988, Mulroy, 2020).

Reagent	Concentration (mM)
MgSO ₄ •7H ₂ O	0.406
Na ₂ SeO ₄	1.0
NaHCO ₃	21.4
CaCl ₂ •6H ₂ O	0.272
CH ₃ COONa	15
Na ₂ CO ₃ •H ₂ O	4.03
Fumaric acid	40
Vitamins and minerals	Trace

3.3 Adsorption Experiments

3.3.1 Solution Experiment for Mo(VI) Adsorption to Hematite

Experiments to characterise the adsorption of molybdenum to hematite were performed by contacting a 0.6×10^{-4} M (6 ppm) and 5×10^{-4} M (50 ppm) Mo(VI) ($\text{Na}_2\text{MoO}_4 \cdot 2\text{H}_2\text{O}$) solution to hematite (2 g/L) in either a 0.1 M or 0.01 M sodium chloride (NaCl) solution within a total volume of 30 ml. The pH was varied between 3 and 13 through adjustment using 0.1 M HCl or 0.1 - 1 M NaOH. In addition, adsorption isotherm experiments were performed at pH 7 in 0.1 M or 0.01 M NaCl solution with an initial Mo(VI) concentration of 0.01×10^{-4} - 2×10^{-3} M (0.1 - 200 ppm). All experiments were maintained on a rotor mixer at a constant speed of 32 rpm for 24 hours and aliquots of solution were filtered (by 0.22 µm syringe filters (Merck Millipore) and acidified (adding 300 µl 70% HNO₃ into 10 ml samples) for analysis by Inductively Coupled Plasma Atomic Emission Spectroscopy (ICP-AES) and Inductively

coupled plasma mass spectrometry (ICP-MS) (PerkinElmer Optima 5300 dual view) to establish Mo concentrations in solution (see section 3.4.3).



Figure 3-4 An example of Mo(VI) adsorption to hematite experiments.

3.3.2 Solution Experiment for V(V) Adsorption to Hematite

The adsorption of vanadium to hematite experiments were carried out by mixing 1.2×10^{-4} M (6 ppm) and 1.2×10^{-3} M (60 ppm) V(V) (Na_3VO_4) with 2 g/L hematite in 30 ml 0.1M or 0.01 M sodium chloride (NaCl) solution. This gave maximum V(V) concentration of 3000 ppm and 30000 ppm on the hematite particle surface, respectively. The pH range was adjusted from 3 to 13 using 0.1 M hydrochloric acid (HCl) and 0.1 - 1 M sodium hydroxide (NaOH). In addition, the isotherm adsorption experiments were performed at an initial V(V) concentration of 2×10^{-6} - 4×10^{-3} M (0.1 - 200 ppm) at pH 7 in 0.1 M and 0.01 M NaCl solution. All experiments were rotated on a rotor mixer with a constant speed of 32 rpm for 24 hours. Then supernatant liquid was filtered by 0.22 μm syringe filters (Merck Millipore) and acidified by adding 300 μl 70% HNO_3 into 10 ml samples before sending to Inductively Coupled Plasma Atomic Emission Spectroscopy (ICP-AES) (PerkinElmer Optima 5300 dual view) to analyse V concentrations.

3.3.3 Solution Experiment for Mo(VI) and V(V) Adsorption to Magnetite and Biogenic Magnetite

Since magnetite and biogenic magnetite are easily oxidized, all experimental procedures were performed in an anaerobic chamber (using a mixed of nitrogen (95 %) and hydrogen (5 %) to provide an oxygen-free condition). Magnetite/biogenic magnetite (60 mg) was added into a 0.1M NaCl or 0.01M NaCl sodium chloride solution giving 2 g/L solid. Similar to the adsorption to hematite experiments, the initial concentrations of Mo(VI)/V(V) in solution were 0.6×10^{-4} M (6 ppm). Adsorption experiments were performed at pH from 3 to 13.5, adjusted using 0.1 M HCl or 0.1-1 M NaOH.

Mo(VI)/V(V) isotherm adsorption to magnetite were performed in a similar manner to the hematite experiments. The concentrations range of Mo(VI)/V(V) were from 0.01×10^{-4} M (0.1 ppm) to 2×10^{-3} M (200 ppm). pH was adjusted to 7 using 0.1 M HCl or 0.1-1 M NaOH. 0.1 M NaCl and 0.01M NaCl were applied to yield solutions with different ionic strengths.

3.4 Aqueous Geochemistry

3.4.1 Geochemical/Isotherm Adsorption Model

Thermodynamic modelling was applied using PHREEQC (version 3.3.5) to characterise the saturation state with respect to Mo/V solid phases and Mo/V poly- vs. mono- speciation of the experimental solutions using the minteq.v4.dat database (Vessey et al., 2020, Winstanley et al., 2019). The calculations were applied to assess the speciation of Mo or V across the full concentration and pH range used in the experimental studies.

A Langmuir isotherm was also modelled in OriginLab software to model the adsorption process of each of the elements on the adsorbents. The Langmuir model equation is as follows:

$$Q_e = Q_{max} \times b \times C_e / (1 + b \times C_e) \quad (3-1)$$

where Q_e (mg Mo/g adsorbent) is the adsorbed amount at equilibrium. Q_{max} (mg/g) is the maximum adsorption capacity. b (l/mg) is a constant. C_e is the residual adsorbent concentration in solution at equilibrium (Verbinnen et al., 2012).

3.4.2 Ferrozine Assay

Ferrozine assay is a simple and quick method for obtaining Fe(II) concentration in solution. It requires two reagents, including ferrozine (monosodium salt hydrate of 3-(2-pyridyl)-5,6-diphenyl-1,2,4-triazine-p,p'-disulfonic acid) and a reducing agent (hydroxylamine hydrochloride). Once these reagents are added and react with a Fe(II) containing sample, a magenta coloured product forms. Then it can be measured by a spectrophotometer to determine Fe(II) concentration using monochromatic light at 562 nm (Stookey, 1970, Viollier et al., 2000).

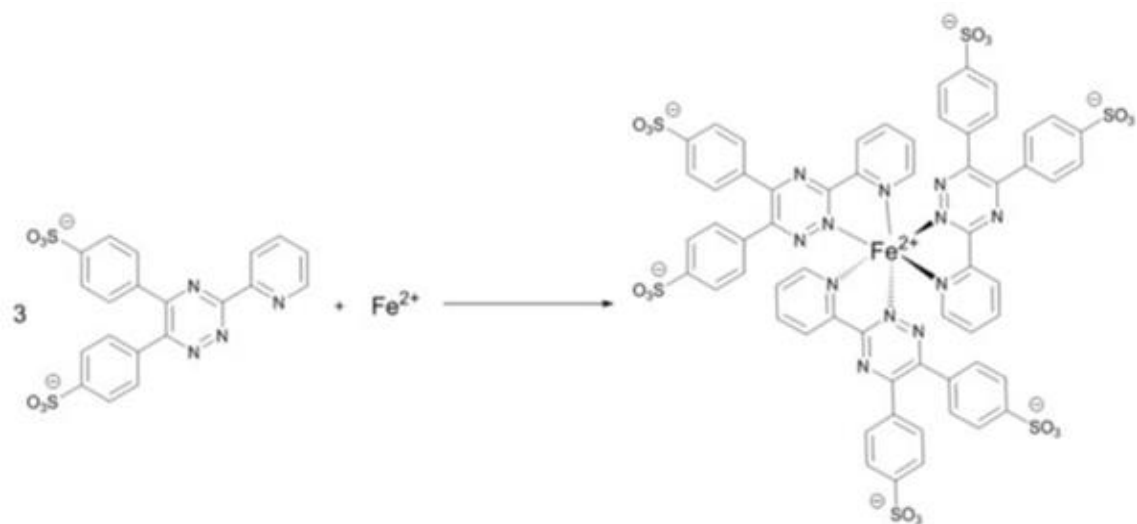


Figure 3-5 The formation of Fe(II)-ferrozine complex from (Stookey 1970, Viollier et al. 2000).

The following protocol was used following the method of Stookey (1970) and Viollier et al. (2000). Standards are obtained by dissolving $\text{FeSO}_4 \cdot 7\text{H}_2\text{O}$ to produce a 50 mM standard and diluted to the concentrations of 20 mM, 10 mM, 5 mM and 1 mM. 0.1 ml of the magnetite slurry and standards was added into 0.24 ml 37% HCl and left overnight to digest. After 24

hours, 0.1 ml 6.25 M hydroxylamine hydrochloride and 4.56 ml DI water were added into the digestion solution and left for 1 hour to fully react. The solution was then diluted by 1:50 in 0.5M HCl. 50 ul aliquots of each sample/standard were mixed with 2.45 ml of ferrozine solution and shaken and the absorbance was measured immediately by the Jenway 6715 UV / Vis. Spectrophotometer at 562 nm in quintuplicate.

3.4.3 Inductively Coupled Plasma Atomic Emission Spectroscopy (ICP-AES) and Inductively Coupled Plasma Mass Spectrometry (ICP-MS)

Inductively Coupled Plasma Atomic Emission Spectroscopy (ICP-AES) and Inductively Coupled Plasma Mass Spectrometry (ICP-MS) are methods for the detection of the concentrations of ions in solutions from low ppb to high ppm levels. For ICP-AES analysis, atoms and ions are excited by inductively coupled plasma and emit electromagnetic radiation at a particular element wavelength. The intensity of emission can indicate the concentration of elements within samples (Olesik, 1991). ICP-MS is applied to measure an atoms' mass by mass spectrometry. The lower detection limit for ICP-AES is typically at the parts per billion (ppb) level, while the lower limit for ICP-MS can extend to parts per trillion (ppt) level (Ammann, 2007).

Aliquots of solution were filtered by 0.22 μ m syringe filters (Merck Millipore) and acidified by adding 300 ml of 70% HNO_3 before being analysed by Inductively coupled plasma mass spectrometry (ICP-MS) (PerkinElmer Optima 5300 dual view) or Inductively Coupled Plasma Atomic Emission Spectroscopy (ICP-AES) (Optima 5300) to establish Mo/V concentrations in solution.

3.5 Solid Analysis

3.5.1 X-ray Diffraction (XRD)

The synthesized hematite and magnetite was analysed using powder X-ray Diffraction (pXRD) (Bruker D8 Advance with X-rays Cu k-alpha with a wavelength of 1.5406 Å), which is a crystallographic technique to identify the crystal structure of solid samples. X-rays are diffracted in a variety of directions by crystallographic planes within a mineral after hitting a crystalline sample to create a diffraction pattern specific to that crystal structure (Epp, 2016).

The Bragg equation (Figure 3-6, Equation 3-2) is applied to describe when a peak is generated by constructive interference in an XRD pattern (Cullity and Stock, 2001).

$$n\lambda = 2d \sin\theta \quad (3-2)$$

where n is an integer, λ is the incident x-ray wavelength, θ is the angle between incident x-ray and crystal surface, and d is lattice spacing.

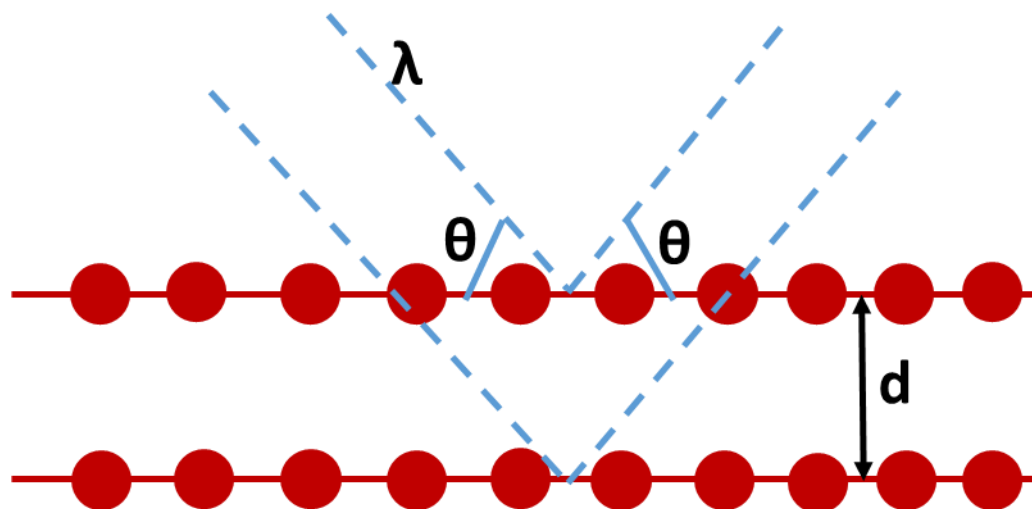


Figure 3-6 An illustration of basic Bragg's law, adapted from (Waseda et al., 2011).

The sample was ground using a pestle and mortar to form a homogenous powder and ~1 ml of amyl acetate was then added to ~0.1 g of sample. The resultant slurry was transferred to a

microscope slide and air dried next to the extractor in the bench-top before XRD analysis on the Bruker D8 Advance Diffractometer with a LynxEye detector, applying Cu K α radiation. Background was subtracted in DIFFRAC.EVA and the XRD patterns were compared to standards from the database of International Centre for Diffraction Data (ICDD) Powder Diffraction File (PDF).

3.5.2 Brunauer-Emmett-Teller (BET) Surface Area Analysis

The surface area of iron oxides plays an important part in their reactivity, thermodynamic stability, sorbent interaction, dehydroxylation and dissolution processes (Cornell and Schwertmann, 2003). BET is the common technique to measure the surface area of iron oxides and other solid phases (Brunauer et al., 1938). This method is based on the adsorption of N₂ gas onto a sample surface, which is modelled using BET-theory which is a multilayer adsorption model from an extension of monolayer Langmuir theory. The BET equation describes a relationship between the amount of adsorbed gas and relative vapour pressure. The equation is as follows (Brunauer et al., 1938):

$$\frac{1}{v\left(\frac{p_0}{p}-1\right)} = \frac{1}{v_m c} + \frac{c-1}{v_m c} \cdot \frac{p}{p_0} \quad (3-3)$$

where v_m is the amount of monolayer gas adsorbed, c is BET constant relating to adsorption energy. The adsorption isotherm can be obtained by plotting 1/(v(p₀/p)-1) and p/p₀ and its intercept and slope can be applied to calculate v_m and c. The surface area of a sample can be calculated by understanding v_m and surface area taken up by one gas molecular.

Samples are required to be outgassed firstly in order to remove adsorbed water which can impact the surface measurement. Samples were outgassed using He for 19 hours at room temperature and measured using a Micromeritics Gemini with N₂ as adsorbed gas (Clausen and

Fabricius, 2000). The surface area of the synthesised hematite and magnetite were 47.2 ± 0.3 m^2/g and 103.5 ± 0.3 m^2/g respectively.

3.5.3 Transmission Electron Microscopy (TEM)

Transmission Electron Microscopy (TEM) is a powerful technique that can characterise the element composition, structure, morphology and various other characteristics of samples at the micro and nano scale (Williams and Carter, 1996, Inkson, 2016). The TEM image is produced by the interaction of electrons and the sample through transmitting a beam of electrons through the sample. The short wavelength of electrons that the electron microscopes applied provides a higher resolution (0.2-0.1 nm) than that of light microscopes (200 nm) (Williams and Carter, 1996, Inkson, 2016).

TEM is applied to image samples by preparing thin particle layers on a nanometre scale (~ 1 - 100 nm) which are imaged using an electron beam with an accelerating voltages of 100-300 kV (Williams and Carter, 1996, Egerton, 2005). A small amount of samples is required for TEM analysis. In a TEM a beam of electrons, which was produced by an electron gun, is focused by electromagnetic fields acting as lens. Then the beam illuminates samples through the diffraction of the incident electron beam by crystal planes of solid samples, producing dark and light areas (Williams and Carter, 1996, Egerton, 2005).

Energy Dispersive Spectroscopy (EDS) relies on the interaction of the electron beam with samples, providing localised elemental analysis. When an inner shell electron is excited by the electron beam, this leaves a vacancy that can be filled by the higher shell electron which drops down to the lower level. Meanwhile this electron releases X-rays of the energy characteristic to the excited elements (Ngo, 1999). Then a qualitative spectrum is produced, each of these emission lines is element-specific and can therefore be identified (Ngo, 1999).

Mo-adsorbed hematite sample slurry (0.6×10^{-4} M Mo(VI) in 0.01 M NaCl at pH 7; ~0.2 ml) was deposited on a carbon-coated copper TEM grid (Agar Scientific) and washed with 70% ethanol 3-5 times. Sample morphology was imaged and composition determined by energy dispersive X-ray (EDX) analysis using a FEI Talos F200A.



Figure 3-7 FEI Talos F200A for TEM analysis.

3.5.4 Attenuated Total Reflection-Fourier Transform Infrared Spectroscopy (ATR-FTIR)

Attenuated total reflectance-Fourier transform infrared (ATR-FTIR) spectroscopy is a technique that is able to *in situ* characterise the solid-liquid interface to determine the adsorption of ions on nanoparticle surfaces in the environmentally relevant media due to its low penetration depth (Mudunkotuwa et al., 2014). The mid-IR region of light, 400-4000 cm⁻¹, is used and when the infrared (IR) radiation passes through samples, molecules will absorb the radiation of specific wavelengths selectively, creating a spectrum as a unique ‘fingerprint’

to determine sample species (Griffiths, 2006). In order to be IR active a molecule must have dipole moment, in which the adsorption of IR light causes a change, resulting in the transition of vibrational energy to an excited state (Griffiths, 2006). The frequency and number of absorption peaks in IR spectrum is associated with vibrational energy gap and vibrational freedom of the molecular species (Griffiths, 2006). If molecules have X atoms, they would have 3X degrees of freedom. Six of them represent transitional and rotational motion about x, y, z axes and the rest of 3X-6 degrees of freedom is the number of vibrational modes (Griffiths, 2006). Vibrational movements can be identified as either deformation vibrations or stretching (changing bond angle or bond length respectively) (Hof, 2003).

Attenuated total reflectance (ATR) is a widely used technique due to its low level requirements for sample preparation and consistent results (Griffiths, 2006). Samples are placed onto the ATR crystal with high refractive index. The IR light passes through crystal and reflects off multiple internal surfaces, which are in contact with the sample. An evanescent wave is formed by these reflections and extends into samples shallowly, with penetration depth (d_p) determined by the wavelength (λ), the light angle (θ), and the ATR crystal refractive indices (n , where n_1 indicates an optically dense medium and n_2 is an optically rare medium) (see Eq. 3-4) (Mudunkotuwa et al., 2014). Samples absorb energy in the IR region and then this evanescent wave is attenuated before returning to crystal. When the beam exits the crystal, it will be recorded by a detector (Mudunkotuwa et al., 2014).

$$d_p = \frac{\lambda}{2\pi n_1 \sqrt{\left[\sin^2 \theta - \left(n_2/n_1 \right)^2 \right]}} \quad (3-4)$$

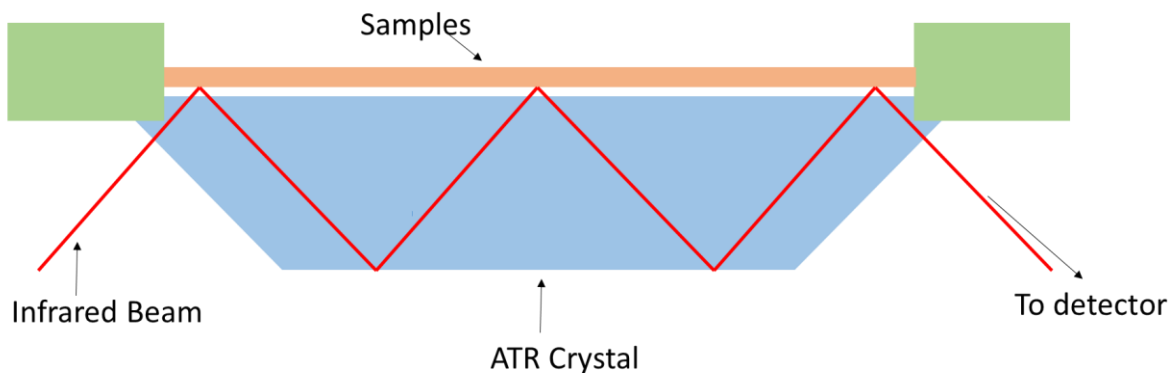


Figure 3-8 Schematic of ATR-FTIR technique presenting the infrared beam reflecting through the ATR crystal and then exiting before being recorded by the detector. Adapted from (Mudunkotuwa et al., 2014).

Attenuated Total Reflection-Fourier Transform Infrared Spectroscopy (ATR-FTIR) is applied to determine the poly- or mono- Mo(VI)/V(V) speciation via spectra changes. The Mo(VI)-adsorbed hematite particles at pH 3-13.5 at initial Mo(VI) concentration of $0.6 \times 10^{-4} - 2 \times 10^{-3}$ M (6 - 200 ppm) were isolated by centrifugation before the wet paste was analysed by ATR-FTIR (Bruker Alpha-P FTIR spectrometer) with a diamond crystal (spectral resolution 2 cm^{-1} , 400 scans per sample). The results were background subtracted using OPUS software and fitted in Origin.

V(V)-adsorbed hematite particles at pH 3-13.5 at initial V(V) concentration of 1.2×10^{-3} M (60 ppm) were also analysed by ATR-FTIR (Perkin Elmer Frontier ATR-FTIR spectrometer) with spectral resolution of 4 cm^{-1} and average spectra of 20 scans. The results were background subtracted and analysed using Know-it-all software and then fitted using Origin.

3.5.5 X-ray Photoelectron Spectroscopy (XPS)

X-ray photoelectron spectroscopy (XPS) is a powerful technique that provides information on the presence, abundance and bonding environment of surface atoms irradiating with either Mg K α (1253.6 eV) or Al K α (1486.6 eV) soft X-rays with low penetrating power (1-10 μm) in a

solid. This means XPS is a surface sensitive technique and can only give details on the surface atoms (Moulder et al., 1992). This powerful technique identifies and determines surface concentration and binding oxidation states of elements by its unique binding energies, of which variation determines information on chemical potential and polarisability (Moulder et al., 1992). The photons interact with atoms on the solid surface, causing electrons to be emitted by the photoelectric effect. The emitted electrons have a measurable kinetic energy (KE), which includes the incident photon energy, $h\nu$, the electron binding energy (BE) from the given atomic orbital and the spectrometer work function, φ_s (Equation 3-5) (Moulder et al., 1992).

$$KE = h\nu - BE - \varphi_s \quad (3-5)$$

XPS was performed for samples of Mo(VI)-adsorbed hematite (0.6×10^{-4} M Mo(VI) in 0.1 M NaCl solution) at pH 3, 4, 5.5, 7, 8. Samples were prepared by drop-casting sample slurry onto a silicon chip (1x1 cm) followed by washing with isopropyl alcohol prior to loading into the XPS system (SPECS NAP-XPS with a SPECS Focus 500 Monochromator and a SPECS Phoibos 150 NAP hemispherical analyser) and exposing to monochromatic Al K α X-rays. An electron flood gun was used (20 μ A at 2 eV) in addition to long acquisition times for the Mo 3d spectra (overnight scanning employed). Mo 3d spectra were charge corrected on the binding energy scale (relative to the C 1s signal at 284.8 eV, which is the standard reference for XPS).

3.6 Synchrotron Techniques

Synchrotron radiation techniques were a key part of this investigation during this research project. The Mo/V adsorbed minerals were investigated at Diamond Light Source (UK).

3.6.1 Synchrotron Radiation

Synchrotron radiation is electromagnetic radiation produced from an electron, which is firstly produced by an electron gun and accelerated by a linear accelerator (linac) producing energy up to \sim 100 MeV by alternating electric fields (Willmott, 2019). Then the produced electrons

are accelerated further in a curve path (booster ring) before being injected into storage ring periodically. They are then focused around the ring by a combination of a radio frequency supply and strong magnetic fields (Willmott, 2019). Then synchrotron radiation is produced because electrons need to maintain angular momentum. Electron energy is lost during the radiation production process and is replenished by a radio frequency in order to maintain synchrotron radiation production. A wide range of techniques from high resolution X-ray diffraction to X-ray absorption are applied at synchrotron facilities using beamlines arranged tangentially around the storage ring (Willmott, 2019).

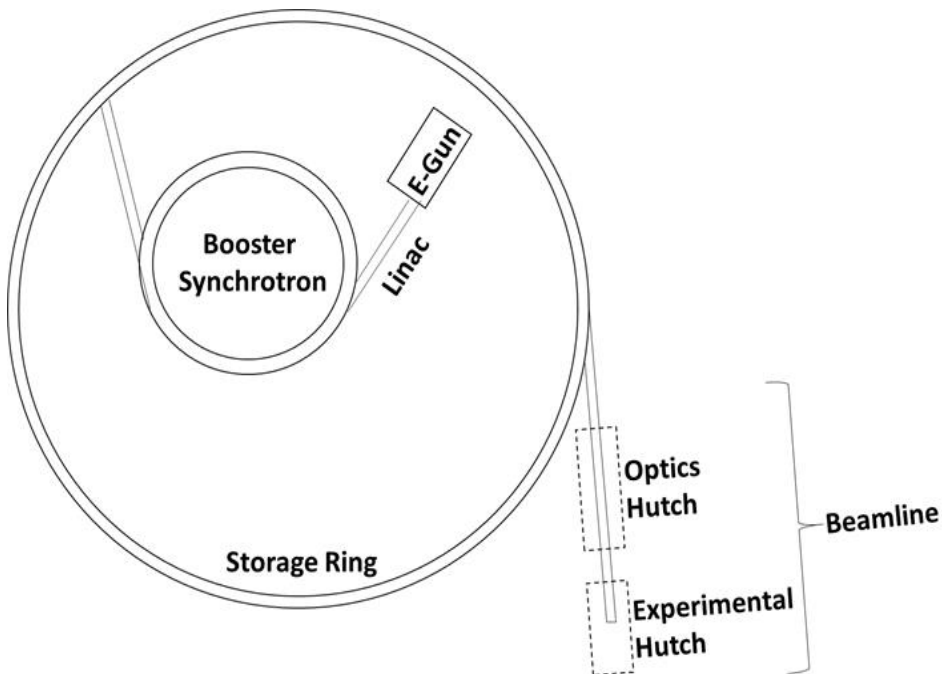


Figure 3-9 A simplified diagram of a modern synchrotron, adapted from Willmott (Willmott 2019).

3.6.2 X-ray Absorption Spectroscopy (XAS)

X-ray Absorption Spectroscopy (XAS) is a widely used analytical technique, which is extensively utilized for characterizing samples in liquid or solid, amorphous or crystalline, nanoscale or bulk form. XAS allows the probing of oxidation states and surrounding atomic conditions of a particular atom by electronic excitation with high energy X-rays (Schnohr and

Ridgway, 2015). A sample is scanned by an intense monochromatic X-ray beam of light and the absorbance of the sample is measured at each step (Schnohr and Ridgway, 2015).

In the X-ray absorption spectroscopy samples are exposed to the X-rays of specific energy and these X-rays can be absorbed by specific atoms in samples, leading to excitation and ejection of core-level electrons. These core electrons exist in every element with well-defined binding energies and XAS can select appropriate X-ray energy for desired elements, making it an element specific technique. These electrons adsorption can be quantified by three ways: 1. comparing the intensity of transmitted beam to that of incident beam, 2. measuring fluorescence emitted as higher-level electrons fill the vacant core orbital, or 3. measuring ejected Auger electrons when the core hole is filled (Calvin, 2013). The spectrum is produced by repeating over a range of energies once the absorbance is determined and the X-rays energy is slightly changed (Calvin, 2013).

The X-ray intensity of emitted through a sample is related to the incident X-ray intensity on a sample and the thickness of a sample and the XAS obeys Beer-Lambert law (Eq. 3-6):

$$I = I_0 e^{-\mu t} \quad (3-6)$$

where I is intensity emitted through a sample, I_0 is incident X-ray intensity on samples, μ is the adsorption coefficient, and t is the thickness of a sample (Newville, 2014).

The adsorption coefficient μ is associated with the X-ray energy (E), the density of a sample (ρ), the atomic mass (A), and the atomic number (Z). It is roughly described as the following equation (Newville, 2014):

$$\mu \approx (\rho Z^4) / (AE^3) \quad (3-7)$$

An example of the molybdate spectrum shows the common features in the X-ray spectroscopy (Figure 3-10). Initially a gradual trend presents towards the lower adsorption with the increasing energy, which is referred to as background. A sharp increase (known as adsorption

edge or white line) within spectrum, corresponding to ejection of a core electron, is produced when the incident beam energy equals the binding energy of a core electron in an atom. This can be diagnostic for specific elements in specific oxidation states (Schnohr and Ridgway, 2015). The X-ray Absorption Near-edge Structure (XANES) contains features of the low energy both before and at adsorption edge (pre-edge and edge regions), while the post edge region is the Extended X-ray Absorption Fine Structure (EXAFS) (Schnohr and Ridgway, 2015).

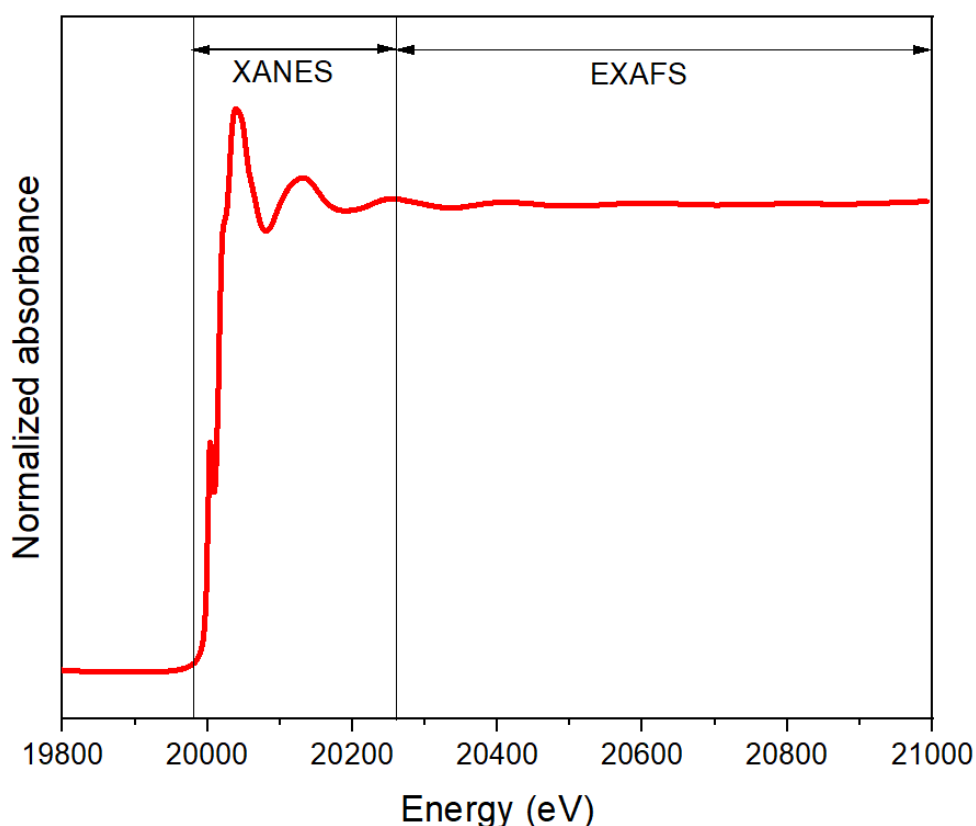


Figure 3-10 An example of the molybdate spectrum showing regions in the X-ray absorption spectroscopy.

3.6.2.1 X-ray Absorption Near Edge Structure (XANES)

XANES is a powerful tool for directly gaining information on the speciation of trace elements using minimal sample pretreatment (Wisawapipat and Kretzschmar, 2017). As described in the last paragraph the XANES region is close to the absorption edge and is related to the transitions

of the photoelectron to the bound states (Figure 3-10). For investigated metals (Mo and V) in this project, abundant information (such as pre-edge peak intensity and position, and edge energy) can be shown in the pre-edge and XANES spectral areas around the K absorption edge (K-edge) (Hard X-rays with energy over 4 keV are used to excite 1s electrons to obtain metal K-edge XAS) (Wisawapipat and Kretzschmar, 2017, Baker et al., 2017). Therefore, XANES details information about different oxidation states of absorbing atoms as well as the symmetry (e.g. octahedral vs. tetrahedral coordination) and type of the first-shell coordination. The increment of the pre-edge peak intensity rises with coordination asymmetry (such as distorted tetrahedral, octahedral or square pyramidal coordination), while pre-edge and edge energies rise with oxidation states (Wisawapipat and Kretzschmar, 2017).

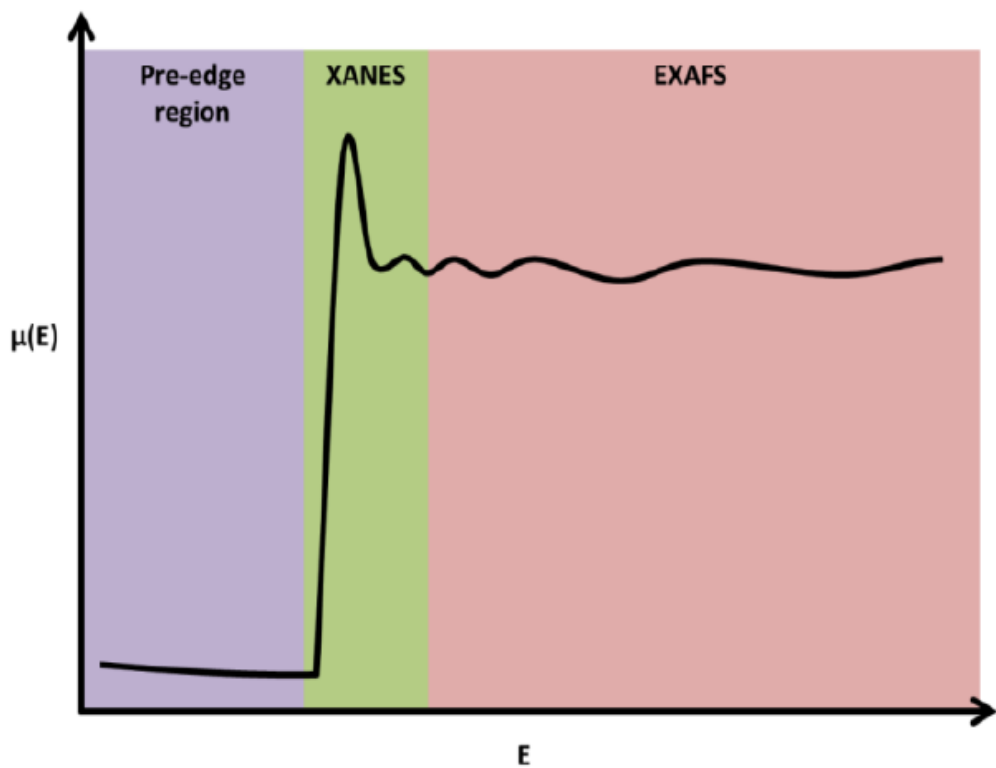


Figure 3-11 A spectrum showing the areas in x-ray absorption spectroscopy from (Ravel and Newville 2005).

3.6.2.2 Extended X-ray Absorption Fine Structure (EXAFS)

Extended X-ray Absorption Fine Structure (EXAFS) is a technique that helps to determine chemical bonding environment of individual elements providing detailed information about interatomic distances, coordination number, thermal disorder and structure around a given atomic species. EXAFS provides a powerful way for structural analysis because it does not need long range order and can be applied to a wide range of disordered and ordered materials (Calvin, 2013, Schnohr and Ridgway, 2015).

In EXAFS region, the sufficient energy can excite photoelectrons, which can be ejected into continuum. This can radiate out in all directions acting as a wave and thus the nearby atoms can be scattered off and photoelectrons return to original atom (Newville, 2004, Calvin, 2013). The formation of EXAFS spectrum is due to the changes in the adsorption probability induced by constructive (increased oscillations) or destructive (decreased oscillations) interference of the photoelectron (Newville, 2004, Calvin, 2013). The equation of EXAFS is described in Eq. 3-8 and Table 3-3 shows the explanation of these parameters in the equation (Calvin, 2013, Newville, 2004, Newville, 2014).

$$\chi(k) = S_0^2 \sum_i N_i \frac{f_i(k)}{k D_i^2} e^{-\frac{2D_i}{\lambda(k)}} e^{-2k^2 \sigma_i^2} \sin(2kD_i + \delta_i(k)) \quad (3-8)$$

Table 3-3 Parameters in EXAFS equation and their explanation (Newville 2004, Calvin 2013, Newville 2014).

Parameter	Explanation
$\chi(k)$	EXAFS
S_0^2	Amplitude reduction factor (highly related to N_i).
N_i	Number of scattering atoms i.
k	Wavenumber of photoelectron.
$\delta_i(k)$	Path shift resulted from backscattering.
$f_i(k)$	Scattering amplitude (correlated with incident X-ray k and atomic number of the backscattering atom).
D_i	Half path length of scattering.
$e^{-(2D_i)/\lambda(k)}$	Mean free path of photoelectron.
$e^{-2k^2\sigma_i^2}$	Debye-Waller factor which corresponds to the amount of disorder observed in positioning of atoms.

3.6.2.3 B18 Beamline

B18 is the key beamline that this research applied. The B18 beamline uses the QEXAFS (Quick EXAFS) approach to collect data. This beamline is equipped with both Si (311) and Si (111) monochromator and has the ability to operate in either standard step-scan mode (similar to I20 below) or in continuous scan mode which provides rapid EXAFS spectra collection (Krishnan et al., 2007, Dent et al., 2009). Data collection for Mo(VI) adsorption to hematite and magnetite utilised B18 beamline in Diamond Light Source.

3.6.2.4 I20 Beamline

I20 beamline was commissioned in 2009. This EXAFS beamline is split into two branches: EDE (Energy Dispersive EXAFS) and scanning. This project used scanning branch which provides high photon flux and spectral purity and it is ideal to collect data for solid samples

with low analyte concentration and increase data quality (Diaz-Moreno et al., 2009). Data for V(V)-adsorbed hematite were collected on beamline I20 in Diamond Light Source.

Table 3-4 key features of B18 and I20 beamline at Diamond Light Source.

Beamline	Energy Range	Monochromator	Flux
B18	2.05 - 35 keV	Si(311)/Si(111)	5×10^{11} at 8 keV
I20	4 - 20 keV	Si(111) four-bounce	$> 10^{12}$ at 10 keV

XANES and EXAFS were collected on Mo(VI)-adsorbed hematite, magnetite and biogenic magnetite samples (0.6×10^{-4} M and 5×10^{-4} M Mo(VI) in 0.01 M NaCl solution at pH 3-13) at the Diamond Light Source (DLS) Ltd. (Oxford, UK) on Beamline B18 at the Mo (20 keV) K-edge. Samples were formed into pellets and measured in a liquid nitrogen cryostat (77 K). The beamline is equipped with a Si (311) monochromator and data was collected in fluorescence mode using a 36 element Ge detector (Dent et al., 2009, Ravel and Newville, 2005). Standard data for molybdenum dioxide ($\text{Mo(IV)}\text{O}_2$), molybdenum trioxide ($\text{Mo(VI)}\text{O}_3$), sodium molybdenum ($\text{Na}_2\text{Mo(VI)}\text{O}_4 \cdot 2\text{H}_2\text{O}$), bamfordite ($\text{Fe(III)}\text{Mo(VI)}_2\text{O}_6(\text{OH}_3) \cdot \text{H}_2\text{O}$) and ammonium heptamolybdate ($(\text{NH}_4)_6\text{Mo(VI)}_7\text{O}_{24} \cdot 4\text{H}_2\text{O}$), were collected in transmission mode at room temperature. Unfortunately, due to COVID-19 it was not able to collect Mo(VI)-adsorbed biogenic magnetite EXAFS for chapter 6, which would allow the bioproduced and synthetic materials to be fully contrasted.

XANES and EXAFS were collected on V(V)-adsorbed hematite samples (1.2×10^{-4} M and 1.2×10^{-3} M V(V) with ionic strength of 0.01 M NaCl at pH 3, 4, 5.5, 7, 9, 12) at the Diamond Light Source (DLS) Ltd. (Oxford, UK) on Beamline I20 at the V (5.46 keV) K-edge. Similar to Mo(VI)-adsorbed samples, V(V)-adsorbed hematite particles were also formed into pellets and measured in a liquid nitrogen cryostat (77 K). Standards data for sodium vanadate ($\text{Na}_3\text{V(V)O}_4$), vanadium pentoxide ($\text{V(V)}_2\text{O}_5$), vanadium(IV) oxide ($\text{V(IV)}_2\text{O}_4$), and vanadium sesquioxide ($\text{V(III)}_2\text{O}_3$), were collected in transmission mode at room temperature. Glitches were removed by EXAFS rewindowing through setting lower bound of 446 and upper bound of 487 in Dawn software. Demeter suite software was used to process Mo(VI)/V(V) adsorbed particles data including background subtraction, calibration and data normalization by Athena and then the data was fitted using Artemis. Briefly, individual scans were imported with their corresponding reference files (Mo foil, K-edge). The adsorption edge was selected, and this was defined as the top of the peak in the first derivative of the spectra and the data $y=0$ intercept in the second derivative. The background interference could be removed by fitting the pre-edge range with a linear regression line by selecting two points in the pre-edge region, one at the start and one near the end. The approach in the post-edge region was as same as the pre-edge's.

3.6.2.5 The F-test

F-test is used to determine one of two ‘good’ fit EXAFS data to be statistically significant by identifying which of them best fits a dataset. It is frequently used in crystallography and assesses the difference and better probability of one good fit to another. It is described as the following equation (Downward et al., 2007):

$$F = \left[\left(\frac{R_1}{R_0} \right)^2 - 1 \right] \frac{(n-m)}{b} \quad (3-9)$$

where R_0 and R_1 are R-factors for the best and the test fit respectively; $n-m$ is degrees of freedom (n is independent data points and m is fit parameters); and b is the dimension of the hypothesis.

Then confidence value, α , can be calculated by:

$$\alpha = P(F > F_{b,n-m,\alpha}) = 1 - I_x[(n-m)/2, b/2] \quad (3-10)$$

where P is probability, $I_x[(n-m)/2, b/2]$ is incomplete beta function, and $x = (n-m)/(n-m+bF) = (R_0/R_1)^2$ (Downward et al., 2007).

If the confidence level (α) of a fit is greater than 67% and preferably greater than 95%, it is considered as a significant and hence good fit. EXAFS fitting can only physically fit a data and a ‘good’ fit can only be considered if it is chemically or structurally sensible. F-test therefore is not the only factor to be considered when determining whether the fit to the data is ‘good’, however, it helps to indicate a reasonable validity of one chemically statistical fit over another (Downward et al., 2007).

4. Adsorption of Octahedral Mono-molybdate and Poly-molybdate onto Hematite: A Multi-technique Approach

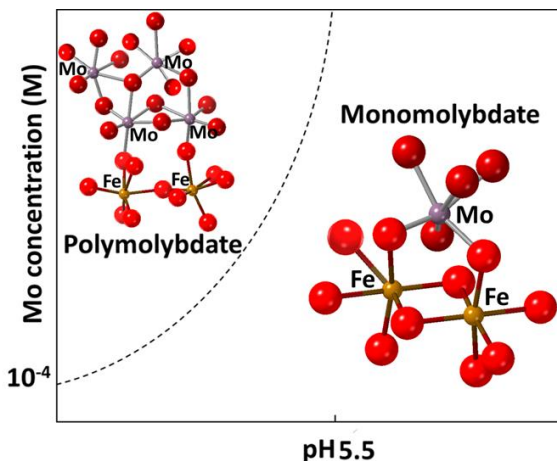
JING ZHANG,[†] VICTORIA S. COKER,[†] J. FREDERICK W. MOSSELMANS,[‡] AND SAMUEL SHAW^{*,†}

[†] Williamson Research Centre for Molecular Environmental Science, Department of Earth and Environmental Sciences, The University of Manchester, Manchester M13 9PL, U.K.

[‡] Diamond Light Source Ltd., Diamond House, Harwell Science and Innovation Campus, Didcot, Oxfordshire OX11 0DE, U.K.

4.1 Abstract

Molybdenum (Mo) is a key trace element and potential environment contaminant in many surface and subsurface environmental systems including acid mine drainage systems. Under oxic conditions Mo can exist in a number of chemical forms, including mono-molybdate ($\text{Mo(VI)}\text{O}_4^{2-}$) and various polymolybdate species (e.g. $\text{Mo(VI)}_7\text{O}_{24}^{6-}$) depending on the geochemical conditions (e.g. pH). In addition,



the mobility and bioavailability of Mo is often controlled by sorption to mineral surfaces, including iron (oxyhydr)oxides e.g. hematite (Fe_2O_3). This study applied multi-techniques including adsorption isotherms, PHREEQC geochemical modelling, Attenuated Total Reflection-Fourier Transform Infrared Spectroscopy (ATR-FTIR), and X-ray Absorption Spectroscopy (XAS) to holistically characterise the molecular scale adsorption mechanism of molybdate to hematite as function of pH (3-13) and Mo(VI) concentration (0.01×10^{-4} - 2×10^{-3} M). PHREEQC and ATR-FTIR indicate both pH and Mo concentration are important

variables forming mono- vs. poly- molybdate and suggest low pH (≤ 4) and high concentration ($[Mo(VI)] > 5 \times 10^{-4}$ M) contribute to the formation of polymolybdate. XAS indicates Mo adsorbed to hematite via inner-sphere corner-sharing bidentate binuclear complex with octahedral mono-molybdate structure at Mo concentration of 0.6×10^{-4} M in all systems, and at 5×10^{-4} M and pH over 5. Heptamolybdate polyanions ($Mo_7O_{24}^{6-}$) were formed at pH 3- 4 and 5×10^{-4} M Mo-adsorbed hematite via inner-sphere corner-sharing bidentate binuclear adsorption complex with octahedral molecule. This study shows that both concentration and pH are key to the surface speciation of Mo at the iron oxide surface with key implications for Mo behaviour in the environment.

Keywords: Molybdenum, Iron oxide, Surface adsorption, XANES, EXAFS, ATR-FTIR, octahedral

4.2 Introduction

Molybdenum (Mo) is an essential micronutrient and an important trace element for plants, microorganisms, animals and human health (Arnon and Stout, 1939). However, at higher concentrations associated with contaminated land Mo can pose a significant environmental hazard with a World Health Organization (WHO) safety-based guideline of 0.07 ppm for Mo in drinking water (WHO, 2003). Mo contamination can occur in a variety of scenarios from mines drainage/wastes to natural groundwater systems e.g. rhyolitic and volcanogenic ash, where Mo is leached into groundwater aquifers (Smedley and Kinniburgh, 2017, Xu et al., 2013, Frascoli and Hudson-Edwards, 2018, Smedley et al., 2014, Solongo et al., 2018). High Mo concentrations have been observed in surface and groundwaters associated with mine wastes at many sites across the world, in some cases containing concentrations > 10 ppm e.g. San Telmo mine, Spanish Iberian Pyrite Belt (10.4 ppm) and the Antamina mine, Peru (13.9 ppm) (Frascoli and Hudson-Edwards, 2018, España et al., 2008, Skierszkan et al., 2016). High

Mo values can have a detrimental effect on environmental systems, for example, causing chlorosis in plants (Gupta, 1997) or molybdenosis in ruminants (Arai, 2010). The mobility and bioavailability of Mo in many oxic surface and sub-surface environmental systems is controlled by the adsorption of Mo(VI) species to mineral surfaces, including ferric (oxyhydr)oxide phases e.g. hematite ($\alpha\text{-Fe(III)}_2\text{O}_3$) (Arai, 2010, Xu et al., 2006a, Zhang and Sparks, 1989, Brinza et al., 2008, Brinza et al., 2015, Gustafsson, 2003, Das et al., 2016, Goldberg et al., 1996, Goldberg et al., 1998, Das and Hendry, 2013). Understanding the atomic scale chemical form (e.g. monomers or polymers (Arai, 2010, Davantes et al., 2017)) and adsorption mechanisms of Mo(VI) as a function of geochemical conditions (e.g. pH and Mo concentration) is key to predicting the environmental behaviour of this contaminant.

Mo exists in natural aqueous environments as the highly soluble tetrahedral monomeric Mo(VI) oxyanion ($\text{Mo(VI)}\text{O}_4^{2-}$) in oxic systems above pH 6 (Xu et al., 2013, Oyerinde et al., 2008, Wichael et al., 2009, Reddy and Gloss, 1993). Heptamolybdate polyanions (e.g. $\text{Mo(VI)}_7\text{O}_{24}^{6-}$), consisting of MoO_6 octahedra, form at lower pH (pH 3-5) and higher total Mo concentrations ($> \sim 10^{-4}$ M) (Davantes et al., 2017, Reddy et al., 1997). Mo is also redox-sensitive and can form poorly soluble Mo(IV) phases, for example $\text{Mo(IV)}\text{S}_2$ or $\text{Mo(IV)}\text{O}_2$ within certain reducing environments (Reddy et al., 1997). The aqueous environmental mobility, speciation and bioavailability of Mo is controlled by a variety of geochemical factors, including pH, ionic strength, presence of competitive adsorbates (e.g. phosphate), adsorbent type and Mo oxidation state (e.g. Mo(VI) and Mo(IV) species) (Xu et al., 2013, Xu et al., 2006b). There is little affinity for absorption of molybdate ($\text{Mo(VI)}\text{O}_4^{2-}$) to most organic compounds, therefore the transport and fate of Mo(VI) anions in many oxic sub-surface environmental systems is controlled by molybdate adsorption to mineral surfaces, in particular, iron (oxyhydr)oxides nanoparticles e.g. goethite ($\alpha\text{-Fe(III)}\text{OOH}$) (Arai, 2010, Xu et al., 2006a, Zhang and Sparks, 1989), ferrihydrite ($\text{Fe(III)}_2\text{O}_3 \bullet 0.5\text{H}_2\text{O}$) (Brinza et al., 2008, Brinza et al.,

2015, Gustafsson, 2003, Das et al., 2016), hematite (Brinza et al., 2015, Goldberg et al., 1996, Goldberg et al., 1998, Das and Hendry, 2013, Davantes et al., 2017) and magnetite ($(Fe(II)Fe(III)_2O_4)$) (Verbinnen et al., 2012, Verbinnen et al., 2013), due to their high surface area, reactivity and prevalence in the natural environment (Xu et al., 2013, Wichard et al., 2009).

In general, Mo(VI) adsorbs to iron (oxyhydr)oxides surfaces at low pH with capacity decreasing above pH 8 (Xu et al., 2013, Xu et al., 2006a, Brinza et al., 2008, Gustafsson, 2003, Goldberg et al., 1996, Verbinne et al., 2012), indicating that lower pH conditions have greater potential to control the mobility of Mo relative to higher pH systems. However, at very low pH (e.g. pH <3.5), Fe(III)-(oxyhydr)oxides can dissolve with the potential to release sorbed Mo (Smedley and Kinniburgh, 2017). X-ray adsorption spectroscopy (XAS) and Attenuated Total Reflection-Fourier Transform Infrared Spectroscopy (ATR-FTIR) of Mo(VI) adsorption to iron (oxyhydr)oxides at near-neutral pH indicate that tetrahedrally coordinated $Mo(VI)O_4^{2-}$ tends to form inner-sphere surface species when adsorbed to goethite, hematite and ferrihydrite (Arai, 2010, Brinza et al., 2015, Das et al., 2016, Gustafsson and Tiberg, 2015). Brinza et al (2015) found that Mo binds to ferrihydrite via a tetrahedral corner-sharing structure at pH 7 - 8.5 (Brinza et al., 2015), however, Das et al. (2016) suggest that at higher pH (~10) Mo(VI) forms an outer-sphere adsorption complex (Das et al., 2016). In addition, Das et al (2016) (Das et al., 2016) indicate that tetrahedral $Mo(VI)O_4^{2-}$ forms a bidentate binuclear complex on the hematite surface at pH 10, although no XAS data exist for lower pH conditions. The local coordination environment of adsorbed molybdate on the goethite surface also changes with pH. At near neutral pH a monomeric Mo(VI) surface species forms, however, at lower pH (\leq pH 4) a mixture of tetrahedrally and octahedrally coordinated Mo(VI) species (Arai, 2010) were identified with evidence of Mo-Mo scattering paths with increasing Mo-Mo coordination numbers with higher surface loading. This suggests the presence of a polymeric species (e.g.

dimer), with Mo in a octahedral coordination environment, similar to the Mo local environment in bamfordite ($\text{Fe(III)}\text{Mo}_2\text{O}_6(\text{OH}_3)\bullet\text{H}_2\text{O}$) (Arai, 2010, Birch et al., 1998). These results are comparable to ATR-FTIR analyses of Mo adsorption to hematite which indicate polymolybdate exists at $\text{pH} < 5$ and Mo concentration over 10^{-4} M (Davantes et al., 2017). The exact nature of the polymolybdate is unclear, but Density Functional Theory + U correction (DFT+U) computational calculations suggest a three-dimensional cluster containing three, four or five molybdate ions in both tetrahedral and octahedral coordination (Davantes et al., 2017). In addition, isotope fractionation of Mo(VI) during adsorption to iron (oxyhydr)oxide surfaces shows that the largest isotope fraction is observed for adsorption is to hematite ($\Delta^{98}\text{Mo} = 2.19 \pm 0.54\text{\%}$), whereas adsorption to other iron (oxyhydr)oxides produces a lower fractionation (e.g. ferrihydrite $\Delta^{98}\text{Mo} = 1.11 \pm 0.15\text{\%}$, goethite $\Delta^{98}\text{Mo} = 1.40 \pm 0.48\text{\%}$). This variation in isotopic fraction indirectly indicates changes to the Mo surface species (Goldberg et al., 2009) and DFT+U modelling suggests that it is due to a change from a tetrahedrally coordinated MoO_4^{2-} species in solution to an octahedrally coordinated $\text{MoO}_3(\text{H}_2\text{O})_3$ surface species (Weeks et al., 2007). However, the interaction of Mo(VI) with hematite and the key molecular scale processes controlling its surface adsorption as a function of changing geochemical conditions remain unresolved.

The aim of this study is to characterise the molecular scale adsorption mechanism of Mo(VI) to hematite ($\alpha\text{-Fe}_2\text{O}_3$) under varying geochemical conditions, including pH, initial Mo(VI) concentration and ionic strength. A combination of aqueous chemical analyses, PHREEQC geochemical modelling, X-ray Absorption Spectroscopy (XAS), Attenuated Total Reflection-Fourier Transform Infrared Spectroscopy (ATR-FTIR), Transmission Electron Microscopy (TEM) and X-ray Photoelectron Spectroscopy (XPS) were used to investigate the key mechanisms of Mo(VI) adsorption to hematite. This holistic approach allowed the molecular

structure and range of chemical stability (pH and [Mo(VI)]) of mono- and poly- molybdate adsorption to hematite to be determined.

4.3 Experimental Methods

Synthesis and absorption experiments. Hematite ($\alpha\text{-Fe}_2\text{O}_3$) was synthesised using the method from Schwertmann and Cornell (2000) (Schwertmann and Cornell, 2000a). The synthesized hematite was analysed using powder X-ray Diffraction (pXRD) (Bruker D8 Advance) and showed the material was pure hematite (Figure SI4-1). Surface area of the synthesized hematite was determined using Brunauer-Emmett-Teller (BET) analysis (Micromeritics Gemini) and was $47.2 \pm 0.3 \text{ m}^2/\text{g}$.

Experiments to characterise the adsorption of molybdenum to hematite were performed by contacting a $0.6 \times 10^{-4} \text{ M}$ (6 ppm) and $5 \times 10^{-4} \text{ M}$ (50 ppm) Mo(VI) ($\text{Na}_2\text{MoO}_4 \cdot 2\text{H}_2\text{O}$) solution to hematite (2 g/L) in either a 0.1 M or 0.01 M NaCl solution within a total volume of 30 ml. The pH was varied between 3 and 12 through adjustment using 0.1 M HCl and 0.1 - 1 M NaOH. In addition, adsorption isotherm experiments were performed at pH 7 in 0.1 M or 0.01 M NaCl solution with initial Mo(VI) concentrations of $0.01 \times 10^{-4} - 2 \times 10^{-3} \text{ M}$ (0.1 - 200 ppm). All experiments were maintained on a rotor mixer at a constant speed of 32 rpm for 24 hours and aliquots of solution were filtered by 0.22 μm syringe filters (Merck Millipore) for analysis by Inductively Coupled Plasma Atomic Emission Spectroscopy (ICP-AES) and Inductively coupled plasma mass spectrometry (ICP-MS) (PerkinElmer Optima 5300 dual view) to establish Mo concentrations.

Thermodynamic geochemical modelling was performed using PHREEQC (version 3.3.5) to determine the saturation state of the experimental solutions with respect to Mo(VI) solid phases and the aqueous speciation of Mo(VI) using the Minteq.v4 database (Winstanley et al., 2019). The isotherm adsorption data were fitted with the Langmuir model as shown in Eq. (4-1), where

Q_e (mg Mo/g adsorbent) is the adsorbed amount at equilibrium. Q_{max} (mg/g) is the maximum adsorption capacity. b (l/mg) is a constant. C_e is the residual adsorbent concentration in solution at equilibrium (Verbinnen et al., 2012).

$$Q_e = Q_{max} \times b \times C_e / (1 + b \times C_e) \quad (4-1)$$

A Mo-adsorbed hematite sample (0.6×10^{-4} M Mo(VI) in (0.01 M NaCl at pH 7) was deposited on a carbon-coated copper TEM grid (Agar Scientific) and washed with 70% ethanol. The sample morphology was imaged and composition determined by energy dispersive X-ray (EDX) analysis using a FEI TF 30 analytical FEG TEM and a FEI Talos F200A. Further information on TEM data is available in the supporting information.

X-ray photoelectron spectroscopy (XPS) was performed on samples of Mo-adsorbed hematite (0.6×10^{-4} M Mo(VI) in 0.1 M NaCl solution) at pH 3, 4, 5.5, 7, 8. Samples were prepared by drop-casting sample slurry onto a silicon chip (1x1 cm) followed by washing with isopropyl alcohol prior to loading into the XPS system. Further information on XPS data is available in the supporting information.

The Mo-adsorbed hematite particles were isolated by centrifugation then analysed by Attenuated Total Reflection-Fourier Transform Infrared Spectroscopy (ATR-FTIR) (Bruker Alpha-P FTIR spectrometer) with a diamond crystal. The spectral resolution was 2 cm^{-1} and spectra were an average of 400 scans. The results were background subtracted using OPUS software.

X-ray Absorption Near Edge Structure (XANES) and Extended X-ray Absorption Fine Structure (EXAFS) were collected on Mo-adsorbed hematite samples (0.6×10^{-4} M and 5×10^{-4} M Mo(VI) in 0.01 M NaCl solution at pH 3, 4, 5.5, 7, 9, 10) at the Diamond Light Source (DLS) Ltd. (Oxford, UK) on Beamline B18 at the Mo K-edge (20 keV). Samples were formed into pellets and measured in a liquid nitrogen cryostat (77 K). The beamline is equipped with

a Si(311) monochromator and data was collected in fluorescence mode using a 36 element Ge detector (Ravel and Newville, 2005, Dent et al., 2009). Standard data for molybdenum dioxide (Mo(IV)O_2), sodium molybdate ($\text{Na}_2\text{Mo(VI)O}_4 \cdot 2\text{H}_2\text{O}$), bamfordite ($\text{Fe(III)Mo(VI)}_2\text{O}_6(\text{OH}_3) \cdot \text{H}_2\text{O}$) and ammonium heptamolybdate ($(\text{NH}_4)_6\text{Mo(VI)}_7\text{O}_{24} \cdot 4\text{H}_2\text{O}$), were collected in transmission mode at room temperature. Demeter suite software was used to process including background subtraction, calibration and data normalization by Athena and then the data was fitted using Artemis (Ravel and Newville, 2005). The validity of the new shells were tested by applying F-test (Downward et al., 2007).

4.4 Results and Discussion

Mo(VI) adsorption to hematite was investigated as a function of pH from 3 to 12 at an initial Mo(VI) concentration of 0.6×10^{-4} M and 5×10^{-4} M, and two ionic strengths of NaCl (0.1M and 0.01M, Figure 4-1A). For an initial Mo(VI) concentration of 0.6×10^{-4} M almost all Mo(VI) (> 99.1 %) was adsorbed at pH up to 8, with adsorption decreasing as pH increases from 8 to 12. In addition, there is no change in magnitude of adsorption with ionic strength. In contrast, at a higher initial concentration of 5×10^{-4} M Mo(VI) at pH 3 adsorption to hematite was found to be ~95% and 87% for 0.1 M and 0.01 M NaCl, respectively, with the amount of adsorbed Mo(VI) decreasing to 2%-5% as pH increases to 11-12, for both ionic strengths. These results are consistent with previous studies which show similar trends in Mo(VI) adsorption to hematite, with maximum adsorption under low pH conditions and decreasing levels of adsorption with increasing pH. This is due to the positive charge on the hematite surface at low pH attracts negative charged MoO_4^{2-} . At high pH, MoO_4^{2-} has to overcome the repulsive electrostatic forces to get close to the negative charged surface (Goldberg et al., 1996, Kim and Jang, 2010). However, the adsorption efficiency at pH 3 in our study is higher than in Goldberg (1996), 93% vs. ~55%, likely due to the lower surface area of hematite ($10.9 \text{ m}^2/\text{g}$) and higher

initial Mo(VI) concentration ($0.292 \text{ mol Mo m}^{-3}$) when compared with our system ($47.2 \text{ m}^3/\text{g}$, $0.64 \times 10^{-6} - 5.30 \times 10^{-6} \text{ mol Mo m}^{-3}$) (Goldberg et al., 1996).

Isotherm adsorption data (pH 7) were fitted using a Langmuir model at $[\text{Mo(VI)}] \leq 6 \times 10^{-4} \text{ M}$, suggesting that adsorption of single ions dominates under these processes ($R^2 = 0.996$ in 0.1 M NaCl and 0.975 in 0.01 M NaCl, Figure SI4-2). Ionic strength has little impact on the Mo(VI) adsorption behaviour. At Mo(VI) concentrations above $6 \times 10^{-4} \text{ M}$, the Langmuir model did not fit the data as the concentration of adsorbed Mo(VI) increased along with the increasing of initial Mo(VI) concentration with no clear uptake maximum. This suggests that at higher concentration polymeric species may be forming on the hematite surface as has been observed in similar systems e.g. tungstate (WO_4^{2-}) adsorption to boehmite ($\gamma\text{-AlOOH}$) (Hur and Reeder, 2016). TEM (pH 7) and XPS (pH 3-8) were also used to analyse the $0.6 \times 10^{-4} \text{ M}$ Mo(VI)-adsorbed hematite and indicate no precipitation of Mo phases and/or oxidation changes occurred when Mo(VI) interacted with hematite (Figure SI4-3 & SI4-4).

PHREEQC was used to model the aqueous speciation of Mo over the pH range (2-11.2) at a Mo concentration of $5 \times 10^{-4} \text{ M}$ in 0.01 M NaCl solution (Figure 4-1B). Mono-molybdate species (e.g. HMO_4^{2-}) dominate across the entire pH range with poly-molybdate species (e.g. heptamolybdate, $\text{Mo}_7\text{O}_{24}^{6-}$) composing a small but significant proportion (0.1 % - 9 %) of the Mo present in aqueous solution between pH 2.0-5.5. At the lower Mo concentration of $0.6 \times 10^{-4} \text{ M}$, there is also a small proportion (up to 0.3%) of polymolybdate present at low pH (Figure SI4-5). The fraction of polymolybdate at a Mo(VI) concentration of $5 \times 10^{-4} \text{ M}$ is 1000 times higher than that at $0.6 \times 10^{-4} \text{ M}$ (Figure 4-1B & SI4-5).

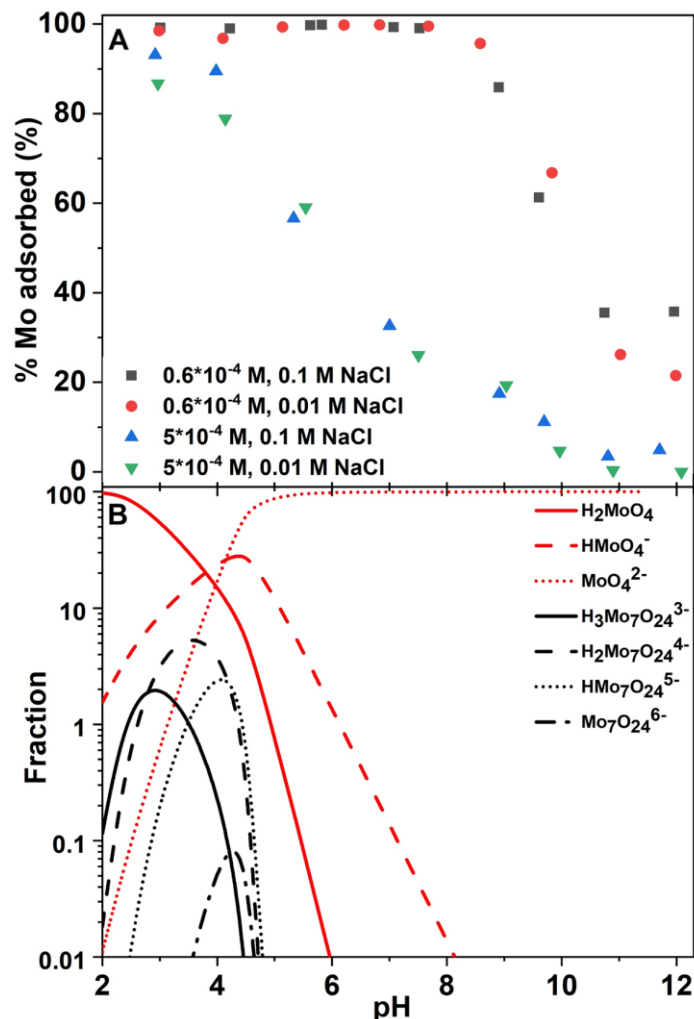


Figure 4-1 A. 0.6×10^{-4} M and 5×10^{-4} M Mo(VI) adsorption onto hematite at pH 3-12 in 0.1 M and 0.01 M NaCl solutions. B. PHREEQC data on Mo speciation at pH 2-11.2 at Mo concentration of 5×10^{-4} M in 0.01 M NaCl.

Attenuated Total Reflection-Fourier Transform Infrared Spectroscopy (ATR-FTIR). Mo(VI)-adsorbed hematite samples were analysed using ATR-FTIR at pH 3 - 10 at an initial Mo(VI) concentration of 5×10^{-4} M, and at pH 4 at Mo(VI) concentrations from 0.6×10^{-4} to 2×10^{-3} M (0.01 M NaCl) (Figure 4-2 & Table SI4-1). ATR-FTIR spectra for 5×10^{-4} M Mo(VI)-adsorbed hematite samples (Figure 4-2B) show peaks at $\sim 790\text{cm}^{-1}$, $\sim 910\text{ cm}^{-1}$ and $\sim 950\text{ cm}^{-1}$ at pH 5.5 and above. However, interestingly, the peak at $\sim 950\text{ cm}^{-1}$ is not present at pH 10 and at pH 4 and below an additional peak at $\sim 970\text{ cm}^{-1}$ is present. A similar trend can

be observed with increasing concentration, with peaks at \sim 790 cm $^{-1}$, \sim 910 cm $^{-1}$ and \sim 950 cm $^{-1}$ at concentrations 5×10^{-4} M and lower, with the appearance of the peaks at \sim 970 cm $^{-1}$ above 1×10^{-4} M (Figure 4-2A). This variation in peak distribution with pH and Mo concentration is consistent with a previous study and indicates that at high pH and low concentration, where the ATR-FTIR spectra is dominated by a band at \sim 910 cm $^{-1}$, Mo(VI) is present as a monomeric adsorbed species (Davantes et al., 2017). At high pH and low Mo(VI) concentration, there are only two peaks at 791 and 913 cm $^{-1}$ (Figure SI4-6A & Table SI4-1) where the peak at \sim 790 cm $^{-1}$ is consistent with Raman studies of Mo adsorption to SiO₂ and TiO₂. Davantes et al. (2017) assigned this band (790 cm $^{-1}$) to a precursor of crystallized MoO₃ phase (subsequently obtained by calcination) (Davantes et al., 2017, Segawa et al., 1992). At lower pH and higher Mo(VI) concentration additional peaks at higher wavenumbers are present at \sim 950 cm $^{-1}$ and 970 cm $^{-1}$ which are indicative of polymeric Mo(VI) species (Davantes et al., 2017). The peaks of \sim 790 cm $^{-1}$ and \sim 910 cm $^{-1}$ at pH 3-4 and high Mo(VI) concentration (Figure 4-2A & 4-2B and Table SI4-1) have wider bands (67 cm $^{-1}$), while this decreases to 24 cm $^{-1}$ for the peaks at \sim 950 cm $^{-1}$ and 970 cm $^{-1}$ indicating a more homogeneous environment, which may correspond with the transition from mononuclear adsorbed Mo(VI) at the oxide/solution interface to Mo(VI) associated with the polymeric species (such as heptamolybdate (Mo₇O₂₄⁶⁻) with C_{2v} symmetry becomes important) at low pH and/or higher [Mo(VI)] (Davantes et al., 2017). This is broadly consistent with the PHREEQC modelling which indicates that heptamolybdate forms in solution at lower pH (2-5) with the proportion in solution increasing with concentration (Figure 4-1B). Overall, the ATR-FTIR data indicates that both concentration and pH are important variables in determining the formation of poly- vs. mono- molybdate.

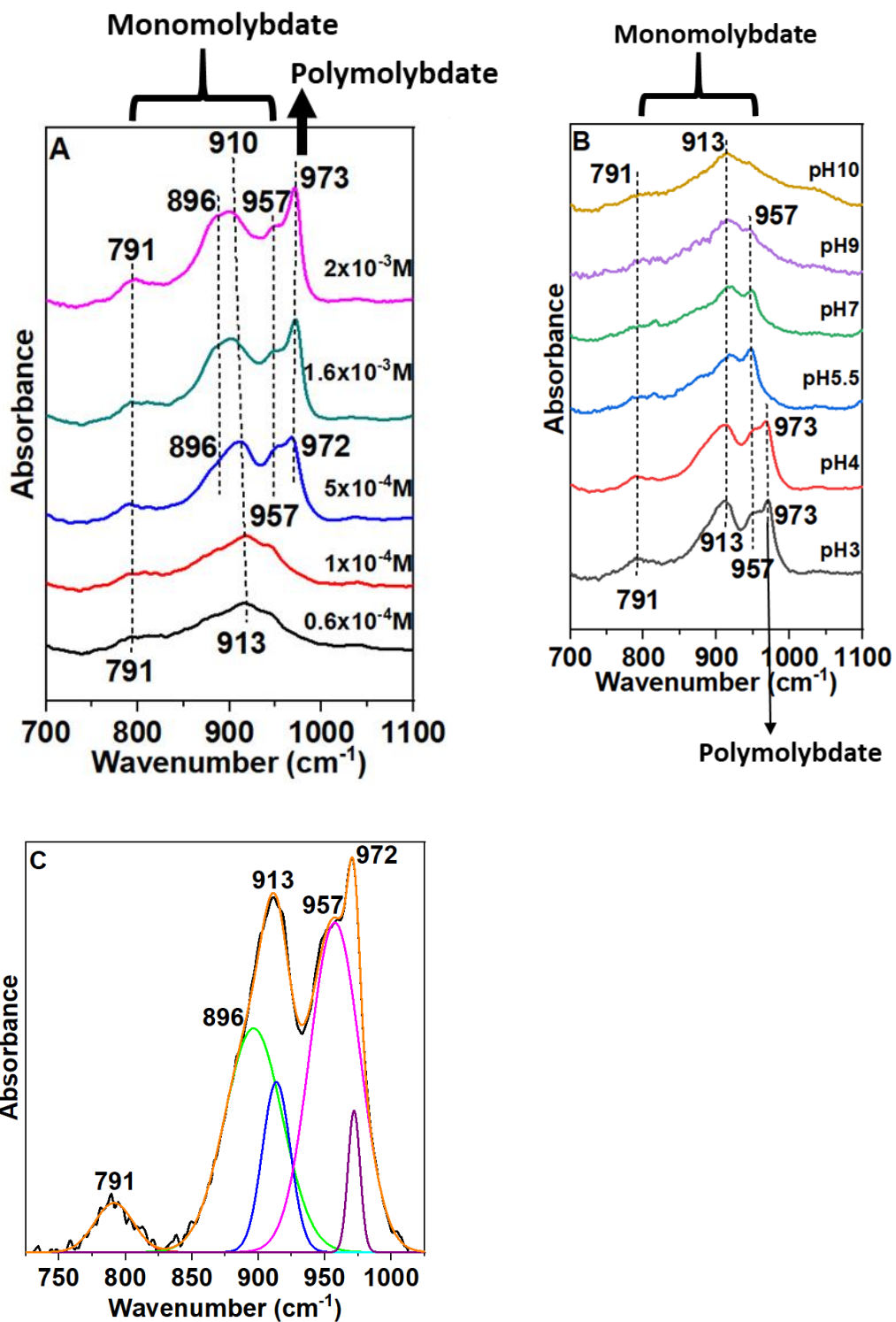


Figure 4-2 A. ATR-FTIR data for Mo(VI)-adsorbed hematite at Mo(VI) concentration of 0.6×10^{-4} - 2×10^{-3} M at pH 4. B. ATR-FTIR data for Mo(VI)-adsorbed hematite at pH 3-10 at Mo(VI) concentration of 5×10^{-4} M. C. Peak fitted for ATR-FTIR data on 5×10^{-4} M Mo(VI)-

adsorbed hematite at pH 3 (black lines are experimental spectra, coloured lines are fitted peaks).

X-ray Absorption Spectroscopy (XAS). The Mo K-edge XANES spectra for 5×10^{-4} M Mo(VI)-sorbed to hematite are shown in Figure 4-3 alongside standards for sodium molybdate ($\text{Na}_2\text{Mo}(\text{VI})\text{O}_4 \cdot 2\text{H}_2\text{O}$), molybdenum dioxide ($(\text{Mo}(\text{IV})\text{O}_2)$), bamfordite ($(\text{Fe}(\text{III})\text{Mo}(\text{VI})_2\text{O}_6(\text{OH}_3) \cdot \text{H}_2\text{O}$), and heptamolybdate ($((\text{NH}_4)_6\text{Mo}(\text{VI})_7\text{O}_{24} \cdot 4\text{H}_2\text{O}$). The experimental spectra all have a pre-edge peak at 20004 eV similar to all Mo(VI) standards. The intensity of the pre-edge peaks for the experimental samples best-match those for bamfordite and heptamolybdate standards (see inset in Figure 4-3), where Mo(VI) is present in octahedral coordination, and they are significantly lower than that of sodium molybdate, where Mo(VI) is present in tetrahedral coordination. The size of the pre edge peak is also consistent with a low intensity pre-edge seen in previous studies where Mo(VI) was incorporated hematite (Das et al., 2016, Görn et al., 2021), directly substituting for Fe(III) in an octahedral coordination environment. In addition, the overall shape of the Mo K-edge XANES spectra for the experimental samples in Figure 4-3 is consistent with those from previous studies where Mo was incorporated into hematite, ferrihydrite and goethite with a strong distortion of MoO_6 octahedra (Görn et al., 2021), and do not match the shape of the standard spectrum for sodium molybdate ($\text{Na}_2\text{MoO}_4 \cdot 2\text{H}_2\text{O}$), which has Mo(VI) in tetrahedral coordination (Arai, 2010). However, if the Mo was incorporated into the hematite the pre-edge peak would be lower than 20004 eV at 19996 eV, but this similarity does support the observation that the Mo is in octahedral rather than tetrahedral coordination for all experimental samples, and that the process of sorption to hematite has facilitated this change in the coordination of the Mo (Görn et al., 2021). So XANES indicated Mo(VI) adsorbed onto hematite in octahedral coordination. From a more detailed examination of the Mo K-edge XANES spectra for pH 3 and pH 4, there are three distinct peaks in the XANES spectra at 20018, 20032 and 20046 eV. These peak

positions and overall structure of these XANES match closely the spectra of heptamolybdate, which is consistent with the ATR-FTIR results in Figure 4-2 indicating the Mo(VI) is present as a polymeric species in octahedral coordination. For samples at pH 7 and 9, the peak in the XANES spectra at ~20018 eV is not present and the overall structure is more similar to that of bamfordite. In the bamfordite structure Mo(VI) is present with an octahedral environment, indicating that the adsorbed Mo(VI) species at neutral pH are also in an octahedral coordinated environment, but may not form a polymeric species. Linear combination fitting is applied for Mo-adsorbed hematite samples at Mo concentration of 5×10^{-4} M and pH 3-9 (Table 4-1). Over 75% of octahedral bamfordite and heptamolybdate are fitted and this provides a hint to fit the EXAFS data.

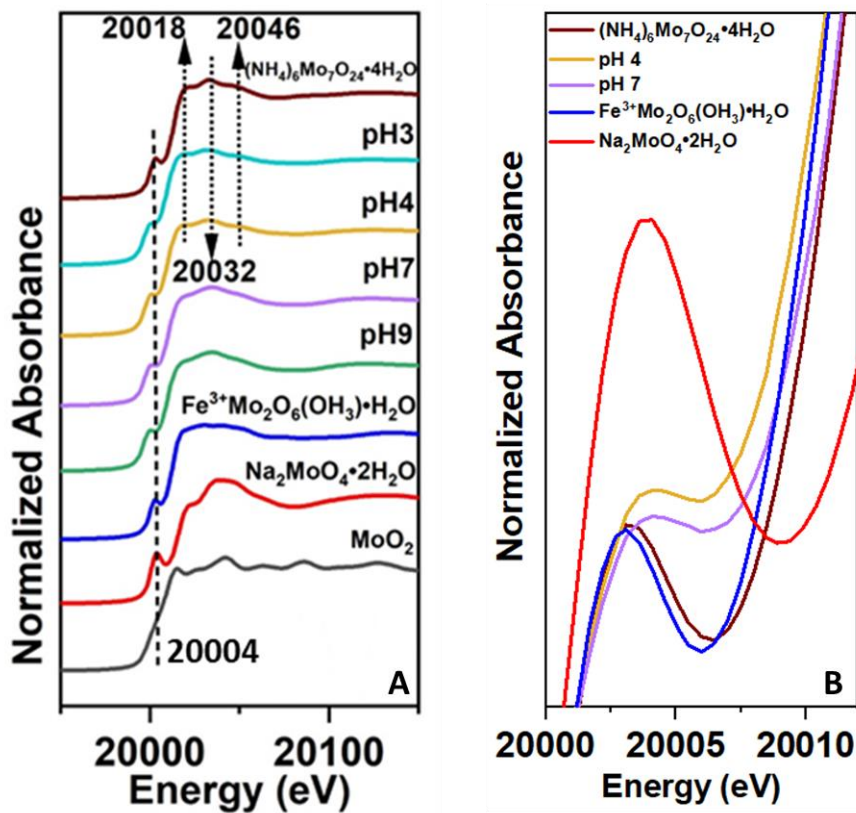


Figure 4-3 XANES data for A. standards and 5×10^{-4} M Mo(VI)-adsorbed hematite samples at pH 3-9, B. zoomed in pre-edge peaks (~ 20004 eV) for standards and samples at pH 4 and 7

Table 4-1 Linear combination fitting for Mo-adsorbed hematite at Mo concentration of 5×10^{-4} M and pH 3-9.

Mo-adsorbed hematite samples	Ammonium heptamolybdate ($(\text{NH}_4)_6\text{Mo}_7\text{O}_{24}$) (%)	Bamfordite ($\text{FeMo}_2\text{O}_6(\text{OH})_3 \cdot \text{H}_2\text{O}$) (%)	Sodium molybdate ($\text{Na}_2\text{VO}_4 \cdot 2\text{H}_2\text{O}$) (%)	R-factor
5×10^{-4} M Mo, pH 3	22.3	64	13.7	0.0027
5×10^{-4} M Mo, pH 4	21.7	69.9	8.4	0.0021
5×10^{-4} M Mo, pH 7	17.9	58.4	23.7	0.0005
5×10^{-4} M Mo, pH 9	8.3	69.5	22.2	0.0006

The results of the Mo K-edge EXAFS fits for Mo(VI)-adsorbed to hematite at Mo(VI) concentrations of 0.6×10^{-4} M and 5×10^{-4} M at a range of pH conditions (Table 4-2 & SI4-2

and Figure SI4-8) show that in all systems Mo(VI) is coordinated by six oxygens at three distances i.e. \sim 1.7 Å, 2 Å and 2.2 Å. This local environment is consistent with that of Mo(VI) in bamfordite and ammonium heptamolybdate, indicating that Mo(VI) is present in a distorted octahedral coordination within all experimental samples. For 0.6×10^{-4} M Mo(VI)-adsorbed hematite samples across the pH range and 5×10^{-4} M samples at pH 7 and 9, the EXAFS fit is completed via addition of two Mo-Fe shells at 3-3.49 Å. This coordination environment indicates the formation of an inner sphere surface adsorption complex. The Mo-Fe distances are significantly longer than Mo-Fe distances in edge sharing octahedral complexes (2.81 Å) and are more consistent with those of a corner-sharing octahedra in goethite (i.e. 3.53 Å, Table 4-2 & SI 4-2) (Arai, 2010). This indicates that Mo(VI) is forming a bidentate binuclear surface complex, via the sharing of oxygens on two adjacent Fe-O octahedra (Arai, 2010). The difference in the Mo-Fe distances observed is due the distorted nature of the Mo-O octahedra, with the shorter Mo-O distance of 1.7 Å adjacent to the shorter Mo-Fe distance of 3 Å, and the longer Mo-O shells contributing to the longer Mo-Fe at 3.49 Å (Figure 4-4A). Overall, the adsorption mechanism of Mo(VI) to hematite is similar to that of on goethite i.e. bidentate binuclear surface complex, however Mo(VI) is octahedrally coordinated on the hematite, but tetrahedrally coordinated on the goethite surface. This change in coordination environment leads to longer Mo-Fe distances for hematite relative to Mo(VI) adsorbed to goethite. i.e. Mo-Fe \sim 3 Å vs 2.8 Å and 3.28-3.49 vs. 3.4 -3.5 (Arai, 2010) (Figure 4-4A). This data represents the first direct analysis of an octahedrally coordinated Mo(VI) complex on an iron (oxyhydro)oxide surface, as all previous XAS and ATR-FTIR investigation have only indicated a tetrahedrally-coordinated Mo(VI) absorption species forms on the surface of other iron oxyhydroxides i.e. goethite, lepidocrocite and ferrihydrite (Arai, 2010, Brinza et al., 2015, Das et al., 2016, Davantes et al., 2017, Davantes et al., 2016), at around neutral pH conditions (Arai, 2010). The contrast in adsorption complexes coordination between hematite and other

iron (oxyhydr)oxides is also supported by the isotope fractionation study which shows a significantly larger Mo isotope fractionation when Mo(VI) adsorbed to hematite ($\Delta^{98}\text{Mo} = 2.19 \pm 0.54\text{\%}$), relative to other iron (oxyhydr)oxides e.g. goethite ($\Delta^{98}\text{Mo} = 1.40 \pm 0.48\text{\%}$) and ferrihydrite ($\Delta^{98}\text{Mo} = 1.11 \pm 0.15\text{\%}$) (Goldberg et al., 2009). DFT+U calculations indicate that this fractionation is due to a change in the Mo(VI) coordination environment, from tetrahedral in solution to an octahedrally coordinated adsorbed species (Davantes et al., 2017), which supports the formation of octahedrally coordinated adsorbed surface species on hematite. In addition, previous studies have linked Mo isotope fractions observed in natural systems to the adsorption of Mo(VI) to birnessite (manganese oxyhydroxide), with the isotope fractionation resulting from the transition from tetrahedral coordinated solution species to a polynuclear Mo structure containing Mo(VI) in a distorted octahedral coordination (Wasylewski et al., 2011). This transition from a dissolved tetrahedral species to octahedral adsorbed species has also been observed for tungstate, where $\text{W(VI)}\text{O}_4^{2-}$ transforms to octahedral coordination when adsorbed to boehmite ($\gamma\text{-AlOOH}$) (Hur and Reeder, 2016).

EXAFS from the 5×10^{-4} M Mo(VI) samples at pH 3 and 4 indicate that the octahedrally coordinated Mo(VI) is surrounded by two Mo-Mo shells at distances of 3.2 Å and 3.62 Å. Attempts were made to add potential Mo-Fe shells, but they did not produce adequate fits to the data, when compared to the fits produced using the Mo-Mo shells. The Mo-Mo distances in our study are not consistent with those in the ammonium heptamolybdate standard which consists of edge sharing octahedrally coordinated Mo(VI) and has Mo-Mo shells ($\text{CN} = 3$) at 3.25 Å and 3.43 Å (Shimao, 1967a, Shimao, 1967b). The two Mo-Mo distances are more consistent with the presence of both edge sharing (3.25 Å) and corner sharing (3.62 Å) octahedra within the polymer. Overall, this indicates that polymolybdate is forming on the surface of hematite at 5×10^{-4} M Mo(VI) at pH 3 - 4 (Figure 4-3). This is consistent with the PHREEQC and ATR-FTIR results which both indicated polymolybdate formation in these

acidic systems at high Mo(VI) concentration (5×10^{-4} M) (Figure 4-1B & 4-2). For samples at low Mo(VI) concentration (0.6×10^{-4} M) under acidic conditions, EXAFS with 2 Mo-Fe shells at 2.95–3.33 Å gave a good fit. Considering the indicative of PHREEQC (Figure 4-1B & SI4-5) that the fraction of polymolybdate at Mo(VI) concentration of 5×10^{-4} M is 1000 times higher than that at 0.6×10^{-4} M and the absence of an ATR-FTIR peak (Figure SI4-6A) at ~970 cm⁻¹ (corresponding with polymolybdate), as well as previous studies which indicate that the formation of polymolybdate only occurs at Mo(VI) concentrations over 10^{-4} M (Davantes et al., 2017, Mitchell, 2009, Ozeki et al., 1988), there is not sufficient evidence to include a Mo-Mo shell for 0.6×10^{-4} M Mo(VI)-adsorbed hematite samples in acidic systems. Davantes et al. (2017) performed a series of simulations (DFT+U) to determine the spectroscopic characteristics of Mo(VI) monomer/polymers adsorbed on the hematite surface. They indicated that the surface species is different from the polymolybdate formed in solution, and suggest that a 3D polymer consisting of 3–5 Mo(VI) polyhedral have ATR-FTIR bands close to experimentally observed values. These 3D polymer structures were modelled with 3–5 Mo(IV) ions with a mixture of edge and corner sharing polyhedra (Davantes et al., 2017). The Mo-Mo distances for the edge sharing and corner sharing octahedra/polyhedra were 3.25–3.31 Å and 3.53–3.64 Å, respectively. These distances are consistent with the Mo-Mo distances and coordination numbers determined from our EXAFS analysis, therefore support the formation of a polymeric species contain a small number of Mo(VI) ions (i.e. 3–5) on the surface of hematite with both corner sharing and edge sharing octahedra (e.g. Figure 4-4B). The reason for the formation of the polymeric species on the surface is unclear, but may be due to the distances between the oxygen atoms on the hematite (0001) surface, which are close to the values in poly-oxomolybdate (Davantes et al., 2017).

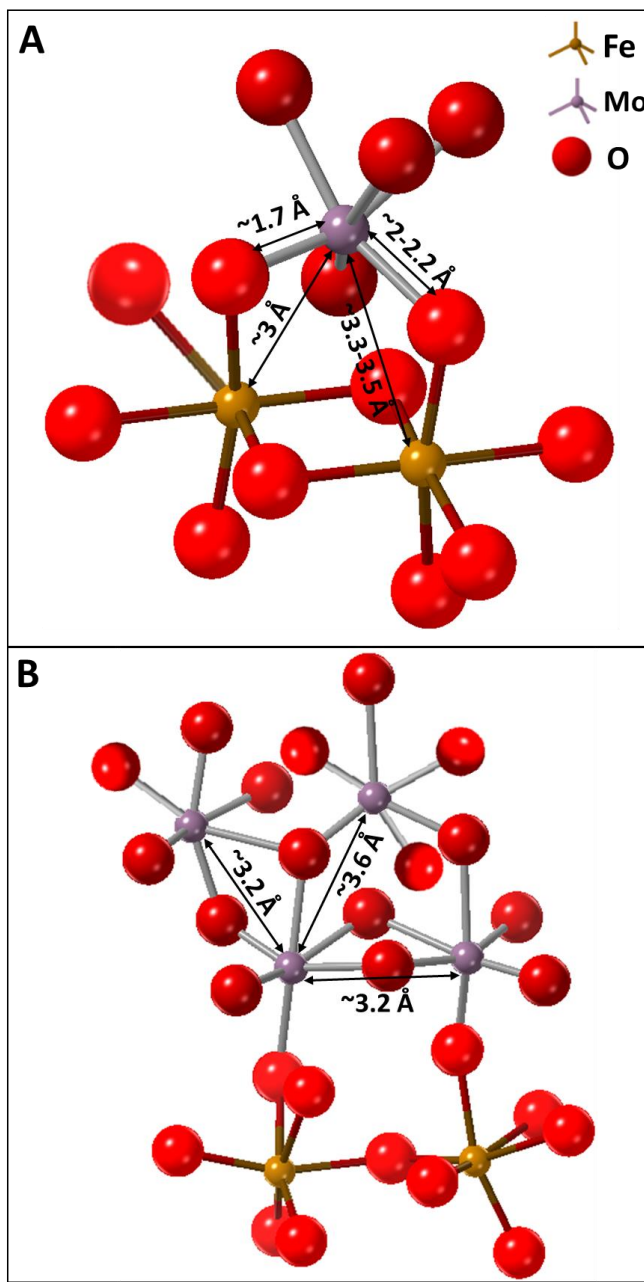


Figure 4-4 Mo(VI) octahedral on the iron octahedral structure of hematite surface via inner-sphere corner-sharing bidentate binuclear adsorption complex. A. Mono-molybdate adsorbed on the hematite surface. B. Polymolybdate adsorbed on the hematite surface.

Table 4-2 Mo(VI) EXAFS fitting parameters.

Samples	path Mo-	CN ^a	R (Å) ^b	σ^2 (Å ²) ^c	S0 ² ^d	R-factor ^e
0.6 x 10 ⁻⁴ , pH4	O	3	1.72(1)	0.003(1)	0.800	0.012
	O	1.5	2.10(2)	0.003(1)	0.800	
	O	1.5	2.27(2)	0.003(1)	0.800	
	Fe	1	2.95(2)	0.006(2)	0.800	
	Fe	1	3.33(3)	0.006(2)	0.800	
0.6 x 10 ⁻⁴ , pH7	O	2.6	1.71(2)	0.003(1)	0.800	0.023
	O	1.6	2.07(2)	0.003(1)	0.800	
	O	1.2	2.29(3)	0.003(1)	0.800	
	Fe	1	2.95(3)	0.006(3)	0.800	
	Fe	1	3.41(4)	0.005(4)	0.800	
5 x 10 ⁻⁴ , pH4	O	2	1.68(1)	0.003(1)	0.800	0.020
	O	2	2.03(1)	0.003(1)	0.800	
	O	2	2.22(2)	0.003(1)	0.800	
	Mo	2	3.20(2)	0.002(1)	0.800	
	Mo	1	3.61(2)	0.007(1)	0.800	
5 x 10 ⁻⁴ , pH7	O	2.6	1.73(1)	0.001(1)	0.800	0.024
	O	1.6	2.12(2)	0.001(1)	0.800	
	O	1.2	2.28(3)	0.001(1)	0.800	
	Fe	1	2.98(3)	0.006(4)	0.800	
	Fe	1	3.28(4)	0.007(6)	0.800	

^acooperation number (CN), ^b Mo bond distance (R (Å)), ^c Debye-Waller factors (σ^2), ^d amplitude factor (S0²), ^e the percentage of misfit between the data and theory (R-factor) (Ravel and Newville, 2005).

4.5 Conclusions

This study has used a multi-technique approach to show that pH and Mo(VI) concentration are key variables when controlling the speciation of adsorbed Mo(VI) to the surface of hematite.

A multi-technique approach including PHREEQC geochemical modelling, ATR-FTIR and XAS analyses holistically show that at low concentration (0.6×10^{-4} M Mo(VI)) and neutral to high pH Mo(VI) forms an octahedrally coordinated inner-sphere corner-sharing bidentate binuclear surface adsorption complex with polymeric species forming at low pH (≤ 4) and higher concentrations (5×10^{-4} M Mo(VI)). These are the first direct observations of octahedrally coordinated Mo(VI) adsorption species on hematite, and support the conclusions from previous isotopes measurements and DFT+U modelling studies that indicate Mo(VI) transitions from a tetrahedral MoO_4^{2-} solution complex to a octahedrally coordinated adsorbed species on hematite. This information has broad implications for the mobility and transport of Mo as a contaminant in the environment.

Supporting Information for Chapter 4

Adsorption of octahedral mono-molybdate and poly-molybdate onto hematite: A multi-technique approach

JING ZHANG,[†] VICTORIA S. COKER,[†] J. FREDERICK W. MOSSELMANS,[‡] AND SAMUEL SHAW

x,†

[†] Williamson Research Centre for Molecular Environmental Science, Department of Earth and Environmental Sciences, The University of Manchester, Manchester M13 9PL, U.K.

[‡] Diamond Light Source Ltd., Diamond House, Harwell Science and Innovation Campus, Didcot, Oxfordshire OX11 0DE, U.K.

This document provides supporting information for the study covering additional XRD, BET, Langmuir isotherm model, TEM, XPS, PHREEQC, ATR-FTIR and XAS analysis.

SI 4-1. XRD and BET analysis for hematite

XRD indicates that the synthesized adsorbent is pure hematite (Figure SI4-1). The BET surface area of the hematite obtained is $47.2 \pm 0.3 \text{ m}^2/\text{g}$.

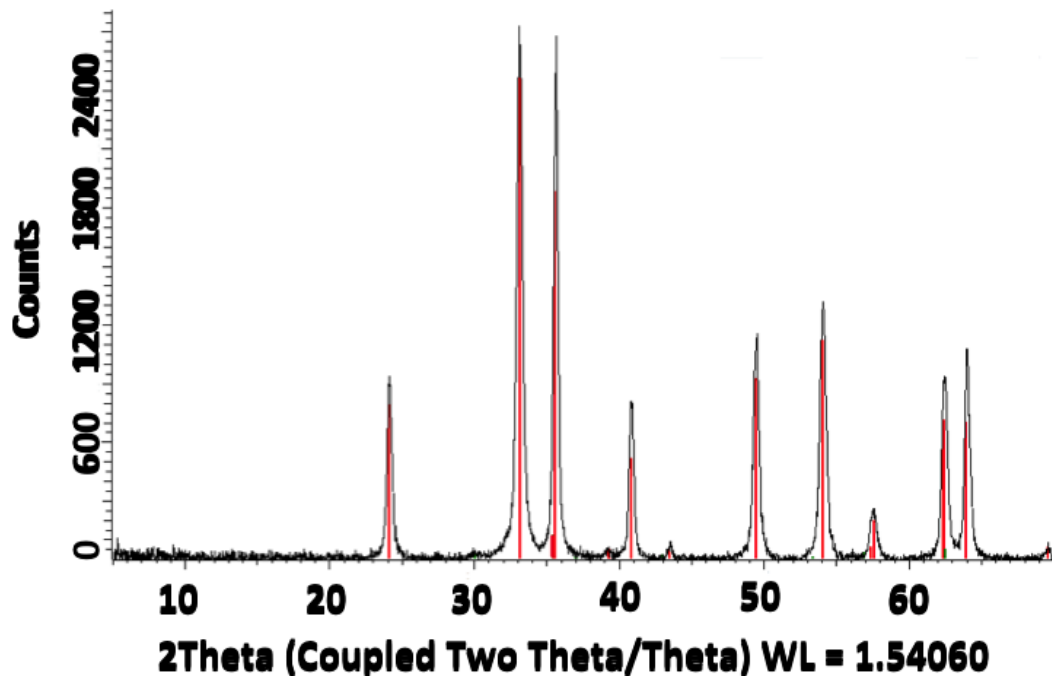


Figure SI4-1 X-ray diffraction of synthesized hematite.

SI 4-2. Aqueous Solution analysis

Isotherm data for Mo(VI) absorption to hematite was collected at pH 7, for both ionic strengths of NaCl, using an initial Mo(VI) concentration between 0.01×10^{-4} - 2×10^{-3} M (Figure SI4-2). The Langmuir model (Eq. 4-1) gives a good fit to the data ($R = 0.996$ and 0.975) at initial Mo(VI) concentrations of less than 6×10^{-4} M for both the 0.1 and 0.01 M NaCl solutions. The maximum adsorption capacity (Q_{\max}) for Mo(VI) adsorption to hematite was 36.7 mg Mo/g adsorbent in 0.1 M NaCl solution and 23.2 mg/g in 0.01 M NaCl solution, respectively.

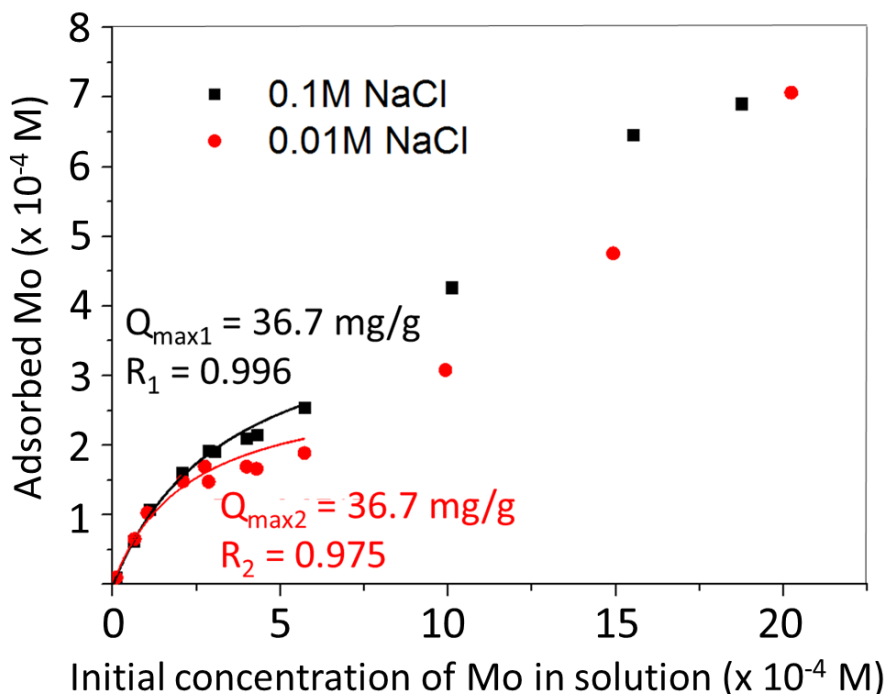


Figure SI4-2 Mo(VI) isotherm adsorption to hematite in 0.1 M (dark spot) and 0.01 M (red spot) NaCl solutions at initial Mo(VI) concentration of 0.01×10^{-4} - 2×10^{-3} M (0.1 - 200 ppm) at pH 7. Langmuir isotherm fitting for Mo(VI) adsorption onto hematite at initial Mo(VI) concentration less than 6×10^{-4} M (60 ppm). The equilibrium of the Langmuir isotherm model is $Q_e = Q_{max} \times b \times C_e / (1 + b \times C_e)$, where Q_e (mg Mo/g adsorbent) is the adsorbed amount at equilibrium. Q_{max} (mg/g) is the maximum adsorption capacity. b (l/mg) is a constant. C_e is the residual adsorbent concentration in solution at equilibrium (Verbinnen et al., 2012).

Si 4-3. TEM

TEM and concurrent EDX elemental mapping (Figure SI4-3) were performed for 0.6×10^{-4} M Mo(VI)-adsorbed hematite (0.03 M Mo(VI) concentration on the solid) at pH 7 in 0.01 M NaCl solution. Images (Figure SI4-3(a) (b)) show the iron oxide particles were present as rhombohedral platelet nanoparticles <50 nm in size. EDX spectra and mapping show a small amount of Mo is present in an evening distributed over hematite particles surface evenly (Figure SI4-3(d)). These TEM observations indicated no precipitation of Mo phases and

indicating adsorbed to hematite is the dominant Mo sequestration mechanism under these conditions.

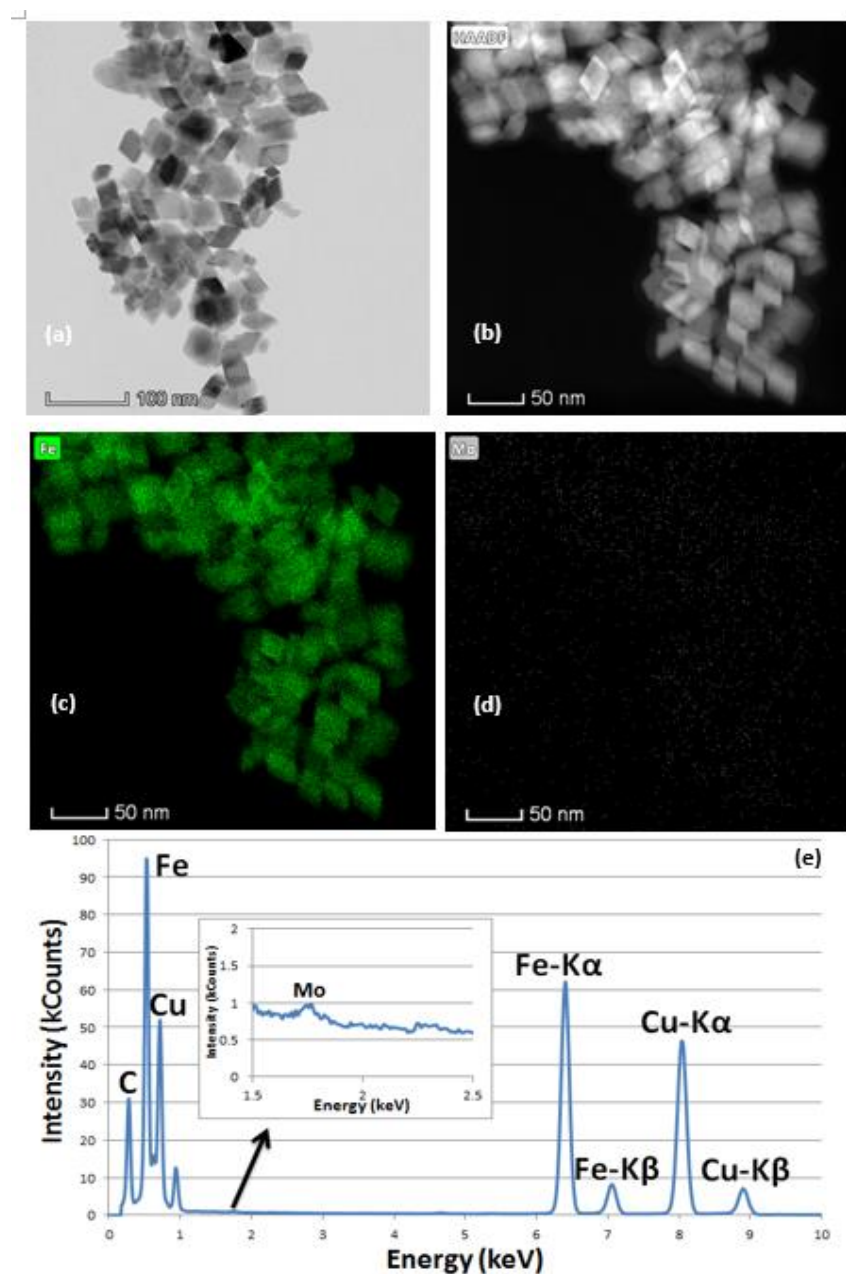


Figure SI4-3 TEM characterization of samples from 0.6×10^{-4} M Mo(VI) in solution adsorption to hematite in 0.01 M NaCl solution at pH 7.

SI 4-4. X-ray photoelectron spectroscopy (XPS)

Mo(VI)-adsorbed hematite samples at pH 3, 4, 5.5, 7, and 8 and Mo(VI) concentration of 0.6×10^{-4} M were drop casted onto Si pieces (1x1 cm) using a solvent (isopropyl alcohol) prior to

loading into the XPS system. The Mo 3d spectra were charge corrected to the C 1s signal which was shifted to the accepted value of 284.8 eV as seen below in Figure SI4-4A. Figure SI4-4B displays the Mo 3d spectra for all the samples analysed. As can be seen from the spectra following charge correction outlined above, all samples appear to be in the same oxidation state as indicated by the common binding energy positions of the Mo 3d doublet peaks. This means Mo(VI) oxidation state has not been changed when adsorbed to hematite in all systems.

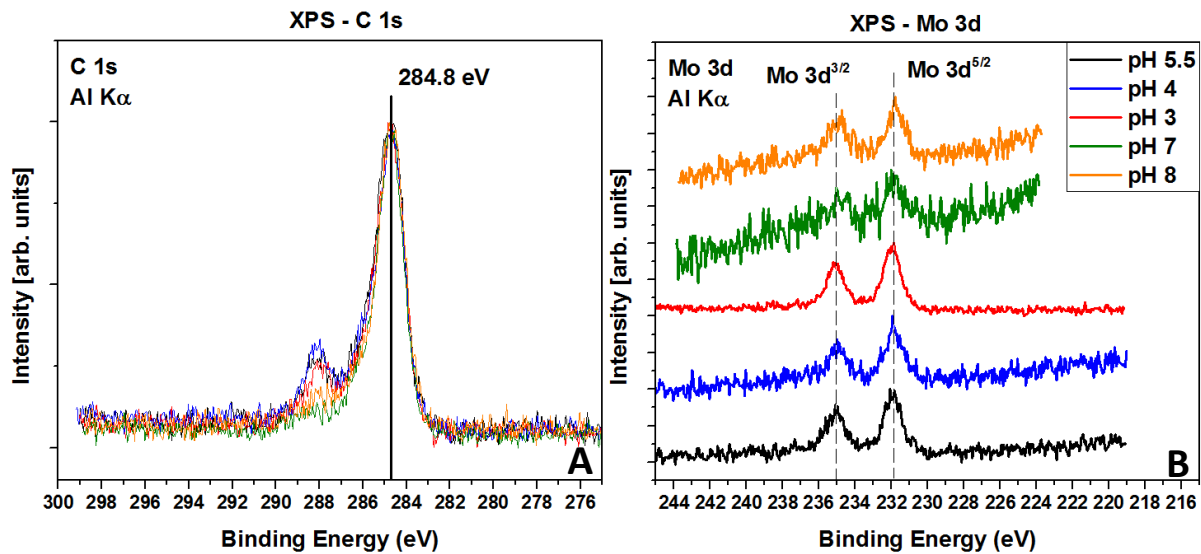


Figure SI4-4 A. C 1s spectra of the analysed hematite samples. Charge correction was applied to the spectra to line the main C-C feature to 284.8 eV. B. Mo 3d spectra for hematite samples. All spectra were charge referenced to the C 1s spectra.

SI 4-5. PHREEQC

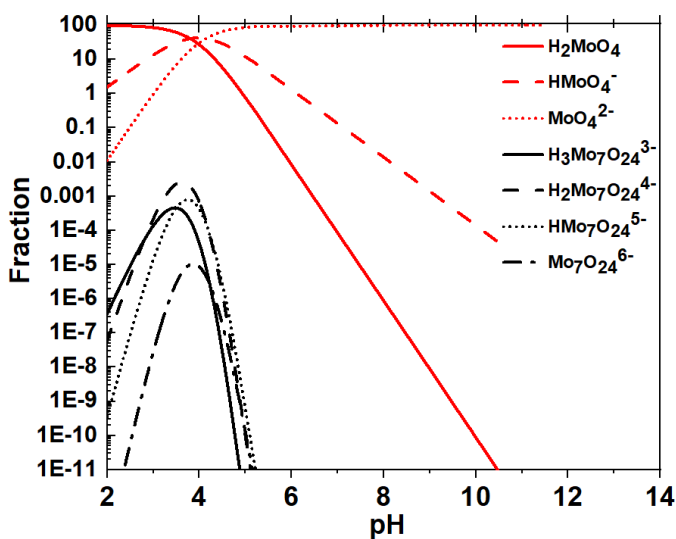


Figure SI4-5 PHREEQC modeling on Mo speciation at pH between 2 to 11 at Mo concentration of 0.6×10^{-4} M in 0.01 M NaCl.

SI 4-6. ATR-FTIR

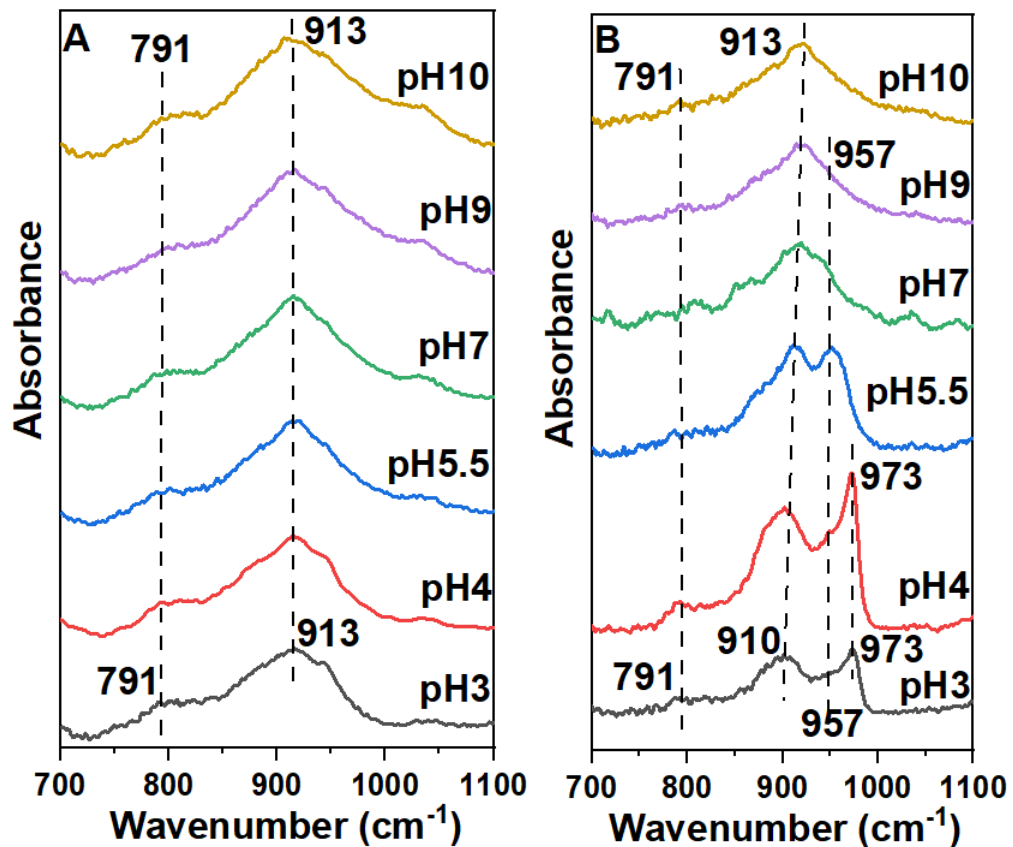


Figure SI4-6 ATR-FTIR analysis for 0.6×10^{-4} M Mo(VI)-adsorbed hematite (A) and 2×10^{-3} M Mo(VI)-adsorbed hematite (B).

Table SI4-1 ATR-FTIR spectra for adsorbed Mo(VI) ions.

Samples	Wavenumber (cm ⁻¹)				
[Mo]=5 x 10 ⁻⁴ M, pH 3	791	896	913	957	972
[Mo]=5 x 10 ⁻⁴ M, pH 4	791	896	913	957	972
[Mo]=0.6 x 10 ⁻⁴ M, pH 4	791		913		
[Mo]=2 x 10 ⁻³ M, pH 4	791	896	910	957	973
Previous Paper Samples (Davantes et al., 2017)	Wavenumber (cm ⁻¹)				
[Mo]=10 ⁻³ M, pH 3	791	887	908	957	974

SI 4-7. XAS

Figure SI4-7 shows XANES analysis for Mo standards and 0.6 x 10⁻⁴ M Mo(VI)-adsorbed hematite at pH 3-10 in 0.01 M NaCl. The pre-edge peak position (20004 eV) and intensity for samples across the whole pH range are consistent with the octahedral coordinated bamfordite (FeMo₂O₆(OH)₃·H₂O) and heptamolybdate ((NH₄)₆Mo₇O₂₄•4H₂O). This means Mo(VI) octahedrally adsorbed to hematite surface at concentration of 0.6 x 10⁻⁴ M. The overall structure of heptamolybdate, especially at the energy from 20020 to 200052 eV, is different from that of samples at pH 3-10, indicating the bonding structure of samples are not consistent with heptamolybdate.

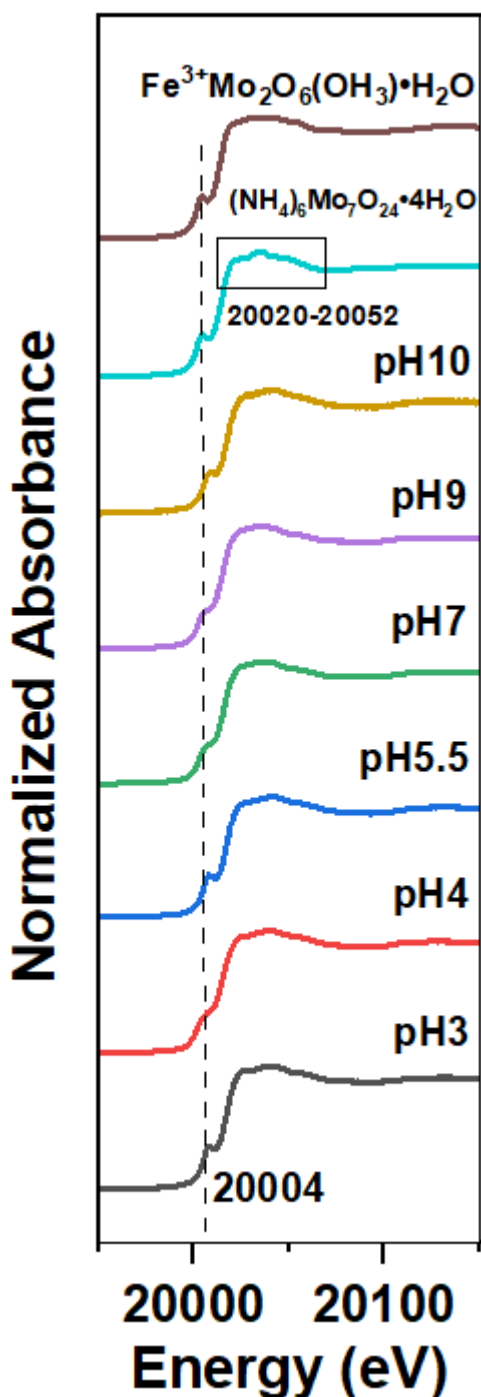


Figure SI4-7 XANES analysis for Mo standards and 0.6×10^{-4} M Mo(VI)-adsorbed hematite at pH 3-10 in 0.01 M NaCl.

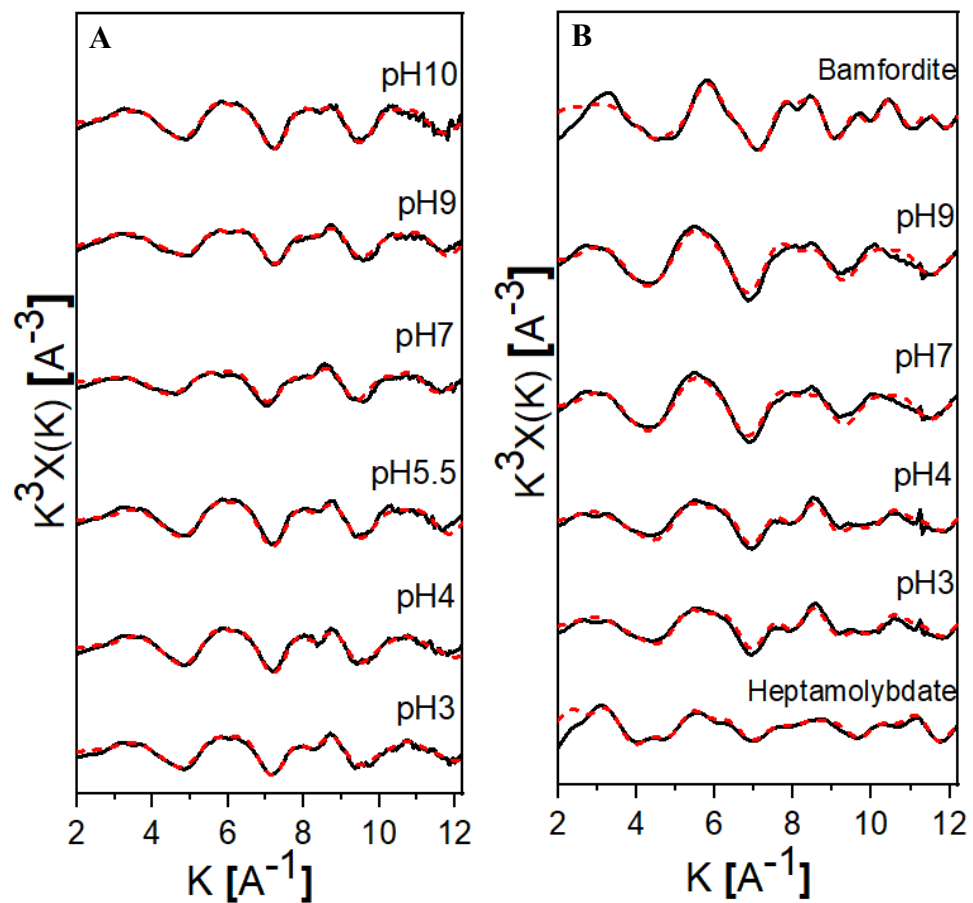


Figure SI4-8 Fourier transform (black lines) and its EXAFS fitting (red dash) of 0.6×10^{-4} M (A) and 5×10^{-4} M (B) Mo(VI)-adsorbed hematite at pH 3-10 in 0.01 M NaCl and Mo(VI) standards.

Table SI4-2 Mo(VI) EXAFS fitting parameters.

Samples	path Mo-	CN ^a	R (Å) ^b	σ2 (Å ²) ^c	S0 ² ^d	R-factor ^e
[Mo]=5 x 10 ⁻⁴ M, pH 3	O	2	1.68(1)	0.003(1)	0.800	0.019
	O	2	2.03(1)	0.003(1)	0.800	
	O	2	2.22(2)	0.003(1)	0.800	
	Mo	2	3.21(2)	0.007(1)	0.800	
	Mo	1	3.62(2)	0.001(1)	0.800	
[Mo]=5 x 10 ⁻⁴ M, pH 9	O	3	1.74(1)	0.001(1)	0.800	0.014
	O	1.5	2.12(2)	0.001(1)	0.800	
	O	1	2.27(3)	0.001(1)	0.800	
	Fe	1	2.98(3)	0.005(3)	0.800	
	Fe	1.2	3.31(4)	0.009(6)	0.800	
[Mo]=0.6 x 10 ⁻⁴ M, pH 3	O	3	1.71(1)	0.004(1)	0.800	0.014
	O	1.5	2.07(2)	0.004(1)	0.800	
	O	1.5	2.25(2)	0.004(1)	0.800	
	Fe	1	2.95(3)	0.007(2)	0.800	
	Fe	1	3.33(3)	0.007(2)	0.800	
[Mo]=0.6 x 10 ⁻⁴ M, pH 5.5	O	3	1.72(1)	0.002(1)	0.800	0.017
	O	1.5	2.09(2)	0.002(1)	0.800	
	O	1.5	2.25(2)	0.002(1)	0.800	
	Fe	1	2.95(3)	0.006(2)	0.800	
	Fe	1	3.32(3)	0.006(2)	0.800	
[Mo]=0.6 x 10 ⁻⁴ M, pH 9	O	3	1.73(1)	0.004(1)	0.800	0.013
	O	1.5	2.03(1)	0.004(1)	0.800	
	O	1	2.21(2)	0.004(1)	0.800	
	Fe	1	3.07(2)	0.003(2)	0.800	
	Fe	1.2	3.49(5)	0.008(5)	0.800	
[Mo]=0.6 x 10 ⁻⁴ M, pH 10	O	3	1.73(1)	0.002(1)	0.800	0.015

	O	1.5	2.11(2)	0.002(1)	0.800	
	O	1	2.29(5)	0.002(1)	0.800	
	Fe	1	2.95(3)	0.006(4)	0.800	
	Fe	1	3.32(5)	0.006(6)	0.800	
Bamfordite	O	3	1.74(1)	0.003(1)	0.800	0.029
(Fe(III)Mo(VI) ₂ O ₆ (OH ₃)•H ₂ O)	O	3	2.14(2)	0.004(2)	0.800	
	Fe	2.5	3.82(2)	0.002(1)	0.800	
	Mo	1	3.38(2)	0.004(2)	0.800	
Heptamolybdate	O	2.5	1.73(1)	0.004(1)	0.800	0.029
((NH ₄) ₆ Mo ₇ O ₂₄ •4H ₂ O)	O	2	1.97(1)	0.004(1)	0.800	
	O	1.3	2.23(2)	0.004(1)	0.800	
	Mo	3	3.25(1)	0.006(1)	0.800	
	Mo	3	3.43(1)	0.006(1)	0.800	

^acooperation number (CN), ^b Mo bond distance (R (Å)), ^c Debye-Waller factors (σ^2), ^d amplitude factor (S0²), ^e the percentage of misfit between the data and theory (R-factor) (Ravel and Newville, 2005).

5. A Multi-technique Approach on the Investigation of Mono- and Poly-vanadate (VO_4^{3-}) Adsorption to Hematite

Jing Zhang,[†] Victoria Coker,[†] J. Frederick W. Mosselmans,[‡] Luís A. E. Batista de Carvalho,[§] and Samuel Shaw^{*,†}

[†] Williamson Research Centre for Molecular Environmental Science, Department of Earth and Environmental Sciences, The University of Manchester, Manchester M13 9PL, U.K.

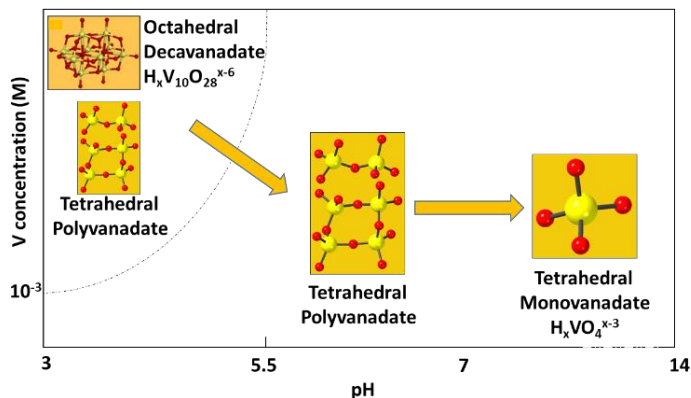
[‡] Diamond Light Source Ltd., Diamond House, Harwell Science and Innovation Campus, Didcot, Oxfordshire OX11 0DE, U.K.

[§] “Química-Física Molecular” R&D Unit, Department of Chemistry, University of Coimbra, 3004-535 Coimbra, Portugal.

5.1 Abstract

Vanadium (V) is a widespread trace element in the environment.

However, at high concentration, it can be toxic to marine systems and terrestrial plants due to anthropogenic emission such as



mining activities and fossil fuels. The contamination of the environment by vanadium is a growing problem, however, the understanding of V geochemistry is relatively poor. The aims of this study were to understand the molecular scale chemical forms (e.g. monomers or polymers), adsorption behaviour and bonding mechanisms of V(V) onto hematite as a function of geochemical factors (pH 3-12 and $[\text{V(V)}] 2 \times 10^{-6} - 4 \times 10^{-3} \text{ M}$), applying a multi-technique approach including aqueous chemical analysis, Attenuated Total Reflection-Fourier Transform Infrared Spectroscopy (ATR-FTIR), PHREEQC geochemical modelling, and X-ray

Absorption Spectroscopy (XAS). From these data tetrahedral monovanadate presents via tetrahedral corner-sharing bidentate surface complex at 1.2×10^{-3} M V(V) and pH 9 and 1.2×10^{-4} M V(V) in all systems when adsorbed to hematite, while octahedral decavanadate forms at a higher V(V) concentration of 1.2×10^{-3} M and pH up to 5.5. The coordination environment changed gradually from a mixture of octahedrally and tetrahedrally coordinated V at pH 3 to dominantly tetrahedral monovanadate at pH 9, and at pH 7 an intermediate species that is polymerized but predominantly in tetrahedral coordination is observed. Our results demonstrate the pH and initial V concentration dependance of the species of V that will form at the surface of hematite and predict the environmental mobility of V(V) under a number of geochemical scenarios.

Keywords: Vanadium, Iron oxide, Surface adsorption, XANES, EXAFS, ATR-FTIR, octahedral, tetrahedral, decavanadate

5.2 Introduction

Vanadium (V) is a widespread element in the earth's crust (WHO, 2000, Vessey et al., 2020), and is naturally present within soils, with an average concentration of 135 mg/kg, ranking V the 5th most abundant element amongst transition metals in the earth crust (Watt et al., 2018). At high concentrations, related to contaminated land, V can have a detrimental impact on the environment, posing a risk to plant growth by causing chlorosis and potential detrimental effects for human health (e.g. increasing blood pressure, reducing the number of red blood cells and neurological effects) (Watt et al., 2018, Wisawapipat and Kretzschmar, 2017, Larsson et al., 2017). When the concentration of V is over 100 µg/L, it can become toxic in marine systems, whereas studies have shown it can become toxic for terrestrial plants above 10 mg/kg in soil (Vessey and Lindsay, 2020). Global anthropogenic activities (such as fossil fuel burning, mining, steel making etc.) are important factors that have led to the increasing concentrations

of V in soil, water and atmospheric systems . V has the highest anthropogenic enrichment factor (AEF) of all the trace elements in the atmosphere and the fourth highest AEF in rivers, primarily resulting from the increasing usage of fossil fuels, particularly crude oil and coal, which account for 56% and 26% of human V discharges respectively (Watt et al., 2018, White and Levy, 2021). The usage of coal increased from 27.4 TW h in 2000 to 43.9 TW h in 2019 and the value for crude oil increased from to 42.9 TW h in 2000 to 53.6 TW h in 2019 (White and Levy, 2021). The rise in anthropogenic discharge of V to the environment has been attributed to the increase of V-rich industrial wastes including steel slags and ash from waste incineration (Watt et al., 2018). Typically, it was estimated that V air emissions from coal combustion aerosols contribute $1\text{--}4 \times 10^9$ g per year and petroleum aerosols contribute $100\text{--}280 \times 10^9$ g per year to the atmosphere (White and Levy, 2021). V concentrations range from 10 to 220 mg/kg in soils, and up to \sim 3500 mg/kg in contaminated soils in mining areas (Watt et al., 2018, Nakamura and Haruyama, 1978, Ceci et al., 2015). In drinking-water, V can range in concentration from 0.2 to over 100 $\mu\text{g/L}$, however it is typically 1–6 $\mu\text{g/L}$, depending on geographical location (WHO, 2000). In many subsurface environmental systems the environmental behaviour i.e. mobility and bioavailability of V is controlled by the molecular scale chemical forms (e.g. monomers or polymers) and adsorption to key environmental mineral phases (e.g. Iron (oxyhydr)oxide minerals). Understanding these processes as a function of geochemical conditions (e.g. pH and V(V) concentration) is key to predicting the environmental behaviour of this contaminant.

V(IV) and V(V) are the predominant oxidation states in subsurface environmental systems (e.g. soils) and the most stable and soluble species under oxic conditions (Vessey et al., 2020, Watt et al., 2018, Wisawapipat and Kretzschmar, 2017, Larsson et al., 2017, Vessey and Lindsay, 2020). V(IV) exists mainly as the oxocation vanadyl ($\text{V(IV)}\text{O}^{2+}$) in aqueous solution, which is stable at pH below 6, while $\text{HV(IV)}_2\text{O}_5^-$ presents at pH over 6 (Zhang et al., 2013,

Nakamura and Haruyama, 1978, Ceci et al., 2015). V(V) occurs as the mobile oxyanions $\text{HV}(\text{V})\text{O}_4^{2-}$, $\text{V}(\text{V})\text{O}_4^{3-}$ or $\text{H}_2\text{V}(\text{V})\text{O}_4^-$. Cationic V(V) species (such as $\text{V}(\text{V})\text{O}_2^+$), occurring under low pH conditions ($\text{pH} < 3.6$), and are regarded as the most toxic V species (Larsson et al., 2017, Ceci et al., 2015). In addition, V(V) is readily reduced to V(IV) near neutral pH under anoxic conditions, often via biologically induced processes (Vessey et al., 2020, Wisawapipat and Kretzschmar, 2017, Larsson et al., 2017, Crans et al., 1998, Martin and Kaplan, 1998). V(V) speciation in solution depends on a number of factors including pH, V(V) concentration and ionic strength. The formation of polyvanadate occurs in a number of different scenarios including higher concentration and lower pH. For example, decavanadate ($\text{H}_x\text{V}(\text{V})_{10}\text{O}_{28}^{x-6}$) and metavanadate ($\text{V}(\text{V})\text{O}_3_x^{x-}$) can form at higher concentrations ($\sim 100 \mu\text{M}$) and acidic conditions ($\text{pH} < 6$), while monovanadate is the dominant species at pH over 7 (Marques et al., 2017, Vessey et al., 2020, Połedniok and Buhl, 2003, Wisawapipat and Kretzschmar, 2017, Peacock and Sherman, 2004, Blackmore et al., 1996). V(V) in monovanadate species are tetrahedral coordinated, and so are V(V) ions in most polyvanadates e.g. $\text{H}_3\text{V}(\text{V})_2\text{O}_7^-$, $\text{V}(\text{V})_3\text{O}_9^{3-}$, $\text{V}(\text{V})_4\text{O}_{12}^{4-}$, with the exception of octahedrally coordinated V(V) in decavanadate with 10 V atoms situated within three distinct sites, including 6 V atoms in the middle (2 of them situated in the center (site a), surrounded by 4 atoms (site b)), and then capped by 2 atoms at top and bottom (site c) (Vessey et al., 2020). In many contaminated subsurface systems the mobility and bioavailability of V is controlled by adsorption to environmentally abundant mineral phases (e.g. iron and aluminum hydrous oxides) within soils and sediments. Previous studies of V(V) adsorption to Fe(III) (oxyhydr)oxide mineral phases e.g. hematite ($\alpha\text{-Fe(III)}_2\text{O}_3$) (Vessey et al., 2020), goethite ($\alpha\text{-Fe(III)}\text{OOH}$) (Peacock and Sherman, 2004), ferrihydrite ($(\text{Fe(III)})_2\text{O}_3 \bullet 0.5\text{H}_2\text{O}$) (Vessey et al., 2020, Larsson et al., 2017, Brinza et al., 2008, Vessey and Lindsay, 2020, Blackmore et al., 1996, Naeem et al., 2007) indicate decreasing adsorption with increasing pH, with low level of adsorption above pH 6.

Attenuated total reflectance–Fourier transform infrared spectroscopy (ATR-FTIR) and PHREEQC geochemical modelling analysis of V(V)-adsorbed onto the surface of ferrihydrite and hematite at V(V) concentrations between 50-2000 μM and pH 3-6 indicate the presence of both (poly)vanadate species and monomeric surface complexes. At pH above 10, the inner-sphere adsorption of HVO_4^{2-} was proposed, exhibiting C_{3v} symmetry, corresponding with ATR-FTIR bands at 877 cm^{-1} (Vessey et al., 2020, Peacock and Sherman, 2004). At pH 5-6 and V(V) concentration less than 500 μM , the low surface loading leads to the formation of inner-sphere tetrahedral monodentate and bidentate adsorption complexes (dominantly tetrahedral H_2VO_4^-) on the ferrihydrite and hematite surfaces, corresponding with peaks at the lower wavenumber range from 650-850 cm^{-1} . Polyvanadate (e.g. $\text{H}_2\text{V}_2\text{O}_7^{2-}$ and $\text{V}_4\text{O}_{12}^{4-}$), produced IR bands at 930 and 968 cm^{-1} , are the dominant aqueous species with increasing V(V) concentration over 1000 μM and adsorbed on the hematite surface via tetrahedral coordinated monodentate complex at pH 3-6, while polymers were identified on the ferrihydrite surface only at pH 3-4. This indicates the hematite surface promotes the formation of polymeric complexes to a higher degree than ferrihydrite (Vessey et al., 2020, Davantes et al., 2017). At pH 3-4, octahedral decavanadate including $\text{H}_3\text{V}_{10}\text{O}_{28}^{5-}$, $\text{NaHV}_{10}\text{O}_{28}^{5-}$, and $\text{HV}_{10}\text{O}_{28}^{6-}$ with a C_{2v} symmetry and IR bands occurring at $\sim 980 \text{ cm}^{-1}$, were dominant aqueous species adsorbed on hematite and ferrihydrite surface, constrained to monodentate adsorption complex because of its rigid and large structure (Vessey et al., 2020). At pH 3 and V(V) concentrations lower than 250 μM , VO_2^+ onto hematite and ferrihydrite was via outer-sphere adsorption and potentially weak inner-sphere monodentate interactions (Vessey et al., 2020, Cornell and Schwertmann, 2004).

The EXAFS analysis of V(V)-adsorbed to goethite and ferrihydrite at pH 3-9 indicated a tetrahedrally coordinated adsorption complex (Peacock and Sherman, 2004, Larsson et al., 2017, Brinza et al., 2015) and suggested that protonated VO_4^{3-} as $\text{VO}_2(\text{OH})_2^-$ or $\text{VO}_3(\text{OH})^{2-}$ are

binding to the surface (Peacock and Sherman, 2004). Distances of 3.2-3.3 Å for V-Fe shells provided evidence of the bidentate corner-sharing adsorption complex to the goethite surface at pH 3-9 (Peacock and Sherman, 2004). However, for V(V) adsorption to ferrihydrite, a distance of 2.8 Å was fitted for the V-Fe shell suggesting an edge-sharing bidentate adsorption complex (almost V-O₂-Fe surface complex) (Larsson et al., 2017). This edge-sharing bidentate structure is different from that described for goethite and is thought to be due to the larger proportion of singly coordinated groups on Fe(III) octahedral of ferrihydrite, relative to goethite that have the ability to form bidentate edge surface complexes (Larsson et al., 2017). However, there are currently no EXAFS studies of V(V) polymers sorption onto iron oxide surfaces.

The aims of this project are to determine the adsorption behaviour and local coordination environment of V(V) to hematite under varying geochemical conditions including pH (3-14), ionic strength and initial V concentrations ($2 \times 10^{-6} - 4 \times 10^{-3}$ M). This study applied a multi-technique approach including aqueous chemical analysis, PHREEQC geochemical modelling, Attenuated Total Reflection-Fourier Transform Infrared Spectroscopy (ATR-FTIR), and X-ray Absorption Spectroscopy (XAS), indicating tetrahedral monovanadate ($H_xVO_4^{x-3}$) and polyvanadate ($V(V)O_3)_x^{x-}$) (with the exception of decavanadate ($H_xV(V)_{10}O_{28}^{x-6}$)) species sorb to the hematite surface at high V(V) concentration (1.2×10^{-3} M) and pH > 7 and low V(V) concentration (1.2×10^{-4} M) in all systems, while decavanadate composed a significant proportion of the sorbed species at high V(V) concentration (1.2×10^{-3} M) and pH up to 5.5.

5.3 Experimental Methods

Synthesis and absorption experiments. Hematite (α -Fe₂O₃) was obtained using the synthesis method from Schwertmann and Cornell (Schwertmann and Cornell, 2000b). The powder X-ray Diffraction (pXRD) (Bruker D8 Advance) using a Cu k-alpha source with a wavelength of

1.5406 Å, was used in order to assess the purity of the synthesized hematite. The surface area of the hematite was analysed by Brunauer-Emmett-Teller (BET) analysis (Micromeritics Gemini) and indicated the surface area is $47.2 \pm 0.3 \text{ m}^2/\text{g}$.

The adsorption of vanadium to hematite was set up by mixing $1.2 \times 10^{-4} \text{ M}$ or $1.2 \times 10^{-3} \text{ M}$ V(V) (Na_3VO_4) with 2 g/L hematite in 30 ml of 0.1M or 0.01 M sodium chloride (NaCl) solution to give a maximum of 3000 ppm or 30000 ppm V (V) on the hematite particles, respectively. Blank experiment was performed by adding $1.2 \times 10^{-4} \text{ M}$ or $1.2 \times 10^{-3} \text{ M}$ sodium vanadate (Na_3VO_4) in 30 ml 0.1M or 0.01 M sodium chloride (NaCl) solution to check the initial V(V) concentration. The pH range was adjusted from 3 to 13 using 0.1 M hydrochloric acid (HCl) or 0.1-1 M sodium hydroxide (NaOH). In addition, isotherm adsorption experiments were performed at an initial V(V) concentration of $2 \times 10^{-6} - 4 \times 10^{-3} \text{ M}$ at pH 7 in 0.1 M or 0.01 M NaCl solution. All experiments were rotated on a rotor mixer with constant speed of 32 rpm for 24 h. After 24 h, an aliquot of supernatant was filtered using a $0.22 \mu\text{m}$ syringe filter (Merck Millipore) for Inductively Coupled Plasma Atomic Emission Spectroscopy (ICP-AES) (PerkinElmer Optima 5300 dual view) analysis of aqueous total vanadium.

Thermodynamic modelling using PHREEQC (version 3.3.5) was performed to characterise the V(V) solution speciation and saturation state of the experimental solutions with respect to V solid phases using the minteq.v4.dat database (Winstanley et al., 2019, Vessey et al., 2020). A Langmuir isotherm was used to model the observed adsorption process using the following equilibrium:

$$Q_e = Q_{\max} \times b \times C_e / (1 + b \times C_e) \quad (5-1)$$

Where Q_e (mg Mo/g adsorbent) is the adsorbed amount at equilibrium. Q_{\max} (mg/g) is the maximum adsorption capacity. b (l/mg) is a constant. C_e is the residual adsorbent concentration in solution at equilibrium (Verbinnen et al., 2012).

Attenuated Total Reflection-Fourier Transform Infrared Spectroscopy (ATR-FTIR) (Perkin Elmer Frontier ATR FTIR spectrometer) with diamond crystal was used to analyse V(V)-adsorbed hematite particles at pH 3, 4, 5.5, 7, 9, 12, 13.5 at an initial V(V) concentration of 1.2×10^{-3} M. Spectral resolution was 4 cm^{-1} and spectra were an average of 20 scans. The results were background subtracted and analysed using Know-it-all software and then fitted peaks using Gaussian function in Origin.

X-ray Absorption Spectroscopy (XAS). X-ray Absorption Near Edge Structure (XANES) and Extended X-ray Absorption Fine Structure (EXAFS) were collected on V(V)-adsorbed hematite samples (maximum concentration of 3000 ppm and 30000 ppm V(V) on solid surface with ionic strength of 0.01 M NaCl at pH 3, 4, 5.5, 7, 9, 12) at the Diamond Light Source (DLS) Ltd. (Oxford, UK) on Beamline I20 at the V (5.46 keV) K-edge. Samples were formed into pellets and measured in a liquid nitrogen cryostat (77 K). The beamline is equipped with a Si (111) monochromator and data was collected in fluorescence mode using a 64 element Ge detector (Townsend et al., 2019, Diaz-Moreno et al., 2018). Standards for sodium vanadate ($\text{Na}_3\text{V(V)O}_4$), vanadium pentoxide ($\text{V(V)}_2\text{O}_5$), and decavanadate ($\text{V}_{10}\text{O}_{28}^{6-}$) were collected in transmission mode at room temperature. Glitches were removed by EXAFS rewindowing through setting lower bound of 446 and upper bound of 487 in Dawn software. Demeter suite software (Athena and Artemis) was used to process the data including background subtraction, calibration, data normalization, and data fitting (Ravel and Newville, 2005). The validity of the adding shells were tested applying F-test (Downward et al., 2007).

5.4 Results and Discussion

Figure 5-1A shows the results for 1.2×10^{-4} M and 1.2×10^{-3} M V(V) adsorption to hematite as function of pH in 0.1 and 0.01 M NaCl solution. For an initial V(V) concentration of 1.2×10^{-4} M, almost 100% of V(V) is adsorbed at pH less than 8.5. The percentage of adsorbed V(V)

decreases to 70% in 0.1 M NaCl and 50% in 0.01 M NaCl, respectively, with the increase in pH to 12. The decreasing adsorption behaviour at high pH is because VO_4^{3-} has to overcome the repulsive electrostatic forces to get close to the negative charged surface at alkaline pH. For an initial V(V) concentration of 1.2×10^{-3} M, the amount of adsorbed V(V) decreases from 88% to 25% with increasing pH from 3 to 12 in 0.1 M NaCl, and decreases from 70% to 25% in 0.01 M NaCl at pH up to 12. Overall, ionic strength has very little impact on the level of V(V) adsorption, however there is a potential minor increase in adsorption removal efficiency at higher ionic strength across the pH range in the 1.2×10^{-3} M system, and at higher pH ($\text{pH} > 9$) in the 1.2×10^{-4} M system. However, ionic strength has little impact on the adsorption behaviour at pH less than 8.5. This adsorption behaviour is consistent with previous studies of V(V) on Fe(III) (hydr)oxides e.g. ferrihydrite and goethite (Peacock and Sherman, 2004, Larsson et al., 2017, Brinza et al., 2008, Blackmore et al., 1996, Naeem et al., 2007).

V(V) isotherm adsorption to hematite data was fitted using a Langmuir model at initial V(V) concentration from 2×10^{-6} M to 1.2×10^{-3} M at pH 7 in 0.1 and 0.01 M NaCl (Figure 5-1B). The Langmuir model fitted the data well ($R = 0.999$ for 0.1 M NaCl and 0.997 for 0.01 M NaCl). The higher ionic strength (0.1 M NaCl) has a higher maximum adsorption capacity (Q_{\max}) than the lower one, with 52.5 mg/g vs. 29.8 mg/g. The good fit of the Langmuir model suggests that adsorption is the main process when V(V) interacts with hematite under the conditions studied and that no precipitation occurred.

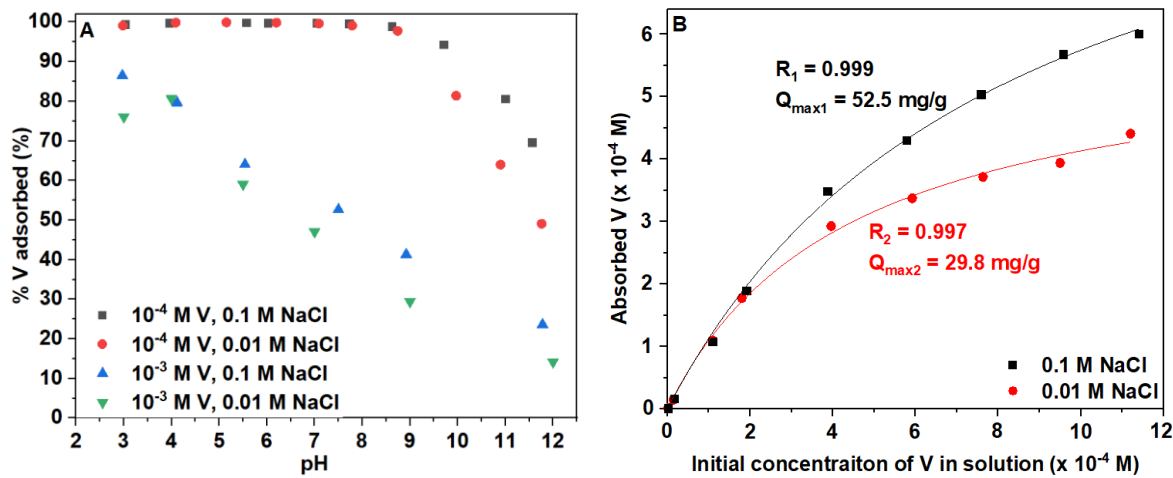


Figure 5-1 A. 1.2×10^{-4} M and 1.2×10^{-3} M V(V) adsorption onto hematite in 0.1 M and 0.01 M NaCl solutions at pH 3-13.5. B. 2×10^{-6} – 1.2×10^{-3} M V(V) isotherm adsorption to hematite with Langmuir isotherm fitting at pH 7 in 0.1 and 0.01 M NaCl.

Figure 5-2 shows V species as function of pH for initial V(V) concentration at both 1.2×10^{-3} M and 1.2×10^{-4} M calculated using PHREEQC. Polyvanadate ($\text{H}_3\text{V}_2\text{O}_7^-$, $\text{V}_3\text{O}_9^{3-}$, $\text{V}_4\text{O}_{12}^{4-}$) species are dominant at pH up to 7 and monovanadate (HVO_4^{2-}) exists dominantly at pH over 8 in 0.01 M NaCl. This is consistent with previous studies of thermodynamic equilibrium modelling of aqueous V(V) speciation (Vessey et al., 2020). At pH up to 6.5, decavanadate ($\text{H}_x\text{V(V)}_{10}\text{O}_{28}^{x-6}$) is predicted to be present in solution, but only at very low concentrations (< $\sim 3 \times 10^{-11}$ M) and the proportion of it at high V(V) concentration (1.2×10^{-3} M) is 10,000 times higher than that at low V(V) concentration (1.2×10^{-4} M).

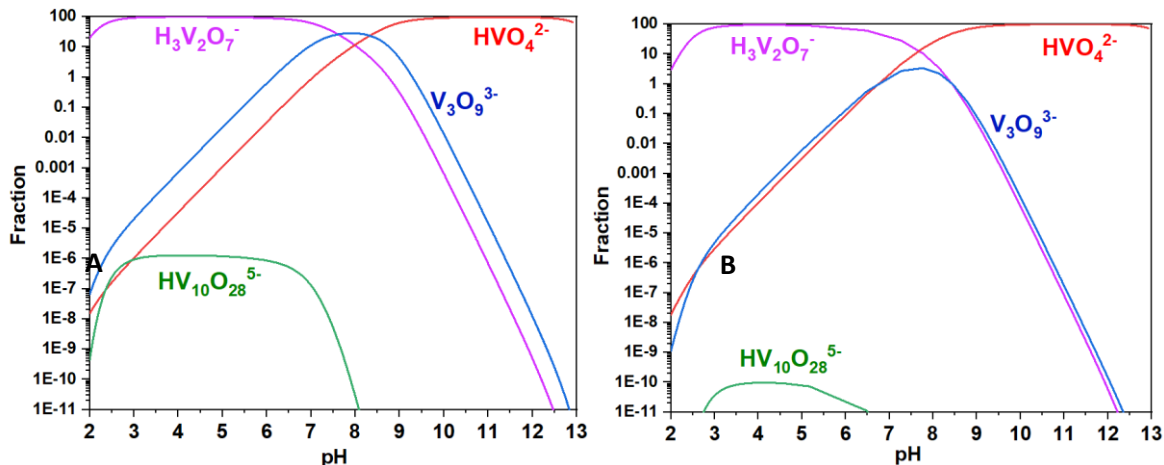


Figure 5-2 PHREEQC modeling on V(V) speciation at pH between 2 to 11 at V(V) concentration of 1.2×10^{-3} M (A) and 1.2×10^{-4} M (B) in 0.01 M NaCl.

Attenuated Total Reflection-Fourier Transform Infrared Spectroscopy (ATR-FTIR).

Figure 5-3 and Table 5-1 shows ATR-FTIR spectra for the higher concentration (1.2×10^{-3} M) V(V) adsorption to hematite in 0.01 M NaCl at a range of pH values. A broad peak at wavenumbers between 660 and 850 cm^{-1} is present at varying intensities in all spectra. These peaks are consistent with previous studies of V(V)-adsorbed hematite and ferrihydrite, where bands at 650-860 cm^{-1} were indicative of a tetrahedrally coordinated vanadate/polyvanadate species (Salak et al., 2012, Griffith and Lesniak, 1969, Vessey et al., 2020). A peak at a wavenumber of 880 cm^{-1} is present in spectra for samples produced at pH 12-13.5. Previous studies indicated that bands around this wave number are related to a tetrahedral monovanadate (HVO_4^{2-}) with C_{3v} symmetry which forms at pH over 10, exhibiting IR band at 877 cm^{-1} (Vessey et al., 2020). A narrower peak between 940 and 952 cm^{-1} is present at pH 3-7, consistent with previous work which showed bands at 930-968 cm^{-1} and indicated a tetrahedral polyvanadate including $\text{H}_2\text{V}_2\text{O}_7^{2-}$ and $\text{V}_4\text{O}_{12}^{4-}$ (C_{2v} symmetry and V-O-V or V-O stretching modes) (Vessey et al., 2020). Previous studies indicate adsorption of these polyvanadate

species occurs via monodentate bonds at the hematite surface (Vessey et al., 2020, Twu and Dutta, 1990, Twu and Dutta, 1989).

At pH 3-5.5, there is a significant IR band at \sim 980 cm⁻¹ (Figure 5-3 and Table 5-1) and this is consistent with the presence of a decavanadate complex according to previous work by Vessey et al (2020) who suggested that a peak at between 970-990 cm⁻¹ for samples at pH 3-4 related to H₂V₁₀O₂₈⁴⁻, HV₁₀O₂₈⁵⁻, and V₁₀O₂₈⁶⁻ on the surface of hematite (Vessey et al., 2020). This also corroborates PHREEQC modelling data in Figure 5-2A that at low pH a proportion of the species of V in solution are decavanadate. Decavanadate is similar to a polymolybdate e.g. Mo₇O₂₄⁶⁻ structure with C_{2v} symmetry in distorted octahedral geometry (Davantes et al., 2017, Davantès and Lefèvre, 2013, Vessey et al., 2020). Previous studies indicate that the adsorption complex of decavanadate on the hematite and ferrihydrite surfaces may be constrained to monodentate complexation which has been attributed to its large and rigid structure (Vessey et al., 2020). The decrease in intensity of the 970-990 cm⁻¹ band with pH from 3 to 5.5 corresponds to a reduction in the amount of decavanadate species present in solution, which is consistent with PHREEQC data (Figure 5-2A) (Vessey et al., 2020), and indicates the decrease in the proportion of this surface species with pH.

Overall, the IR data indicates that pH is a key variable in determining the formation of mono- vs. poly- vanadate. The octahedral decavanadate complex is present on the hematite surface in acidic systems (pH 3-5.5), which agrees with PHREEQC results and supports previous work. In addition, tetrahedral polyvanadate (e.g. H₂V₂O₇²⁻ and V₄O₁₂⁴⁻) forms at low and neutral pH tested and monovanadate presented at pH over 9 (Figure 5-4).

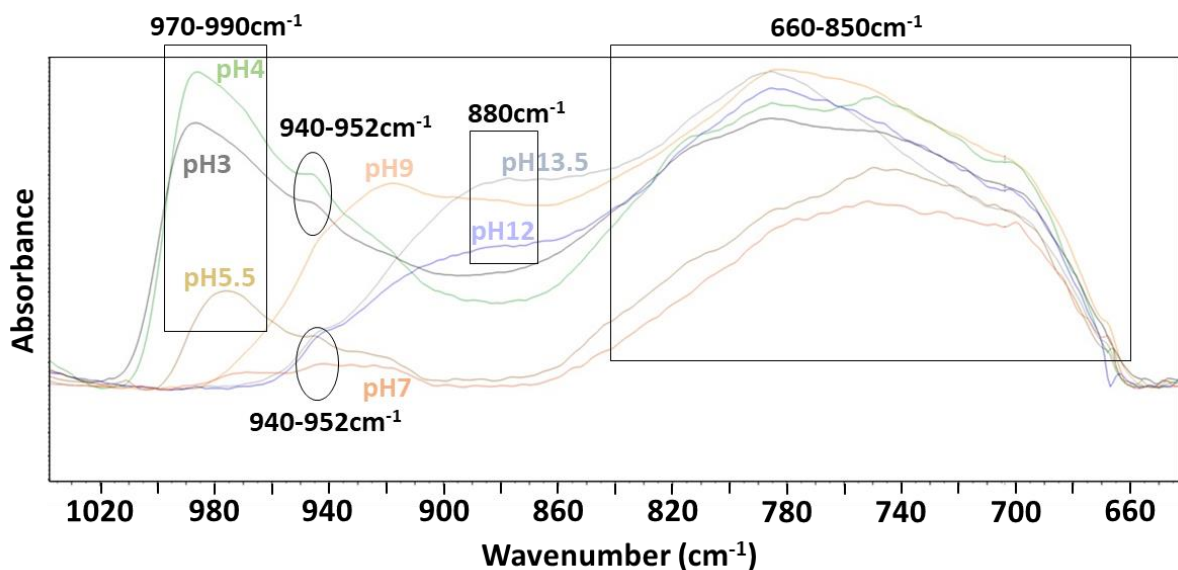


Figure 5-3 ATR-FTIR on 1.2×10^{-3} M V adsorption to hematite at pH 3-13.5 in 0.01 M NaCl.

Table 5-1 Adsorbed vanadate ions and dissolved V species IR band from literature (Griffith 1967, Griffith and Lesniak 1969, Twu and Dutta 1989, Twu and Dutta 1990, Salak et al. 2012, Vessey et al. 2020).

Samples	Wavenumber		
pH 3-4	970-990	940-952	660-850
pH 5.5-7		940-952	660-850
pH 9			660-850
pH 12-13.5		880	660-850
Species	Wavenumber		
$\text{H}_x\text{V}_{10}\text{O}_{28}^{(6-x)-}$	960-998		
$\text{H}_2\text{V}_2\text{O}_7^{2-}/\text{V}_4\text{O}_{12}^{4-}$	930-968		
HVO_4^{2-}	875-877		
$[\text{H}_x\text{V}_2\text{O}_7]^{(4-x)-}$	760-850		
VO_4^{3-}	780-827		

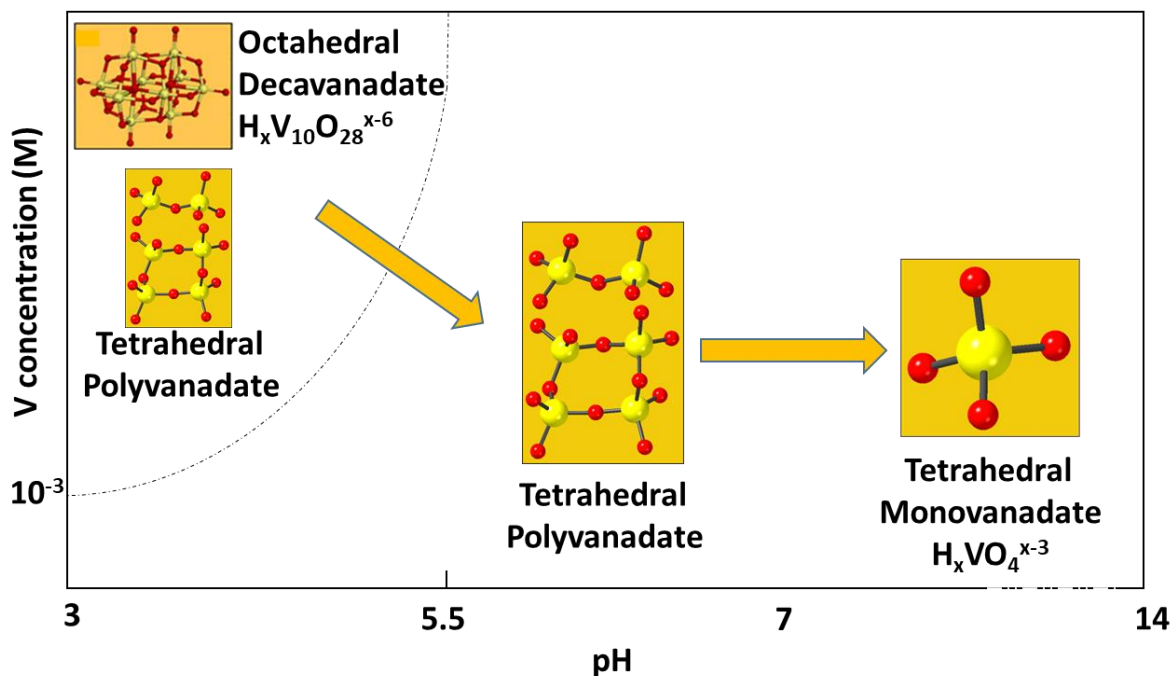


Figure 5-4 V(V) species present in different pH and V(V) concentration systems. Structure is adapted from Vessey et al (2020) (Vessey et al., 2020).

X-ray Absorption Spectroscopy (XAS). XANES V K-edge spectra for V_2O_5 , Na_3VO_4 , and $V_{10}O_{28}^{6-}$ standards and 1.2×10^{-4} M and 1.2×10^{-3} M V(V)-adsorbed hematite samples at pH from 3-13.5 are shown in Figure 5-5. All 1.2×10^{-4} M and 1.2×10^{-3} M V(V)-adsorbed samples have a pre-edge peak at ~5470 eV similar to the V_2O_5 , Na_3VO_4 , and $V_{10}O_{28}^{6-}$ standards (Figure 5-5). The overall shape of the XANES of the experimental samples is most similar to the tetrahedrally coordinated Na_3VO_4 , and octahedrally coordinated $V_{10}O_{28}^{6-}$ standards and differs from the V_2O_5 standard, which contains a VO_5 square base pyramidal (Wisawapipat and Kretzschmar, 2017). The similarity of the sample spectra to the V(V) standards overall suggests that there is no reduction of vanadium during the adsorption process and a comparison with literature spectra for V(IV) and V(III) confirms this (Wisawapipat and Kretzschmar, 2017). Interestingly, the peak intensity of the pre-edge peak increases and peak position shifts to lower energy as pH increases (Figure 5-5C). Samples at an initial V(V) concentration of 1.2×10^{-3} M and pH 3-5.5 present pre-edge peak intensities that are in close agreement with $V_{10}O_{28}^{6-}$.

standard, however, the peak position of $\text{V}_{10}\text{O}_{28}^{6-}$ is shifted to slightly higher energy (~0.5 eV) and the pre-edge peaks of the samples sit between the position of the decavanadate and Na_3VO_4 standards, with a shift towards the Na_3VO_4 position as pH increases to 12 (Figure 5-5C). Therefore the spectra for samples at 1.2×10^{-3} M and pH 3-5.5 indicate a mixture of octahedrally coordinated decavanadate ($\text{V}_{10}\text{O}_{28}^{6-}$) with a tetrahedrally coordinated V species. As pH increases the spectra display an increase in the intensity of pre-edge peaks, samples at pH 7 and 9 are similar and pH 12 has the largest peak intensity. The pre-edge peak for pH 12 is a close match to the peak intensity and position of the Na_3VO_4 standard which has V in tetrahedral coordination. For samples containing a high initial V(V) concentration of 1.2×10^{-3} M the increase in pre-edge peak intensity and shift in peak position to lower energy with the increase of pH indicates the proportion of octahedral $\text{V}_{10}\text{O}_{28}^{6-}$ decreases with an increase in pH and samples change gradually from a mixture of octahedrally and tetrahedrally coordinated V to a dominantly tetrahedral coordination (Figure 5-5C). This is proved by linear combination fitting (Table 5-2), which indicates that the percentage of octahedral decavanadate decreases from 55% at pH 3 to 10.4% at pH 9, and there are no decavanadate fitted at pH 12. However, the percentage of tetrahedral vanadate increases from 30.2% at pH 3 to 79.2% at pH 12. This also agrees with the ATR-FTIR result summarized in Figure 5-4. For samples at low V(V) concentration of 1.2×10^{-4} M the overall shape of the XANES spectra again is more similar to that of $\text{V}_{10}\text{O}_{28}^{6-}$ and Na_3VO_4 (Figure 5-5B). From a closer examination of the pre-edge peaks (Figure 5-5D) there is a shift from higher to lower energy however it is much less pronounced than for the higher concentration V samples and overall the peak position is close to that of the Na_3VO_4 standard. A small amount of decavanadate cannot be discounted as there is still a small but significant peak shift but from PHREEQC modelling (Figure 5-2) the amount of decavanadate present at acidic pH and low vanadium concentration (1.2×10^{-4} M) is 10,000 times less than that present at high concentration (1.2×10^{-3} M). These data indicate that the V

coordination environment in the adsorbed species on hematite is highly dependent on pH and V(V) concentration.

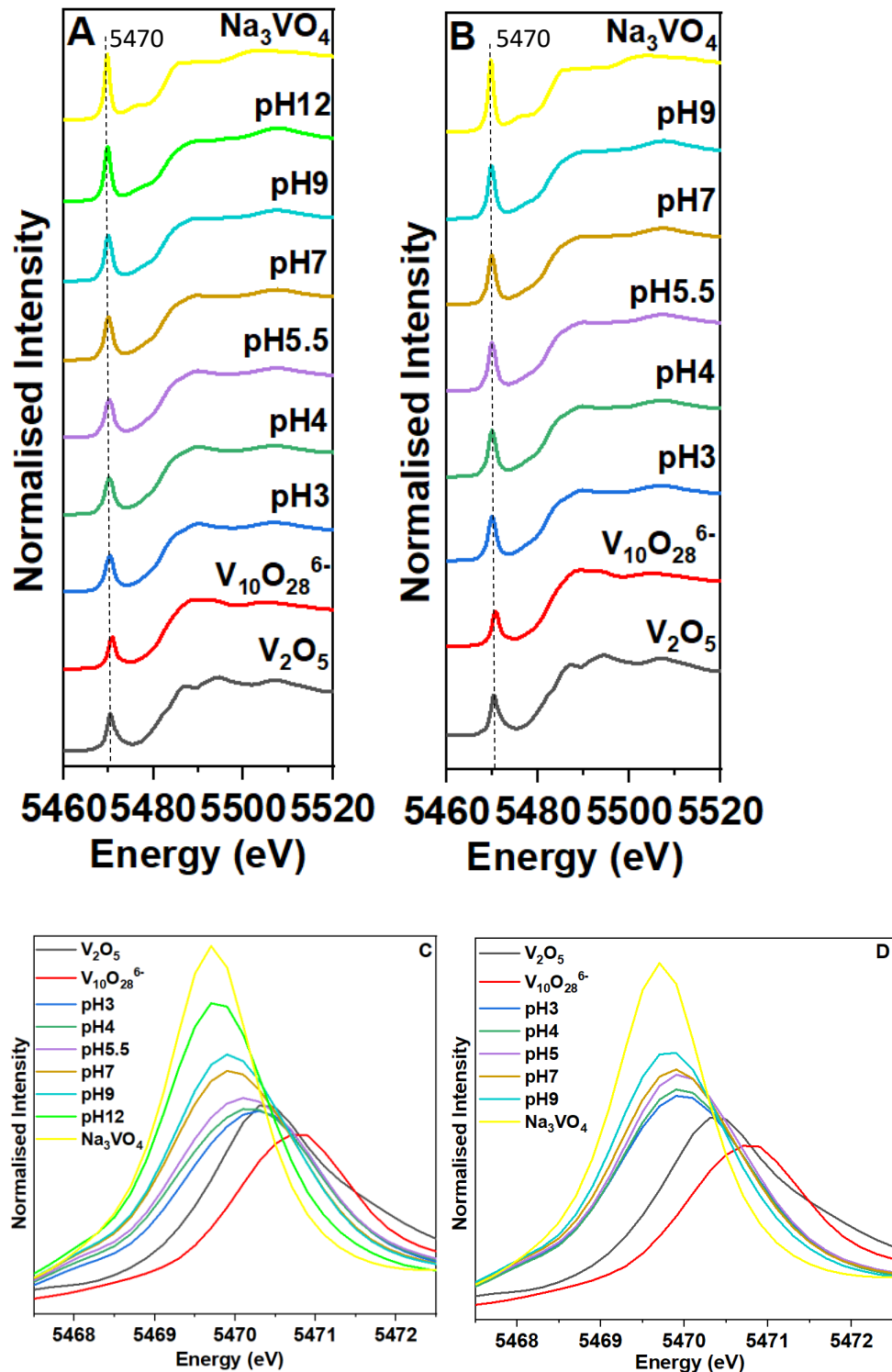


Figure 5-5 XAS spectra for 1.2×10^{-3} M and 1.2×10^{-4} M V(V) adsorbed to hematite at a variety of pH. A. XANES for standards and 1.2×10^{-3} M V(V)-adsorbed hematite samples at

pH 3-12. B. XANES for standards and 1.2×10^{-4} M V(V)-adsorbed hematite samples at pH 3-9. C. and D. are zoomed in pre-edge feature for 1.2×10^{-3} M and 1.2×10^{-4} M V(V)-adsorbed hematite, respectively.

Table 5-2 Linear combination fitting for V-adsorbed hematite samples at V concentration of 1.2×10^{-3} M and pH 3-12.

V-adsorbed hematite samples	Decavanadate ($\text{V}_{10}\text{O}_{28}^{6-}$) (%)	Vanadium pentoxide (V_2O_5) (%)	Sodium vanadate (Na_3VO_4) (%)	R-factor
1.2×10^{-3} M, pH 3	55	14.8	30.2	0.0023
1.2×10^{-3} M, pH 4	51.6	13.2	35.2	0.0036
1.2×10^{-3} M, pH 5.5	39.9	21.1	39	0.0031
1.2×10^{-3} M, pH 7	21.4	27.1	51.4	0.0028
1.2×10^{-3} M, pH 9	10.4	33.5	56	0.0027
1.2×10^{-3} M, pH 12	0	20.8	79.2	0.0037

Figure 5-6 shows the EXAFS and Fourier transform from the 1.2×10^{-3} M and 1.2×10^{-4} M V(V)-adsorbed hematite at pH 3-9 in 0.01 M NaCl. The spectra are similar for V(V)-adsorbed to hematite at pH 3-5.5 and V(V) concentration of 1.2×10^{-3} M and 1.2×10^{-4} M, with five peaks at 2.5-3.5, 6, and 8-9 Å⁻¹. For samples for both V(V) concentrations at pH 7 and 9, they also have three peaks at 2.5-3.5 and 6 Å⁻¹. However, they only have one peak at 8-9 Å⁻¹, different to samples at pH 3-5.5 who have two peaks at this position.

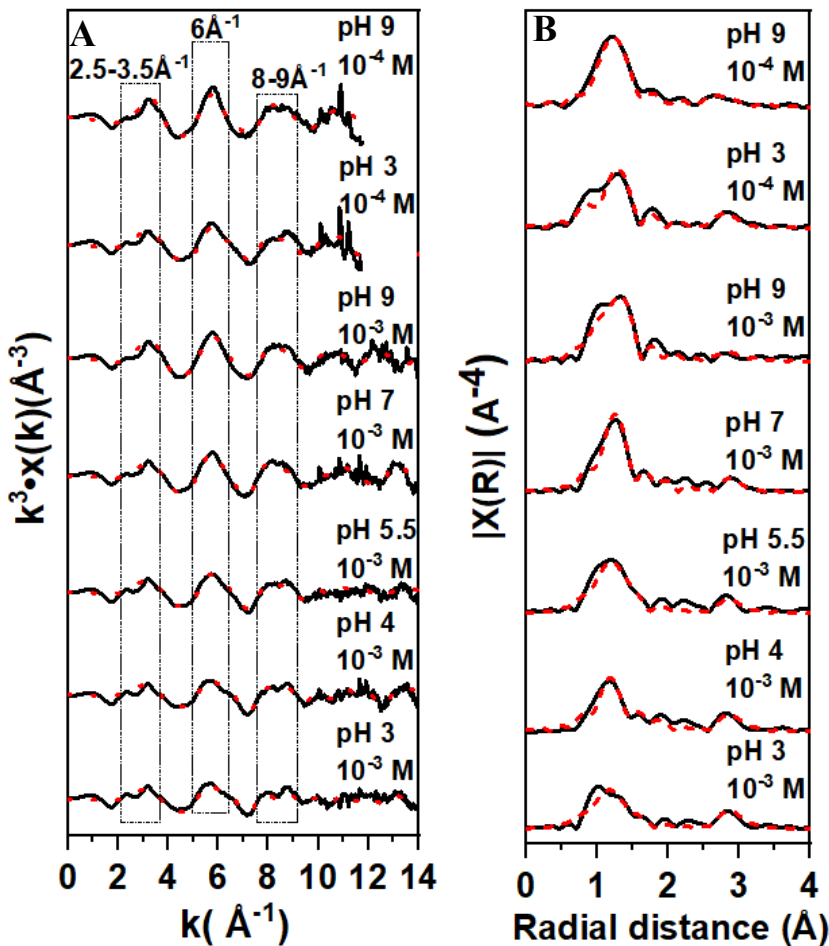


Figure 5-6 EXAFS (A) and Fourier Transform (B) spectra for $1.2 \times 10^{-3} \text{ M}$ and $1.2 \times 10^{-4} \text{ M}$ V(V) adsorption to hematite at pH 3-9 in 0.01 M NaCl. The 10^{-3} M in figures represent samples at $1.2 \times 10^{-3} \text{ M}$ V(V) and the 10^{-4} M in figures represent samples at $1.2 \times 10^{-4} \text{ M}$ V(V).

V(V) EXAFS fitting parameters are shown in Table 5-3. For $1.2 \times 10^{-3} \text{ M}$ V(V)-adsorbed hematite at pH 3-5.5, the best fit to the EXAFS data indicates there are ~5 oxygens in 3 V-O shells at the distances of 1.58-2.05 \AA . In addition, there is one V-V at ~3.3 \AA . For V-adsorbed hematite at pH 7, there are 4.3 oxygens at 1.63 \AA – 2.07 \AA bonded, with 0.6 V at 3.3 \AA . At pH 9, only 4.1 oxygens are bound to the V at 1.55-1.68 \AA with two V-Fe shells fitted at distances of 3.29 and 3.47 \AA . The coordination number for the V-O shells decreases as pH increases. EXAFS fitting for samples at low V(V) concentration of $1.2 \times 10^{-4} \text{ M}$ and pH 3 and 9 includes

multiple V-O scattering paths to improve the model, with four O fitted at 1.5-1.78 Å and two Fe bonded further at 3.26-3.29 Å, similar to the sample at 1.2×10^{-3} M V(V) and pH 9.

For 1.2×10^{-3} M V(V)-adsorbed hematite, the ~4 O are present in the first shell at 1.55-1.68 Å for the sample at pH 9, consistent with previous literature of tetrahedral Na_3VO_4 standard, which is fitted with 4 O at ~1.7 Å (Brinza et al., 2015, Larsson et al., 2017). Previous studies on V(V) adsorption to goethite and ferrihydrite also fit 4 V-O shells at 1.52-1.81 Å, suggesting a tetrahedral complex (Larsson et al., 2017, Peacock and Sherman, 2004). One more V-O shell at ~2.0 Å was attempted in the fit for the sample at pH 9 and tested using F-test, indicating there is only 37.4% confidence to add one more O-O shell at ~2.0 Å in the fitting. Considering the low F-test result, we believe V(V) sorbs to hematite at pH 9 via tetrahedral adsorption complex.

The sample at pH 7 was fitted with 4.3 O at 1.63-2.07 Å, giving it a potential tetrahedral complex. Samples at pH 3-5.5 were also fitted with V-O shells at 1.58-2.05 Å, but the coordination number (CN) is ~5, higher than that for samples at pH 7 (CN = 4.3). In addition, the longer V-O shell at 2.05 Å is consistent with previous literature of octahedral decavanadate ($\text{V}_{10}\text{O}_{28}^{6-}$) which presents a V-O shell at 2.05 Å (Evans Jr, 1966). This indicates samples at pH 3-5.5 are most likely a mixture of octahedral coordinated decavanadate with the V-O bond length of 1.58-1.76 Å indicative of a proportion of tetrahedral vanadium species also present. The decreasing coordination number from ~5 at pH 3 to ~4 at pH 9 and a similar V-O distances (~2.05 Å) between samples at low pH and decavanadate indicate that the coordination environment changes gradually between pH 3 and pH 9 and the proportion of octahedral decavanadate decreases with the increase of pH and the sample at pH 9 presents as tetrahedral monovanadate, which agrees with PHREEQC (Figure 5-2A) that tetrahedral monovanadate (e.g. HVO_4^{2-}) are dominant species at high pH (over 9).

Around 5 O coordinated for samples at pH 3-5.5, indicating a mixed tetrahedral and octahedral structure, consistent with ATR-FTIR (Figure 5-3 & 5-4) and XANES result (Figure 5-5A & 5-5C) and PHREEQC (Figure 5-2A). ATR-FTIR shows a peak at \sim 980 cm⁻¹ (corresponding with the formation of decavanadate) that is only present at 3-5.5 and it disappears at pH over 7, indicating octahedral V₁₀O₂₈⁶⁻ forms at low pH (3-5.5). XANES result of the increased pre-edge peak intensity and shifted peak position to lower energy with the increase of pH indicates the proportion of octahedral V₁₀O₂₈⁶⁻ decreases as the increase of pH and samples change gradually from a mixture of octahedral and tetrahedrally coordinated V to a dominantly tetrahedral coordination. PHREEQC also supports this data that octahedral decavanadate is present in solution at pH 3-5.5 alongside the more dominant tetrahedral polyvanadates at this pH range. The important role that decavanadate plays at this pH range indicates there could be surface accumulation for the increase concentration of decavanadate on the hematite surface, which favors and enhances the formation of polymeric complexes (decavanadate in this study) to a higher degree. Hematite surface enhancing polymerization is a universal process and has been observed amongst different elements (e.g. Mo, W) (Vessey et al., 2020, Davantes et al., 2017).

For V-Fe shells of 1.2×10^{-3} M V(V)-adsorbed hematite, two V-Fe at 3.3-3.47 Å for the sample at pH 9 is consistent with Peacock and Sherman (2004)'s EXAFS and surface complexation modelling (DLM and TLM) investigation of V(V) adsorption to goethite which presents 2 Fe shells at 3.3 Å suggesting the formation of Fe₂O₂VO(OH)⁰ and Fe₂O₂V(OH)₂⁺ bidentate corner-sharing surface complex (Peacock and Sherman, 2004, Brinza et al., 2019). The second V-Fe shell at 3.47 Å from our sample is 0.17 Å longer than that from Peacock and Sherman (2004) probably related to the different surface i.e. hematite vs. goethite. However, a V-Fe shell at 2.8 Å was fitted for V(V) adsorption to ferrihydrite in previous work, indicating an edge-sharing bidentate adsorption complex (Larsson et al., 2017). The V-Fe distance of 2.8 Å is

shorter than those observed in this study and may be due to the larger proportion of singly coordinated groups on Fe(III) octahedra in ferrihydrite, resulting in less ability to forming bidentate edge surface complex (Larsson et al., 2017). So V(V) adsorption to hematite at pH 9 is via tetrahedral corner-sharing bidentate surface complex (Figure 5-7).

There are very few XAS investigations on V(V) adsorption to Fe(III) oxides under similar experimental conditions to those in this study and no EXAFS decavanadate or polyvanadate adsorption has been studied. From EXAFS at 1.2×10^{-3} M V(V) and pH 3-5.5 there is a V-V shell fitted at 3.30-3.32 Å, similar to the sample at pH 7 with a V shell at 3.31 Å. Previous data on the polyvanadate structure indicates both octahedral decavanadate and tetrahedral polyvanadate present a V-V shell at ~ 3.31 Å (Evans Jr, 1966). We believe samples at pH 3-5.5 is a mixture octahedral decavanadate and tetrahedral V species (e.g. polyvanadate), as PHREEQC (Figure 5-2A), ATR-FTIR (Figure 5-4) and XANES (Figure 5-5) have holistically proved it. It is unable to determine whether decavanadate is present at pH 7 if we only consider the V-V shell. However, considering the ATR-FTIR result (Figure 5-3 & 5-4) which shows an absence of a peak at ~ 980 cm⁻¹ (corresponding with decavanadate) at pH 7 and the XANES with an increased pre-edge peak intensity and shifted peak position to lower energy with the increase of pH suggests this sample (pH 7) most closely fits a tetrahedral coordination rather than octahedral decavanadate, as only 4.3 V-O were fitted at this pH, it indicates that the sample at pH 7 is most likely a tetrahedral polyvanadate surface complex.

For samples at low V(V) concentration of 1.2×10^{-4} M, four O fitted for V-O shells at pH 3 and 9 give the best fit, similar to samples at 1.2×10^{-3} M V(V) and pH 9, indicating a tetrahedral V coordination. Two Fe were fitted at 3.26-3.29 Å, consistent with the sample at high V(V) concentration of 1.2×10^{-3} M and pH 9 as well. This agrees with previous literature of V(V) adsorption to goethite at pH ~ 3 -8.3, suggesting bidentate corner-sharing adsorption complex (Peacock and Sherman, 2004).

Table 5-3 V(V) EXAFS fitting parameters.

Sample	Path (V-)	CN ^a	R (Å) ^b	σ2 (Å ²) ^c	S0 ² ^d	R ^e
1.2 x 10 ⁻³ M, pH 3	O	2	1.58(3)	0.006(3)	0.800	0.027
	O	1.8	1.71(4)	0.008(6)	0.800	
	O	1.1	2.05(3)	0.008(5)	0.800	
	V	1	3.30(2)	0.002(1)	0.800	
1.2 x 10 ⁻³ M, pH 4	O	2	1.60(3)	0.002(1)	0.800	0.022
	O	1.8	1.76(2)	0.004(2)	0.800	
	O	1	2.01(9)	0.002(2)	0.800	
	V	1	3.32(5)	0.002(2)	0.800	
1.2 x 10 ⁻³ M, pH 5.5	O	2	1.59(2)	0.003(2)	0.800	0.022
	O	1.8	1.72(3)	0.005(3)	0.800	
	O	0.8	2.02(2)	0.002(3)	0.800	
	V	0.9	3.31(3)	0.004(3)	0.800	
1.2 x 10 ⁻³ M, pH 7	O	2.6	1.63(1)	0.002(1)	0.800	0.021
	O	0.8	1.76(3)	0.002(1)	0.800	
	O	0.9	2.07(2)	0.002(1)	0.800	
	V	0.6	3.31(3)	0.002(3)	0.800	
1.2 x 10 ⁻³ M, pH 9	O	1.5	1.57(3)	0.002(3)	0.800	0.033
	O	2.6	1.68(2)	0.001(2)	0.800	
	Fe	0.8	3.29(9)	0.005(2)	0.800	
	Fe	0.6	3.47(7)	0.009(7)	0.800	
1.2 x 10 ⁻⁴ M, pH 3	O	1.5	1.50(2)	0.007(6)	0.850	0.025
	O	2.5	1.65(1)	0.002(2)	0.850	
	O (MS) ^f	1.5	2.94(2)	0.013(6)	0.850	
	O (MS) ^f	4.0	2.95(2)	0.013(6)	0.850	
	Fe	2.0	3.29(3)	0.009(3)	0.850	
1.2 x 10 ⁻⁴ M, pH 9	O	2.5	1.63(3)	0.001(4)	0.850	0.028

O	1.5	1.78(8)	0.002(7)	0.850
Fe	2.0	3.26(8)	0.012(9)	0.850
O (MS) ^f	1.5	3.49(8)	0.004(7)	0.850
O (MS) ^f	4.0	3.54(8)	0.005(7)	0.850

^acooperation number (CN), ^b Mo bond distance (R (Å)), ^c Debye-Waller factors (σ^2), ^d amplitude factor ($S0^2$), ^e the percentage of misfit between the data and theory (R-factor) (Ravel and Newville, 2005). ^f MS is multiple V-O scattering paths.

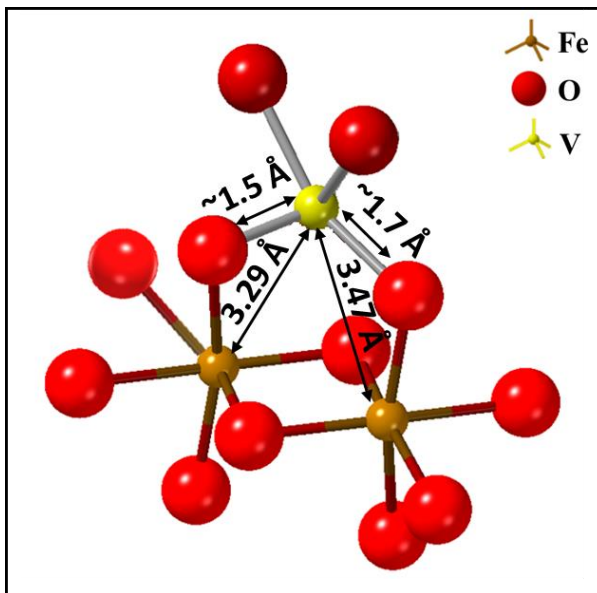


Figure 5-7 V(V) tetrahedral on the iron octahedral structure of hematite via inner-sphere corner-sharing bidentate binuclear adsorption complex (1.2×10^{-3} M V(V) at pH 9, & 1.2×10^{-4} M V(V) at pH 3-9).

5.5 Conclusions

This study has applied a powerful combination of techniques to determine that pH and initial V(V) concentration are important variables when studying V(V) adsorption behaviour to hematite. The higher concentration (1.2×10^{-3} M) of V(V) forms an inner-sphere tetrahedral corner-sharing bidentate binuclear adsorption complex on the hematite surface at high pH (over 9) with polymerisation occurring predominantly at pH less than 7. Tetrahedral polyvanadate presents as the dominant species at pH 7, while a mixture of octahedral decavanadate and tetrahedral V species (e.g. polyvanadate) is observed at pH 3-5.5. At low V(V) concentration

of 1.2×10^{-4} M in all systems tetrahedral monovanadate forms on the hematite surface via corner-sharing bidentate binuclear surface complex, similar to samples. These are the first direct observation of decavanadate adsorption species on hematite using EXAFS and support the conclusion from previous ATR-FTIR analyses that decavanadate forms under acidic conditions as an octahedrally coordinated adsorbed species. The adsorption of V(V) polymers at Fe(III) (oxyhydr)oxides has the potential to passivate reactive hematite octahedra (Vessey et al., 2020). Therefore, these reactions may have implications for V distribution and transport in a variety of geochemical systems.

6. Molybdate ($\text{Mo(VI)}\text{O}_4^{2-}$) Adsorption to Magnetite and Biogenic magnetite

JING ZHANG,[†] VICTORIA S. COKER,[†] J. FREDERICK W. MOSSELMANS,[‡] AND SAMUEL SHAW^{,†}*

[†] Williamson Research Centre for Molecular Environmental Science, Department of Earth and Environmental Sciences, The University of Manchester, Manchester M13 9PL, U.K.

[‡] Diamond Light Source Ltd., Diamond House, Harwell Science and Innovation Campus, Didcot, Oxfordshire OX11 0DE, U.K.

6.1 Abstract

Molybdenum (Mo) is both an important trace element and potential environment contaminant in surface and subsurface environmental systems. Monomolybdate ($\text{Mo(VI)}\text{O}_4^{2-}$) is the dominant species under oxic conditions and its chemical form is dependent on the geochemical conditions (e.g. pH). The mobility and bioavailability of Mo can be controlled by sorption to a mineral surface, including iron (oxyhydr)oxides, which are ubiquitous in the natural environment e.g. magnetite ($\text{Fe(II)}\text{Fe(III)}_2\text{O}_4$), which contains Fe(II) and therefore has potential not only for sorption but also for reduction of Mo(VI) under certain conditions. This study combined aqueous solution analysis, Langmuir isotherm modelling, PHREEQC geochemical modelling, and X-ray Absorption Spectroscopy (XAS) to characterise the molecular scale adsorption and reduction mechanisms of $\text{Mo(VI)}\text{O}_4^{2-}$ to magnetite and biogenic magnetite as function of pH (5.5-13.2) and Mo concentration ($0.01 \times 10^{-4} - 1.7 \times 10^{-3}$ M). Analyses indicated pH and initial Mo(VI) concentration are key variables for adsorption behaviour and that there was the added potential for reduction of Mo(VI) to Mo(IV) to form poorly soluble MoO_2 under more alkaline conditions (pH>9). Two processes were observed at pH 7, with Mo(VI) dominantly adsorbed on magnetite via octahedral corner-sharing surface

complex and 3.7% of Mo(VI) reduced to Mo(IV) to form MoO_2 . At pH 5.5, Mo(VI) adsorbed to magnetite via an inner-sphere octahedral corner-sharing bidentate binuclear adsorption complex. This study provides a detailed molecular scale understanding of Mo(VI) adsorption and reduction processes to Fe(II)-bearing iron oxides (magnetite) under a variety of geochemical conditions to inform the environmental behaviour of Mo(VI).

Keywords: Molybdenum, Iron oxide, Surface adsorption, XANES, EXAFS, octahedral, reduction, incorporation

6.2 Introduction

Molybdenum (Mo) is an essential micronutrient and important trace element for animals, microorganisms, plants, and human health (Arnon and Stout, 1939, Lazaridis and Asouhidou, 2003). However, at high concentration, in association with contaminated land, Mo can cause chlorosis in plants (Gupta, 1997) or molybdenosis in ruminants (Arai, 2010). Mo contamination can occur in a variety of scenarios some caused by anthropogenic activities, such as drainage from sulfide mines, mine wastes or as an industrial byproducts, and others from natural occurrences, such as from rhyolite and rhyolitic ash as well as black shales, where Mo can be leached into groundwater aquifers (Smedley and Kinniburgh, 2017, Xu et al., 2013, Smedley and Nicoll, 2014, Solongo et al., 2018). High Mo concentrations have been observed in surface and groundwaters associated with mine wastes at many sites across the world, with concentrations $> 10 \text{ mg/L}$ (Frascoli and Hudson-Edwards, 2018, España et al., 2008, Skierszkan et al., 2016).

The aqueous environmental mobility, speciation and bioavailability of Mo is impacted by a variety of geochemical factors, including pH, ionic strength, adsorbent type and oxidation state (e.g. Mo(VI), Mo(IV)). Mo exists in the natural aqueous environment as a highly soluble tetrahedral monomeric Mo(VI) oxyanion ($\text{Mo(VI)}\text{O}_4^{2-}$) in oxic systems above pH 6 (Xu et al.,

2013, Oyerinde et al., 2008, Reddy and Gloss, 1993). Heptamolybdate polyanions (e.g. Mo(VI)₇O₂₄⁶⁻), containing MoO₆ octahedra, can form at lower pH (pH 3-5) when the total Mo concentration is over ~10⁻⁴ M (Davantes et al., 2017, Reddy et al., 1997). Mo is also redox-active and can form poorly soluble Mo(IV) phases, for example Mo(IV)O₂, within certain reducing environments (Reddy et al., 1997).

The transport and fate of Mo(VI) anions in many oxic sub-surface environmental systems is controlled by Mo(VI) adsorption on mineral surfaces, in particular, iron oxide and hydroxide nanoparticles e.g. goethite (α -Fe(III)OOH), ferrihydrite (Fe(III)(OH)₃), hematite (a-Fe(III)₂O₃) and the mixed valence iron oxide, magnetite (Fe(III)₂Fe(II)O₄) (Arai, 2010, Verbinnen et al., 2012, Verbinnen et al., 2013, Alfaro et al., 2019, Brinza et al., 2008, Brinza et al., 2019, Brinza et al., 2015, Gustafsson, 2003, Das et al., 2016, Das and Hendry, 2013, Xu et al., 2006a, Goldberg et al., 1996, Goldberg et al., 1998), due to their high surface area, reactivity and high prevalence in the natural environment (Xu et al., 2013, Wichard et al., 2009). In general, Mo(VI) adsorbs to Fe(III)-bearing oxide surfaces at low pH with capacity decreasing above pH 8, indicating that lower pH conditions have greater potential to control the mobility of Mo relative to higher pH systems. However, the interaction between molybdate and magnetite is comparatively poorly studied and has the potential for not only sorption but also reduction of the Mo(VI) by structural Fe(II) (Xu et al., 2013, Verbinnen et al., 2012, Verbinnen et al., 2016, Brinza et al., 2008, Gustafsson, 2003, Xu et al., 2006a, Goldberg et al., 1996). Previous work on oxic, redox active metals, metalloids and actinides has shown magnetite to be a highly efficient absorbant and reductant e.g. uranium (U), chromium (Cr), technetium (Tc) (Das et al., 2010, Roberts et al., 2017, Marshall et al., 2015, Jiang et al., 2014, Rajput et al., 2016, Watts et al., 2015, Yalçıntaş et al., 2016).

X-ray adsorption spectroscopy (XAS) studies of Mo(VI) adsorption to iron (oxyhydr)oxides at near-neutral pH indicate that tetrahedrally coordinated Mo(VI)O₄²⁻ tends to form inner-sphere

surface species when adsorbed to goethite and ferrihydrite, with a mixture of edge-sharing bidentate mononuclear and corner-sharing bidentate binuclear complexes for Mo-adsorbed goethite at pH 7-8.5 (Arai, 2010, Brinza et al., 2015, Das et al., 2016, Gustafsson and Tiberg, 2015). In contrast, at higher pH (~10) Mo(VI) was reported to form an outer-sphere adsorption complex (Das et al., 2016). There are no known EXAFS studies on Mo(VI) adsorption to magnetite or the subsequent interactions of Mo(VI) with magnetite given the potential for reduction of Mo(VI) to Mo(IV) by the structural Fe(II) within the magnetite. Therefore, the key molecular scale processes controlling molybdate adsorption and/or reduction on magnetite, as a function of changing geochemical conditions, remains unresolved. Understanding the atomic scale adsorption mechanisms of Mo(VI) as a function of geochemical parameters is key to predicting the environmental behaviour of this contaminant.

Biogenic nanomagnetite is formed through the reductive transformation of ferrihydrite at circumneutral pH using dissimilatory metal reducing bacteria (DMRB), such as *Geobacter sulfurreducens* (Lovley et al., 1987). These specialist bacteria are able to couple the oxidation of organic matter to the reduction of oxidized metals in the environment, such as Fe(III) in ferrihydrite, in order to gain energy for growth (Lloyd, 2003). Biogenic nanomagnetite has previously been found to be a highly effective sorbent and reductant of the toxic contaminant Cr(VI) O_4^{2-} and its effectiveness as an adsorbent of Mo(VI) is untested (Watts et al., 2015).

The aim of this study is to characterise the molecular scale adsorption mechanism of Mo(VI) to magnetite and biogenic magnetite under varying geochemical conditions, including pH, initial Mo(VI) concentration and ionic strength. A combination of aqueous chemical analyses, PHREEQC geochemical modeling and X-ray Absorption Spectroscopy (XAS) are used to investigate the key mechanisms of Mo(VI) adsorption onto these iron oxides and allow the molecular structure and oxidation changes of Mo(VI) adsorption to magnetite and biogenic magnetite to be determined.

6.3 Experimental Methods

Synthesis and absorption experiments. Magnetite (Fe_3O_4) was synthesised using the method from Roberts (2017) (Roberts et al., 2017). The purity of the magnetite particles was checked by the powder X-ray Diffraction (pXRD) (Bruker D8 Advance), which uses a Cu k-alpha source with a wavelength of 1.5406 Å. The surface area of the obtained magnetite was analysed by Brunauer-Emmett-Teller (BET) analysis (Micromeritics Gemini) and indicated the surface area is $103.52 \text{ m}^2/\text{g}$.

Biogenic magnetite was produced using the method in (Coker et al., 2008) by the reduction of Fe(III)-oxyhydroxide coupled to the oxidation of sodium acetate in the presence of AQDS using *G. sulfurreducens*, under an atmosphere of $\text{N}_2\text{-CO}_2$ (80:20). Bottles were incubated in the dark at 30 °C for 2 days. The purity of the magnetite particles was checked by the powder X-ray Diffraction (pXRD) (Bruker D8 Advance).

The adsorption of Mo onto magnetite and biogenic magnetite was performed under oxygen-free conditions in an anaerobic chamber. Mo(VI) ($\text{Na}_2\text{MoO}_4 \cdot 2\text{H}_2\text{O}$) with the concentration of $0.6 \times 10^{-4} \text{ M}$ (6 ppm) was contacted to 2 g/L magnetite in 30 ml 0.01 M or 0.1 M NaCl solution giving a maximum 3000 ppm Mo(VI) on the magnetite or biogenic magnetite surface. The pH was adjusted using 0.1 M HCl or 0.1 - 0.01 M NaOH to give a range from 3 to 13.2. In addition, an isotherm adsorption experiment was performed for Mo(VI)-adsorbed magnetite at initial Mo(VI) concentration of $0.1 \times 10^{-5} - 1.7 \times 10^{-3} \text{ M}$ at pH 7 in 0.1 or 0.01 M NaCl. All experiments were rotated for 24 h on a rotor mixer with a constant speed of 32 rpm. Samples were filtered using a $0.22 \mu\text{m}$ syringe filter (Merck Millipore) for Inductively Coupled Plasma Atomic Emission Spectroscopy (ICP-AES) (PerkinElmer Optima 5300 dual view) to analyse total aqueous Mo.

Thermodynamic modelling using PHREEQC (version 3.3.5) was applied to characterise the saturation state and mono- vs. poly- species of experimental solutions with respect to Mo solid phase using the minteq.v4.dat database (Winstanley et al., 2019, Vessey et al., 2020). A Langmuir isotherm model was applied to the adsorption process using the following equilibrium:

$$Q_e = Q_{\max} \times b \times C_e / (1 + b \times C_e) \quad (6-1)$$

Where Q_e (mg Mo/g adsorbent) is the adsorbed amount at equilibrium. Q_{\max} (mg/g) is the maximum adsorption capacity. b (l/mg) is a constant. C_e is the residual adsorbent concentration in solution at equilibrium (Verbinnen et al., 2012).

X-ray Absorption Spectroscopy (XAS). X-ray Absorption Near Edge Structure (XANES) and Extended X-ray Absorption Fine Structure (EXAFS) were collected on Mo(VI)-adsorbed magnetite samples at 0.6×10^{-4} M (max. concentration of 3000 ppm Mo(VI) on solid surface with ionic strength of 0.01 M NaCl at pH 5.5, 7, 9, and 13.2) at the Diamond Light Source (DLS) Ltd. (Oxford, UK) on Beamline B18 at the Mo (20 keV) K-edge. Samples were formed into pellets under anaerobic condition and measured in a liquid nitrogen cryostat (77 K). The beamline is equipped with a Si (311) monochromator and data was collected in fluorescence mode using a 36 element Ge detector (Krishnan et al., 2007). Standard data for molybdenum dioxide (Mo(IV)O_2), molybdenum trioxide (Mo(VI)O_3), sodium molybdenum ($\text{Na}_2\text{Mo(VI)O}_4 \cdot 2\text{H}_2\text{O}$), bamfordite ($\text{Fe(III)Mo(VI)}_2\text{O}_6(\text{OH})_3 \cdot \text{H}_2\text{O}$) and ammonium heptamolybdate ($(\text{NH}_4)_6\text{Mo(VI)}_7\text{O}_{24} \cdot 4\text{H}_2\text{O}$), were collected in transmission mode at room temperature. Demeter suite software was used to process the data including background subtraction, calibration and data normalization by Athena and then data fitting in Artemis (Ravel and Newville, 2005). F-test was applied to test the validity of new shells (Downward et al., 2007).

6.4 Results and Discussion

Solution Analysis of Mo Adsorption to Magnetite and Biogenic magnetite. Mo(VI) (0.6×10^{-4} M) adsorption to magnetite and biogenic magnetite is shown in Figure 6-1. Near 100 % Mo(VI) was adsorbed onto magnetite at pH values up to 7 at which point absorption decreased sharply to 10-20 % at pH 10-11 (Figure 6-1A). Ionic strength had no significant impact on the adsorption behaviour at acidic and circumneutral pH, however at pH values above 8.5 a higher ionic strength led to a higher adsorption capacity (20 %) when compared to lower ionic strength (10 %). Showing a similar trend to Mo(VI)-adsorbed magnetite, the majority of the Mo(VI) was adsorbed onto biogenic magnetite between pH 5-7 with decreased absorption at higher pH, however the decrease with increasing pH was less sharp and did not fall to the same minimum values as for magnetite. The lowest absorption of Mo on biogenic magnetite was recorded as 42 % at pH 11.7 (Figure 6-1B). Net surface charge on the magnetite surface can be impacted by pH, with a positive surface charge reported at pH less than 6 and a negative surface charge at pH values above 6 (Shahid et al., 2019, Legodi and de Waal, 2007). The decreasing adsorption efficiency under alkaline conditions may be due to the negative surface charge on magnetite and biogenic magnetite resulting in repulsion of molybdate anions ($\text{Mo(VI)}\text{O}_4^{2-}$). The reduction of Mo(VI) to Mo(IV) to form MoO_2 may have potential to passivate reactive hematite and reduce its surface, resulting in the decrease of adsorption efficiency. Competition for the magnetite surface between Mo(VI) ions and hydroxyl is also expected (Shahid et al., 2019, Almasri et al., 2019). However, the point of zero charge (pH_{pzc}) for Mo(VI) adsorption to zeolite-supported magnetite was previously investigated and indicated a negative surface charge over the a pH range of 2-10, suggesting chemical adsorption (chemisorption) of Mo(VI) to zeolite-supported magnetite (Verbinnen et al., 2012). The better adsorption efficiency for biogenic magnetite is due to its smaller particle size and higher level of Fe(II), compared with chemical synthesised magnetite.

Mo(VI) isotherm adsorption to magnetite was performed at initial Mo(VI) concentration from 0.1×10^{-5} M (0.1 ppm) to 1.7×10^{-3} M at pH 7 in 0.1 and 0.01 M NaCl solution (Figure 6-1C). Over 98 % Mo(VI) was adsorbed at an initial Mo(VI) concentration less than 1.2×10^{-3} M and the amount absorbed dropped to 80 % at initial Mo(VI) concentration of $\sim 1.7 \times 10^{-3}$ M in either 0.1 or 0.01 M NaCl solution. The Mo(VI) isotherm adsorption to magnetite data was fitted with a Langmuir model (Figure 6-1D), giving an R factor of 0.998 for both 0.1 and 0.01 M NaCl solution. The maximum adsorption capacity in 0.1 M NaCl solution was lower than for 0.01M NaCl, with values of 269 mg/g and 286 mg/g, respectively. A previous Langmuir model of Mo(VI) adsorption to zeolite-supported magnetite indicated the maximum adsorption capacity was only 17.92 mg/g (Verbinnen et al., 2012), significantly lower than ours, perhaps due to the combination of zeolite and magnetite used in the previous study and differing environmental conditions (Mthombeni et al., 2016). The low ionic strength dependence of Mo(VI) adsorption to magnetite indicates the adsorption may be via an inner-sphere adsorption complex (Goldberg et al., 1993).

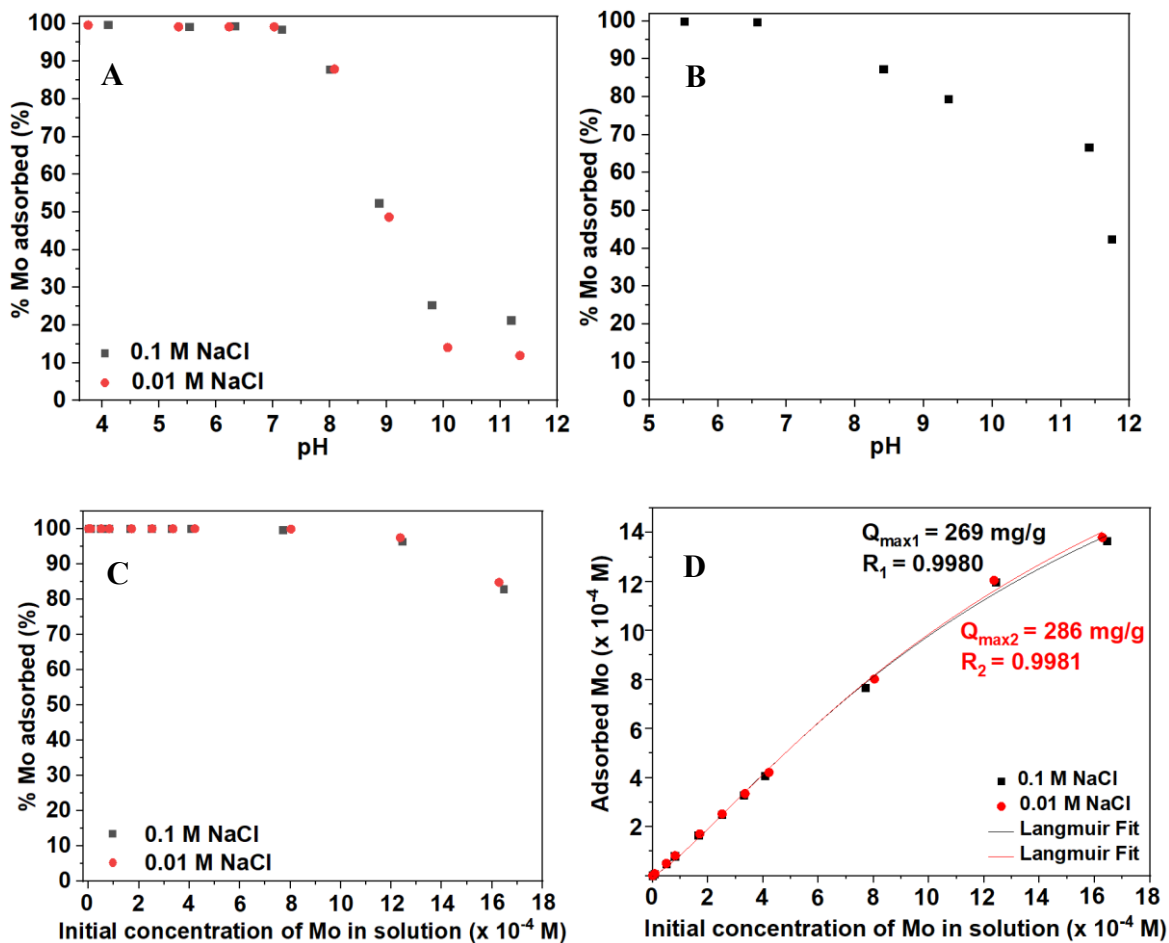


Figure 6-1 Mo(VI) adsorption onto magnetite and biogenic magnetite. (A) Mo(VI) adsorption to magnetite at pH from 4 to 12 in 0.1 and 0.01 M NaCl solution at initial Mo(VI) concentration of 0.6×10^{-4} M. (B) Mo(VI) adsorption to biogenic magnetite at pH from 5.5 to 12 in 0.01 M NaCl solution at initial Mo(VI) concentration of 0.6×10^{-4} M. (C) Mo(VI) adsorption to magnetite at pH 7 at initial Mo(VI) concentration of 0.1×10^{-5} M - 1.7×10^{-3} M. (D) Mo(VI) isotherm adsorption to magnetite at pH 7 at initial Mo(VI) concentration from 0.1×10^{-5} M to 1.7×10^{-3} M with Langmuir isotherm fitting.

PHREEQC geochemical modelling was applied to model the aqueous Mo species over the pH range 2-11.5 with a Mo concentration of 0.6×10^{-4} M in 0.01 M NaCl solution (Figure 6-2). Figure 6-2A shows tetrahedral monomolybdate species dominate in solution across the whole pH range, whereas octahedral polymolybdate species only form a small proportion (up to 0.3 %) of the Mo present in aqueous solution at pH 2-5.

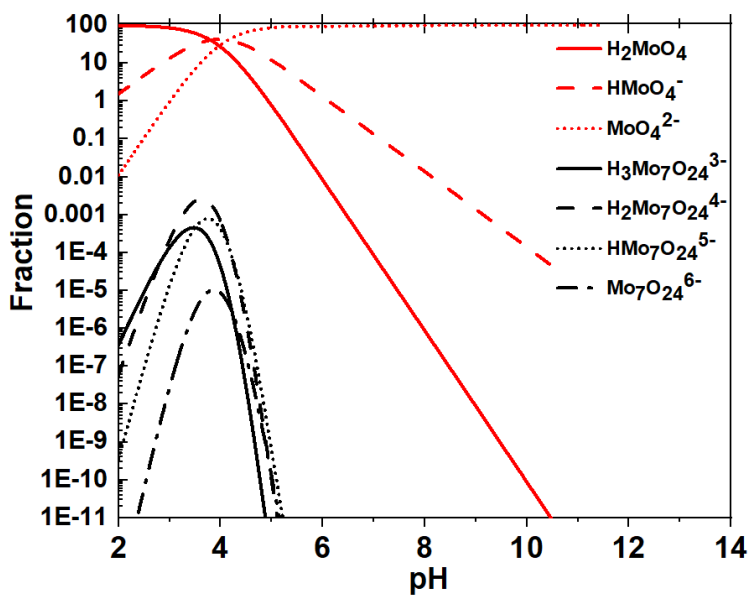


Figure 6-2 PHREEQC modeling of Mo(VI) speciation at pH between 2 to 11.5 at a Mo concentration of 0.6×10^{-4} M in 0.01 M NaCl.

Mo K-edge X-ray Absorption Spectroscopy (XAS) of Mo(VI)-adsorbed Magnetite. Mo K-edge XANES of five samples (pH 5.5 - 13.2) for Mo(VI) adsorption to magnetite and biogenic magnetite were collected where the initial Mo(VI) concentration was 0.6×10^{-4} M and ionic strength 0.01 M NaCl (Figure 6-3). A pre-edge peak was observed at ~ 20004 eV for magnetite samples formed at pH 5.5 and 7 and biogenic magnetite at pH 7, similar to Mo(VI) standards including molybdenum trioxide ($\text{Mo(VI)}\text{O}_3$), sodium molybdate ($\text{Na}_2\text{Mo(VI)}\text{O}_4 \cdot 2\text{H}_2\text{O}$), bamfordite ($(\text{Fe(III)}\text{Mo(VI)})_2\text{O}_6(\text{OH}_3)\cdot\text{H}_2\text{O}$) and ammonium heptamolybdate ($((\text{NH}_4)_6\text{Mo(VI)}_7\text{O}_{24})\cdot 4\text{H}_2\text{O}$) (Figure 6-3). Three peaks were also observed at 20022 eV, 20035 eV and 20053 eV for magnetite samples at pH 5.5 and 7 and biogenic magnetite at pH 7 with the initial, tetrahedrally coordinated, sodium molybdate standard giving the poorest match to the relative intensity of these peaks compared to the other Mo(VI) standard materials. The intensity of the pre-edge peak and overall structure for magnetite samples at pH 5.5 and 7 and biogenic magnetite at pH 7 are in fact most similar to octahedrally coordinated MoO_3 and heptamolybdate, indicating a change to an octahedral adsorption complex (Das et al., 2016).

The pre-edge peak at 20004 eV and the peak at 20053 eV were not apparent in spectra for samples created at pH 9 or 13.2, which was consistent with the spectrum for the Mo(IV)O₂ standard. These observations indicated that Mo(VI) was reduced to Mo(IV) on the magnetite surface at pH values above 9. Linear combination fitting for magnetite samples using Mo(VI)O₃ and Mo(IV)O₂ standard spectra confirmed that the amount of Mo(VI) decreased from 99.7 % at pH 5.5 to 26.4 % at pH 9 with no Mo(VI) observed at pH 13.2, whereas the proportion of MoO₂ increased from 0.3-3.7 % at pH 7 or lower to 73.6 % at pH 9 and then to 100 % at pH 13.2 (Table 6-1). Linear combination fitting for Mo(VI)-adsorbed biogenic magnetite at pH 7 showed the proportion of MoO₂ was 9 %, higher than the magnetite sample at pH 7 (5 % MoO₂). This may be due to biogenic magnetite containing more Fe(II) compared to magnetite, leading to more potential to reduce Mo(VI) to Mo(IV) (Crean et al., 2012).

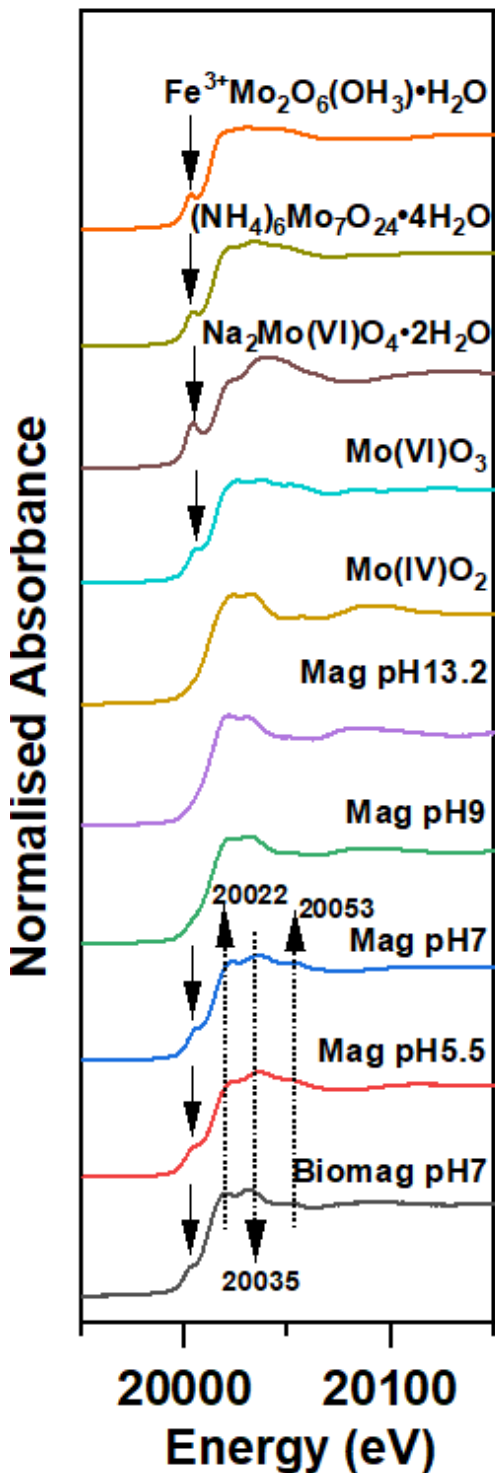


Figure 6-3 Mo K-edge XANES spectra for Mo(IV) and Mo(VI) standards and 0.6×10^{-4} M Mo-adsorbed magnetite and biogenic magnetite at pH 5.5-13.2 in 0.01 M NaCl solution. Mag is magnetite and Biomag is biogenic magnetite.

Table 6-1 Linear Combination Fitting of Mo K-edge XANES Mo(VI)-adsorbed magnetite and biogenic magnetite at pH 5.5-13.2 in 0.01 M NaCl.

Mo-adsorbed samples	MoO ₂ (%)	MoO ₃ (%)	R-factor
Magnetite, pH 5.5	0.3 %	99.7 %	0.0032
Magnetite, pH 7	3.7 %	96.3 %	0.0014
Magnetite, pH 9	73.6 %	26.4 %	0.0011
Magnetite, pH 13.2	100 %	N/A	0.0048
Biogenic magnetite, pH 7	9 %	91 %	0.0020

Figure 6-4 shows that samples at pH 9 and 13.2 have similar Mo K-edge EXAFS spectra, and that they differ from that for samples at pH 5.5 and 7. Both pH 9 and 13.2 have a peak at 4.7 Å⁻¹, which is absent in the spectrum at pH 5.5. There is a shoulder at 5.5 Å⁻¹ for spectra at pH 5.5 and 7 and the intensity of the peak at 6.2 Å⁻¹ increases with an increase of pH from 5.5 to 13.2. This may be attributed to the change in speciation from Mo(VI) to Mo(IV) with an increase in pH that is indicated from the XANES Linear combination fitting result (Table 6-1). In addition, at pH 5.5, the peak at ~8.5 Å⁻¹ is consistent with Mo-adsorbed hematite EXAFS in chapter 4 (Figure SI4-8), suggesting Mo sorbed to magnetite at pH 5.5 may via similar surface complex to Mo-adsorbed hematite (via octahedral corner-sharing bidentate binuclear complex) at similar pH and low concentration (0.6×10^{-4} M Mo(VI)).

Table 6-2 shows the Mo K-edge EXAFS fitting for samples of Mo-adsorbed magnetite at pH 5.5-13.2. At pH 5.5, 5.7 oxygens were fitted at distances between 1.74 Å⁻¹ and 2.38 Å⁻¹ from the central Mo absorber, indicating an octahedral coordination with a further ~2 Fe atoms at 3-3.4 Å⁻¹. For pH 7, again the fit describes an octahedral Mo surface complex as 6 O are found surrounding the Mo between 1.72 Å⁻¹ and 2.31 Å⁻¹. In addition, the fit at pH 7 gives 0.4 Mo at 2.59 Å⁻¹ and a further 4 Fe between 3.1-3.4 Å⁻¹. Samples at pH 9 and 13.2 are similar to samples

at 5.5 and 7, in that ~ 6 Mo-O are fitted in the first shell(s) again indicative of an octahedral Mo surface complex, however the organization of those 6 O atoms gradually alters from being 3 distinct Mo-O shells with different distances for the two low pH samples, to two shells at pH 9 and finally only one distinct shell at 2.06 \AA^{-1} containing all 6 O atoms at the highest pH 13.2. The two high pH samples also differ from the low pH samples as they both have Mo-Mo distances fitted with a total coordination number of ~ 10 between $2.55\text{-}3.44 \text{ \AA}^{-1}$.

The Mo K-edge EXAFS fit for pH 13.2 is in good agreement with the coordination environment within the MoO_2 standard, with the main discrepancy in the longest Mo-Mo distance for MoO_2 at 3.69 \AA^{-1} , $\sim 0.25 \text{ \AA}^{-1}$ longer than the pH 13.2 sample, and the linear combination fit for the XANES (Figure 6-4 and Table 6-1) for pH 13.2 also suggested the Mo is 100% reduced to MoO_2 . For pH 9 there is also reasonably good agreement with the MoO_2 standard, with the same minor discrepancy in the longest Mo-Mo distance as for pH 13.2, and also a splitting of the 6 O at $\sim 2 \text{ \AA}^{-1}$ into two shells. The mixture of 75:25 $\text{MoO}_2/\text{MoO}_3$ indicated by the XANES linear combination fitting for pH 9 would account for the difference in the Mo-O shells between these two samples, as the shorter distance is apparent in the standard for MoO_3 . For the pH 9 sample a Mo-Fe shell was attempted, however, F-test indicated that there was only an 80.5 % confidence to add this shell and therefore it was not included since the confidence level is preferably greater than 95%.

At pH 7, six oxygens were fitted confirming the XANES analysis that the structure of the Mo changed during the experiment from tetrahedral to an octahedral coordination environment. Furthermore, 2.5 Fe atoms were fitted at distances between $3.18\text{-}3.47 \text{ \AA}^{-1}$, and these are consistent with Mo(VI) adsorption to goethite (Arai, 2010) and hematite at pH 7 in chapter 4 (Table SI4-2), with two Mo-Fe shells fitted at $\sim 3\text{-}3.5 \text{ \AA}^{-1}$, indicating a corner-sharing bidentate binuclear surface complex. This means Mo(VI) adsorbed on the magnetite surface at pH 7, and this adsorption action can also be supported by the Langmuir isotherm model (Figure 6-1D).

Apart from Mo-Fe shells, one Mo-Mo were also fitted at distance of 2.59 Å⁻¹ and are consistent with the MoO₂ standard, which has one Mo-Mo shell at distance of 2.51 Å⁻¹, confirming the XANES analysis that a proportion (3.7 %) of Mo(VI) was reduced to Mo(IV)O₂. These data suggest that Mo(VI) dominantly adsorbed on the hematite surface at pH 7 via corner-sharing bidentate binuclear surface complex. There were also 3.7% of Mo(VI) reduced to Mo(IV) to form Mo(IV)O₂ by magnetite.

For the sample at pH 5.5, there is no Mo-Mo shell to suggest reduction of the Mo, and this is consistent with XANES linear combination fitting that no Mo(VI) was reduced to Mo(IV) at low pH. The EXAFS fitting of ~ 6 Mo-O and 2 Mo-Fe at pH 5.5 is consistent with previous EXAFS studies of Mo-adsorbed goethite (Arai, 2010), as well as Mo-adsorbed hematite at pH 5.5 and 0.6 x 10⁻⁴ M Mo(VI) in Chapter 4 of this thesis (Table SI4-2), and therefore the conclusion is that an octahedral inner-sphere corner-sharing bidentate binuclear adsorption complex forms (Arai, 2010).

It was not possible to collect EXAFS data on biogenic magnetite due to COVID-19 epidemic and this would be the part of the further work section, which would allow the bioproduced and synthetic materials to be fully contrasted.

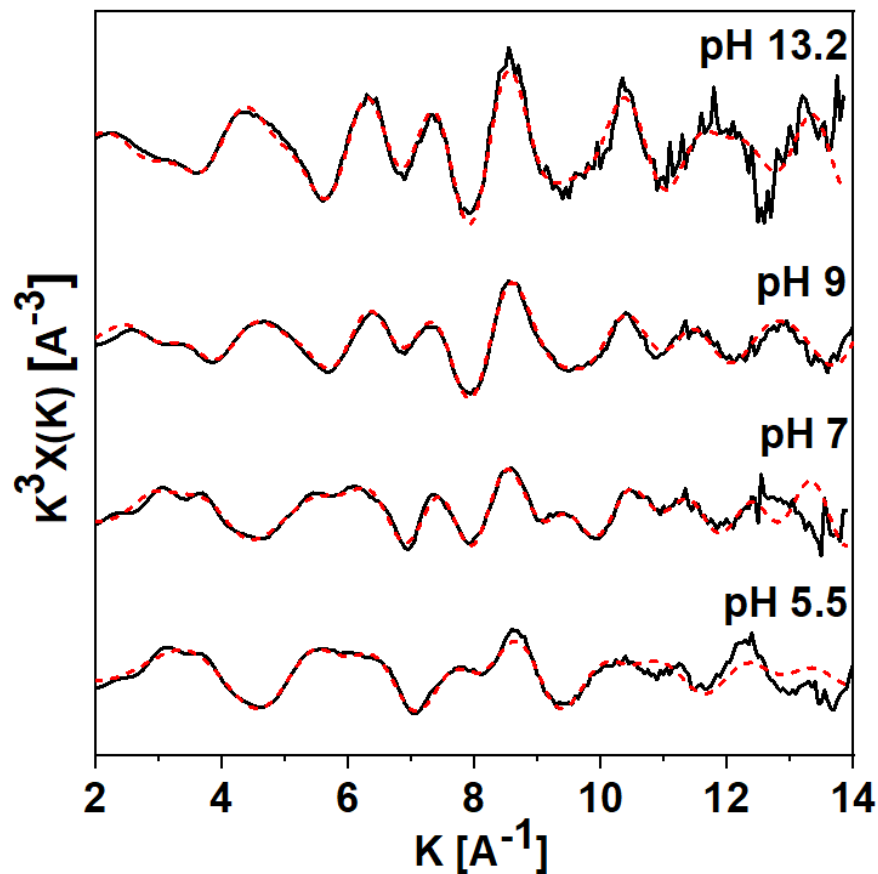


Figure 6-4 K^3 -weighted Mo EXAFS spectra for 0.6×10^{-4} M Mo(VI)-adsorbed magnetite at pH 5.5-13.2 in 0.01 M NaCl solution.

Table 6-2 EXAFS fitting parameter for 0.6×10^{-4} M Mo(VI)-adsorbed to magnetite at pH 5.5-13.2 and MoO₂ standard.

Samples	path Mo-	CN ^a	R (\AA) ^b	$\sigma^2 (\text{\AA}^2)$ ^c	$S0^2$ ^d	R-factor ^e
pH 5.5	O	3.5	1.74(1)	0.005(1)	0.800	0.013
	O	1.0	2.06(3)	0.005(1)	0.800	
	O	1.2	2.38(4)	0.005(1)	0.800	
	Fe	1.0	3.00(2)	0.003(2)	0.800	
	Fe	0.8	3.40(9)	0.010(2)	0.800	
pH 7	O	3.0	1.72(1)	0.005(1)	0.800	0.014
	O	1.4	1.98(2)	0.005(1)	0.800	
	O	1.6	2.32(2)	0.005(1)	0.800	
	Mo	1	2.59(2)	0.008(3)	0.800	
	Fe	1	3.18(3)	0.004(3)	0.800	
	Fe	1.5	3.47(2)	0.003(1)	0.800	
pH 9	O	1.3	1.70(2)	0.005(1)	0.800	0.016
	O	4.3	2.04(1)	0.005(1)	0.800	
	Mo	1	2.60(1)	0.002(1)	0.800	
	Mo	1	3.02(2)	0.005(3)	0.800	
	Mo	8	3.44(2)	0.013(2)	0.800	
pH 13.2	O	6	2.06(2)	0.005(1)	0.800	0.027
	Mo	1.2	2.55(1)	0.001(2)	0.800	
	Mo	1.2	2.97(3)	0.001(2)	0.800	
	Mo	8	3.40(2)	0.008(1)	0.800	
MoO ₂ ^f	O	6	2.00			
	Mo	1	2.51			
	Mo	1	3.12			
	Mo	8	3.69			
MoO ₃ ^g	O	2	1.58			

O	4	2.19
Mo	2	3.27
Mo	4	3.87

^acooperation number (CN), ^b Mo bond distance (R (Å)), ^c Debye-Waller factors (σ^2), ^d amplitude factor ($S0^2$), ^e the percentage of misfit between the data and theory (R-factor) (Ravel and Newville, 2005). ^f and ^g are EXAFS fitting from literature (Wharton et al., 2003).

6.5 Conclusions

This paper combines aqueous solution analysis, PHREEQC modelling and XAS to determine that pH and Mo(VI) concentration are key variables of adsorption and/or reduction processes associated with Mo(VI) interactions with magnetite and biogenic magnetite. Mo(VI) was fully removed by both magnetite and biogenic magnetite at pH less than 7, with an increase to more alkaline pH leading to a subsequent decrease in Mo adsorption. Three main processes were identified depending on pH through XANES and EXAFS analysis: 1. Greater potential for reduction of Mo(VI) to Mo(IV) to form MoO₂ at pH > 9, 2. Two processes at pH 7 with dominantly adsorption on magnetite via corner-sharing octahedra and 3.7% of reduction to Mo(IV) to form MoO₂, and 3. Adsorption onto magnetite at pH 5.5 via an inner-sphere octahedral bidentate binuclear adsorption complex. These results show the ability of Fe(II)-bearing iron oxides (magnetite) to act as a possible remediation agent for controlling the environmental mobility of Mo through absorption and reduction processes under a variety of environmental conditions. This study has implications for Mo distribution and transport in a varying geochemical scenarios and its use as a paleoredox indicator. It was not able to collect EXAFS data on biogenic magnetite due to COVID-19. Future work for the EXAFS analysis for biogenic magnetite would allow the bioproduced and synthetic materials to be fully contrasted and would aid the evaluation of the behaviour of this key contaminant under environmentally relevant conditions.

7. Conclusions and Future Work

7.1 Conclusions

The aims of this thesis were to holistically evaluate the adsorption and redox action of poly- or mono- molybdate ($\text{Mo(VI)}\text{O}_4^{2-}$) and vanadate ($\text{V(V)}\text{O}_4^{3-}$) to iron (oxyhydr)oxides including hematite ($\alpha\text{-Fe}_2\text{O}_3$), magnetite ($\text{Fe(II)}\text{Fe(III)}_2\text{O}_4$) and biogenic magnetite under a variety of environmental conditions (such as pH, adsorbate concentrations and ionic strength), and identify the changes in Mo and V speciation and their oxidation states, and determine the bonding environment of Mo(VI) and V(V) onto these widespread iron oxide surfaces. Previous studies focused on Mo(VI) and V(V) adsorption to iron oxides such as goethite and ferrihydrite (Arai, 2010, Brinza et al., 2019, Gustafsson, 2003, Das et al., 2016, Larsson et al., 2017, Xu et al., 2006a, Peacock and Sherman, 2004), but there are only limited studies of their adsorption behaviour on hematite, magnetite and biogenic magnetite at the molecular scale ; especially rare are any previous works that address poly- molybdate/vanadate adsorption on these iron oxide surfaces (Vessey et al., 2020, Davantes et al., 2017). This thesis applied a multi-technique approach (including aqueous chemical analyses, PHREEQC geochemical modelling, Attenuated Total Reflection-Fourier Transform Infrared Spectroscopy (ATR-FTIR) and X-ray absorption spectroscopy (XAS)) to provide a detailed molecular scale understanding of the poly- or mono- Mo(VI) and V(V) adsorption mechanisms resulting in a comprehensive dataset for determining the environmental mobility of Mo and V under a variety of geochemical scenarios. The main aims that were proposed in thesis were:

- To characterise the molecular scale adsorption mechanism of Mo(VI) to hematite ($\alpha\text{-Fe}_2\text{O}_3$) under varying geochemical conditions, including pH, initial Mo(VI) concentration and ionic strength. The holistic approach allowed the molecular structure and range of chemical stability (pH 3-14, $[\text{Mo(VI)}] 0.1 \times 10^{-5} - 2 \times 10^{-3} \text{ M}$, ionic strength

0.1 M and 0.01 M NaCl) of mono- and poly- molybdate adsorption to hematite to be determined (Chapter 4).

- To determine the adsorption behaviour, local coordination environment and bonding mechanisms of mono- or poly- V(V) to hematite under varying geochemical conditions including pH (3-14), ionic strength (0.1 M and 0.01 M NaCl) and initial V concentrations ($2 \times 10^{-6} - 4 \times 10^{-3}$ M) (Chapter 5).
- To characterise the molecular scale adsorption and reduction mechanism and identify the molecular structure and oxidation changes of Mo(VI) to magnetite and biogenic magnetite under varying geochemical conditions (Chapter 6).

In **Chapter 4**, the adsorption of mono- and poly-molybdate onto hematite surface was investigated using a multi-technique approach, indicating pH and Mo(VI) concentration are key variables for Mo(VI) adsorption behaviour to hematite. For an initial low Mo(VI) concentration of 0.6×10^{-4} M over 99 % Mo(VI) was adsorbed up to pH up 8, with adsorption decreasing as pH increased beyond this point. At an initial high Mo(VI) concentration of 5×10^{-4} M maximum adsorption (~92%) occurred at pH 3 with decreasing levels of adsorption with increasing pH. At the higher initial Mo(VI) concentration overall there was lower adsorption efficiency compared with the lower initial Mo(VI) concentration across the pH range. There was no change in the magnitude of adsorption under different ionic strengths for either Mo(VI) concentration. Langmuir isotherm modelling for samples at pH 7 indicated adsorption of single ions dominates under low Mo(VI) concentration ($\leq 5.7 \times 10^{-4}$ M) and at higher concentration polymeric species may form on the hematite surface. This multi-technique approach, including PHREEQC, ATR-FTIR and XAS analyses, holistically showed that at low concentrations (0.6×10^{-4} M Mo(VI)) and neutral - high pH Mo(VI) forms an octahedral inner-sphere corner-sharing bidentate binuclear surface adsorption complex with polymeric species forming at low pH (<4) and higher concentrations (5×10^{-4} M Mo(VI)). These are the first

direct observations of octahedrally coordinated Mo(VI) adsorption species on hematite, and support the conclusions from previous isotope measurements and Density Functional Theory + U correction (DFT+U) computational calculation studies that indicated Mo(VI) transitions from a tetrahedral MoO_4^{2-} solution complex to a octahedrally coordinated adsorbed species (Davantes et al., 2017, Goldberg et al., 2009).

In **Chapter 5** the study employed similar processes and techniques to Chapter 4 to study the adsorption of mono- and poly-vanadate (VO_4^{3-}) onto hematite under varying pH and V(V) concentrations. Similar to Mo(VI) adsorption to hematite, almost 100% of V(V) was adsorbed at pH up to 8 at the initial low V(V) concentration of 1.2×10^{-4} M with the quantity adsorbed decreasing along with the increase of pH. At a high V(V) concentration of 1.2×10^{-3} M, the maximum adsorption (~85%) occurred at pH 3 and again absorption decreased with an increase in pH. Langmuir isotherm modelling suggested that adsorption is the main process when V(V) interacts with hematite at an initial V(V) concentration of up to 1.2×10^{-3} M and pH 7 and that no precipitation occurs. A multi-technique approach including PHREEQC geochemical modelling, ATR-FTIR and XAS analysis holistically indicated that the coordination environment changes gradually from a mixture of octahedrally and tetrahedrally coordinated V at pH 3 to a tetrahedral monovanadate dominating at pH 9. This shows a clear trend during the adsorption process and is different from Mo(VI) adsorption to hematite in Chapter 4 in that the polymolybdate only occurred in acidic systems with monomolybdate present under neutral and alkaline conditions. For V(V)-adsorbed hematite at high V(V) concentration of 1.2×10^{-3} M, and pH above 9, V(V) forms an inner-sphere tetrahedral corner-sharing bidentate binuclear adsorption complex with polymerisation occurring at a pH less than 7. Tetrahedral polyvanadate presents at pH 7, while a mixture of octahedral decavanadate and tetrahedral V species (e.g. polyvanadate) is observed at pH 3-5.5. For V(V)-adsorbed hematite at low V(V) concentration of 1.2×10^{-4} M in all systems V(V) sorbs hematite via a tetrahedral corner-

sharing bidentate binuclear adsorption complex, which is similar to the sample at high V(V) concentration (1.2×10^{-3} M) and pH 9. These are the first direct observations of a decavanadate adsorption species on hematite using EXAFS and support the conclusions from previous ATR-FTIR analysis that decavanadate forms under acidic conditions as octahedrally coordinated adsorbed species (Vessey et al., 2020).

In **Chapter 6** the adsorption of Mo(VI) to magnetite and biogenic magnetic was analysed through aqueous solution chemistry and XAS and indicated that, as with the hematite results in Chapter 4, pH and initial Mo(VI) concentration are key variables of adsorption, but that there was the added potential for reduction of Mo(VI) under certain conditions as magnetite contains both Fe(II) as well as Fe(III). Mo(VI) (initial concentration 0.6×10^{-4} M) was fully removed by the magnetite at pH values below 7 and that as pH was increased the amount of Mo(VI) removed from solution decreased. Langmuir isotherm modelling suggests that adsorption is the main process when Mo(VI) interacts with magnetite at Mo(VI) concentration up to 2×10^{-3} M and pH 7. For Mo(VI) (0.6×10^{-4} M) adsorption to biogenic magnetite, the majority of the Mo(VI) was reduced by biogenic magnetite between pH 5-7 with decreased absorption at higher pH, however the decrease with increasing pH was less sharp and did not fall to the same minimum values as for magnetite (~40% vs. 10%). XAS analysis for Mo(VI) (0.6×10^{-4} M) adsorption to magnetite indicates high pH (pH>9) has more potential to reduce Mo(VI) to Mo(IV) to form $\text{Mo(IV)}\text{O}_2$. Two processes are observed at pH 7, with Mo dominantly adsorbed on magnetite via corner-sharing octahedra and 3.7% of Mo(VI) reduced to $\text{Mo(IV)}\text{O}_2$. At pH 5.5, Mo(VI) sorbs to magnetite via an inner-sphere octahedral bidentate binuclear adsorption complex. These results show the ability of Fe(II)-bearing iron oxides (magnetite) to act as a possible remediation agent for controlling the environmental mobility of molybdenum through absorption and reduction processes under a variety of environmental conditions. It was not able

to collect EXAFS data on the biogenic magnetite due to the COVID-19. So this would be part of the further work to allow the bioproduced and synthetic materials to be fully contrasted.

Overall, this project highlights the key role that iron (oxyhydr)oxides, including hematite, magnetite and biogenic magnetite, have in controlling the mobility and speciation of Mo(VI) and V(V) in the environment. The amount of removal from solution of Mo(VI) and V(V) is highly dependent on pH, initial concentration of the sorbent and the chemistry of the iron oxide. From investigations presented in this thesis three main processes were identified: 1. Formation of poly- or mono- molybdate/vanadate adsorption complexes on hematite, and 2. Reduction to a lower oxidation state (e.g. Mo(IV)) and concurrent adsorption to Fe(II)-bearing iron oxide (magnetite). This project combining multiple technique approach holistically provides a detailed molecular scale understanding of the poly- or mono- Mo(VI) and V(V) adsorption and reduction mechanisms and gives a comprehensive dataset for determining the environmental mobility of Mo and V in a variety of geochemical scenarios.

7.2 Future Work

I. Density Functional Theory + U correction (DFT+U) Computational Calculations for V(V) Adsorption to Hematite

Chapter 5 studied mono- or poly- vanadate adsorption to hematite and multiple techniques including PHREEQC, ATR-FTIR, and XAS indicated octahedral decavanadate was present at low pH (3-5.5). However, the complexation of decavanadate on the hematite surface is still unclear since no V-Fe shell was fitted using EXAFS. Previous work on Mo(VI) and W(VI) adsorption to hematite applied Density Functional Theory + U correction (DFT+U) computational calculations to provide detailed information on the complexity of Mo solution chemistry and polymerisation of Mo on the hematite surface, suggesting a three-dimensional cluster containing three, four or five molybdate ions in both tetrahedral and octahedral

coordination (Davantes et al., 2017). Using DFT+U calculations to model the surface complexation of V on the hematite would provide a detailed understanding, at the atomic scale, of the degree of V polymerization upon adsorption on the hematite surface. Combined with the obtained PHREEQC, ATR-FTIR and EXAFS results, it would provide a comprehensive dataset for determining the adsorption complex of polyvanadate (especially decavanadate) on the hematite surface.

II. Investigation of V(V) and Mo(VI) Adsorption to Magnetite and Biogenic Magnetite Applying Multi-technique Approach

Future work would initially focus on V(V) and Mo(VI) adsorption to magnetite and biogenic magnetite under varying environmental conditions (pH 5.5-12, [V(V)] 1.2×10^{-4} M – 1.2×10^{-3} M, [Mo(VI)] 0.6×10^{-4} M - 5×10^{-4} M) by applying Attenuated Total Reflection-Fourier Transform Infrared Spectroscopy (ATR-FTIR) and X-ray absorption spectroscopy (XAS) analyses to contrast the synthetic with the bioproduced materials. The aqueous geochemical analyses for V(V) and Mo(VI) adsorption onto magnetite and biogenic magnetite has been performed and shown in Appendix 2 and Chapter 6 respectively. Attenuated Total Reflection-Fourier Transform Infrared Spectroscopy (ATR-FTIR) is an advanced technique that can provide information of speciation of V on the iron oxide surfaces. In chapter 5 the ATR-FTIR study of V(V) adsorption to hematite was a key component of the evidence supporting polyvanadate forming in acidic systems at V(V) concentration of 1.2×10^{-3} M. In addition, the EXAFS result in Chapter 6 of Mo(VI) adsorption to magnetite indicated that reduction of Mo(VI) occurred under certain geochemical conditions. Therefore, studying the speciation of V(V) on magnetite surface using ATR-FTIR and EXAFS would provide detailed information at the molecular scale absorption mechanisms and determine whether there are mono- or polyvanadate adsorption complexes and also whether there is any reduction of V(V) to V(II-IV) on the magnetite surface at certain pH.

Additionally, Chapter 6 studied Mo(VI) (0.6×10^{-4} M) adsorption to the Fe(II)-bearing iron oxides (magnetite) and indicated varying absorption processes occurred under the range of pH conditions tested, with EXAFS identifying adsorption under acidic conditions, incorporation at neutral pH and reduction under alkaline systems. The application of ATR-FTIR for both substrates and completing the EXAFS analyses for key pH values for biogenic magnetite would allow the bioproduced and synthetic materials to be fully contrasted and would aid the evaluation of the behaviour of these two key contaminants under environmentally relevant conditions.

III. Mo(VI) and V(V) Adsorption to Different Fe(II)-bearing Iron Oxides

Chapter 6 involved Fe(II)-bearing iron oxides including magnetite and biogenic magnetite to sorb the emerging contaminant (Mo). Future work would also investigate Mo(VI) and V(V) adsorption to a variety of Fe(II)-bearing phase such as Fe(II)-bearing clay minerals and Fe(II)/Fe(III) Hydroxide (Green Rust) under varying conditions (pH 3-12, [Mo(VI)] 0.6×10^{-4} M - 5×10^{-4} M, [V(V)] 1.2×10^{-4} M – 1.2×10^{-3} M) applying multiple techniques including aqueous chemical analyses, ATR-FTIR and XAS. There have been some work that Fe(II)-bearing clays and green rust can reduce uranium (U(VI)) to U(IV) or U(V) and form UO_2 phase (O'Loughlin et al., 2003, Latta et al., 2012). In Chapter 6 work studied the Mo(VI) adsorption to Fe(II)-bearing iron oxides (magnetite) indicated magnetite has the ability to reduce Mo(VI) to (Mo(IV)). It would be interest to investigate these two anions within more environmental conditions to determine whether there are Mo(VI) and V(V) adsorption complexes and also whether there is any reduction of Mo(VI) and V(V) on the Fe(II)-bearing clays and green rust surfaces at certain geochemical conditions.

The potential future work detailed within this section, in addition to the research performed in this project, provides a detailed molecular scale understanding of Mo and V interactions with iron oxides and would extend the knowledge base for these key contaminants.

8. References

- AGARWALA, S., SHARMA, C., FAROOQ, S. & CHATTERJEE, C. 1978. Effect of molybdenum deficiency on the growth and metabolism of corn plants raised in sand culture. *Canadian Journal of Botany*, 56, 1905-1908.
- AL KUISI, M., AL-HWAITI, M., MASHAL, K. & ABED, A. M. 2015. Spatial distribution patterns of molybdenum (Mo) concentrations in potable groundwater in Northern Jordan. *Environmental monitoring and assessment*, 187, 148.
- ALFARO, I., MOLINA, L., GONZÁLEZ, P., GAETE, J., VALENZUELA, F., MARCO, J. F., SÁEZ, C. & BASUALTO, C. 2019. Silica-coated magnetite nanoparticles functionalized with betaine and their use as an adsorbent for Mo (VI) and Re (VII) species from acidic aqueous solutions. *Journal of Industrial and Engineering Chemistry*, 78, 271-283.
- ALMASRI, D. A., SALEH, N. B., ATIEH, M. A., MCKAY, G. & AHZI, S. 2019. Adsorption of phosphate on iron oxide doped halloysite nanotubes. *Scientific reports*, 9, 1-13.
- AMMANN, A. A. 2007. Inductively coupled plasma mass spectrometry (ICP MS): a versatile tool. *Journal of mass spectrometry*, 42, 419-427.
- ARAI, Y. 2010. X-ray Absorption Spectroscopic Investigation of Molybdenum Multinuclear Sorption Mechanism at the Goethite– Water Interface. *Environmental science & technology*, 44, 8491-8496.
- ARCE, F., IGLESIAS, A. C., LÓPEZ, R., GONDAR, D., ANTELO, J. & FIOL, S. 2011. Interactions Between Ionic Pesticides and Model Systems for Soil Fractions. *Pesticides in the Modern World-Risks and Benefits*. InTech.
- ARENA, G., COPAT, C., DIMARTINO, A., GRASSO, A., FALLICO, R., SCIACCA, S., FIORE, M. & FERRANTE, M. 2015. Determination of total vanadium and vanadium (V) in groundwater from Mt. Etna and estimate of daily intake of vanadium (V) through drinking water. *Journal of water and health*, 13, 522-530.
- ARNON, D. & STOUT, P. 1939. Molybdenum as an essential element for higher plants. *Plant physiology*, 14, 599.
- AYOTTE, J. D., GRONBERG, J. M. & APODACA, L. E. 2011. *Trace elements and radon in groundwater across the United States, 1992-2003*, US Department of the Interior, US Geological Survey.
- BAKER, M. L., MARA, M. W., YAN, J. J., HODGSON, K. O., HEDMAN, B. & SOLOMON, E. I. 2017. K-and L-edge X-ray absorption spectroscopy (XAS) and resonant inelastic X-ray scattering (RIXS) determination of differential orbital covalency (DOC) of transition metal sites. *Coordination chemistry reviews*, 345, 182-208.
- BALANDIS, V., ZAMANA, L. & PTITSYN, A. 2005. Chemical characteristics of natural waters: dependence on the geologic structure of the Uronai ore unit, eastern Transbaikalia. *RUSSIAN GEOLOGY AND GEOPHYSICS*, 46, 632-639.
- BARAN, E. & NRIAGU, J. 1998. Vanadium in the environment. Part 2. Health effects. Wiley, New York.
- BIRCH, W. D., PRING, A., MCBRIAR, E. M., GATEHOUSE, B. M. & MCCAMMON, C. A. 1998. Bamfordite, $\text{Fe}^{3+}\text{Mo}_2\text{O}_6(\text{OH})_3 \cdot \text{H}_2\text{O}$, a new hydrated iron molybdenum oxyhydroxide from Queensland, Australia: Description and crystal chemistry. *American Mineralogist*, 83, 172-177.
- BLACKMORE, D., ELLIS, J. & RILEY, P. 1996. Treatment of a vanadium-containing effluent by adsorption/coprecipitation with iron oxyhydroxide. *Water Research*, 30, 2512-2516.

- BORDAGE, A., BALAN, E., DE VILLIERS, J. P., CROMARTY, R., JUHIN, A., CARVALLO, C., CALAS, G., RAJU, P. S. & GLATZEL, P. 2011. V oxidation state in Fe–Ti oxides by high-energy resolution fluorescence-detected X-ray absorption spectroscopy. *Physics and Chemistry of Minerals*, 38, 449-458.
- BORG, H. 1984. Background levels of trace metals in Swedish freshwaters.
- BRADFORD, G., BAKHTAR, D. & WESTCOT, D. 1990. Uranium, vanadium, and molybdenum in saline waters of California. Wiley Online Library.
- BREILLAT, N., GUERROT, C., MARCOUX, E. & NÉGREL, P. 2016. A new global database of ^{89}Mo in molybdenites: A literature review and new data. *Journal of Geochemical Exploration*, 161, 1-15.
- BREIT, G. N. & WANTY, R. B. 1991. Vanadium accumulation in carbonaceous rocks: a review of geochemical controls during deposition and diagenesis. *Chemical Geology*, 91, 83-97.
- BRINZA, L., BENNING, L. G. & STATHAM, P. J. 2008. Adsorption studies of Mo and V onto ferrihydrite. *Mineralogical Magazine*, 72, 385-388.
- BRINZA, L., VU, H. P., NEAMTU, M. & BENNING, L. G. 2019. Experimental and simulation results of the adsorption of Mo and V onto ferrihydrite. *Scientific reports*, 9, 1-12.
- BRINZA, L., VU, H. P., SHAW, S., MOSSELMANS, J. F. W. & BENNING, L. G. 2015. Effect of Mo and V on the hydrothermal crystallization of hematite from ferrihydrite: An in situ energy dispersive X-ray diffraction and X-ray absorption spectroscopy study. *Crystal Growth & Design*, 15, 4768-4780.
- BRUNAUER, S., EMMETT, P. H. & TELLER, E. 1938. Adsorption of gases in multimolecular layers. *Journal of the American chemical society*, 60, 309-319.
- CALVIN, S. 2013. *XAFS for Everyone*, CRC press.
- CAPPUYNS, V. & SLABBINCK, E. 2012. Occurrence of vanadium in Belgian and European alluvial soils. *Applied and Environmental Soil Science*, 2012.
- CAPPUYNS, V. & SWENNEN, R. 2014. Release of vanadium from oxidized sediments: insights from different extraction and leaching procedures. *Environmental Science and Pollution Research*, 21, 2272-2282.
- CECI, A., RHEE, Y. J., KIERANS, M., HILLIER, S., PENDLowski, H., GRAY, N., PERSIANI, A. M. & GADD, G. M. 2015. Transformation of vanadinite [Pb₅(VO₄)₃Cl] by fungi. *Environmental microbiology*, 17, 2018-2034.
- CHEN, L., LIU, J.-R., GAO, J., HU, W.-F. & YANG, J.-Y. 2020. Vanadium in Soil-Plant System: Source, Fate, Toxicity, and Bioremediation. *Journal of Hazardous Materials*, 124200.
- CLAUSEN, L. & FABRICIUS, I. 2000. BET measurements: outgassing of minerals. *Journal of Colloid and Interface Science*, 227, 7-15.
- COKER, V. S., PEARCE, C. I., LANG, C., VAN DER LAAN, G., PATTRICK, R. A., TELLING, N. D., SCHÜLER, D., ARENHOLZ, E. & LLOYD, J. R. 2007. Cation site occupancy of biogenic magnetite compared to polygenic ferrite spinels determined by X-ray magnetic circular dichroism. *European Journal of Mineralogy*, 19, 707-716.
- COKER, V. S., PEARCE, C. I., PATTRICK, R. A., VAN DER LAAN, G., TELLING, N. D., CHARNOCK, J. M., ARENHOLZ, E. & LLOYD, J. R. 2008. Probing the site occupancies of Co-, Ni-, and Mn-substituted biogenic magnetite using XAS and XMCD. *American Mineralogist*, 93, 1119-1132.
- COOK, R. B. 2001. Handbook of Mineralogy. *Rocks and Minerals*, 76, 278.
- CORNELL, R. M. & SCHWERTMANN, U. 2003. *The iron oxides: structure, properties, reactions, occurrences and uses*, John Wiley & Sons.

- CORNELL, R. M. & SCHWERTMANN, U. 2004. Crystal structure. *The Iron Oxides: Structure, Properties, Reactions, Occurrences and Uses, Second Edition*, 9-38.
- COUNCIL, N. R. 1989. National Academy of Science (1989) Recommended Dietary Allowance. *Food and Nutrition Board. USA.*
- CRANS, D. C., AMIN, S. S. & KERAMIDAS, A. D. 1998. Chemistry of relevance to vanadium in the environment. *ADVANCES IN ENVIRONMENTAL SCIENCE AND TECHNOLOGY-NEW YORK-*, 30, 73-96.
- CREAN, D. E., COKER, V. S., VAN DER LAAN, G. & LLOYD, J. R. 2012. Engineering biogenic magnetite for sustained Cr (VI) remediation in flow-through systems. *Environmental science & technology*, 46, 3352-3359.
- CRUYWAGEN, J. 1999. Protonation, oligomerization, and condensation reactions of vanadate (V), molybdate (VI), and tungstate (VI). *Advances in inorganic chemistry*. Elsevier.
- CULLITY, B. & STOCK, S. 2001. Elements of x-ray diffraction, Prentice Hall. *Upper Saddle River, NJ*, 388.
- DAHL, T. W., CHAPPAZ, A., FITTS, J. P. & LYONS, T. W. 2013. Molybdenum reduction in a sulfidic lake: Evidence from X-ray absorption fine-structure spectroscopy and implications for the Mo paleoproxy. *Geochimica et Cosmochimica Acta*, 103, 213-231.
- DAS, A. K., CHAKRABORTY, R., CERVERA, M. L. & DE LA GUARDIA, M. 2007. A review on molybdenum determination in solid geological samples. *Talanta*, 71, 987-1000.
- DAS, D., SURESHKUMAR, M., KOLEY, S., MITHAL, N. & PILLAI, C. 2010. Sorption of uranium on magnetite nanoparticles. *Journal of Radioanalytical and Nuclear Chemistry*, 285, 447-454.
- DAS, S., ESSILFIE-DUGHAN, J. & HENDRY, M. J. 2016. Sequestration of molybdate during transformation of 2-line ferrihydrite under alkaline conditions. *Applied geochemistry*, 73, 70-80.
- DAS, S. & HENDRY, M. J. 2013. Adsorption of molybdate by synthetic hematite under alkaline conditions: effects of aging. *Applied geochemistry*, 28, 194-201.
- DAVANTES, A., COSTA, D. & LEFÈVRE, G. 2016. Molybdenum (VI) adsorption onto lepidocrocite (γ -FeOOH): in situ vibrational spectroscopy and DFT+ U theoretical study. *The Journal of Physical Chemistry C*, 120, 11871-11881.
- DAVANTES, A., COSTA, D., SALLMAN, B., RAKSHIT, S. & LEFÈVRE, G. 2017. Surface polymerization of Mo (VI) and W (VI) anions on hematite revealed by in situ infrared spectroscopy and DFT+ U theoretical study. *The Journal of Physical Chemistry C*, 121, 324-332.
- DAVANTÈS, A. & LEFÈVRE, G. 2013. In situ real time infrared spectroscopy of sorption of (poly) molybdate ions into layered double hydroxides. *The Journal of Physical Chemistry A*, 117, 12922-12929.
- DENT, A., CIBIN, G., RAMOS, S., SMITH, A., SCOTT, S., VARANDAS, L., PEARSON, M., KRUMPA, N., JONES, C. & ROBBINS, P. B18: A core XAS spectroscopy beamline for Diamond. *Journal of Physics: Conference Series*, 2009. IOP Publishing, 012039.
- DIAZ-MORENO, S., AMBOAGE, M., BASHAM, M., BOADA, R., BRICKNELL, N. E., CIBIN, G., COBB, T. M., FILIK, J., FREEMAN, A. & GERAKI, K. 2018. The spectroscopy village at diamond light source. *Journal of synchrotron radiation*, 25, 998-1009.
- DIAZ-MORENO, S., HAYAMA, S., AMBOAGE, M., FREEMAN, A., SUTTER, J. & DULLER, G. I20; the versatile X-ray absorption spectroscopy beamline at diamond light source. *Journal of Physics: Conference Series*, 2009. IOP Publishing, 012038.

- DOE, U. 1999. Final site observational work plan for the UMTRA project Old Rifle site GJO-99-88-TAR. *Department of Energy US, editor. Grand Junction, CO.*
- DOWNWARD, L., BOOTH, C., LUKENS, W. & BRIDGES, F. A Variation of the F - Test for Determining Statistical Relevance of Particular Parameters in EXAFS Fits. *AIP Conference Proceedings*, 2007. American Institute of Physics, 129-131.
- EFROYMSON, R., SUTER, G., SAMPLE, B. & JONES, D. 1996. Preliminary remediation goals for ecological endpoints. Oak Ridge National Lab.
- EGERTON, R. F. 2005. *Physical principles of electron microscopy*, Springer.
- EMSLEY, J. 2011. *Nature's building blocks: an AZ guide to the elements*, Oxford University Press.
- EPP, J. 2016. X-ray diffraction (XRD) techniques for materials characterization. *Materials characterization using nondestructive evaluation (NDE) methods*. Elsevier.
- ESPAÑA, J. S., TORIL, E. G., PAMO, E. L., AMILS, R., ERCILLA, M. D., PASTOR, E. S. & SAN MARTÍN-ÚRIZ, P. 2008. Biogeochemistry of a hyperacidic and ultraconcentrated pyrite leachate in San Telmo mine (Iberian Pyrite Belt, Spain). *Water, air, and soil pollution*, 194, 243-257.
- EVANS JR, H. T. 1966. The molecular structure of the isopoly complex ion, decavanadate (V₁₀O₂₈6-). *Inorganic Chemistry*, 5, 967-977.
- FRANK, A., MADEJ, A., GALGAN, V. & PETERSSON, L. 1996. Vanadium poisoning of cattle with basic slag. Concentrations in tissues from poisoned animals and from a reference, slaughter-house material. *Science of the total environment*, 181, 73-92.
- FRASCOLI, F. & HUDSON-EDWARDS, K. A. 2018. Geochemistry, mineralogy and microbiology of molybdenum in mining-affected environments. *Minerals*, 8, 42.
- GEHRING, A., FRY, I., LUSTER, J. & SPOSITO, G. 1993. The chemical form of vanadium (IV) in kaolinite. *Clays and Clay Minerals*, 41, 662-667.
- GOLDBERG, S., FORSTER, H. & GODFREY, C. 1996. Molybdenum adsorption on oxides, clay minerals, and soils. *Soil Science Society of America Journal*, 60, 425-432.
- GOLDBERG, S., FORSTER, H. & HEICK, E. 1993. Boron adsorption mechanisms on oxides, clay minerals, and soils inferred from ionic strength effects. *Soil Science Society of America Journal*, 57, 704-708.
- GOLDBERG, S., JOHNSTON, C. T., SUAREZ, D. L. & LESCH, S. M. 2007. Mechanism of molybdenum adsorption on soils and soil minerals evaluated using vibrational spectroscopy and surface complexation modeling. *Developments in Earth and Environmental Sciences*, 7, 235-266.
- GOLDBERG, S., SU, C. & FORSTER, H. S. 1998. Sorption of molybdenum on oxides, clay minerals, and soils. *Adsorption of Metals by Geomedia*. Academic Press, San Diego, 401-426.
- GOLDBERG, T., ARCHER, C., VANCE, D. & POULTON, S. W. 2009. Mo isotope fractionation during adsorption to Fe (oxyhydr) oxides. *Geochimica et Cosmochimica Acta*, 73, 6502-6516.
- GÖRN, M. G., BOLANZ, R. M., PARRY, S., GÖTTLICHER, J., STEININGER, R. & MAJZLAN, J. 2021. INCORPORATION OF Mo 6+ IN FERRIHYDRITE, GOETHITE, AND HEMATITE. *Clays and Clay Minerals*, 1-17.
- GRIFFITH, W. & LESNIAK, P. 1969. Raman studies on species in aqueous solutions. Part III. Vanadates, molybdates, and tungstates. *Journal of the Chemical Society A: Inorganic, Physical, Theoretical*, 1066-1071.
- GRIFFITHS, P. R. 2006. Introduction to the theory and instrumentation for vibrational spectroscopy. *Applications of Vibrational Spectroscopy in Food Science; Part One: Introduction and Basic Concepts*, 31-46.

- GUO, H. & WANG, Y. 2005. Geochemical characteristics of shallow groundwater in Datong basin, northwestern China. *Journal of Geochemical Exploration*, 87, 109-120.
- GUPTA, U. C. 1997. Symptoms of molybdenum deficiency and toxicity in crops.
- GUPTA, U. C. & GUPTA, S. C. 1998. Trace element toxicity relationships to crop production and livestock and human health: implications for management. *Communications in Soil Science and Plant Analysis*, 29, 1491-1522.
- GUSTAFSSON, J. P. 2003. Modelling molybdate and tungstate adsorption to ferrihydrite. *Chemical geology*, 200, 105-115.
- GUSTAFSSON, J. P. 2019. Vanadium geochemistry in the biogeosphere—speciation, solid-solution interactions, and ecotoxicity. *Applied Geochemistry*, 102, 1-25.
- GUSTAFSSON, J. P. & TIBERG, C. 2015. Molybdenum binding to soil constituents in acid soils: an XAS and modelling study. *Chemical Geology*, 417, 279-288.
- HAYES, K. F., PAPELIS, C. & LECKIE, J. O. 1988. Modeling ionic strength effects on anion adsorption at hydrous oxide/solution interfaces. *Journal of Colloid and Interface Science*, 125, 717-726.
- HOF, M. 2003. Basics of optical spectroscopy. *Handbook of Spectroscopy*, 1, 39-47.
- HUANG, X., SILLANPÄÄ, M., GJESSING, E. T., PERÄNIEMI, S. & VOGT, R. D. 2010. Environmental impact of mining activities on the surface water quality in Tibet: Gyama valley. *Science of the total environment*, 408, 4177-4184.
- HUANG, Y. H., TANG, C. & ZENG, H. 2012. Removing molybdate from water using a hybridized zero-valent iron/magnetite/Fe (II) treatment system. *Chemical engineering journal*, 200, 257-263.
- HUR, H. & REEDER, R. J. 2016. Tungstate sorption mechanisms on boehmite: Systematic uptake studies and X-ray absorption spectroscopy analysis. *Journal of colloid and interface science*, 461, 249-260.
- IMTIAZ, M., RIZWAN, M. S., XIONG, S., LI, H., ASHRAF, M., SHAHZAD, S. M., SHAHZAD, M., RIZWAN, M. & TU, S. 2015. Vanadium, recent advancements and research prospects: a review. *Environment international*, 80, 79-88.
- INKSON, B. 2016. Scanning electron microscopy (SEM) and transmission electron microscopy (TEM) for materials characterization. *Materials characterization using nondestructive evaluation (NDE) methods*. Elsevier.
- JANSSON-CHARRIER, M., GUIBAL, E., ROUSSY, J., DELANGHE, B. & LE CLOIREC, P. 1996. Vanadium (IV) sorption by chitosan: kinetics and equilibrium. *Water Research*, 30, 465-475.
- JIANG, W., CAI, Q., XU, W., YANG, M., CAI, Y., DIONYSIOU, D. D. & O'SHEA, K. E. 2014. Cr (VI) adsorption and reduction by humic acid coated on magnetite. *Environmental science & technology*, 48, 8078-8085.
- KABATA-PENDIAS, A. & PENDIAS, H. 1999. Biogeochemistry of trace elements. PWN, Warszawa. *Polish Google Scholar*.
- KASHIWABARA, T., TAKAHASHI, Y., MARCUS, M. A., URUGA, T., TANIDA, H., TERADA, Y. & USUI, A. 2013. Tungsten species in natural ferromanganese oxides related to its different behavior from molybdenum in oxic ocean. *Geochimica et Cosmochimica Acta*, 106, 364-378.
- KIM, M. & JANG, M. 2010. Adsorption of molybdate onto hematite: kinetics and equilibrium. *Water Geosci*, 30, 170-173.
- KRAUSKOPF, K. B. 1979. *Introduction to geochemistry*, McGraw-Hill.
- KRISHNAN, C., GARNETT, M., HSIAO, B. & CHU, A. B. 2007. Electrochemical measurements of isopolyoxomolybdates: 1. pH dependent behavior of sodium molybdate. *Int. J. Electrochem. Sci*, 2, 29-51.

- KROPSCHOT, S. J. 2010. Molybdenum-A Key Component of Metal Alloys. US Geological Survey.
- KUBOTA, J. 1975. Areas of molybdenum toxicity to grazing animals in the western states. *Journal of Range Management*, 252-256.
- LARSSON, M. A., PERSSON, I., SJÖSTEDT, C. & GUSTAFSSON, J. P. 2017. Vanadate complexation to ferrihydrite: X-ray absorption spectroscopy and CD-MUSIC modelling. *Environmental Chemistry*, 14, 141-150.
- LATTA, D. E., BOYANOV, M. I., KEMNER, K. M., O'LOUGHLIN, E. J. & SCHERER, M. M. 2012. Abiotic reduction of uranium by Fe (II) in soil. *Applied geochemistry*, 27, 1512-1524.
- LAZARIDIS, N. & ASOUHIDOU, D. 2003. Kinetics of sorptive removal of chromium (VI) from aqueous solutions by calcined Mg-Al-CO₃ hydrotalcite. *Water Research*, 37, 2875-2882.
- LEGODI, M. A. & DE WAAL, D. 2007. The preparation of magnetite, goethite, hematite and maghemite of pigment quality from mill scale iron waste. *Dyes and Pigments*, 74, 161-168.
- LEYBOURNE, M. I. & CAMERON, E. M. 2008. Source, transport, and fate of rhenium, selenium, molybdenum, arsenic, and copper in groundwater associated with porphyry-Cu deposits, Atacama Desert, Chile. *Chemical Geology*, 247, 208-228.
- LLOYD, J. R. 2003. Microbial reduction of metals and radionuclides. *FEMS microbiology reviews*, 27, 411-425.
- LLOYD, J. R., LEANG, C., MYERSON, A. L. H., COPPI, M. V., CUIFO, S., METHE, B., SANDLER, S. J. & LOVLEY, D. R. 2003. Biochemical and genetic characterization of PpcA, a periplasmic c-type cytochrome in *Geobacter sulfurreducens*. *Biochemical Journal*, 369, 153-161.
- LOURIGAN, J. & PHELPS, W. 2013. Caledonia Groundwater Molybdenum Investigation Southeast Wisconsin. *Wisconsin Department of Natural Resources*.
- LOVLEY, D. R. & PHILLIPS, E. J. 1988. Novel mode of microbial energy metabolism: organic carbon oxidation coupled to dissimilatory reduction of iron or manganese. *Applied and environmental microbiology*, 54, 1472-1480.
- LOVLEY, D. R., STOLZ, J. F., NORD, G. L. & PHILLIPS, E. J. 1987. Anaerobic production of magnetite by a dissimilatory iron-reducing microorganism. *Nature*, 330, 252-254.
- MARQUES, M. P. M., GIANOLIO, D., RAMOS, S., BATISTA DE CARVALHO, L. A. & AURELIANO, M. 2017. An EXAFS approach to the study of polyoxometalate-protein interactions: the case of decavanadate-Actin. *Inorganic chemistry*, 56, 10893-10903.
- MARSHALL, T. A., MORRIS, K., LAW, G. T., MOSSELMANS, J. F. W., BOTS, P., ROBERTS, H. & SHAW, S. 2015. Uranium fate during crystallization of magnetite from ferrihydrite in conditions relevant to the disposal of radioactive waste. *Mineralogical Magazine*, 79, 1265-1274.
- MARTIN, H. & KAPLAN, D. 1998. Temporal changes in cadmium, thallium, and vanadium mobility in soil and phytoavailability under field conditions. *Water, air, and soil pollution*, 101, 399-410.
- MARTIN, S., SACO, D. & ALVAREZ, M. 1995. Nitrogen metabolism in Nicotiana a rustica L. grown with molybdenum. II. flowering stage. *Communications in soil science and plant analysis*, 26, 1733-1747.
- MEJIA, J., RODRIGUEZ, R., ARMIENTA, A., MATA, E. & FIORUCCI, A. 2007. Aquifer vulnerability zoning, an indicator of atmospheric pollutants input? Vanadium in the Salamanca aquifer, Mexico. *Water, air, and soil pollution*, 185, 95-100.

- MITCHELL, P. 2009. Speciation of molybdenum compounds in water. *Report for the International Molybdenum Association REACH Molybdenum Consortium in Ultraviolet Spectra and REACH Read Across*.
- MONTERO-SERRANO, J., MARTINEZ-SANTANA, M., TRIBOVILLARD, N., RIBOULLEAU, A. & GARBAN, G. 2009. Geochemical behavior of molybdenum and its isotopes in the sedimentary environment—a bibliographic review. *Rev. Biol. Mar. Oceanogr.*, 44, 263-275.
- MOON, J.-W., RAWN, C. J., RONDINONE, A. J., WANG, W., VALI, H., YEARY, L. W., LOVE, L. J., KIRKHAM, M. J., GU, B. & PHELPS, T. J. 2010. Crystallite sizes and lattice parameters of nano-biomagnetite particles. *Journal of nanoscience and nanotechnology*, 10, 8298-8306.
- MORRISON, S. J. & SPANGLER, R. R. 1992. Extraction of uranium and molybdenum from aqueous solutions: a survey of industrial materials for use in chemical barriers for uranium mill tailings remediation. *Environmental Science & Technology*, 26, 1922-1931.
- MOSKALYK, R. & ALFANTAZI, A. 2003. Processing of vanadium: a review. *Minerals Engineering*, 16, 793-805.
- MOSSER, C., BOUDEULLE, M., WEBER, F. & PACQUET, A. 1996. Ferriferous and vanadiferous kaolinites from the hydrothermal alteration halo of the Cigar Lake uranium deposit (Canada). *Clay Minerals*, 31, 291-299.
- MOULDER, J. F., STICKLE, W. F., SOBOL, P. E. & BOMBEN, K. D. 1992. Handbook of X-ray photoelectron spectroscopy; Chastain, J. *Perkin-Elmer Corp., Eden Prairie, MN*.
- MTHOMBENI, N. H., MBAKOP, S., OCHIENG, A. & ONYANGO, M. S. 2016. Vanadium (V) adsorption isotherms and kinetics using polypyrrole coated magnetized natural zeolite. *Journal of the Taiwan Institute of Chemical Engineers*, 66, 172-180.
- MUDUNKOTUWA, I. A., AL MINSHID, A. & GRASSIAN, V. H. 2014. ATR-FTIR spectroscopy as a tool to probe surface adsorption on nanoparticles at the liquid–solid interface in environmentally and biologically relevant media. *Analyst*, 139, 870-881.
- MULROY, D. 2020. *The microbiology of lateritic Co-Ni-bearing manganese oxides*. University of Manchester.
- NAEEM, A., WESTERHOFF, P. & MUSTAFA, S. 2007. Vanadium removal by metal (hydr) oxide adsorbents. *Water Research*, 41, 1596-1602.
- NAKAMURA, T. & HARUYAMA, S. 1978. Anodic dissolution of vanadium in solutions of varying pH. *Denki Kagaku*, 46, 100-106.
- NEWVILLE, M. 2004. Fundamentals of X-ray absorption fine structure. *Consortium for Advanced Radiation Sources, University of Chicago (USA)*[<http://xafs.org>].
- NEWVILLE, M. 2014. Fundamentals of XAFS. *Reviews in Mineralogy and Geochemistry*, 78, 33-74.
- NGO, P. D. 1999. Energy dispersive spectroscopy. *Failure Analysis of Integrated Circuits*. Springer.
- NIELSEN, F. H. & UTHUS, E. O. 1990. The essentiality and metabolism of vanadium. *Vanadium in biological systems*. Springer.
- O'LOUGHLIN, E. J., KELLY, S. D., COOK, R. E., CSENCITS, R. & KEMNER, K. M. 2003. Reduction of uranium (VI) by mixed iron (II)/iron (III) hydroxide (green rust): formation of UO₂ nanoparticles. *Environmental science & technology*, 37, 721-727.
- OCH, L. M., SHIELDS-ZHOU, G. A., POULTON, S. W., MANNING, C., THIRLWALL, M. F., LI, D., CHEN, X., LING, H., OSBORN, T. & CREMONESE, L. 2013. Redox changes in Early Cambrian black shales at Xiaotan section, Yunnan Province, south China. *Precambrian Research*, 225, 166-189.

- OLESIK, J. W. 1991. Elemental analysis using ICP-OES and ICP/MS. *Analytical Chemistry*, 63, 12A-21A.
- OYERINDE, O. F., WEEKS, C. L., ANBAR, A. D. & SPIRO, T. G. 2008. Solution structure of molybdic acid from Raman spectroscopy and DFT analysis. *Inorganica Chimica Acta*, 361, 1000-1007.
- OZEKI, T., KIHARA, H. & IKEDA, S. 1988. Study of equilibria in 0.03 mM molybdate acidic aqueous solutions by factor analysis applied to ultraviolet spectra. *Analytical Chemistry*, 60, 2055-2059.
- PANICHEV, N., MANDIWANA, K., MOEMA, D., MOLATLHEGI, R. & NGOBENI, P. 2006. Distribution of vanadium (V) species between soil and plants in the vicinity of vanadium mine. *Journal of hazardous materials*, 137, 649-653.
- PARNELL, J. & LINDGREN, P. 2016. Anomalous supply of bioessential molybdenum in mid-Proterozoic surface environments. *Precambrian Research*, 275, 100-104.
- PEACOCK, C. L. & SHERMAN, D. M. 2004. Vanadium (V) adsorption onto goethite (α -FeOOH) at pH 1.5 to 12: a surface complexation model based on ab initio molecular geometries and EXAFS spectroscopy. *Geochimica et Cosmochimica Acta*, 68, 1723-1733.
- POŁĘDNIOK, J. & BUHL, F. 2003. Speciation of vanadium in soil. *Talanta*, 59, 1-8.
- RAJPUT, S., PITTMAN JR, C. U. & MOHAN, D. 2016. Magnetic magnetite (Fe₃O₄) nanoparticle synthesis and applications for lead (Pb²⁺) and chromium (Cr⁶⁺) removal from water. *Journal of colloid and interface science*, 468, 334-346.
- RANGO, T., BIANCHINI, G., BECCALUVA, L. & TASSINARI, R. 2010. Geochemistry and water quality assessment of central Main Ethiopian Rift natural waters with emphasis on source and occurrence of fluoride and arsenic. *Journal of African Earth Sciences*, 57, 479-491.
- RAVEL, B. & NEWVILLE, M. 2005. ATHENA, ARTEMIS, HEPHAESTUS: data analysis for X-ray absorption spectroscopy using IFEFFIT. *Journal of synchrotron radiation*, 12, 537-541.
- REDDY, K. J. & GLOSS, S. P. 1993. Geochemical speciation as related to the mobility of F, Mo and Se in soil leachates. *Applied Geochemistry*, 8, 159-163.
- REDDY, K. J., MUNN, L. C. & WANG, L. 1997. Chemistry and mineralogy of molybdenum in soils. *Molybdenum in agriculture*, 4-22.
- REDDY, K. J., WANG, L. & LINDSAY, W. L. 1990. *Molybdenum supplement to Technical Bulletin 134: Selection of standard free energies of formation for use in soil chemistry*, Colorado State University, Agricultural Experiment Station, Department of Agronomy.
- REEDER, S. 2006. *Geochemical atlas of Europe. Part 2, Interpretation of geochemical maps, additional tables, figures, maps, and related publications*, Geological Survey of Finland.
- ROBERTS, H. E., MORRIS, K., LAW, G. T., MOSSELMANS, J. F. W., BOTS, P., KVASHNINA, K. & SHAW, S. 2017. Uranium (V) incorporation mechanisms and stability in Fe (II)/Fe (III)(oxyhydr) oxides. *Environmental Science & Technology Letters*, 4, 421-426.
- ROSBORG, I., NIHLGÅRD, B., GERHARDSSON, L., GERNERSSON, M.-L., OHLIN, R. & OLSSON, T. 2005. Concentrations of inorganic elements in bottled waters on the Swedish market. *Environmental Geochemistry and Health*, 27, 217-227.
- ROSS, S. M., WOOD M.D., COPPLESTONE, D., WARRINER, M. AND CROOK, P. 2007. UK Soil and Herbage Pollutant Survey.
- SALAK, A. N., TEDIM, J., KUZNETSOVA, A. I., RIBEIRO, J. L., VIEIRA, L. G., ZHELUDKEVICH, M. L. & FERREIRA, M. G. 2012. Comparative X-ray diffraction

- and infrared spectroscopy study of Zn-Al layered double hydroxides: Vanadate vs nitrate. *Chemical Physics*, 397, 102-108.
- SCHLESINGER, W. H., KLEIN, E. M. & VENGOSH, A. 2017. Global biogeochemical cycle of vanadium. *Proceedings of the National Academy of Sciences*, 114, E11092-E11100.
- SCHNOHR, C. S. & RIDGWAY, M. C. 2015. Introduction to x-ray absorption spectroscopy. *X-ray absorption spectroscopy of semiconductors*. Springer.
- SCHWERTMANN, U. & CORNELL, R. 2000a. Iron oxide in the laboratory Wiley. vch, Weinheim, Germany.
- SCHWERTMANN, U. & CORNELL, R. 2000b. Iron oxides in the laboratory: preparation and characterization., 2nd edn (Wiley-VCH Verlag GmbH: Weinheim, Germany).
- SEAL II, R. R. 2012. Geologic and environmental characteristics of porphyry copper deposits with emphasis on potential future development in the Bristol Bay Watershed, Alaska (Appendix H). US Environmental Protection Agency.
- SEGAWA, K., SOEYA, T. & WACHS, I. E. 1992. Surface structures of supported molybdenum oxide catalysts under ambient conditions. *Journal of Catalysis*, 136, 539-553.
- SHAHID, M. K., KIM, Y. & CHOI, Y.-G. 2019. Adsorption of phosphate on magnetite-enriched particles (MEP) separated from the mill scale. *Frontiers of Environmental Science & Engineering*, 13, 1-12.
- SHIMAO, E. 1967a. The structure of Mo₇O₂₄⁶⁻ ion in the crystal of ammonium heptamolybdate tetrahydrate. *Bulletin of the Chemical Society of Japan*, 40, 1609-1613.
- SHIMAO, E. 1967b. Structure of the M₇O₂₄⁶⁻ Ion in a Crystal of Ammonium Heptamolybdate Tetrahydrate. *Nature*, 214, 170-171.
- SINGH, B. 1971. Effect of vanadium on the growth, yield and chemical composition of maize (*Zea Mays L.*). *Plant and soil*, 34, 209-213.
- SINGH, B. T. & WORT, D. 1969. Effect of vanadium on growth, chemical composition, and metabolic processes of mature sugar beet (*Beta vulgaris L.*) plants. *Plant physiology*, 44, 1321-1327.
- SKIERSZKAN, E., MAYER, K., WEIS, D. & BECKIE, R. 2016. Molybdenum and zinc stable isotope variation in mining waste rock drainage and waste rock at the Antamina mine, Peru. *Science of the Total Environment*, 550, 103-113.
- SLACK, A. V. 1968. *Phosphoric acid*, M. Dekker.
- SMEDLEY, P., COOPER, D., ANDER, E., MILNE, C. & LAPWORTH, D. 2014. Occurrence of molybdenum in British surface water and groundwater: Distributions, controls and implications for water supply. *Applied Geochemistry*, 40, 144-154.
- SMEDLEY, P., ZHANG, M., ZHANG, G. & LUO, Z. 2003. Mobilisation of arsenic and other trace elements in fluviolacustrine aquifers of the Huhhot Basin, Inner Mongolia. *Applied Geochemistry*, 18, 1453-1477.
- SMEDLEY, P. L. & KINNIBURGH, D. G. 2017. Molybdenum in natural waters: A review of occurrence, distributions and controls. *Applied Geochemistry*, 84, 387-432.
- SMEDLEY, P. L. & NICOLLI, H. B. 2014. Molybdenum distributions and controls in groundwater from the Pampean aquifer of La Pampa Province, Argentina.
- SMUDA, J., DOLD, B., SPANGENBERG, J. E., FRIESE, K., KOBEK, M. R., BUSTOS, C. A. & PFEIFER, H.-R. 2014. Element cycling during the transition from alkaline to acidic environment in an active porphyry copper tailings impoundment, Chuquicamata, Chile. *Journal of Geochemical Exploration*, 140, 23-40.
- SOLONGO, T., FUKUSHI, K., ALTANSUKH, O., TAKAHASHI, Y., AKEHI, A., BAASANSUREN, G., ARIUNTUNGALAG, Y., ENKHJIN, O., DAVAAJARGAL, B. & DAVAADORJ, D. 2018. Distribution and Chemical Speciation of Molybdenum

- in River and Pond Sediments Affected by Mining Activity in Erdenet City, Mongolia. *Minerals*, 8, 288.
- STIEFEL, E. I. 2002. The biogeochemistry of molybdenum and tungsten. *Metal ions in biological systems*, 39, 1-29.
- STOOKEY, L. L. 1970. Ferrozine---a new spectrophotometric reagent for iron. *Analytical chemistry*, 42, 779-781.
- TANAKA, T., YAMASHITA, H., TSUCHITANI, R., FUNABIKI, T. & YOSHIDA, S. 1988. X-ray absorption (EXAFS/XANES) study of supported vanadium oxide catalysts. Structure of surface vanadium oxide species on silica and γ -alumina at a low level of vanadium loading. *Journal of the Chemical Society, Faraday Transactions 1: Physical Chemistry in Condensed Phases*, 84, 2987-2999.
- TAYLOR, J., KEITH, S., CSEH, L., INGERMAN, L., CHAPPELL, L., RHOADES, J. & HUEBER, A. 2012. Toxicological profile for vanadium. *Atlanta, US: Agency for Toxic Substances and Disease Registry*, 255.
- TENG, Y., JIAO, X., WANG, J., XU, W. & YANG, J. 2009. Environmentally geochemical characteristics of vanadium in the topsoil in the Panzhihua mining area, Sichuan Province, China. *Chinese Journal of Geochemistry*, 28, 105-111.
- TOWNSEND, L. T., SHAW, S., OFILI, N. E., KALTZOYANNIS, N., WALTON, A. S., MOSSELMANS, J. F. W., NEILL, T. S., LLOYD, J. R., HEATH, S. & HIBBERD, R. 2019. Formation of a U (VI)-Persulfide Complex during Environmentally Relevant Sulfidation of Iron (Oxyhydr) oxides. *Environmental Science & Technology*, 54, 129-136.
- TWU, J. & DUTTA, P. K. 1989. Structure and reactivity of oxovanadate anions in layered lithium aluminate materials. *The Journal of Physical Chemistry*, 93, 7863-7868.
- TWU, J. & DUTTA, P. K. 1990. Decavanadate ion-pillared hydrotalcite: spectroscopic studies of the thermal decomposition process. *Journal of Catalysis*, 124, 503-510.
- UNDERWOOD, E. J. 1971. *Trace elements in human and animal nutrition*. Ed. 3, New York, USA, Academic Press, Inc.
- VERBINNEN, B., BLOCK, C., HANNES, D., LIEVENS, P., VACLAVIKOVA, M., STEFUSOVA, K., GALLIOS, G. & VANDECASTEELE, C. 2012. Removal of molybdate anions from water by adsorption on zeolite-supported magnetite. *Water Environment Research*, 84, 753-760.
- VERBINNEN, B., BLOCK, C., LIEVENS, P., VAN BRECHT, A. & VANDECASTEELE, C. 2013. Simultaneous removal of molybdenum, antimony and selenium oxyanions from wastewater by adsorption on supported magnetite. *Waste and Biomass Valorization*, 4, 635-645.
- VERBINNEN, B., BLOCK, C. & VANDECASTEELE, C. 2016. Adsorption of Oxyanions from Industrial Wastewater using Perlite - Supported Magnetite. *Water Environment Research*, 88, 408-414.
- VESSEY, C. J. & LINDSAY, M. B. 2020. Aqueous Vanadate Removal by Iron (II)-Bearing Phases under Anoxic Conditions. *Environmental science & technology*, 54, 4006-4015.
- VESSEY, C. J., SCHMIDT, M. P., ABDOLAHNEZHAD, M., PEAK, D. & LINDSAY, M. B. 2020. Adsorption of (Poly) vanadate onto Ferrihydrite and Hematite: An In Situ ATR-FTIR Study. *ACS Earth and Space Chemistry*, 4, 641-649.
- VIOLIER, E., INGLETT, P., HUNTER, K., ROYCHOUDHURY, A. & VAN CAPPELLEN, P. 2000. The ferrozine method revisited: Fe (II)/Fe (III) determination in natural waters. *Applied geochemistry*, 15, 785-790.
- VORLICEK, T. P., KAHN, M. D., KASUYA, Y. & HELZ, G. R. 2004. Capture of molybdenum in pyrite-forming sediments: role of ligand-induced reduction by polysulfides 1. *Geochimica et Cosmochimica Acta*, 68, 547-556.

- WAHL, B., REICHMANN, D., NIKS, D., KROMPHOLZ, N., HAVEMEYER, A., CLEMENT, B., MESSERSCHMIDT, T., ROTHKEGEL, M., BIESTER, H. & HILLE, R. 2010. Biochemical and spectroscopic characterization of the human mitochondrial amidoxime reducing components hmARC-1 and hmARC-2 suggests the existence of a new molybdenum enzyme family in eukaryotes. *Journal of Biological Chemistry*, 285, 37847-37859.
- WANG, D., ALLER, R. C. & SAÑUDO-WILHELMY, S. A. 2011. Redox speciation and early diagenetic behavior of dissolved molybdenum in sulfidic muds. *Marine Chemistry*, 125, 101-107.
- WANG, F. & TESSIER, A. 2009. Zero-valent sulfur and metal speciation in sediment porewaters of freshwater lakes. *Environmental science & technology*, 43, 7252-7257.
- WANG, P., WILSON, L. L., WESOLOWSKI, D. J., ROSENQVIST, J. & ANDERKO, A. 2010. Solution chemistry of Mo (III) and Mo (IV): Thermodynamic foundation for modeling localized corrosion. *Corrosion Science*, 52, 1625-1634.
- WASEDA, Y., MATSUBARA, E. & SHINODA, K. 2011. *X-ray diffraction crystallography: introduction, examples and solved problems*, Springer Science & Business Media.
- WASYLENKI, L. E., WEEKS, C. L., BARGAR, J. R., SPIRO, T. G., HEIN, J. R. & ANBAR, A. D. 2011. The molecular mechanism of Mo isotope fractionation during adsorption to birnessite. *Geochimica et Cosmochimica Acta*, 75, 5019-5031.
- WATT, J. A. J., BURKE, I. T., EDWARDS, R. A., MALCOLM, H. M., MAYES, W. M., OLSZEWSKA, J. P., PAN, G., GRAHAM, M. C., HEAL, K. V., ROSE, N. L., TURNER, S. D. & SPEARS, B. M. 2018. Vanadium: A Re-Emerging Environmental Hazard. *Environ Sci Technol*, 52, 11973-11974.
- WATTS, M. P., COKER, V. S., PARRY, S. A., PATTRICK, R. A., THOMAS, R. A., KALIN, R. & LLOYD, J. R. 2015. Biogenic nano-magnetite and nano-zero valent iron treatment of alkaline Cr (VI) leachate and chromite ore processing residue. *Applied Geochemistry*, 54, 27-42.
- WEATHERILL, J. S., MORRIS, K., BOTS, P., STAWSKI, T. M., JANSSEN, A., ABRAHAMSEN, L., BLACKHAM, R. & SHAW, S. 2016. Ferrihydrite formation: the role of Fe13 Keggin clusters. *Environmental science & technology*, 50, 9333-9342.
- WEEKS, C. L., ANBAR, A. D., WASYLENKI, L. E. & SPIRO, T. G. 2007. Density functional theory analysis of molybdenum isotope fractionation. *The Journal of Physical Chemistry A*, 111, 12434-12438.
- WEHRLI, B. & STUMM, W. 1989. Vanadyl in natural waters: adsorption and hydrolysis promote oxygenation. *Geochimica et Cosmochimica Acta*, 53, 69-77.
- WEIDNER, E. & CIESIELCZYK, F. 2019. Removal of hazardous oxyanions from the environment using metal-oxide-based materials. *Materials*, 12, 927.
- WHARTON, J., ROSS, D., TREACY, G., WILCOX, G. & BALDWIN, K. 2003. An EXAFS investigation of molybdate-based conversion coatings. *Journal of applied electrochemistry*, 33, 553-561.
- WHITE, A. F. & PETERSON, M. L. 1996. Reduction of aqueous transition metal species on the surfaces of Fe (II)-containing oxides. *Geochimica et Cosmochimica Acta*, 60, 3799-3814.
- WHITE, D. J. & LEVY, L. S. 2021. Vanadium: environmental hazard or environmental opportunity? A perspective on some key research needs. *Environmental Science: Processes & Impacts*, 23, 527-534.
- WHO 1988. International Programme on Chemical Safety.
- WHO 2000. *Air quality guidelines for Europe*, Copenhagen: WHO Regional Office for Europe.
- WHO 2003. Molybdenum in drinking-water: background document for development of WHO guidelines for drinking-water quality.

- WICHARD, T., MISHRA, B., MYNNENI, S. C., BELLENGER, J.-P. & KRAEPIEL, A. M. 2009. Storage and bioavailability of molybdenum in soils increased by organic matter complexation. *Nature Geoscience*, 2, 625.
- WILLIAMS, D. B. & CARTER, C. B. 1996. The transmission electron microscope. *Transmission electron microscopy*. Springer.
- WILLMOTT, P. 2019. *An introduction to synchrotron radiation: techniques and applications*, John Wiley & Sons.
- WINSTANLEY, E. H., MORRIS, K., ABRAHAMSEN-MILLS, L. G., BLACKHAM, R. & SHAW, S. 2019. U (VI) sorption during ferrihydrite formation: Underpinning radioactive effluent treatment. *Journal of hazardous materials*, 366, 98-104.
- WISAWAPIPAT, W. & KRETZSCHMAR, R. 2017. Solid phase speciation and solubility of vanadium in highly weathered soils. *Environmental science & technology*, 51, 8254-8262.
- WONG, J., LYTLE, F., MESSMER, R. & MAYLOTTE, D. 1984. K-edge absorption spectra of selected vanadium compounds. *Physical Review B*, 30, 5596.
- WRIGHT, M. T. & BELITZ, K. 2010. Factors controlling the regional distribution of vanadium in groundwater. *Groundwater*, 48, 515-525.
- XU, N., BRAIDA, W., CHRISTODOULATOS, C. & CHEN, J. 2013. A review of molybdenum adsorption in soils/bed sediments: speciation, mechanism, and model applications. *Soil and Sediment Contamination: An International Journal*, 22, 912-929.
- XU, N., CHRISTODOULATOS, C. & BRAIDA, W. 2006a. Adsorption of molybdate and tetrathiomolybdate onto pyrite and goethite: effect of pH and competitive anions. *Chemosphere*, 62, 1726-1735.
- XU, N., CHRISTODOULATOS, C. & BRAIDA, W. 2006b. Modeling the competitive effect of phosphate, sulfate, silicate, and tungstate anions on the adsorption of molybdate onto goethite. *Chemosphere*, 64, 1325-1333.
- YALÇINTAŞ, E., SCHEINOST, A. C., GAONA, X. & ALTMAIER, M. 2016. Systematic XAS study on the reduction and uptake of Tc by magnetite and mackinawite. *Dalton Transactions*, 45, 17874-17885.
- ZHANG, M. & REARDON, E. J. 2003. Removal of B, Cr, Mo, and Se from wastewater by incorporation into hydrocalumite and ettringite. *Environmental science & technology*, 37, 2947-2952.
- ZHANG, P. C. & SPARKS, D. L. 1989. Kinetics and mechanisms of molybdate adsorption/desorption at the goethite/water interface using pressure-jump relaxation. *Soil Science Society of America Journal*, 53, 1028-1034.
- ZHANG, Y., ZHU, X., LIU, T., HUANG, J. & SONG, S. 2013. Effect of colloidal potassium alum formation on vanadium recovery from acid leach solutions of stone coal. *Hydrometallurgy*, 138, 54-58.
- ZHU, H., XIAO, X., GUO, Z., PENG, C., WANG, X. & YANG, A. 2020. Characteristics and behaviour of vanadium (V) adsorption on goethite and birnessite. *Environmental Earth Sciences*, 79, 1-10.
- ZOPFI, J., FERDELMAN, T. G., JØRGENSEN, B. B., TESKE, A. & THAMDRUP, B. 2001. Influence of water column dynamics on sulfide oxidation and other major biogeochemical processes in the chemocline of Mariager Fjord (Denmark). *Marine Chemistry*, 74, 29-51.

9. Appendices

9.1 Appendix 1: Vanadate (V(V)O_4^{3-}) Adsorption to Magnetite and Biogenic Magnetite

XRD and BET Analysis for Magnetite

XRD indicates that the synthesized adsorbent is pure magnetite (Figure 9-1). The BET surface area of the magnetite obtained is $103.5 \pm 0.3 \text{ m}^2/\text{g}$.

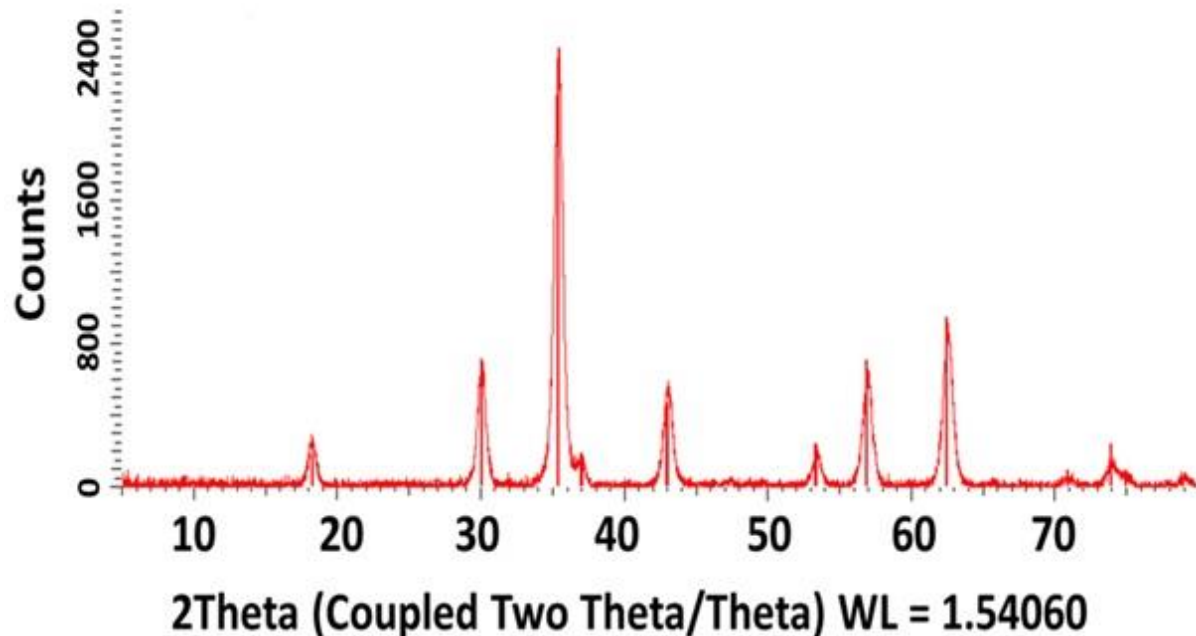


Figure 9-1 X-ray diffraction of synthesized magnetite.

Solution Analysis for V(V) Adsorption to Magnetite and Biogenic Magnetite

V(V) adsorption to magnetite and biogenic magnetite were operated at initial concentration of $1.2 \times 10^{-4} \text{ M}$ at pH 4-13 and shows over 99% of V(V) are adsorbed onto both magnetite and biogenic magnetite surface across the whole pH range (Figure 9-2A and B).

V(V) isotherm adsorption to magnetite at initial V(V) concentration of $2 \times 10^{-6} - 4 \times 10^{-3} \text{ M}$ at pH 7 in 0.1 and 0.01 M NaCl shows near 100% of V(V) are adsorbed onto magnetite at initial

V(V) concentration less than 2×10^{-3} M and the adsorption efficiency decreased to 70% at V(V) concentration of 4×10^{-3} M in 0.01 M NaCl solution (Figure 9-2C).

Different ionic strength was performed for V(V) adsorbed to magnetite experiments using 0.1 M and 0.01 M NaCl solution and shows ionic strength has little impact on the adsorption behaviour, which is similar to the result of Mo(VI) adsorption to magnetite in Chapter 6.

Figure 9-2D shows V(V) isotherm adsorption data (V(V) concentration 2×10^{-6} - 4×10^{-3} M, pH 7) was fitted using the Langmuir model. The maximum adsorption capacity for samples in 0.1 M and 0.01 M NaCl solution are 1047 mg/g and 410 mg/g, respectively. The R factors for the high ionic strength (0.1 M NaCl) of 0.999 and low ionic strength (0.01 M NaCl) of 0.997 indicate Langmuir model fit the data quite well, suggesting adsorption is the key process when V(V) interacts with magnetite at neutral pH.

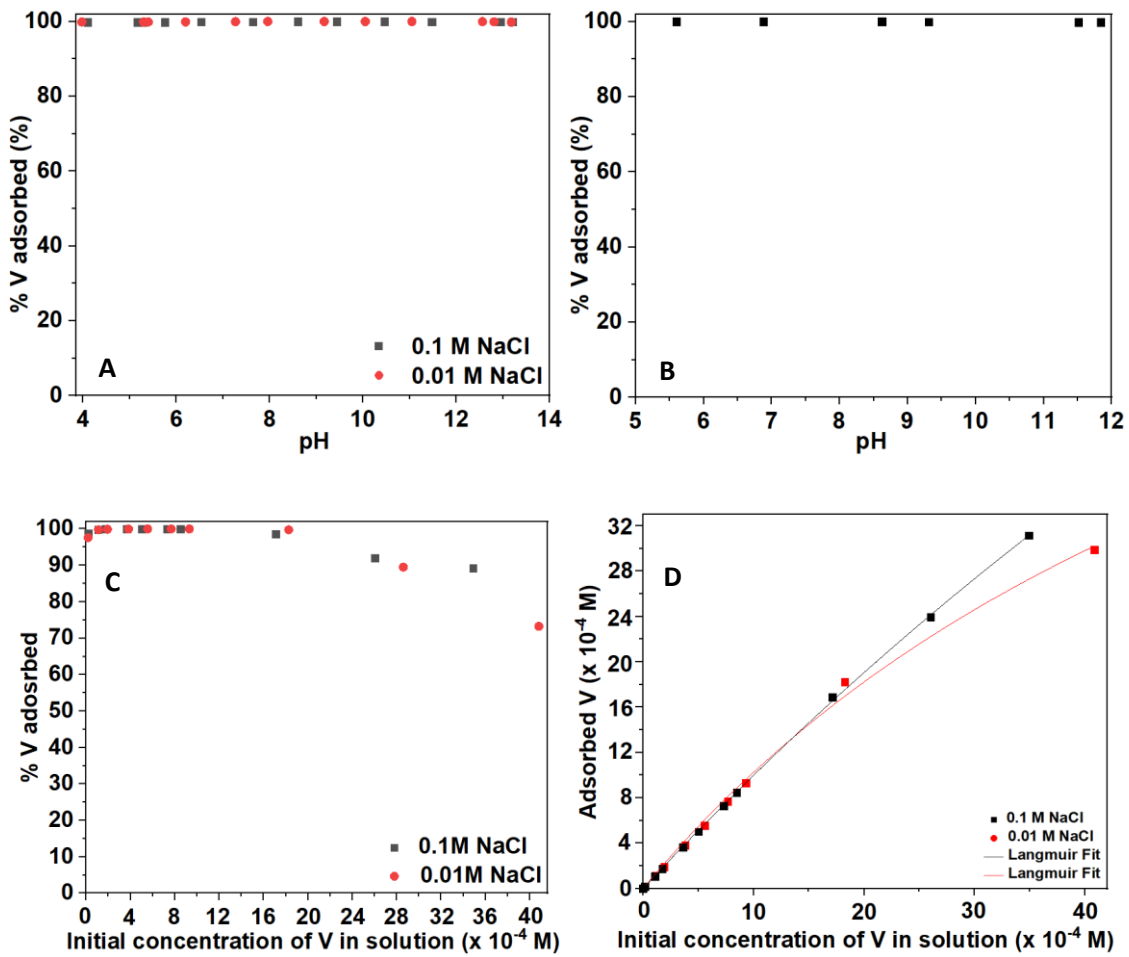


Figure 9-2 V(V) adsorption onto magnetite and biogenic magnetite at a variety of conditions.

(A) V(V) adsorption to magnetite at pH from 2 to 13 in 0.1 and 0.01 M NaCl solution at initial V(V) concentration of 10^{-4} M. (B) V(V) adsorption to biogenic magnetite at pH 5.5-12 in 0.01 M NaCl solution at initial V(V) concentration of 10^{-4} M. (C) V(V) adsorption to magnetite at pH 7 in 0.1 and 0.01 M NaCl solution at initial V(V) concentration of $2 \times 10^{-6} - 4 \times 10^{-3}$ M. (D) V(V) isotherm adsorption to magnetite at pH 7 at initial V(V) concentration from $2 \times 10^{-6} - 4 \times 10^{-3}$ M with Langmuir isotherm fitting.

9.2 Appendix 2: Travel Bursaries and Conference Presentations

Travel Bursaries

- ACS GEOC Student Travel Award (\$ 330) to attend the 2019 American Chemical Society Spring National Meeting & Expo in Orlando.

Oral Presentations

- 2021 Goldschmidt conference in Lyon (Virtual), 5th July 2021.
- 2021 American Chemical Society (ACS) Spring National Meeting & Expo (Virtual), 6th April 2021.
- 2020 American Chemical Society (ACS) Fall National Meeting & Expo (Virtual), 18th August 2020.
- 2020 Goldschmidt Exhibition (Virtual), 22nd June 2020.
- 2019 Clay minerals conference of Clay minerals in the natural and built environment: formation, chemistry & applications in Newcastle, 17th May 2019.
- 2019 American Chemical Society (ACS) Spring National Meeting & Expo in Orlando, 31st March 2019.
- 2018 Postgraduate Research Conference, School of Earth and Environmental Sciences, University of Manchester, 4th December 2018.

Poster Presentations

- Postgraduate Summer Research Showcase, University of Manchester, 12th June 2019.
- Postgraduate Summer Research Showcase, University of Manchester, 26th June 2018.

- Royal society of Chemistry conference in the Geochemistry and Mineralogy of Contaminated Environments in London, 6th June 2018.